Lawrence Berkeley National Laboratory
Recent Work

Title
SUBTHRESHOLD PION PRODUCTION IN THE REACTION [SUP]L39 LA + [SUP]139 LA RIGHT ARROW PI [SUP]+- + X

Permalink
https://escholarship.org/uc/item/40b721cm

Author
Miller, J.

Publication Date
1988

eScholarship.org Powered by the California Digital Library
University of California

LBL-24275
Preprint

Lawrence Berkeley Laboratory
UNIVERSITY OF CALIFORNIA

RECEIVED
LAWRENCE
BERKELEY LABORATORY
MAY 10 1988
LIBRARY AND
DOCUMENTS SECTION

Subthreshold Pion Production in the Reaction $^{139}La + {}^{139}La \rightarrow \pi^{\pm} + X$

J. Miller
(Ph.D. Thesis)

January 1988

TWO-WEEK LOAN COPY

This is a Library Circulating Copy which may be borrowed for two weeks.

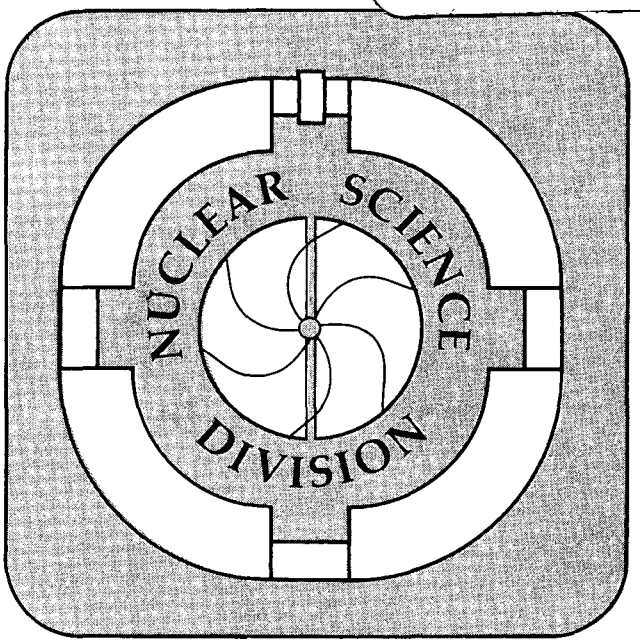

Prepared for the U.S. Department of Energy under Contract DE-AC03-76SF00098

LBL-24275

DISCLAIMER

This document was prepared as an account of work sponsored by the United States Government. While this document is believed to contain correct information, neither the United States Government nor any agency thereof, nor the Regents of the University of California, nor any of their employees, makes any warranty, express or implied, or assumes any legal responsibility for the accuracy, completeness, or usefulness of any information, apparatus, product, or process disclosed, or represents that its use would not infringe privately owned rights. Reference herein to any specific commercial product, process, or service by its trade name, trademark, manufacturer, or otherwise, does not necessarily constitute or imply its endorsement, recommendation, or favoring by the United States Government or any agency thereof, or the Regents of the University of California. The views and opinions of authors expressed herein do not necessarily state or reflect those of the United States Government or any agency thereof or the Regents of the University of California.

LBL-24275

Subthreshold Pion Production in the Reaction $^{139}La + ^{139}La \rightarrow \pi^{\pm} + X$

Jack Miller
(Ph.D. Thesis)

Lawrence Berkeley Laboratory
University of California
Berkeley, California 94720

January 1988

This work was supported by the Director, Office of Energy Research, Division of Nuclear Physics of the Office of High Energy and Nuclear Physics of the US Department of Energy under contracts DE-AC03-76SF00098 and DE-AS05-76ER04699 and the National Science Foundation under grant No. PHY83-12245.

Jack Miller
January 1988
Physics

Subthreshold Pion Production in the Reaction $^{139}\mathrm{La} + ^{139}\mathrm{La} \rightarrow \pi^{\pm} + X$

Abstract

We have measured charged pion production in the reaction ^{139}La $+^{139}$ La $\rightarrow$ $\pi^{\pm} + X$ at three beam energies (246, 183 and 138 MeV/nucleon) below the nucleon–nucleon threshold. Associated multiplicity for charged participants was obtained using a 110–element scintillator multiplicity array. Data were taken over the angular range of 21°–67° in the laboratory (equivalent to 30°–90° in the center of mass). Dependence of the spectra upon pion charge, energy and angle, beam energy, system mass and associated multiplicity was investigated. Based on the isotropic angular distributions and the associated multiplicities for pion production, it appears that subthreshold pions in the range of our experiment are produced predominantly from a source at rest in the center of mass and involving a large number of nucleons. The general character of the subthreshold pion spectra is comparable to previous results above threshold. However, the scaling of the subthreshold pion yield with system mass deviates from the dependence observed in light systems, to an extent which cannot be explained by a simple nucleon–nucleon model. We also found charge dependent structure in the pion spectra, which we analysed in the framework of both Coulomb distortion and clustering models. We conclude that while we did not find clear evidence of collective effects in subthreshold pion production, it would be very worthwhile to conduct a systematic investigation of pion production for all charge states and over a range of angles, system masses and beam energies, below threshold.

Acknowledgements

The experiment which is the subject of this dissertation was carried out by physicists from Lawrence Berkeley Laboratory, Michigan State and Louisiana State Universities and the Université de Clermont II-IN2P3. I gratefully acknowledge the work of the other members of the collaboration: Drs. Goran Claesson, Gary Krebs, Guy Roche, Lee Schroeder, Walter Benenson, Hans van der Plicht, John Winfield, Gilbert Landaud and Jean-François Gilot. We also benefited from the experience of the INS-University of Tokyo group of Prof. S. Nagamiya, whose spectrometer and data acquisition system we used. Drs. Osamu Hashimoto, Isao Tanihata, Toshio Kobayashi and U. of Tokyo graduate students T. Nagae and Shige Hayashi were extremely generous with their time and resources, and shared in the design, construction and testing of the multiplicity array.

Throughout the preparation and running of the experiment we received strong support from the Bevalac operations and engineering staffs. John Bercovitz designed and fabricated on short notice several key elements of the multiplicity array and the absorber. His engineering talents were essential to the success of the experiment, and it was a pleasure working with him.

Several members of the collaboration contributed significantly to the data analysis. Goran Claesson carried out much of the early development of the track reconstruction programs and Gilbert Landaud did extensive work on the acceptance calculation. Gilbert was also responsible for the conception and design of the absorber and the trigger reduction scheme for positive particles. In addition, he is possessed of a keen, critical intellect, of which I made use on a number of occasions. Guy Roche probably answered more of my questions than anyone else, and I appreciated his unfailing patience and his deep knowledge of physics.

Walt Benenson's considerable physical insight helped to guide the course of the research, and his sharp humor always helped to keep things in perspective.

My advisor at LBL, Lee Schroeder, contributed greatly to every phase of this work, starting with the original proposal to do the experiment, and continuing throughout with characteristic intelligence and good humor. I can sum up my experience working with Lee in this way: he believes in doing physics right, and translates that belief into practice. I've learned a tremendous amount from him, and I hope I can emulate his professionalism in my own work as a physicist.

I'm indebted to the other members of my committee, Prof. John Rasmussen and my faculty advisor, Prof. William Knox, for reading the thesis and for a number of interesting discussions on the material. I especially thank Bill Knox for the many kindnesses he extended to me during my time as a student. Others who helped along the way are Prof. Phil Yager, stimulating teacher and regular guy, and Jim Carroll, Shawn Carlson, John Harris, Paul Kirk and Don Murphy.

The friendship of other graduate students has been very important to me. Among others, they are Drew Baden, Jonathan Scheiner, Les Rosenberg, Karl Mallman, Joan Hanley-Hyde, Pete Rowson, Mike Gold, Oren Cheyette, Bill Schmidke, Cary Zeitlin, Amrit Yegneswaran, Bill Christie, Craig Tull and Carol Nichols.

Finally, I'd like to express my appreciation for the graduate students and faculty in the Physics Department at San Francisco State University during 1978–1981. They helped me get back into physics after a long absence, and provided me with the most rewarding educational experience of my life. I'm especially grateful to three of them: to Prof. Gerald Fisher, who got me started, to Prof. Oliver Johns, a true gentleman and a true scholar, and the best teacher I've ever had, and to Dr. Andrew Baden, a gifted physicist and a steadfast friend. Jerry, Oliver, Drew: Thanks.

Contents

List of Figures

List of Tables

1. Introduction

This dissertation reports on the preparation, running and results of an experiment to measure charged pion production in the reaction $^{139}La+^{139}La \rightarrow \pi^{\pm}+X$ at beam energies per nucleon near, but below the production threshold in free nucleon collisions. Associated multiplicity for charged particles was recorded, and used to characterize pion–producing events according to impact parameter. Inclusive pion spectra were taken and analysed with the objective of understanding the reaction dynamics of nucleus-nucleus collisions in the energy range of 138-246 MeV/nucleon.

Motivation

To a first approximation, the nucleus may be taken to be a degenerate Fermi gas of protons and neutrons with a ground state temperature of zero and a ground state density, ρ_0, of approximately 0.17 nucleons/fm^3 [1]. Interactions with leptons, hadrons and nuclei can take a target nucleus on limited excursions from the ground state, by inducing low energy nuclear excitations, or by depositing a large amount of energy in a small part of the nucleus. However, high energy heavy ion projectiles have the unique capability to heat and compress nuclei over an extended volume.

Beam energies per nucleon in such collisions range (at different facilities) from tens of MeV to (currently) 200 GeV. At energies well above the typical nuclear binding energy of about 8 MeV/nucleon, it is in general not meaningful to treat the colliding nuclei as integral objects, subject to whole-body excitations; rather it may be instructive to think in terms of bulk hadronic or nuclear matter, in which individual nucleons (or, at sufficiently high interaction energy,

quarks) are the elemental components.† One may then ask whether a high energy nucleus-nucleus interaction can be understood as a simple superposition of binary nucleon-nucleon collisions, or whether bulk nuclear matter exhibits collective behavior radically different from that found in nuclei near the ground state.

The interaction dynamics is ultimately reflected in the energy and angular distribution of the particles emitted during the collision. Understanding the dynamics therefore requires identifying those features in the detected particle spectra which uniquely characterize the collision process. For example, the angular distribution of particles emitted during a given event has been taken as evidence of collective flow of nuclear matter[2,3], and discrepancies between measured pion multiplicities and predictions of an intranuclear cascade have been cited as evidence for bulk compression of nuclear matter[4,5]. Nevertheless, an explanation based on nucleon-nucleon processes cannot be ruled out in either case[6-10].

Another approach is to look for irregularities in the particle spectra, in the hope that exotic effects might manifest themselves in some deviation from the norm[11-13]. However such signatures might well be obscured by the incoherent background from simple binary processes.

These examples are representative of a general problem in understanding heavy ion collisions, which is that many features of the particle spectra are well-reproduced by a number of models with different assumptions about the collision dynamics. This has been interpreted as being due to the general dominance of geometrical and statistical factors over dynamics in these collisions[14].

Observables related to particles created during the interaction are unique in the respect that the large amount of energy required for particle production

†In this context, a "whole-body excitation" refers to a state where the nucleus retains its identity, as in a rotational or vibrational deformation, for example. "Bulk nuclear matter" refers to matter comprised of nucleons in some configuration other than a nucleus. Such matter may be short-lived, as in a plasma, or long-lived, as in a neutron star.

makes it likely that it occurs in the early stages of the collision and therefore may carry information about nuclear matter at the highest density and temperature reached during the interaction. This assumes, however, that the effects of final state interactions can be unfolded, a non-trivial task, as will be discussed later.

Why subthreshold?

It might be expected that particle production at beam energies per nucleon below the nucleon-nucleon threshold would be a clear signature of collective effects. However, the threshold in nucleus-nucleus collisions is not clearly defined. Fermi motion makes particle production below the free nucleon-nucleon threshold possible, and thus the conclusions of experiments measuring subthreshold production depend upon assumptions about the momentum distribution of the constituent nucleons. However, even assuming that binary production can proceed at beam energies well below the free nucleon threshold, the contribution of such processes to the production cross section should be greatly reduced, perhaps revealing collective effects which are obscured at higher energies.

Why pions?

At the typical nuclear distance scale of the order of 1 fm, hadron-hadron interactions are well–described in terms of meson exchange, and thus meson observables may give direct insight into the interaction dynamics. The pion is the lightest meson, with masses of 139.6 MeV and 135.0 MeV for charged and neutral pions, respectively;[15] this corresponds to a threshold value of about 290 MeV for pion creation in nucleon-nucleon collisions. Pion production has been extensively measured both above and below threshold, providing a considerable body of data for comparison purposes. This is an important point, since changes in the behavior of the pion spectra as the beam energy is lowered might signal changes in the primary pion production mechanism.

Organization of this dissertation

The search for interesting physics relating to pion production below threshold was the principal motivation for the experiment to be described here. To this end, Chapter 2 surveys prior experimental and theoretical work on pion production near threshold in nucleon-nucleon *(NN)*, nucleon-nucleus *(NA)* and nucleus-nucleus *(AA)* collisions. The extensive data above threshold (and in *pA* collisions below threshold) will be used to characterize the phenomenology of pion production in binary *NN* collisions, which can serve as a baseline for the study of subthreshold *AA* collisions. The limited data previously taken below threshold will also be used for comparison purposes: to study mass and beam energy dependences, for example. In addition, it has been proposed that in some cases the data contain direct evidence of collective effects, and these conjectures, along with some of the theoretical models of pion production, will serve as guidelines for this study.

Chapters 3 and 4 describe the experimental methodology. Chapter 4 contains details of background subtraction and particle identification, which are particularly important in the case of π^+. Sec. 4.6 is a discussion of the calibration of the detection system against other experimental results, which is important in the studies of mass and beam energy dependence.

The results of our experiment are presented and discussed in Chapter 5, and Chapter 6 contains a summary and our conclusions.

The inclusive cross sections (both variant and invariant) are tabulated in Appendix A, the associated multiplicity distributions are presented in Appendix B and the raw pion data are tabulated in Appendix C. The detector specifications are given in Appendix D. Appendix E contains some basic definitions of cross sections and kinematics. Appendix F contains some details of the intranuclear cascade of Cugnon *et al.*, including a description of how ratios of charged and

neutral pions are calculated in a pure delta isobar model.

The reader interested only in the experimental results can reasonably begin with Chapter 5, referring to the other material as needed.

2. Pion production–phenomenology and theory

The pion was postulated by Yukawa in 1935[16] as the exchange particle of the strong nuclear force, and naturally occurring charged pions were first detected in 1947, in emulsion studies of cosmic ray interactions[17]. Shortly thereafter, the first laboratory observations of negative[18] and positive[19] pions were made at the 184-inch cyclotron at Berkeley. These studies used beams of 380 MeV (95 MeV/nucleon) α-particles incident on a carbon target; thus the first confirmed artificially-produced pions were produced in subthreshold nucleus-nucleus collisions. This possibility had been discussed the previous year by McMillan and Teller[20], who calculated that the Fermi momenta of the target nucleons would reduce the required incident beam energy per nucleon to below the free nucleon threshold.

The first systematic accelerator studies of pion production with nucleon projectiles were carried out at cyclotrons during the early nineteen-fifties. Due to the limited beam energies available before the advent of the first proton synchrotrons (the Cosmotron at Brookhaven and the Bevatron at Berkeley), the early data were taken near (but above) threshold.

2.1 Pion production in nucleon-nucleon collisions

The early data on pion production in *NN* collisions with beam energies below about 500 MeV were well-described by phenomenological models[21-23] based upon consideration of angular momentum and isospin. These studies pointed to the importance of the state with I=$\frac{3}{2}$, J=$\frac{3}{2}$, which had already been identified in pion-nucleon scattering, and led in turn to the formulation of the resonance, or isobar model[24-26], in which pion production occurs when one of the interacting

nucleons is excited to an isobaric state which subsequently decays to a nucleon and a pion. Additional experimental [27-32] and theoretical[33] work established the dominance of the $(\frac{3}{2}, \frac{3}{2})$ resonance (now known as the $\Delta(3,3)$ or $\Delta(1232)$) in pion production at beam energies below 1 GeV, with non-resonant contributions to pion production becoming significant near threshold. Pion angular distributions exhibit a dependence of the form $1 + B\cos^2\theta$, with the value of the coefficient depending upon the relative contributions of resonant and non-resonant production at a given beam energy and upon the relative momenta of the pion and nucleon in the final state[25,26]. For production near threshold, B is found to be between 1 and 3, with the distribution becoming more isotropic as the beam energy is increased by several hundred MeV[26]. The coefficient is generally smaller for neutral than for charged pions[26].

Due to the difficulty of obtaining beams of neutrons, the bulk of the data on $NN \rightarrow NN\pi$ is for pp and pn initial states. The most complete excitation function near threshold is that for the reaction $pp \rightarrow pp\pi^0$[28], shown in Fig. 2.1. Results for the reactions $pp \rightarrow pn\pi^+$[34] and $pn \rightarrow pn\pi^0$[29] are comparable. Total cross sections range from the order of .01 mb near threshold to 5-10 mb at $T_p \simeq$ 700 MeV, and are generally consistent with predictions of the isobar model.

An early attempt to calculate meson production in high energy NN collisions was the statistical model of Fermi[35]. The essential assumption in this model is that the production is governed by statistics rather than by dynamics, with cross sections determined by the available phase space, subject to conservation laws. The assumption of statistical equilibrium is justified as follows: all of the incident kinetic energy is deposited in a small volume where, due to the strong coupling between pions and nucleons, it is very quickly distributed among all the available degrees of freedom. Although Fermi pointed out the limitations of

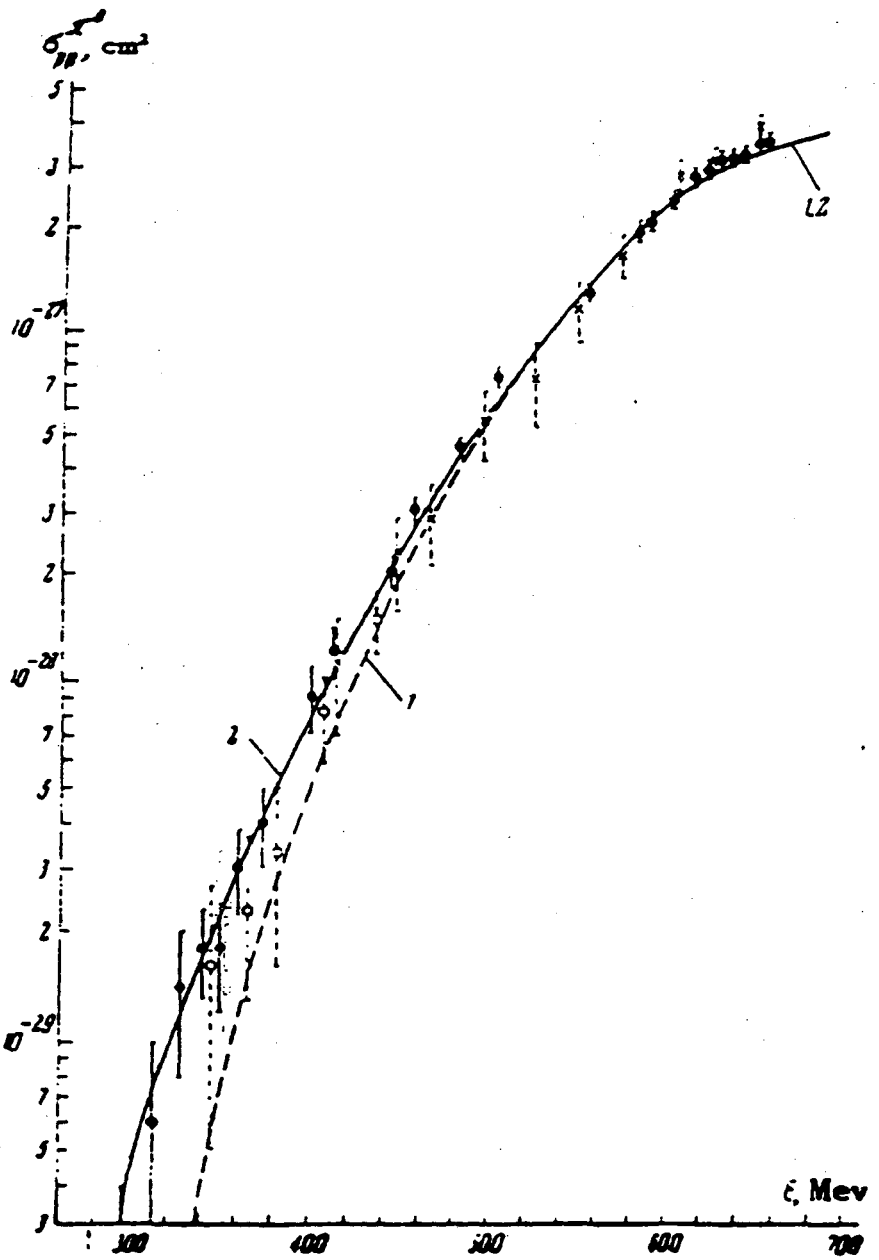

Figure 2.1. Excitation function near threshold for the reaction $pp \rightarrow pp\pi^0$. (From Ref. 28.) The dashed curve (1) is calculated from the resonance (isobar) model of Mandelstam [26]. The solid curve (2) is result of the same calculation, with non-resonant production taken into account.

this approach near threshold, where the phase space is limited, the model is in reasonable agreement with the data up to about 800 MeV. However, it fails to reproduce the data for beam energies between 1 and 2 GeV. Lindenbaum and Sternheimer, who considered[25] the low energy results in the context of the isobar model, suggested that the agreement between the Fermi theory and the data in that region is probably coincidental.

Its limitations as a theory of low energy elementary interactions notwithstanding, recent models based upon the Fermi theory have had some success in predicting particle production in nucleus-nucleus collisions, where its statistical assumptions have more validity. This will be discussed later in this chapter, as well as in Chapter 5.

2.2 Pion production in nucleon-nucleus collisions

If simple binary interaction models are to account for particle production in nucleus-nucleus collisions, they must first be tested in the elementary case of a single nucleon incident on a complex target. The transition from nucleon to nuclear targets introduces several new considerations related to the propagation of particles through the nuclear medium. Scattering, absorption, energy loss and charge exchange must be taken into account for the projectile and for any emitted particles. Arguably the most important feature affecting particle production is the momentum distribution of the target nucleons. This is perhaps the simplest example of a collective effect, in the sense that it is arises in the confinement of nucleons within the nuclear volume. Still, its role in pion production is through binary NN interactions.[†]

The isobar model is implicitly a nucleon-nucleon model, and tests of its validity are closely linked to tests of binary production. Early work by Peaslee[37]

[†] A related effect is the presence of high momentum components which arise due to short range nucleon–nucleon correlations[36].

established the validity of isobar model predictions of charged pion production ratios from 0.35–2.3 GeV protons incident on light nuclear targets. Calculations incorporating isobar production and Fermi motion have been successfully applied to a wide range of energies and mass systems, including the simplest NA interaction: $p + d \rightarrow \pi + X$ from threshold to 700 MeV[29,38].

Extensive measurements of π^0 production in pA collisions near threshold were made at Dubna[29,39,40]. Fig. 2.2 summarizes the mass and energy dependence of production near threshold for deuterium, carbon and lead targets. The excitation functions reflect the influence of the delta resonance, especially in the tendency of the yield to peak near a proton energy of about 600 MeV. The dependence of the total π^0 cross section on target neutron (N) and proton (Z) numbers was found to be[40]

$$\sigma_{\pi_0} \sim [Z + N \cdot (\sigma_{\pi_0}(np)/\sigma_{\pi_0}(pp))]^{\frac{2}{3}},$$

which corresponds roughly to production at the nuclear surface. The yield is seen to fall off somewhat faster for light nuclei than for heavier targets. This is interpreted[39,40] as being due to higher momentum components in the Fermi distribution in the heavier nuclei; however the nucleon-nucleon single collision model of Guet and Prakash[36], which uses momentum distributions obtained from (γ, p) and $(e, e'p)$ reactions, predicts subthreshold production in the reaction $p+^{12}\mathrm{C} \rightarrow \pi^0 + X$ to be as much as two orders of magnitude below the data. Uncertainty as to details of the calculation of Ref. 39 makes it difficult to choose between the two, although the momentum distributions used in Ref. 36 might be more realistic.

Charged pion production by protons incident on a range of nuclear targets up to ^{238}U was measured by Cochran *et al.*[30] (proton energy, T_p=730 MeV), Crawford *et al.*[32] (T_p=585 MeV) and DiGiacomo *et al.*[41] (T_p=330, 400 and 500 MeV). For the heavier targets (A $\geq$ 27), the π^+ and π^- total cross sections are

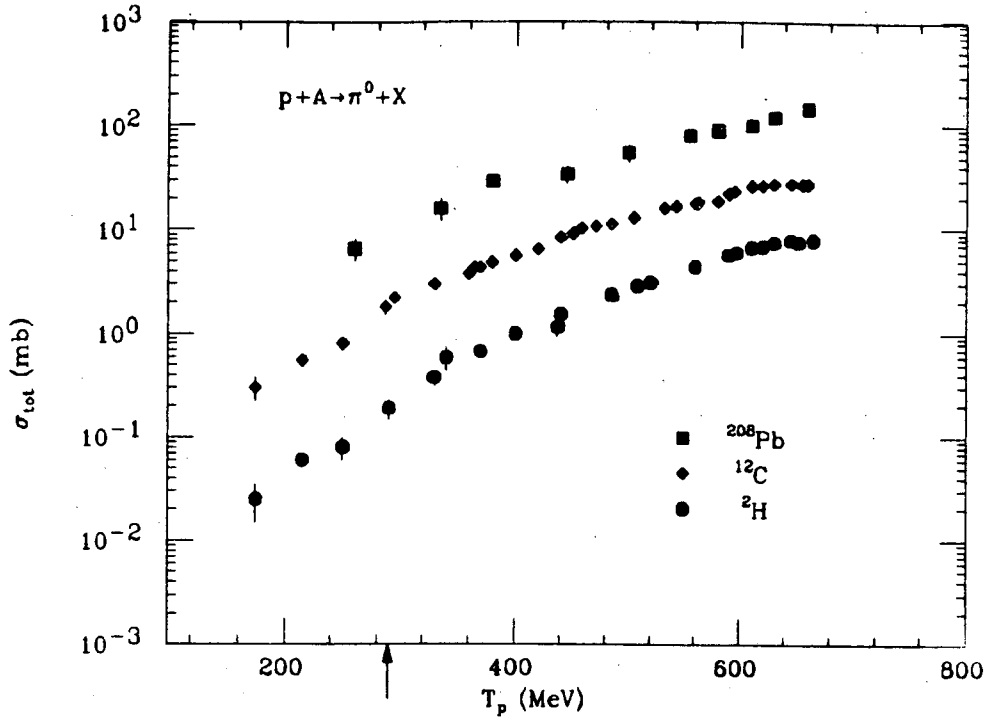

Figure 2.2. Excitation function for π^0 production by 175–665 MeV protons on nuclei, from data of Refs. 29, 39 and 40. The arrow denotes the free nucleon threshold energy of 290 MeV.

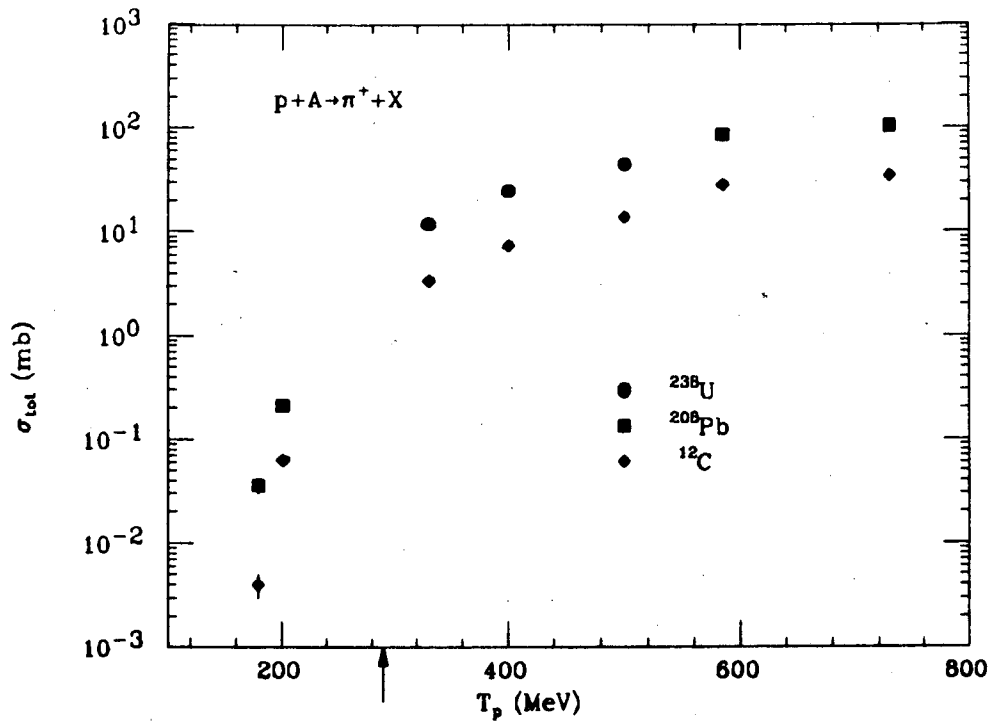

Figure 2.3. Excitation functions for production of positive pions by 180–730 MeV protons incident on light and heavy nuclei, from Refs. 30, 32, 41 and 42.

roughly proportional to $Z^{\frac{1}{3}}$ and $N^{\frac{2}{3}}$, respectively. Spectral shapes and angular distributions were found to be not very sensitive to the target mass for either charged pion, and an approximate scaling law was found to hold[30] for targets from ^{27}Al to ^{232}Th:

$$\frac{d^2\sigma(A)}{d\Omega dE}/\sigma_{tot}(A) = \frac{d^2\sigma(B)}{d\Omega dE}/\sigma_{tot}(B),$$

where A and B denote different nuclear targets.

The general features of the data of Cochran *et al.* are reproduced by a calculation of Sternheim and Silbar[43], who treat charged pion production within an isobar model framework, with nucleon and pion absorption, rescattering, energy degradation and charge exchange taken into account. This calculation was later extended to neutrons.[44] Ratios of total cross sections for charged pions are in good agreement with the data. While the calculation does not reproduce the Z and N-dependence of the π^+ and π^- cross sections, the authors make a qualitative argument to explain the dependence: Δ production is assumed to become geometric for $A \simeq 20 - 50$, and initial pion production is proportional to $A^{\frac{2}{3}}$ (the area of the disk in which the deltas are made). Absorption removes all pions except those on the edge of the disk, which reduces the dependence to $A^{\frac{1}{3}}$. However, positive pions are made mainly from protons, which introduces an additional factor of Z/A. The net result for π^+, is:

$$(A^{\frac{1}{3}}) \cdot (Z/A) = Z/(A^{\frac{2}{3}}) \sim Z^{\frac{1}{3}}.$$

For π^-, absorption is balanced by charge exchange, but π^- and π^0 come mainly from neutrons, hence:

$$(A^{\frac{2}{3}}) \cdot (N/A) = N/(A^{\frac{1}{3}}) \sim N^{\frac{2}{3}}.$$

The (p,π) reactions comprise a distinct class of reactions, near threshold (Refs. 42,45–48). These certainly exhibit some degree of collectivity, in that they

leave the residual nucleus in an excited state, but whether the pion production process is a collective one is still not clear. For example, data for the (p,π) reaction $^{209}\mathrm{Bi}\,(p,\pi^-\ xn)\,^{210-x}\mathrm{At}$ at 200 MeV incident energy[48] are reproduced by an intranuclear cascade (INC).[49] In this model, pion production takes place in binary collisions, with the coherent effect coming into play later in the interaction, as the recoiling particles heat the nucleus, which then cools by evaporation of neutrons. On the other hand, the very different nucleon-nucleon model of Ref. 36 generally underpredicts the total pion cross sections for the closely related reactions $^{208}\mathrm{Pb}(p,\pi^{\pm})X$ at $T_p = 180$ and 201 MeV, measured by Bimbot *et al.*[42]. The fact that the latter model *does* reproduce the general shape of the excitation function suggests[42] that in pion production, the shapes of the spectra do not seem to reflect the underlying dynamics.

Fig. 2.3 summarizes the measurements of total inclusive cross section for positive pions from pA collisions at proton energies between 180 and 730 MeV. The results are similar to those for π^0 (and for π^- , not shown). The approximate $Z^{\frac{1}{3}}$ dependence for π^+ production is seen to persist down to at least $T_p = 200$ MeV, with the possibility of a stronger dependence at lower beam energies.

The magnitudes of the π^+ and π^0 cross sections are closer than expected from resonance production, but the data are from different experiments and are not relatively normalized, making comparison difficult. As noted earlier, the charged pion ratios found in Ref. 30 and 32 conform to the isobar model.

A recent experiment[50-52] measured the inclusive differential cross section for charged pions from 240-500 MeV protons incident on $^{64}\mathrm{Cu}$ and 240 MeV protons on $^{12}\mathrm{C}$ at several angles. As shown by Fig. 2.4, the dependence of the invariant cross section at a given laboratory angle on pion kinetic energy has a characteristic form over a range of beam energies above and below threshold. The spectra may be fit assuming a dependence of the form

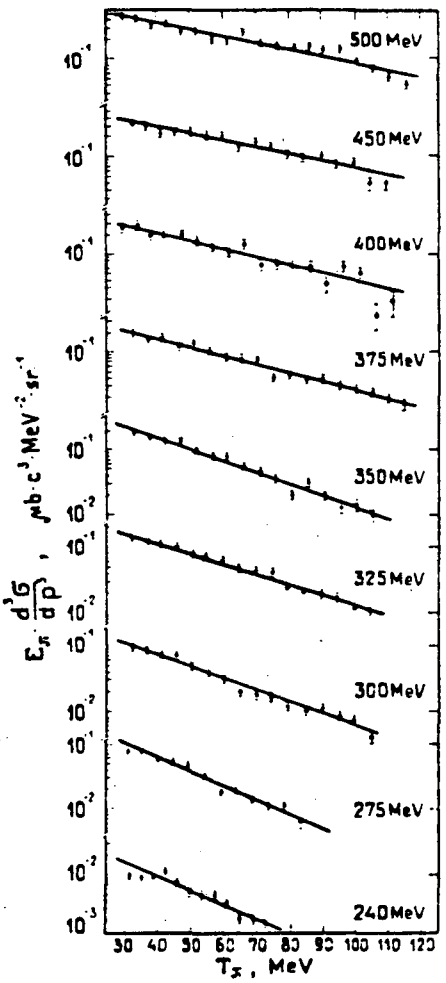

Figure 2.4. Dependence of the positive pion cross section at $\theta_{lab} = 90°$ on pion lab kinetic energy for the reaction 240-500 MeV p+Cu $\rightarrow \pi^+ + X$. The solid lines are least square fits to $Ae^{-\frac{T}{T_0}}$. (From Ref. 52.)

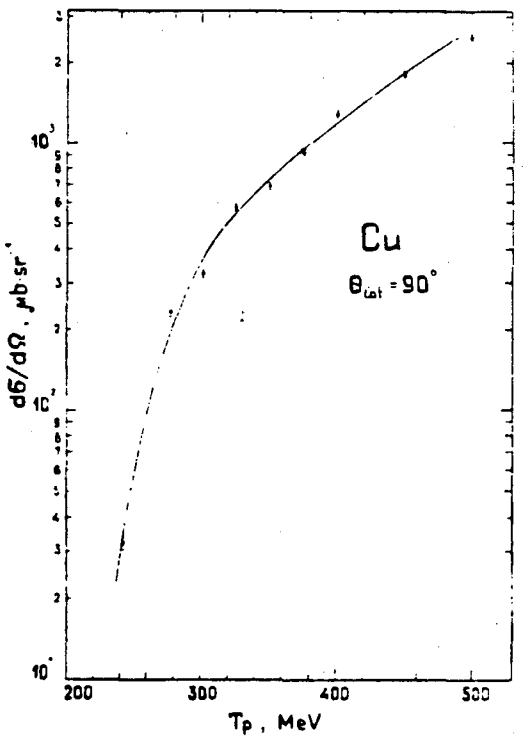

Figure 2.5. Beam energy dependence of the differential cross section for positive pion production by protons on ^{64}Cu at $\theta_{lab} = 90°$. (From Ref. 52.)

$$E\frac{d^3\sigma}{dp^3} = Ae^{-\frac{T}{T_0}},$$

where T is the pion kinetic energy and E is the total pion energy. The slope parameter, T_0, and intercept, A, are found to vary smoothly with proton energy across the free nucleon threshold, with the exception of the point at $T_p = 350$ MeV, which is attributed to possible dibaryon production[52]. Interestingly, a comparison of data for carbon and copper targets at $T_p = 240$ MeV shows T_0 to be insensitive to the mass of the target, which may indicate a dependence upon "some bulk properties of nuclear matter." [52]

Fig. 2.5 shows the excitation function for the π^+ differential cross section for protons on ^{64}Cu at $\theta_{lab} = 90°$. The cross section falls by almost an order of magnitude between 500 and 300 MeV, and by another order of magnitude between 300 and 240 MeV. A similar trend was seen in the total inclusive cross section for pions from pp and pA collisions, and was attributed to the effects of the delta resonance. Comparisons between Figs. 2.4 and 2.5 and AA data plotted in the same way will provide a simple phenomenological test for coherent effects.

One other feature of the charged pion data of Cochran *et al.*[30] which is not reproduced by the calculation of Ref. 43 is an increase in the π^-/π^+ ratio at the lowest pion energies at lab angles between 15° and 150° for heavy targets (Cu-Th). A similar effect was observed by Crawford *et al.*[32], who found that for targets heavier than ^{27}Al and lab angles between 22.5° and 135°, the π^+ spectra were peaked at higher pion energies than the π^- spectra. These features are illustrated for $\theta_{lab} = 90°$[†] by Fig. 2.6. Note that although both spectra in Fig. 2.6a turn down at low pion energy, the effect is sharper for π^+ , as can be seen when the ratio of π^- to π^+ cross sections is plotted (Fig. 2.6b). The authors of Ref. 32 speculate that this effect "may be due to the Coulomb force between the emitted pions and the nuclear protons."

[†]For a proton incident on a heavy target, the lab and c.m. frames are almost the same.

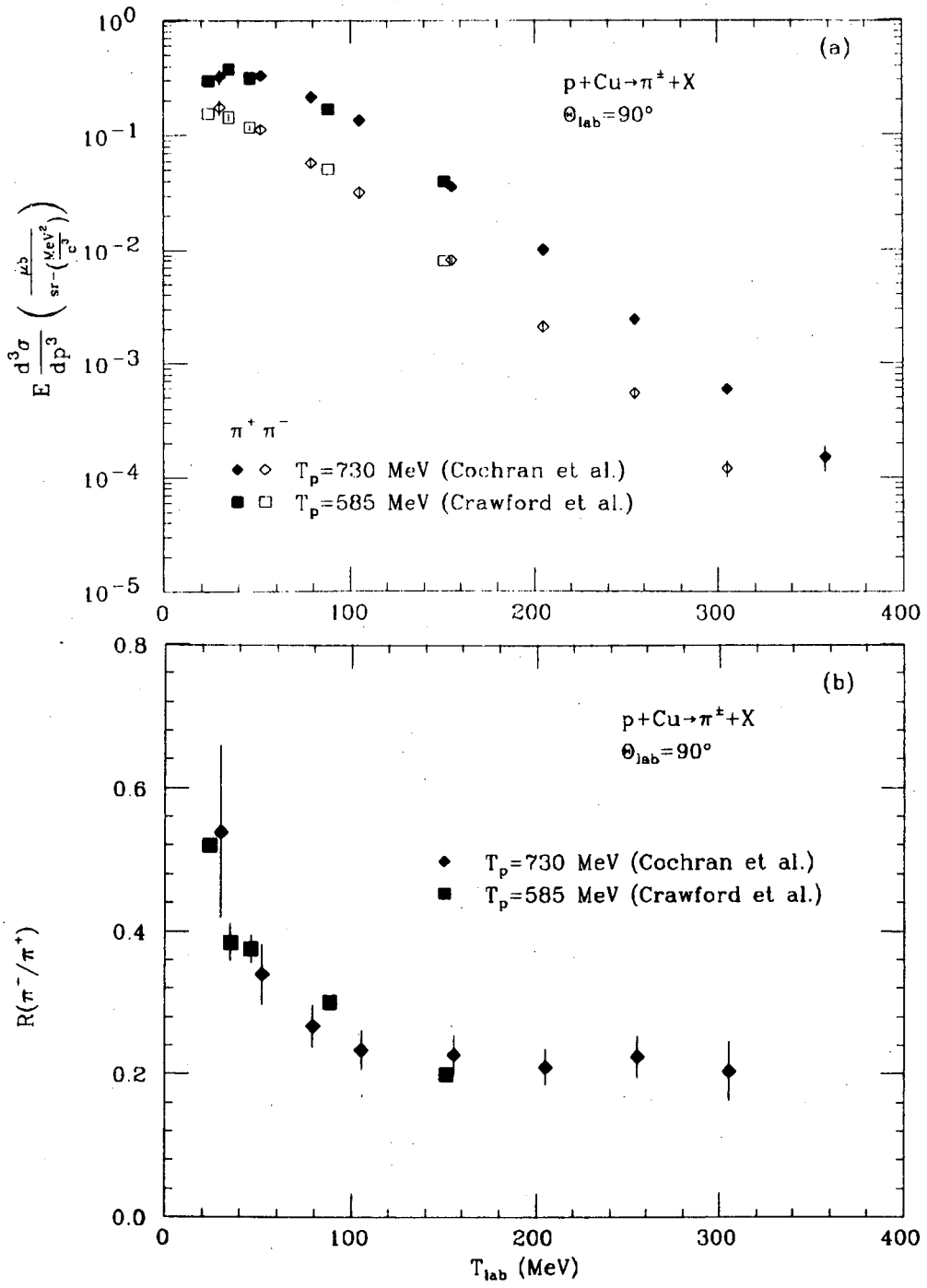

Figure 2.6. (a) Invariant cross section as a function of pion lab kinetic energy for the reaction $p + \mathrm{Cu} \rightarrow \pi^{\pm} + X$ at $\theta_{lab} = 90°$ for beam energies of 585 MeV (Ref. 32) and 730 MeV (Ref. 30). (b) Ratio, $R(\pi^- / \pi^+)$ of the π^- and π^+ cross sections as a function of pion energy.

2.3 Pion production in nucleus-nucleus collisions

We will first review the experimental results on pion production between threshold and 2.1 GeV/nucleon, followed by a brief discussion of models which have been put forth to describe the data. Lastly, we will survey the data on subthreshold pion production and discuss the theories specific to that energy regime.

2.3.1 Experimental results above threshold

The data surveyed in this section were taken at the LBL Bevalac. Both inclusive[53-62] and exclusive[4,5,63-65] data have been taken, the former with magnetic spectrometers and range-energy telescopes, the latter with a streamer chamber.

The inclusive data are of particular interest, for two related reasons. First the data were taken on a spectrometer very similar to that used in the present experiment, thus reducing the uncertainty due to relative normalization. (This will be discussed in more detail in Chapter 3.) Second, the data for a wide range of targets, projectiles and beam energies have been presented in a consistent form. Since much of the discussion in Chapter 5 concerns the comparison between present and past data, these are important attributes. The review which follows will serve the dual function of surveying earlier work and introducing some of the analytical tools to be used later.

Pion energy and angle dependence

Fig. 2.7 shows the variation of the inclusive π^- cross section with pion lab momentum and lab angle for two different mass systems at a beam energy of 800 MeV/nucleon. The cross section at all angles decreases approximately exponentially with increasing pion momentum. The slope and inclusive yield depend

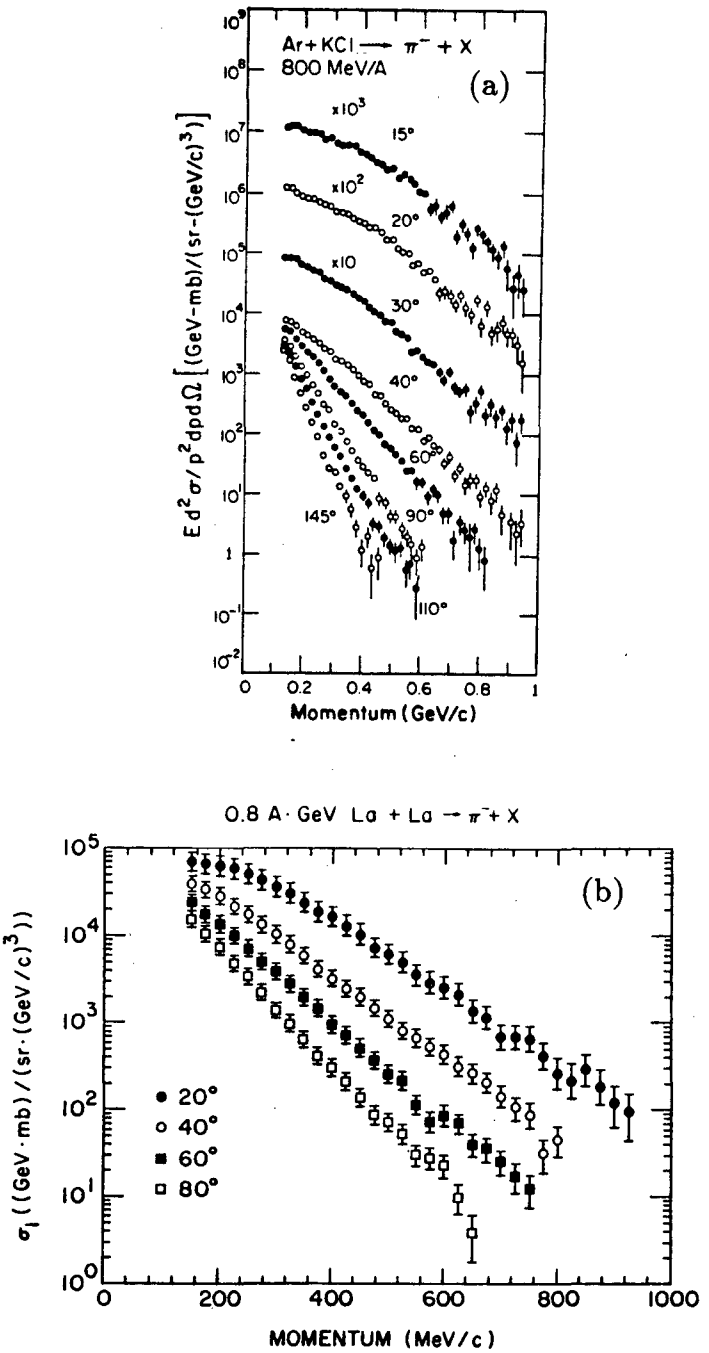

Figure 2.7. Invariant cross section as a function of pion lab momentum for two symmetric mass systems at a beam energy of 800 MeV/nucleon. (a) ^{40}Ar + KCl $\rightarrow \pi^- + X$ for $15° \leq \theta_{lab} \leq 110°$ (From Ref. 57.) (b) ^{139}La $+^{139}$La $\rightarrow \pi^- + X$ for $20° \leq \theta_{lab} \leq 80°$ (From Ref. 62.)

strongly upon lab angle. However, the results may be more clearly interpreted when viewed in a different rest frame. In a heavy ion collision, two natural reference frames, in addition to those of the laboratory and the projectile, are the respective rest frames of the nucleon–nucleon and nucleus–nucleus centers of mass. In a symmetric collision, i.e. $A_{tgt} \simeq A_{proj}$, these are of course the same, while in an asymmetric collision only the nucleon-nucleon c.m. is well-defined.

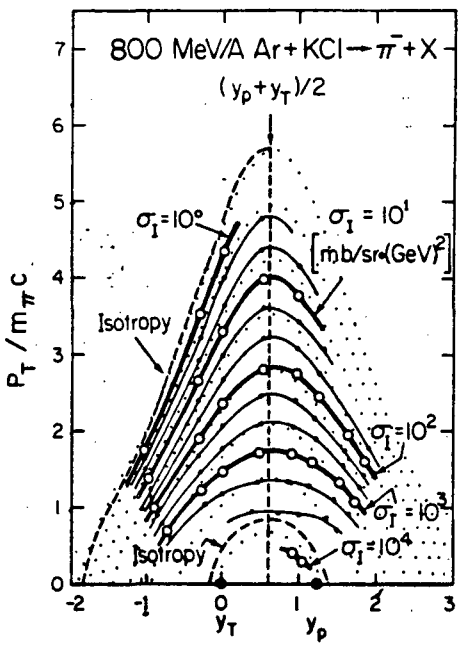

Figure 2.8. Contour plot of inclusive π^- spectra in the plane of transverse momentum and rapidity for the reaction 800 MeV/nucleon ^{40}Ar + KCl $\rightarrow \pi^- + X$. The dotted curves denote isotropic emission. (From Ref. 57.)

Fig. 2.8 shows Lorentz-invariant π^- cross sections plotted in the plane of transverse momentum (in units of the pion mass) and rapidity for the approximately symmetric ^{40}Ar + KCl system. Plotted in this way, the angular distribution for high transverse momentum (p_T) pions is seen to be almost isotropic in the center of mass. There is some forward–backward peaking around $p_T \simeq m_\pi c$,[53] while for p_T <50 MeV emission is once again isotropic.[55]

To test the importance of nucleon-nucleon processes (and the Δ isobar) in NA collisions, Chiba *et al.*[55] compared the data for the reaction Ne+Pb $\rightarrow \pi^+ + X$ at 800 MeV/nucleon to an incoherent superposition of the cross sections measured for 730 MeV/nucleon p + Pb $\rightarrow \pi^+ + X$ in Ref. 30, finding good agreement for pion lab momenta below 500 MeV/c. Forward–backward peaking consistent with isobar production was also observed at 400 MeV/nucleon[56]. In the latter study, a rudimentary multiplicity selection was done using eight tag counters, and the observed peaking was found to be insensitive to the associated multiplicity of charged particles.

Beam energy dependence

Fig. 2.9 illustrates both the beam energy dependence and the characteristic exponential shape of the pion spectra. As in the p-nucleus case (Fig. 2.4), the

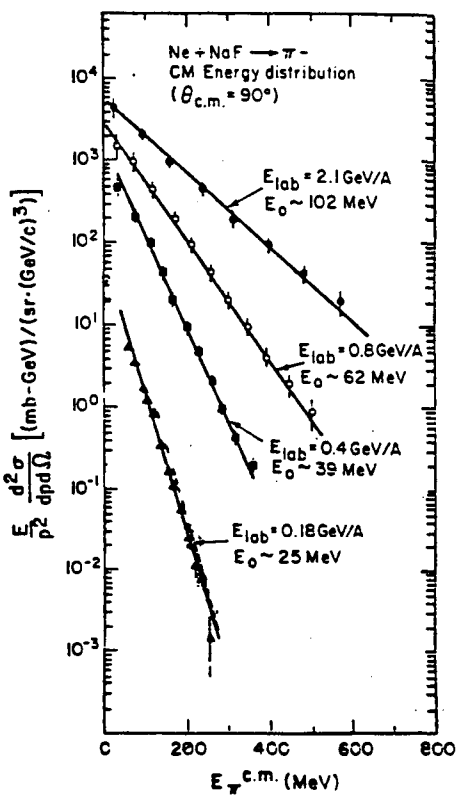

Figure 2.9. Invariant cross section as a function of pion kinetic energy for π^- production at $\theta_{c.m.} = 90°$ from the system ^{20}Ne + NaF beam energies between 183 and 2100 MeV/nucleon. (From Ref. 12.) Note that this figure includes some subthreshold data.

data may be fit by an exponential of the form $Ae^{-\frac{T}{T_0}}$. Here again, the slope parameter T_0 is seen to increase with increasing beam energy. The beam energy dependence is shown in a different way in Fig. 2.10, in which the inclusive yield at $\theta_{c.m.} = 90°$ is seen to fall more rapidly near threshold than at higher energies.

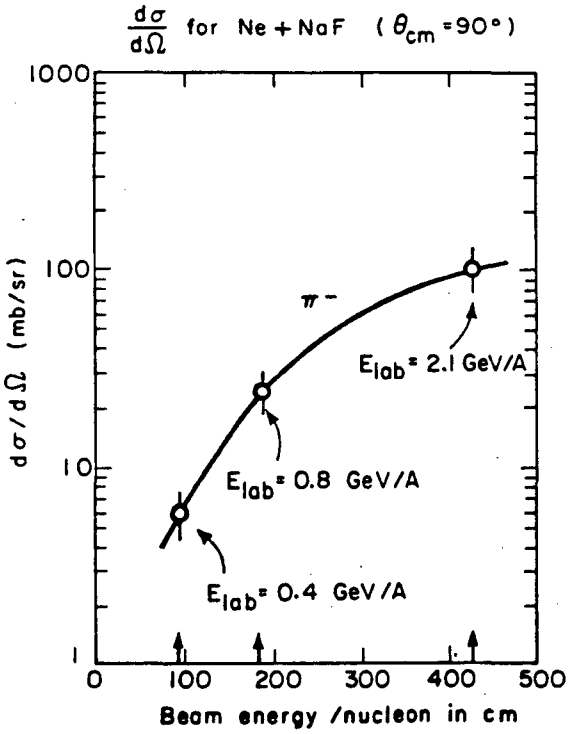

Figure 2.10. Differential inclusive cross section $d\sigma/d\Omega$ at $\theta_{c.m.} = 90°$ as a function of beam energy for the reaction $^{20}\mathrm{Ne} + \mathrm{NaF} \rightarrow \pi^- + X$. (From Ref. 57.)

Stock *et al.*[4] measured π^- multiplicity in central collisions of 0.36-1.8 GeV/nucleon ^{40}Ar with KCl, and found pion production to rise rapidly but smoothly with beam energy.

Target and projectile mass dependence

Data are available at a beam energy of 800 MeV/nucleon for the equal mass systems C+C, Ne+NaF, Ar+KCl and La+La[57,62]. Fig. 2.11 shows the π^- spectra at $\theta_{c.m.} = 90°$. The slope parameter increases by 10% between C+C and Ar+KCl, but is the same for La+La as for Ar+KCl. The pion yield for the lighter systems

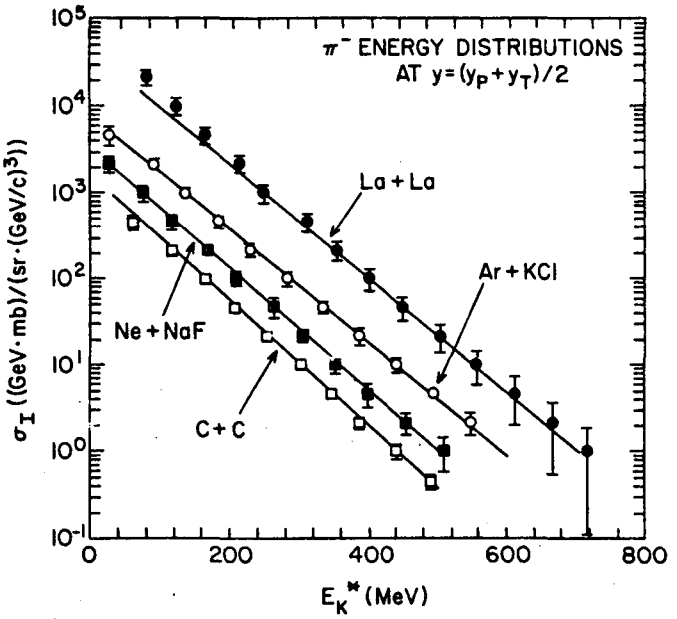

Figure 2.11. Invariant cross section as a function of pion kinetic energy for π^- production at $\theta_{c.m.} = 90°$ from the systems C+C, Ne+NaF, Ar+KCl and La+La at 800 MeV/nucleon beam energy. The corresponding slope parameters are 60, 62, 66 and 66 MeV. (From Ref. 62.)

has been parameterized by $A^{\alpha(E_K^*)}$, where E_K^* is the pion c.m. kinetic energy and $A = A_{tgt} = A_{proj}$. For the low energy pions, which comprise the bulk of the yield, α is close to 4/3 (i.e. $A_{tgt}^{\frac{2}{3}} \cdot A_{proj}^{\frac{2}{3}}$), which corresponds to surface production. α also increases with energy, which is equivalent to saying that the slope parameter generally increases with increasing system mass. For the two heaviest systems ($A_{tgt} + A_{proj} = 80$ and 278, respectively), which have the same slope, $\alpha = 4/3$. The dependence of pion yield on target mass was also studied for 800 MeV/nucleon Ne projectiles incident on Na, Cu and Pb targets,[53] and was found to be close to $A_{tgt}^{\frac{2}{3}}$.

Multiplicity dependence

The number of participant nucleons associated with pion production can be an important clue to the nature of the production process. The streamer chamber is well suited to studying this. It is sensitive to charged particles over almost 4π of solid angle, and it can be triggered on a selected range in impact parameter as reflected in the associated multiplicity of charged projectile fragments.

Fung *et al.*[63] studied total π^- production for 0.4-2.1 GeV/nucleon ^{12}C and ^{40}Ar projectiles incident on a range of light to target masses. They found the pion multiplicity to be proportional to charged particle multiplicity, with a proportionality constant which increases sharply with energy but is approximately independent of the target and projectile mass. These results are quantitatively consistent with the data of Harris *et al.*[5], who recently measured pion multiplicity as a function of beam energy and number of participants for the ^{139}La + ^{139}La system at beam energies between 0.53 and 1.35 GeV/nucleon. Combining these results with earlier work[65] for ^{40}Ar + KCl they find the ratio of produced pions to participant nucleons at each beam energy to be a constant, independent of target and projectile mass, but increasing with beam energy. Based on this, they argue for a volume (A) rather than surface ($A^{\frac{2}{3}}$) dependence for pion production.

In another streamer chamber study, Brockmann *et al.*[64] used a "central" (i.e. highly charged projectile fragment) trigger to study small impact parameter collisions in the reaction Ar+KCl $\rightarrow \pi^- + X$ at 1.8 GeV/nucleon. They found an overall isotropic distribution for the emitted pions, but with some anisotropy—characteristic of resonance production—at intermediate pion energies. The fact that this is true even for central collisions is interpreted as evidence that the intermediate energy pions are produced at the edge of the collision region, and therefore undergo little or no rescattering, so that the Δ kinematics are not washed out. These results are consistent with those of Ref. 56, which did a

simple multiplicity selection, as noted above (p. 20).

DeJarnette *et al.*[66] studied production of charged and neutral pions from central (i.e. high participant multiplicity, low impact parameter) collisions of 1–2 GeV/nucleon ^{12}C with Pb. The central trigger was implemented via an 8 element scintillator multiplicity array. Pion production was found to increase smoothly with beam energy, and a correlation was found between high energy pions and high participant multiplicity. The same detector system was used for more extensive measurements on the same system at beam energies down to 0.4 GeV/nucleon[67]. All the parameters relating to pion production were found to depend smoothly upon beam energy, with no evidence of unusual production thresholds. The authors concluded that beam energy was the most important factor in determining the number of pions produced, with increased pion multiplicities in high (participant) multiplicity collisions attributable to the increase in the number of hard nucleon–nucleon collisions.

Pion production beyond the kinematic limit

An alternative to studying subthreshold particle production is to measure pions produced with energies greater than the maximum permitted in a simple *NN* collision. As in the subthreshold case, such production may be due to a relatively well–understood process such as Fermi–boosted *NN* collisions, or it may be due to collective effects.

Papp *et al.*[68,69] measured charged pion production at $\theta_{lab} = 2.5°$ in collisions of light nuclei (A=1-12) with nuclear targets (Be, C, Cu and Pb) at beam energies of 1.05–2.1 GeV/nucleon. The results were consistent with a calculation assuming production in *NN* collisions. Schroeder *et al.*[70] studied charged pion production at the other kinematical pole, at $\theta_{lab} = 180°$. Beams of 0.8–4.89 GeV protons were directed at targets ranging from ^{12}C to Pb. The pion spectra were found to

be exponential, with slope parameters only weakly dependent upon target mass. A possible trend away from pure NN production at the highest beam energies was noted. Chessin[71] extended this study to include beams of ^{40}Ar at 1.05 and 1.83 GeV/nucleon. Once again, the results were found to be consistent with production (with the aid of Fermi motion) in NN collisions.

Charge-dependent effects

Charge-dependent structure in the pion cross sections will figure prominently in the discussion of our results in Chapter 5. Several authors[57,59,61,72] have reported a dependence on pion energy of the ratio, $R_{-/+}$, of charged pion cross sections. In particular, Benenson *et al.*[72], Sullivan *et al.*[59] and Frankel *et al.*[61] found $R_{-/+}$ to be strongly peaked for pions near the beam rapidity, an effect which they attribute to the Coulomb field of the projectile.

Wolf *et al.*[54] measured the cross section for the reaction $^{40}\mathrm{Ar}+^{40}\mathrm{Ca} \rightarrow \pi^+ + X$ at 1.05 GeV/nucleon and found a maximum at mid-rapidity ($\theta_{c.m.} = 90°$, $p_T \simeq .4 m_\pi c$). No such effect is seen in the pp or p-nucleus data. Some indication of a similar effect was seen in $^{40}\mathrm{Ar} + ^{40}\mathrm{Ca} \rightarrow \pi^+ + X$ at 1.05 GeV/nucleon[58] and in $^{20}\mathrm{Ne} + \mathrm{NaF} \rightarrow \pi^+ + X$ at 800 MeV/nucleon[55], but not at 400 MeV/nucleon[56]. A purely Coulomb explanation is placed in doubt by the data of Frankel *et al.*[61], who subsequently reported seeing the mid-rapidity peak for π^-, as well, and by preliminary data of Harris *et al.*[60] for 1.05 GeV/nucleon $^{40}\mathrm{Ca} + ^{40}\mathrm{Ca}$, for which $R_{-/+} \simeq 1$ in the region of the enhancement observed by Wolf *et al.*[54].

2.3.2 Models (general)

In this section, we review a number of different models which attempt to account for pion production in nucleus-nucleus collisions. Some of them will be compared with our results; the remainder are included for completeness. (The

term model is used advisedly. Since there is no exactly calculable theory of nucleus-nucleus interactions, we are at present limited to a descriptive approach.) The models are loosely grouped in several classes, among which there is considerable overlap. All of the models to be discussed have had success at accounting for some of the data, while none of them account for all of the data. (This led Hüfner and Knoll to speculate[73] that "only a few basic ingredients common to all approaches are responsible for the success" and, more poetically, that "agreement with the data is invariant under theory.") The models may be grouped in the following general classes: thermal, statistical, hydrodynamical, collision and microscopic.

Thermal

The essential assumption of thermal models[74-78] is that the available energy (projectile kinetic energy − nuclear binding energy) heats the participants into "a quasi-equilibrated nuclear fireball", which may be treated as a relativistic ideal gas, subject to description using the formalism of statistical mechanics. In particular, the particle spectra should be characterized by a Maxwell-Boltzmann distribution:†

$$\sigma_{var} = \frac{d^3\sigma}{dp^3} = const \cdot e^{-\frac{T}{T_0}},$$

where the negative inverse slope, T_0, corresponds to the temperature of a thermalized particle source. In this respect, the model is strikingly consistent with the data.

†There is a distinction between parameterizing the variant (σ_{var}) and invariant (σ_{inv}) cross sections in this way. While $\sigma_{var} = d^3\sigma/dp^3$ is directly proportional to particle number, $\sigma_{inv} = Ed^3\sigma/dp^3$ has an additional multiplicative energy dependence, and thus cannot, strictly speaking, be described by a Maxwell-Boltzmann distribution. In this work, we will present variant cross sections wherever possible, but for ease of comparison with other data it will sometimes be more appropriate to use the invariant cross section. In any event the difference between the slope parameter extracted from σ_{inv} and from σ_{var} is usually small.

The fireball model assumes that the number of participants and the number of collisions which they undergo is sufficiently large to be treated statistically. Kapusta[76], following the arguments of Chapline *et al.*[74] that a prerequisite for fireball formation is that the mean free path of the interacting nucleons and mesons be much smaller than the fireball size, arrives at an approximate value of 50 for the number of participants required for thermalization. However the exponential shape of the pion spectra is also observed in collisions where the number of participants must be much smaller (Fig. 2.4). Furthermore, the isotropic emission of pions predicted by the model is not always observed in connection with exponential spectra[56,64]. Lastly, the model, while reproducing the shape of the pion spectra reasonably well, consistently overpredicts the yield by a factor of about two[78]. The fact that some observables are statistical in character does not necessarily imply the formation of a fireball.

Siemens and Rasmussen[79] have proposed a variation on the thermal model. In the "blast wave" model, a heated, compressed fireball explodes, producing a characteristic peak in the pion kinetic energy spectrum. The authors make two points which are of relevance to our experiment. First, the peak in the kinetic energy spectrum should be independent of charge (to rule out Coulomb effects), and second, the probability for the blast wave to be formed should be enhanced in central collisions. These points will be taken up in chapter 5.

Statistical

The statistical model of Knoll and Bohrmann[80,81] assumes that a nucleus-nucleus collision may be treated as a number of uncorrelated interactions between groups of nucleons. Particle production in each group interaction is considered to proceed according to the Fermi statistical theory (p. 7), with particles distributed according to the available phase space. The final momentum distributions are

derived from an incoherent superposition of the products of these interactions. Some of the difficulties of the fireball and related models may arise in the fact that statistical methods are being applied to finite numbers of particles.The underlying assumptions of the statistical and thermal (such as the "firestreak" [78]) models are quite similar, but whereas the thermal models assume equilibration of the nuclear system as a starting point, the statistical model takes into consideration the conditions under which it occurs, and in particular the consequences of the limited phase space available to the nucleon clusters. Consequently, the latter model does somewhat better [81] at reproducing the high energy (i.e. near the phase space limit) tails of the pion spectra, while overpredicting the yield to about the same degree as the thermal calculation.

Hydrodynamical

In the limit of many participants undergoing many interactions, the colliding nuclei may behave in some respects as a fluid. Hydrodynamical models [82-84] assume a nuclear equation of state and solve equations for conservation of particle number, momentum and energy. The basic assumptions are similar to those of thermal models (p. 26), however in the fluid dynamical picture some energy which might otherwise go into pion production goes into bulk nuclear matter effects such as collective flow. Hydrodynamical models typically underpredict the pion yield. One possible explanation for this is that the hydrodynamic limit—if it is reached at all in nucleus-nucleus collisions—is not reached in all cases, or for that matter even for all the nucleons in a given collision. The blast wave model [79] incorporates features of both thermal and hydrodynamical models.

Collision

This class incorporates several types of models, which share the the assumption that pion production proceeds through one or more binary nucleon-nucleon collisions. At beam energies in excess of several hundred MeV/nucleon, binary collisions are known to dominate the production process, through the delta and higher resonances. The most interesting energy regime is that near and below threshold, where pions produced in this way comprise the background from which signatures of collective effects, if any, must be extracted.

Mention should also be made here of a very important subclass, the intranuclear cascade (INC). The INC is probably the most elementary model of pion production in nucleus-nucleus collisions. The interacting nuclei are considered to be collections of hard, point-like particles, which follow straight line trajectories and interact according to free nucleon scattering cross sections. Pion production proceeds through resonances, and effects such as pion absorption, isospin, nuclear binding and Pauli blocking, which might modify the experimental cross section, may or may not be included. The simple assumptions of the cascade make it a very useful baseline model.

Microscopic

The theory of non-equilibrium transport processes in a plasma has been adapted[85,86] to nucleus-nucleus collisions by adding to the Boltzmann (or Vlasov) equation[87] a quantum mechanically correct collision term which includes Pauli blocking. The collision term is due to Uehling and Uhlenbeck[88], hence the appellation BUU (or VUU) for this type of calculation. Dynamical input to the model is in the form of the external field assumed to drive the transport process. Pion production and absorption are assumed to proceed through the delta resonance, and are calculated using the experimental elastic and inelastic scat-

tering cross sections. This feature connects the VUU calculation to the cascade; if the Pauli blocking is removed from the collision term, and the mean field is turned off, the cascade is recovered. VUU theory has been used to calculate the π^- excitation function for beam energies between 0.3 and 2.0 GeV/nucleon[86], and does considerably better than a simple INC, although it still overpredicts the pion yield.

2.3.3 Experimental results below threshold

The experimental record of subthreshold pion production will be divided here into three sections: inclusive production above 60 MeV/nucleon beam energy, inclusive production below 60 MeV/nucleon and "coherent" production, with beam energy near the absolute threshold. The demarcation at 60 MeV/nucleon is somewhat arbitrary, but is suggested by the work of Bertsch[89] who has shown that, although it is energetically possible for the total excitation energy to go into production of a single pion, the true absolute threshold is higher, at $T_{beam} \simeq 54$ MeV/nucleon, due to limitations on the final state phase space.[†]

$\mathbf{T_{beam} = 60-290}$ MeV/nucleon

For light projectiles (typically ^{12}C) at beam energies between 60 and 85 MeV/nucleon, the exponential dependence of cross section upon pion energy continues to hold[90-94]. The dependence of the slope parameter upon beam energy is consistent with results at higher energies. Mass dependences of the form $(A_{tgt} \cdot A_{proj})^{\alpha}$, with α between 0.65 and 0.8, have been reported. Charge dependence of the spectra has been seen at forward angles[93] and at mid-rapidity[94].

[†]In his "first collision" model[89], Bertsch calculates the effective scattering cross section for two nucleons in the endcaps of colliding Fermi spheres, on the assumption that only nucleons of the highest relative momentum can create a pion. The cross section is a function of the elementary nucleon-nucleon scattering cross sections, the initial separation between the Fermi spheres (equivalent to the c.m. energy/nucleon of the interaction) and the final states permitted by the Pauli principle. It is the last factor that turns out to determine the threshold.

The data have been variously interpreted in a binary collision framework[91] and as evidence for collective effects[92,95]. Michel[95] compared the total inclusive cross section for π^0 production by 84 MeV/nucleon ^{12}C projectiles incident on a number of different targets to three possible target-projectile mass dependences:

$$\sigma \propto A_{proj} \cdot A_{tgt}$$
$$\sigma \propto A_{proj}^{\frac{2}{3}} \cdot A_{tgt}^{\frac{2}{3}}$$
$$\sigma \propto (A_{tgt} \cdot A_{proj}^{\frac{2}{3}} + A_{proj} \cdot A_{tgt}^{\frac{2}{3}})$$

These expressions represent respectively, volume, surface and participant- number dependences. The results are summarized in Fig. 2.12. The fact that the

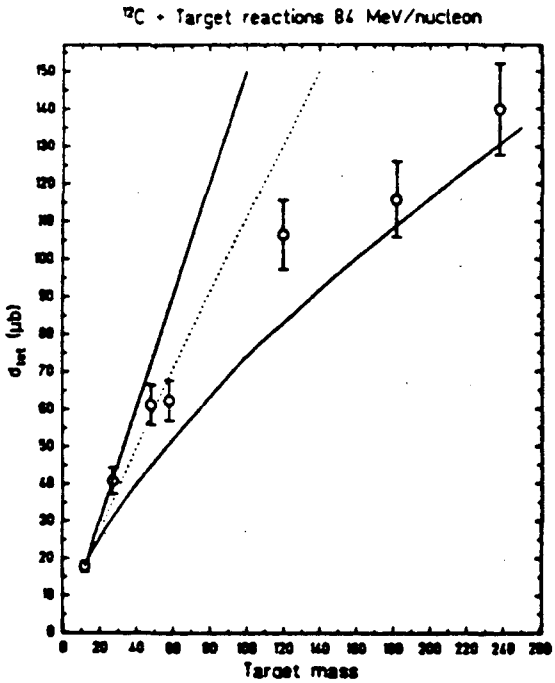

Figure 2.12. Target mass dependence of the total inclusive π^0 cross section for 84 MeV/nucleon ^{12}C on a variety of projectiles. The upper and lower solid lines represent volume and surface dependence, respectively. The dashed line represents dependence on the mean number of participant nucleons. (From Ref. 95.)

data does not seem to depend on the number of participants is taken to suggest the influence of cooperative mechanisms in pion production at this energy.

As pointed out by Bertsch[89], the energy range between 100 and 300 MeV/nucleon offers a favorable combination of high density and suppression of

incoherent production, and also spans the free nucleon pion production threshold of about 290 MeV/nucleon. Data in this region is still limited, and has previously been confined to light and intermediate projectiles ($A \leq 20$). Early studies measured total multiplicities for charged pions produced in nuclear emulsions. McNulty *et al.*[96] found an anomalously high production rate from beams of 100 and 280 MeV/nucleon ^{20}Ne. However, these results were shown to be in error due to misidentification of fast protons as pions[97,98]. In subsequent emulsion experiments, no pion production was observed, presumably because emulsion techniques are not sensitive enough to measure the small cross sections at these energies.

Benenson *et al.*[72] measured charged pion production in the reaction ^{20}Ne + NaF $\rightarrow \pi^{\pm} + X$ at 0° for beam energies between 80 and 383 MeV/nucleon. Some data was also taken on Cu and U targets, and angular distributions for $0° \leq \theta_{lab} \leq 30°$ were taken at 219 MeV/nucleon for NaF and U targets. The cross section was found to rise by about four orders of magnitude between the minimum and maximum beam energy. The target mass dependence was approximately $A^{\frac{2}{3}}$, and the angular distribution was isotropic for θ_{lab} between 0° and 30°.

Charge-dependent distortion of the spectra, similar to that observed above threshold (p. 25) was observed by Benenson and also by Sullivan *et al.*[59] for 280 MeV/nucleon ^{20}Ne incident on C, NaF, Cu and U.

A more extensive angular distribution was taken by Nagamiya *et al.*[12] for the 183 MeV/nucleon Ne incident on NaF and Pb targets. Pion emission was found to be approximately isotropic between 20° and 90° in the laboratory. (30° and 110° in the center of mass.) The pion spectra for both targets exhibited the familiar exponential shapes, and the slope parameters were almost independent of target mass. The variation of the pion yield with target mass was found to be approximately consistent with an $A^{\frac{2}{3}}$ dependence. The object of this experiment

was to search for evidence of a proposed "pionic instability"[11] which would be a precursor to a pion condensate. The signature for this effect was conjectured to be an enhancement in the pion production cross section at a center of mass pion momentum $\simeq (2-3)m_\pi c$. This part of the experiment produced a null result.

Finally, in a predecessor to the experiment reported on here, π^- production was measured at $\theta_{c.m.} = 90°$ in ^{139}La $+^{139}$La collisions at 246 MeV/nucleon.[13] The results were consistent with those of Ref. 12, but with a higher yield and slope parameter. Once again, no evidence of the pionic instability was found.

Probably the most significant feature of the limited data between 100 MeV/nucleon and threshold is its consistency with results above threshold. This is illustrated by Fig. 2.9, showing the smooth variation in slope and yield as the beam energy changes by more than an order of magnitude.

$T_{beam} < 60$ MeV/nucleon

Considerable data[99-102] has been accumulated at beam energies approaching the "absolute" threshold, where all the incident nucleons would have to pool their energy to produce a single pion. (This is also well below the 54 MeV/nucleon limit of Ref. 89.) One might expect the onset of collective effects to be evident in at least some of this data. In fact, as is the case for the higher energy subthreshold data, there are no dramatic deviations from the trends established above threshold. The exponential shape of the pion spectra continues to hold, the slope parameter decreases with beam energy and is approximately independent of system mass,[102] and the yield scales with $A^{\frac{2}{3}}$.[100] There is, however, some evidence of an approach to saturation in both the A-dependence of the yield[100] and the T_{beam}-dependence of the slope[101,102] at the lowest beam energies.

Coherent production

Lastly, we note the evidence for fully coherent production of pions in collisions of light ions[103-108]. These experiments, in analogy to the (p,π) experiments discussed earlier (p. 12), measure pion production where the final state includes a product nucleus in the ground state or in a low-lying excited state. For example, Bimbot *et al.* observed the reaction ^{4}He(^{3}He, π^+)^{7}Li,^{7}Li* for the ground and first two excited states of ^{7}Li.

Aslanides *et al.*[103] and Bressani *et al.*[108] observed apparent coherent production superimposed upon the exponential spectrum characteristic of incoherent binary production in the reaction $^3\mathrm{He}+^6\mathrm{Li} \rightarrow \pi^- + X$ at 303 MeV/nucleon beam energy (Fig. 2.13). While this beam energy is actually slightly above threshold, the relevance of this work to the present study is that it is the only data which clearly shows the influence of both coherent and incoherent effects in the same reaction.

2.3.4 Models (below threshold)

Collision

In the spirit of the work of McMillan and Teller[20], Bertsch[89] proposed a "first-chance" model for subthreshold pion production with the aid of Fermi momentum, assuming that only the first collision undergone by a nucleon would be sufficiently energetic to create a particle. Other collision calculations[36,91,94,109,110] have used the same general ideas, although not always restricted to single collisions. The success of such models at low energies is highly sensitive to the shape of the Fermi distribution assumed, and especially to the high momentum tail of the distribution. While it has been shown that much of the data may be fit in this way, there are also some problems with this approach. In addition to the effective threshold of 54 MeV/nucleon calculated by Bertsch, reservations

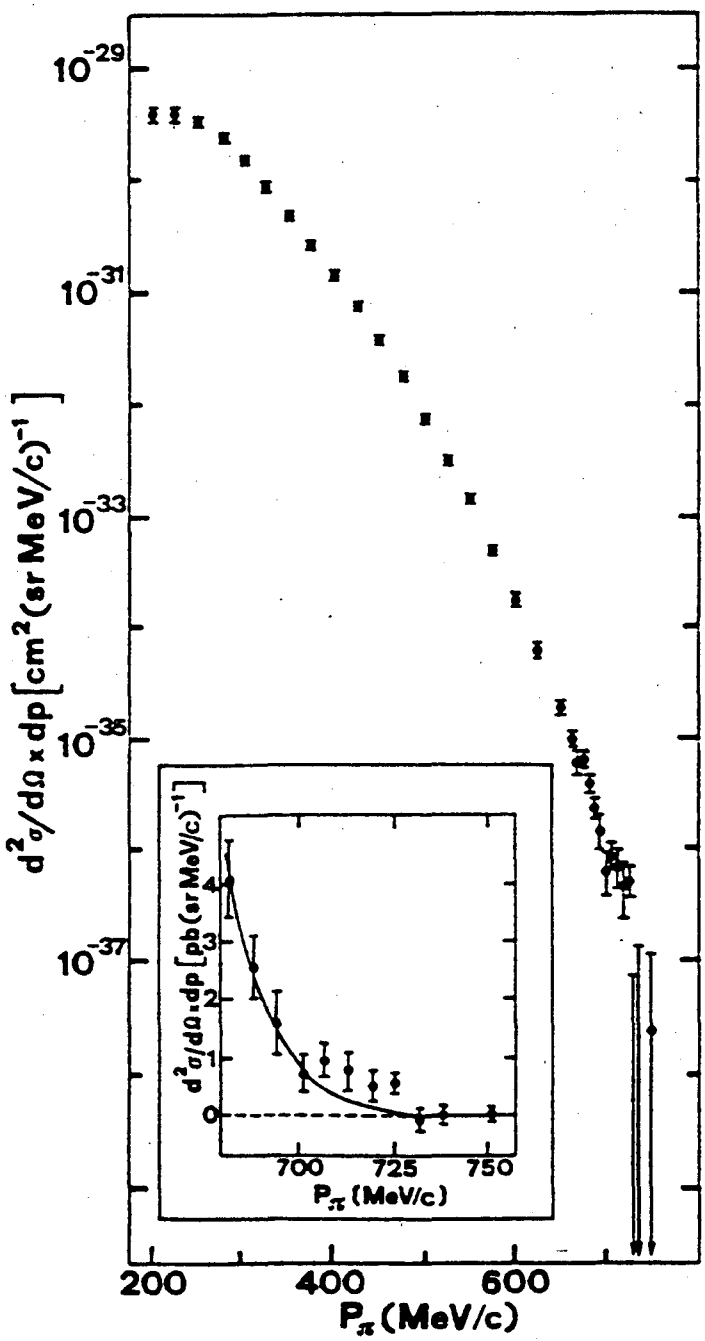

Figure 2.13. Cross section, $d^2\sigma/dpd\Omega$, as a function of pion momentum for the reaction ^{3}He $+^6$ Li $\rightarrow \pi^- + X$ at 303 MeV/nucleon beam energy. Note the apparent coherent signal at slightly above 700 MeV/c. (From Ref. 103.)

have been expressed by Shyam and Knoll[111] regarding the reliance upon the high momentum components in the Fermi gas model. They calculated that a single collision model with a more realistic shell model prescription cannot reproduce the data. Most of the objections center on the region below 100 MeV/nucleon; collision models do better at the higher subthreshold energies[36], although the feasibility of a binary production mechanism for the highest momentum pions is still questionable[12,13].

Statistical

The statistical, "phase space" model (p. 27) has been extended to pion production below threshold[112]. Pion spectra are built up from an incoherent sum of the final state pions from all possible clusters of nucleons. The final states are once again determined according to the Fermi statistical model. In this way, the model is implicitly collective, although the nature of possible collective phenomena is not addressed. Contact with the INC is made through the use of the cascade[113] to obtain the cross sections for cluster formation. Good agreement is found with the data above 60 MeV/nucleon, including that of Ref. 12 at 183 MeV/nucleon. The latter finding is in contrast to the results with an earlier version of the model. This will be discussed further in Chapter 5.

An alternative statistical model, proposed by Aichelin and Bertsch[114], calculates pion production in the form of evaporation of particles from a compound nucleus. The basic framework is that of the compound nucleus model of Weisskopf[115]. This approach has much in common with the work of Fermi[35] and Bohrmann, Shyam and Knoll[80,81,111,112], in its assumptions of the applicability of statistical methods to high energy processes and spectra determined by the available phase space. Further studies along these lines have been carried out by Aichelin[116], Prakash, Braun-Munzinger and Stachel[117] and Bonasera and

Bertsch[118].

Other models

In conclusion, we briefly mention other collective models which have been proposed, mainly to account for the data below 100 MeV/nucleon.

Pion bremsstrahlung Vasak, Müller, Greiner and collaborators[119-121] envision pions being radiated from a decelerating projectile nucleus in analogy with the radiation of photons from a decelerated electric charge. This model gives good agreement with some of the data below 100 MeV/nucleon.

Weizsäcker-Williams Hiller and Pirner[122] generalized this method to the nuclear case: the cloud of virtual pions surrounding the projectile scatters on the target, with some of the pions scattering to on-shell final states. This picture has been applied with some success to the coherent pions in the data of Ref. 103.

Pionic fusion Klingenbeck, Dillig and Huber[123] point out that in the case coherent production from light ions (p. 34), the well-defined final states preclude a statistical or thermal interpretation. They suggest that the target and projectile undergo fusion, with the energy released in the form of a pion.

Coherent isobar This model[124,125] proposes the coherent excitation of a Δ isobar in a nucleus undergoing a peripheral collision, with subsequent de-excitation and pion emission.

3. Experimental Apparatus and Procedures

3.1 The Accelerator

This experiment used beams of heavy ions (^{20}Ne and ^{139}La) accelerated by the LBL Bevalac. The Bevalac facility is comprised of two accelerators, the SuperHILAC, a heavy ion linear accelerator, and the Bevatron, a weak–focusing synchrotron (Fig. 3.1). Ions are accelerated in the SuperHILAC to a maximum energy of 8.5 MeV/nucleon, then transferred to the Bevatron for acceleration to the full beam energy desired. A detailed description of the Bevalac and its experimental facilities may be found in Ref. 126.

3.2 The Detector

3.2.1 The Magnetic Spectrometer

The particle detector used in this experiment was the magnetic spectrometer system installed at the end of beam line 30 (B30-2) in the Bevalac External Particle Beam (EPB) area. An earlier but similar version of it is described in Ref. 57, from which some of the specifications in this section are taken. Fig. 3.2 shows the spectrometer as it was configured for our experiment.

The spectrometer magnet is a "C" dipole of length=24″ and width=13″, with a 6″ pole gap. (Detailed magnet specifications may be found in Ref. 126.) It can be rotated about a central pivot to measure particles emitted at different angles. For all of the pion running, the magnetic field was 3.13 kGauss (kG), measured at the center of the magnet. The field has been mapped previously, and an expression for the particle *rigidity* (momentum per unit charge) which assumes a constant field has been found to be accurate to within 2% over the entire acceptance of the spectrometer[57]. The spectrometer acceptance is approximately

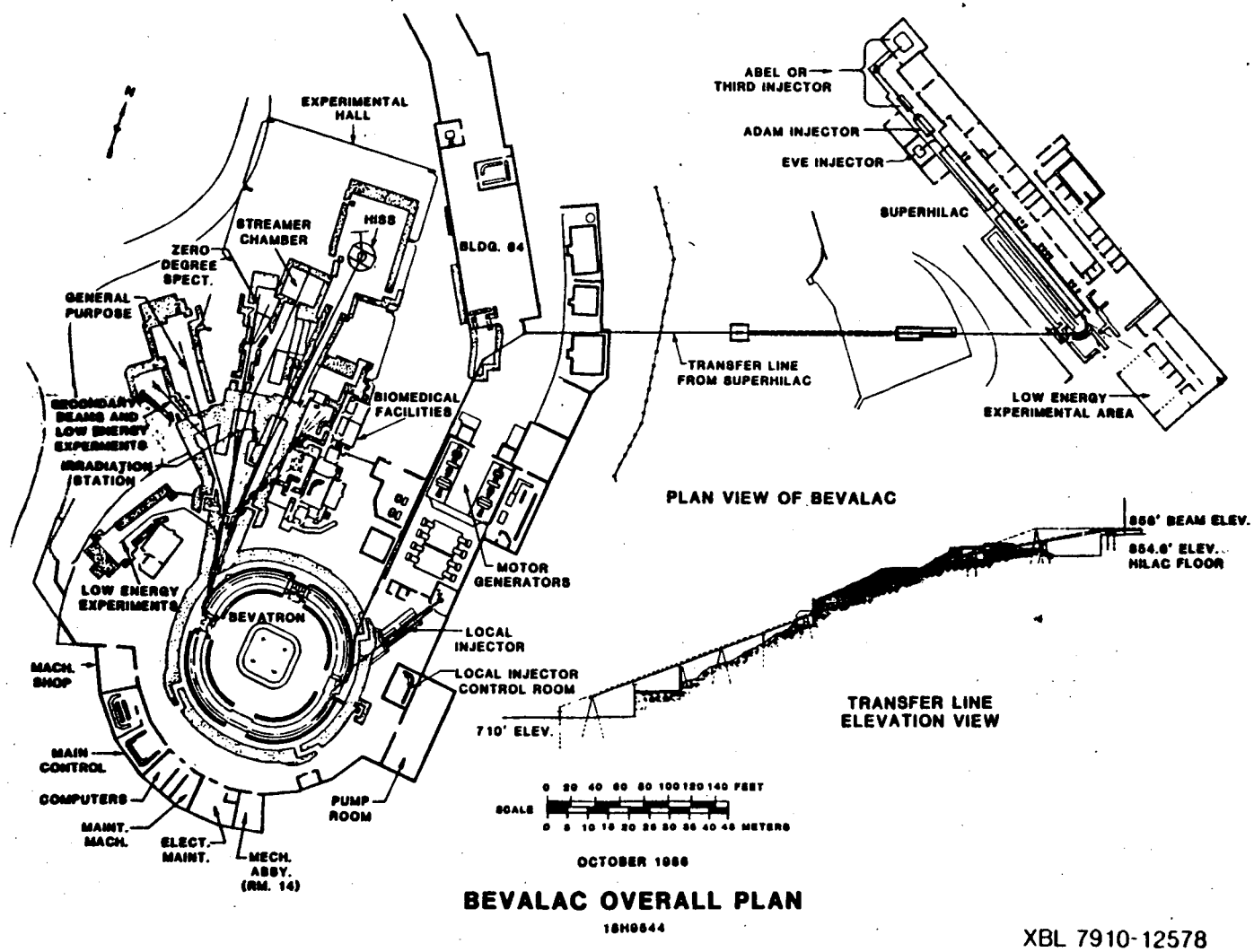

Figure 3.1. The Bevalac and its experimental areas.

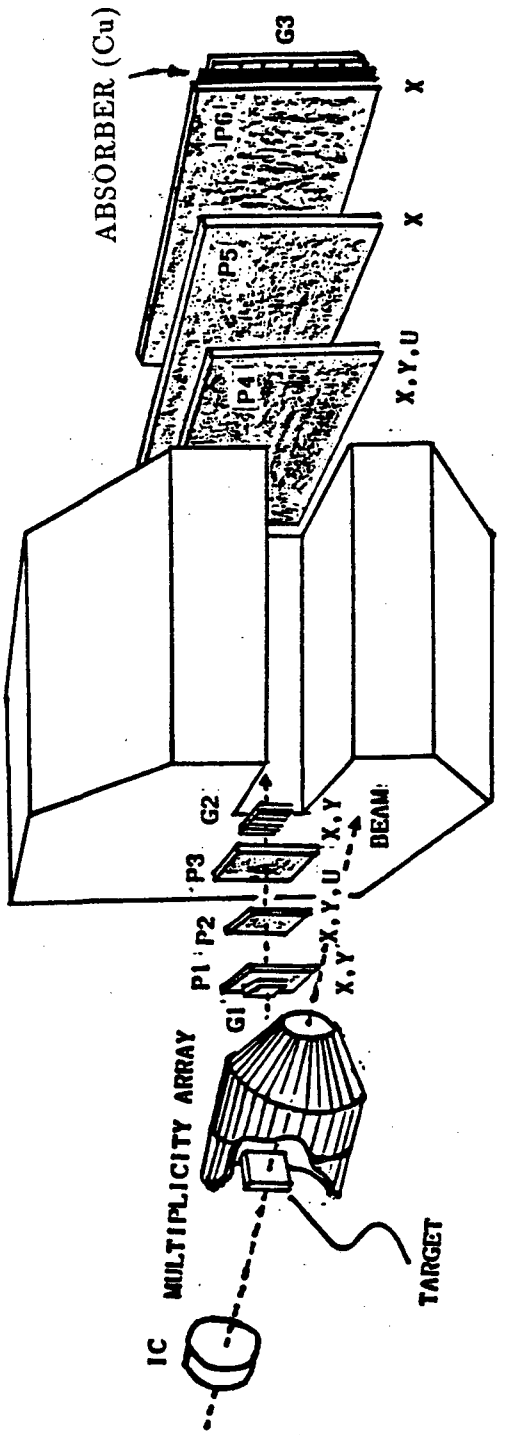

Figure 3.2. The B30-2 Spectrometer System. (From Ref. 127.)

12 msr over most of the rigidity range. The acceptance, tracking and calibration will be discussed in detail later in the next chapter. The magnetic field current was monitored visually using a digital voltmeter in the counting shack, and was recorded at the beginning of each run. During most of the data taking the field remained constant to within 0.2%, except for a brief period when it varied by about 0.8%, which was not a large enough change to affect the data analysis.

The magnetic field separates particles according to rigidity. The particle tracks were reconstructed from hits on six multi-wire proportional chambers (MWPC's or wire chambers), P1–P6. Plastic scintillators G1–G3 were used to obtain time-of-flight and energy loss information, and for triggering the system.

Associated multiplicity for charged particles was given by a 110-element scintillator array. During the π^+ running, a copper absorber of graduated thickness was inserted into the system and used to suppress triggers from protons and light positive fragments.

The specifications of the scintillators and wire chambers are given in Appendix D. The absorber and multiplicity array were added specifically for this experiment, and are discussed in the following sections.

3.2.2 The Multiplicity Array[†]

The multiplicity array consists of 110 1/4″-thick plastic scintillator paddles arrayed in three rings centered around the beam axis. The array covered polar angles (measured from the target, with respect to the beam) between 10° and 90°, over almost 2π in azimuth. (There were gaps for a target rotation apparatus and viewing ports, and to allow for the passage of particles into the spectrometer.) The individual rings subtended lab angles of 10°–25°, 25°–44° and 44°–90°, respectively. Each paddle was connected via a lucite light guide to a Hamamatsu

[†]The multiplicity array is also described in Ref. 128, from which some of the specifications and figures in this section are taken.

R647-09 photomultiplier tube (phototube, or PMT). Each PMT signal was sent to a time-to-digital converter (TDC). The pulse heights were not recorded, and consequently the experimental multiplicity distributions do not discriminate between singly charged particles and fragments. Fig. 3.3 shows the general layout of the array. Detailed specifications are in Appendix D.

Two of the salient considerations in the design of the multiplicity array were segmentation and overall size. Maximizing the number of elements was important, in order to reduce the incidence of multiple hits. The size of the array was limited by the small distance between the beam and the detector: a larger radius for the cylinders in the array allowed for more elements, but also limited the polar angle through which the detector could be moved. The final design represented a compromise between these factors, with an additional constraint in the form of the size (1/2″) of the PMT's.

The emission of charged particles from the collision zone was simulated using the intranuclear cascade simulation computer code of Cugnon *et al.* (Appendix F), and the array was designed so that each element had a roughly equal probability of being hit, assuming azimuthally-symmetric particle emission. The rearmost (44°–90°) ring had about a 10% greater hit probability. The predicted frequency of multiple hits at our beam energies was found to be 20–25% for all elements, almost independent of multiplicity. This implies that in the cascade the emitted particles are correlated in configuration space; in a real collision, many of the correlated particles would be bound in clusters.

Two factors acted to distort the multiplicity distributions produced by the array. The first, common to all run conditions, was the incidence of multiple hits. The second problem was that of pile up of signals in the TDC's, and was a factor only for the Ne+NaF running, for reasons which will be explained shortly.

Multiple hits. The constant 20–25% incidence of multiple hits predicted by the

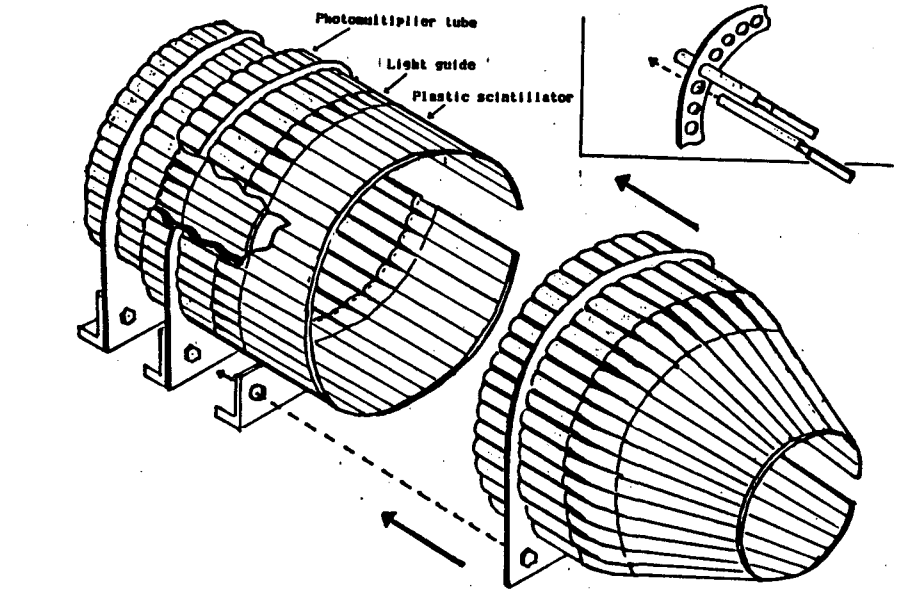

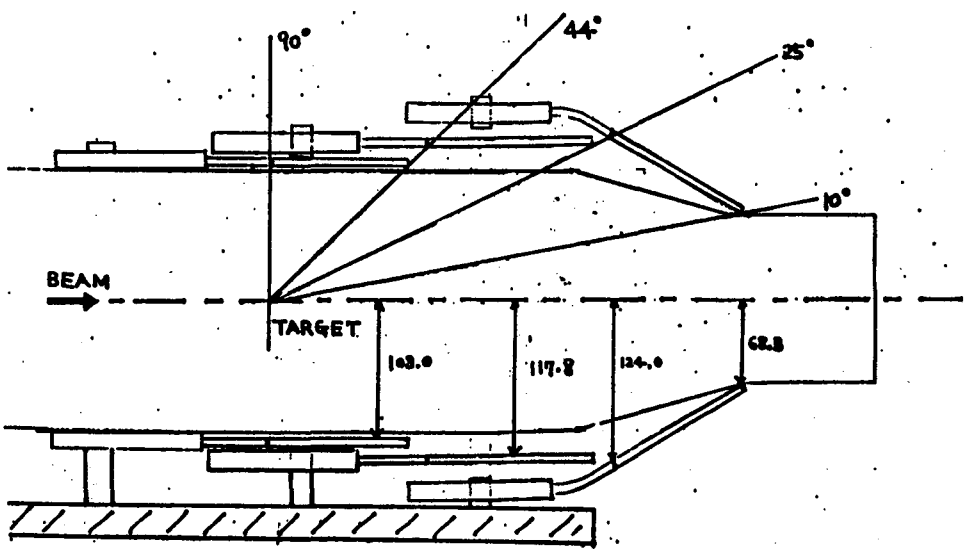

Figure 3.3. The multiplicity array.

cascade leads to an underestimation of the associated multiplicity by an amount which increases with the multiplicity, as can be seen from (Fig. 3.4). The "true" cascade distribution (i.e. with multiple hits counted) exhibits the same steep fall–off at low multiplicity, but has a broader peak and a longer high multiplicity tail. (This behavior is independent of angle.) We decided not to try to correct

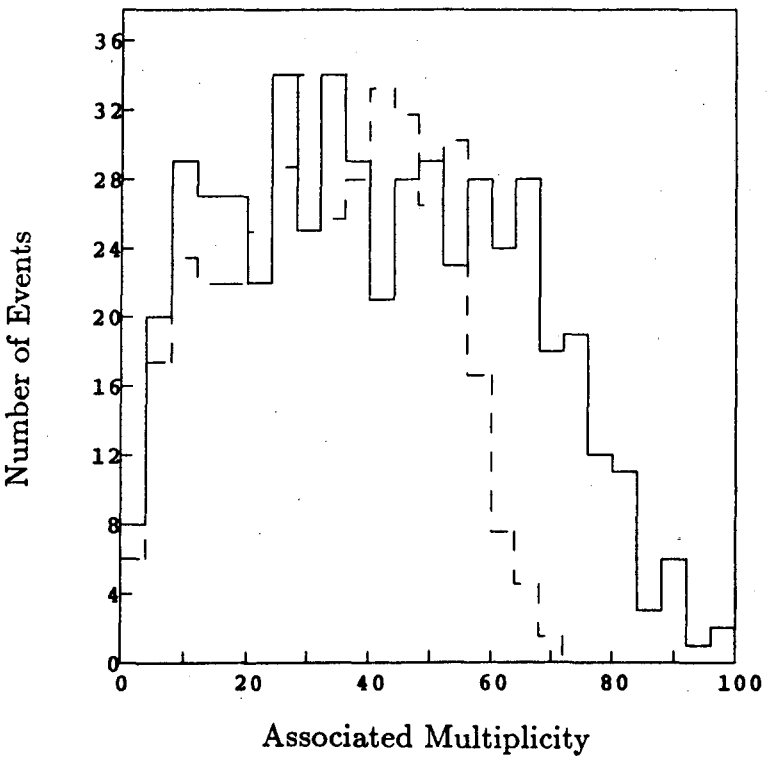

Figure 3.4. Associated multiplicity in the cascade for pion production in La+La collisions at 246 MeV/nucleon, with (dashed line) and without (solid line) inclusion of multiple hits. The results are integrated over impact parameter from b=0 to b=11.6 fm, and the distributions are normalized to have the same peak value.

for this effect, for two reasons. First, the absence of clusters in the cascade makes it difficult to estimate the true magnitude of the effect in the data, although it is most likely smaller than predicted by the cascade. Second, as will be evident from the discussion of the multiplicity distributions in Chapter 5, the usefulness of the associated multiplicity is as an indicator of the relative centrality of the

collision; the most significant feature in the experimental distributions is the peaking at moderate to high multiplicities, and this is seen in the cascade even when multiple hits are included.

Pile–up. While the associated multiplicity distributions in the experimental data for La+La collisions are consistent with the cascade predictions and with each other, This was not the case for the Ne+NaF distributions. They vary with angle, and in some cases the apparent multiplicity is much greater than the total charge of the Ne+NaF system (Fig. 3.5). The Ne+NaF associated multiplicities at $\theta_{lab} = 42°$ and 67° are, in fact, spurious, and result from pile–up in the multiplicity array TDC's of counts from more than one event. This effect was a function of the interaction rate and the beam intensity, as follows.

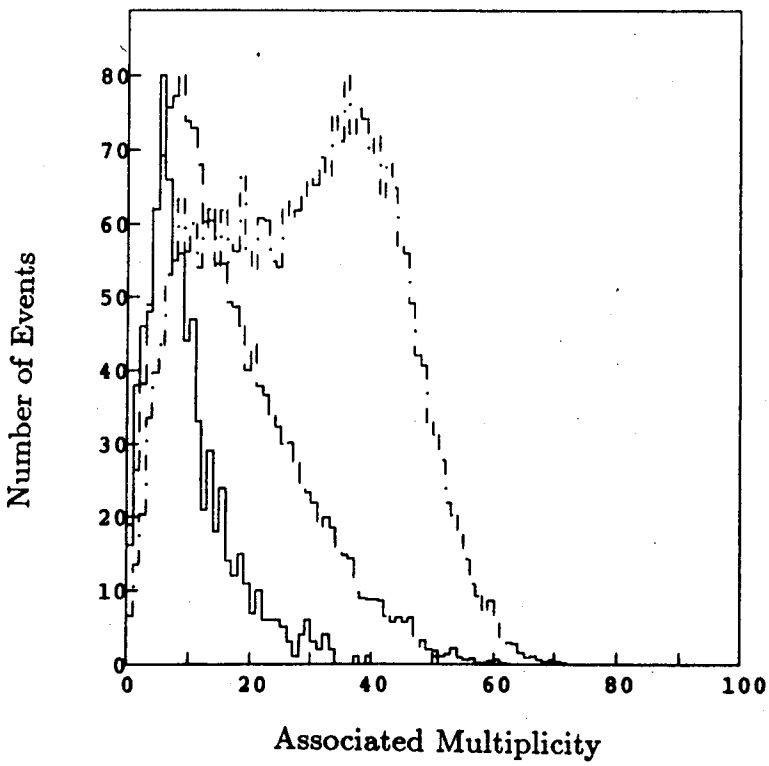

Figure 3.5. Associated multiplicity distributions for π^- from 244 MeV/nucleon Ne+NaF interactions. The solid, dashed and dot-dashed lines correspond to data at $\theta_{lab} = 21°, 42.5°$ and 67°, respectively.

The array was instrumented with LeCroy 4291 TDC's, which have a minimum full scale time of 512 ns ((1ns/channel)×(512 channels)). The data acquisition software defined a hit in a multiplicity array element to be a TDC output between 0 and 512. This allowed the system to resolve events at a rate of 1/512 ns$\simeq 2\times10^6$ sec^{-1}. The experimental event rate is approximately equal to the product of the interaction probability, P_{int}, and the beam intensity, R, in particles per second. Assuming a geometrical interaction cross section (which is reasonable for a simple estimate of the total rate), then,

$$P_{int} = \left(\frac{N_0}{A_{tgt}}\right) \rho\Delta x \cdot \sigma_{geom}$$

where $\sigma_{geom} = \pi[r_0(A_{beam}^{1/3} + A_{tgt}^{1/3})]^2$ ($r_0 = 1.12$ fm). For a symmetric system, $\sigma_{geom} = 4\pi r_0^2 A^{\frac{2}{3}}$. Thus, for La+La, with a target thickness $\rho\Delta x = .408$ gm/cm^2, $P_{int} = 0.007$. For Ne+NaF, $\rho\Delta x = .410$ gm/cm^2 and $P_{int} = 0.014$. The *maximum* intensity for 246 MeV/nucleon La was 3×10^7/spill,[†] with a spill length of about 1 sec. This yields an interaction rate of $(0.007)(3\times10^7) \simeq 2\times10^5$ sec^{-1}, which was well within the resolution of the array TDC's. The ability of the array to handle at least this rate was confirmed during test running, by monitoring the number of hits per element per spill. This number was found to remain constant as the beam intensity was increased from 5×10^6 to 2×10^7. For 244 MeV/nucleon Ne, however, the maximum intensities were approximately 5, 1 and 0.4×10^8 for $\theta_{lab} = 67°, 42.5°$ and 21°, respectively. (The correlation with angle is accidental, and reflects the fact that the beam intensity was deteriorating during the Ne running and that the larger angles were run first.) The corresponding interaction rates were 7, 1.4 and 0.6×10^6 sec^{-1}. Only for 21° is the rate safely within the TDC resolution. For 42.5° it is marginal, and for 67° it is clearly too high. (One must also consider that the spill has a microstructure, and therefore the interaction rate may vary during a given spill.) This is consistent with the

[†]The uncertainty in the beam intensity is about 10%.

multiplicity distributions plotted in Fig. 3.5.

This problem severely constrains the use of the multiplicity array with higher intensity beams. One way to alleviate it would be to apply a read-and-clear to the TDC at some specified time after the TDC start is received, the exact time to be determined according to the interaction rate and the velocity spectrum of charged participants.

δ-rays. Another factor which could act to distort the multiplicity distributions is the production of high energy knock–on electrons, or δ-rays. The maximum energy which can be transferred to an electron is[129]

$$E_{max} = \frac{2mc^2\beta^2}{1-\beta^2}$$

where mc^2=0.511 MeV is the rest energy of the electron. For a 246 MeV/nucleon projectile, $\beta \simeq 0.61$, and $E_{max} \simeq 0.6$ MeV. Electrons of this energy will stop in about 0.2 gm/cm^2 of Al (Ref. 15, p. 46), which is considerably less than the thickness of the beam pipe (0.446 gm/cm^2). By comparison, 800 MeV/nucleon beams can produce δ-rays with energies in excess of 4 MeV, which can pass through the beam pipe and be detected in the array. So while δ-rays were not a problem in our experiment, it has been necessary to shield the array for operation at higher beam energies.[130]

3.2.3 The Absorber

The absorber was located between P6 and G3, and was graduated in thickness according to the range of energies of the particles to be stopped. It was constructed of eight copper plates of varying thickness, held in an aluminum frame which was raised out of the way for π^- and light fragment (p, d, t, etc.) running. The use of the absorber is described in detail starting on p. 52.

3.2.4 Beam Pipe and Targets

The beam line from the Bevatron to the spectrometer was enclosed in aluminum pipe, which was evacuated during the running. Removable beam wire chambers (BWC's) were used to monitor the beam position, and a fixed ion chamber measured the beam intensity. At the spectrometer, the beam pipe was terminated by a tapered aluminum vacuum chamber 0.165 cm (0.446 gm/cm^2) in thickness which enclosed the targets and also helped support the surrounding multiplicity array. The chamber was isolated from the rest of the beam line by a gate valve, allowing it to be pumped down separately, for quick target changing. To minimize scattering back into the spectrometer, the downstream end of the chamber was sealed with a 5 mil Kapton window, which had to be periodically changed due to radiation damage produced by the highly charged beam particles. The chamber also held two BWC's, a removable one upstream and one in an outside holder at the downstream end. These were used to monitor the beam profile in the crucial region close to the target.

The targets were held in a metal frame, which could be moved in and out of the beam by means of a rod extending outside the vacuum chamber. The targets could also be rotated in place, so that the beam would hit at an angle, but we did not make use of this feature. Access to the targets was through a port on the side of the chamber. The targets were 2″ square, with thicknesses, .408 gm/cm^2 for La and .410 gm/cm^2 for NaF. These thicknesses were a compromise, dictated by the desire to maximize the interaction rate while minimizing the uncertainty in beam energy due to dE/dx in the target material.

3.2.5 Electronics and Data Acquisition Computing

The electronics was a mixture of NIM and CAMAC modules, with both NIM and ECL logic. All data to be stored were eventually sent to CAMAC crates,

which were read out through a Multi-Branch Driver (MBD) by a PDP 11/44. The data were then written to tape, and also made available for some limited on-line analysis. The data acquisition software was based on the DATACQ system then in general use at the Bevalac, and the on-line analysis software was tailored to the B30-2 system.[131] On-line displays were generated using the "DISPLAY" graphics package.[132]

3.3 Experimental Techniques

3.3.1 Run Preparations

MWPC's and Scintillators. The wire chambers were first "conditioned", i.e the high voltage on each chamber was gradually raised towards a peak value near that used in previous running. (This was done slowly, to avoid arcing in the chamber.) In most cases, this was about 4000 volts. Next, the chambers were "plateaued". This was done by measuring the response of each wire plane to a ^{90}Sr source as a percentage of counts in two counters of known characteristics placed on either side. The high voltage was raised until the wire chamber efficiency reached a constant value (usually $\geq 96\%$), independent of the applied high voltage. This was done for several different locations on the surface of the wire chamber. During the data taking we attempted to operate all of the MWPC's in the plateau region. Occasionally, some of the chambers experienced arcing, as evidenced by sudden drastic increases in the current in the MWPC power supplies. This forced us to lower the high voltage for varying periods,† with consequent decrease in the efficiency. (See Sec. 4.4.5.)

The procedure for plateauing the scintillation counters was similar to that used for the wire chambers. In addition, the output of each scintillator element was checked for light-tightness and strong signal-to-noise ratio.

†In some cases this was correlated with running with high beam current at forward angles.

Multiplicity Array. Since the architecture of the array made it impractical to plateau each array element with an external source, we placed a small amount of ^{207}Bi on each array element. This source emits conversion electrons at 0.5 and 1 MeV. The second of these peaks is minimum ionizing, and this was confirmed by using a multi–channel analyser to compare the source output with a cosmic ray spectrum. Each counter was plateaued both offline and after installation in the array. Due to its low activity (count rate $\leq$ 60 Hz) the source did not present any background problems. A computer–controlled high voltage system was used to set each counter voltage separately. Typical high voltage for an array element was 750–800 volts.

The effect of the spectrometer magnetic field on the array was studied prior to installation by monitoring the response of a single element in various locations near the array as the field was increased. As a result of these tests, it was decided that it was not necessary to shield the array from the magnetic field.

3.3.2 Beams

Intensity and Monitoring. Beam intensities were on the order of 10^7 for La and 10^8 for Ne. The intensity was monitored by an ion chamber (IC) placed in the beam line. The ion chamber provided a relative measure of the beam intensity, and had to be calibrated. For the 246 MeV/nucleon La running, this was done in two ways, by carbon activation[133] and by counting with a plastic scintillator. The latter method required that the beam intensity be reduced, in order to avoid saturating the scintillation counter. For the lower energy La beams, the IC calibrations were done using the scintillator only, and for Ne beams, calibrations were obtained from previous running.[134] For consistency, we used the scintillator results for La running. (The activation technique gave a 33% higher value.) The calibrations used are given in Table 3.1. As expected, the numbers for ^{20}Ne are

Beam	Energy (MeV/nucl)	Beam ions/IC count (±10%)
La	246	33000
	183	27000
	138	21000
Ne	244	1.30×10^6
	800	1.86×10^6

Table 3.1. Ion chamber calibrations

higher than for the more highly ionizing ^{139}La.

Tuning. The beam was steered onto the target by bending and focusing magnets, based on positioning information from the BWC's. The position of the beam at the target was determined using a phosphor-coated target viewed by a television camera, and also by inserting polaroid film in the beam at the exit of the beam pipe. The beam spot had a typical cross section of about 1 cm×1 cm.

Energy Loss. Table 3.2 gives the energy loss in different elements of the beamline and target. Incident beams lost energy mainly in electromagnetic interac-

System	Energy (MeV) at extraction†	at target entrance	at target center	at target exit	ΔE in target (MeV)
La+La	265.	255.	246.	233.	22.
	207.	195.	183.	171.	24.
	165.	151.	138.	125.	26.
Ne+NaF	250.	247.	244.	241.	6.

Table 3.2. Beam energy loss in the target and in other material in the beamline. All energies are in MeV/nucleon. The greatest losses were in a scintillator at focus XF1, in the beam ion chamber and in the target. The calculations assume fully stripped ions.‡

tions with material in the beamline, principally in the target. The beam energies

†There is an approximately ±2% uncertainty in extraction energy, due to the uncertainty in the radius of the particle trajectory within the Bevatron.[135]

‡La ions are only partially stripped (+29) at extraction from the Bevalac; however they become fully or almost fully stripped (+57 or +56) after traversing .002 gm/cm^2 of aluminum[136]. The scintillator at XF1 (at the interface between the Bevatron and the EPB) is covered with .01 gm/cm^2 aluminum.

quoted in this paper are estimates of the energy at the target center. The total energy loss in the target provides a measure of the uncertainty in the quoted beam energies.

3.3.3 Triggering and Data Acquisition

Fig. 3.6 is a schematic of the trigger and data acquisition logic for pion running. The event trigger was defined by a coincidence of hits in the three scintillators: G1·G2·G3. Acceptance of an event by the computer required the additional coincidence $R \cdot S \cdot \overline{B}$: computer running (R), beam spill on (S) and computer not busy ($\overline{B}$). Given the small cross section for pion production below threshold, computer dead–time should not have been a problem. Nevertheless, for π^- the data rate at the most forward angles was computer–limited. We attribute this to an increased background of very rigid protons (p. 58), which triggered the spectrometer even though they were bent in the wrong direction. The percentage of events accepted was about 70% for $\theta_{lab} \leq 30°$, and 98% for $\theta_{lab} \geq 40°$. For positive pions, the dead–time problem was much more serious, and called for special handling.

Positive Pion Running

Enhancing the percentage of π^+ triggers. When the spectrometer was set to measure positive particles (i.e. to bend positive charges into P4–P6 and G3), the large majority of the triggers were generated by "light positives": protons and light fragments. This presented problems for the π^+ running in the form of increased background and depressed data rate. While the tracking, time-of-flight and energy loss measurements were adequate for separating the pions from the light positives (Chapter 4), it was especially important to increase the π^+ signal relative to the background, since good pion events were lost while the

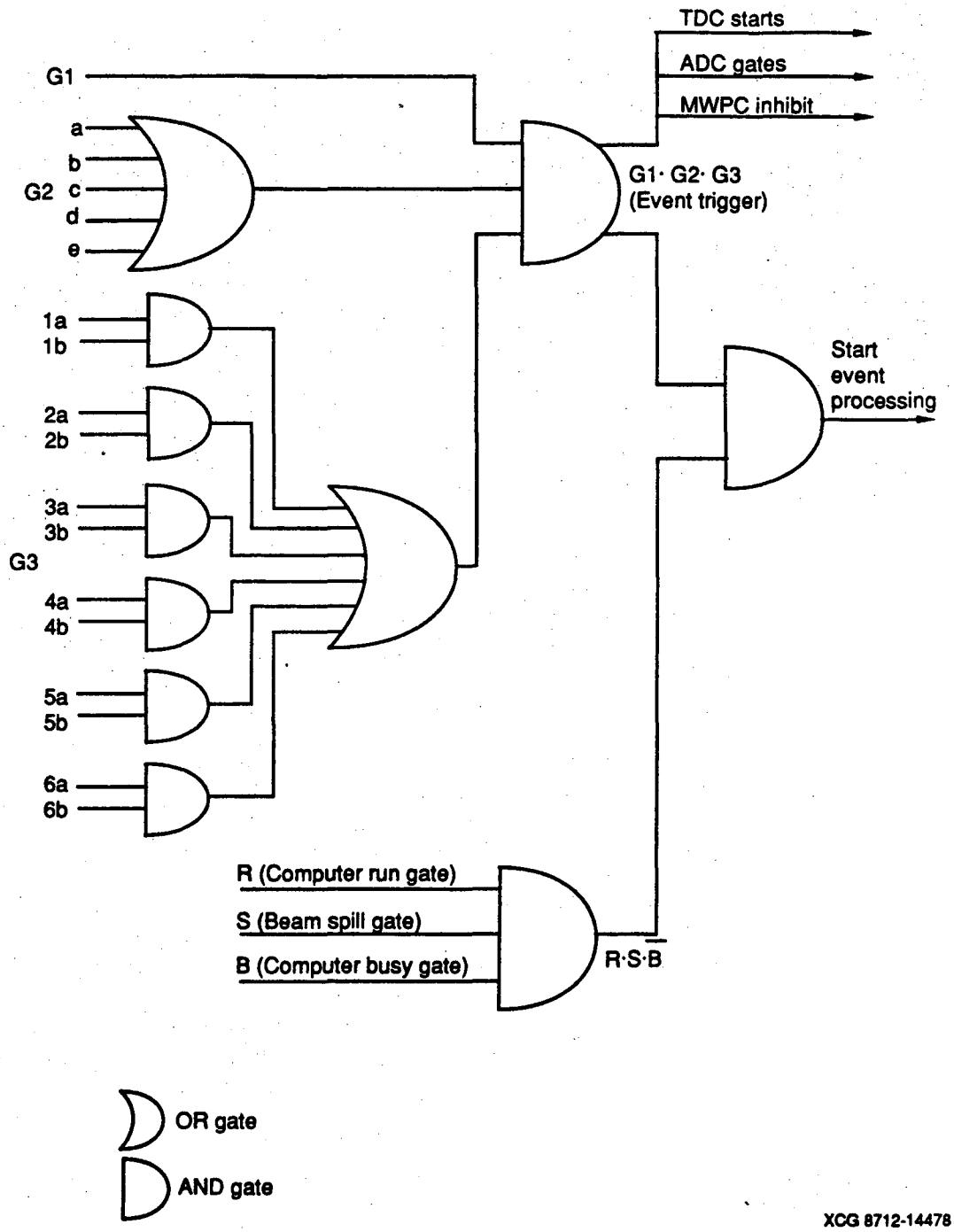

Figure 3.6. Trigger and data acquisition logic for pion running.

computer was busy processing non-pion tracks. We accomplished this by means of a combination of two passive detection techniques: we disabled three of the five elements of G2 to reduce the acceptance for the most rigid particles and we installed the copper absorber to range out the slowest of the less rigid particles.[†]

The geometry of the spectrometer was such that the G2 elements closest to the magnet yoke preferentially passed high-rigidity particles. This was so because G3 was displaced to the left of G2 (looking from the target through the magnet), and therefore a low-rigidity particle which passed through an inside G2 element would bend out of the system before hitting G3. Thus, disabling the innermost elements tended to have a greater effect on protons, which generally have higher momenta—and therefore straighter trajectories—than on pions. Furthermore, the protons which remained were relatively slow and could be stopped in a reasonable thickness of copper. Fig. 3.7 summarizes the situation. The absorber varied in thickness between 0.22 and 7.90 cm (1.97–70.8 gm/cm^2). Note that pions and protons are well separated in range over the entire spectrometer acceptance. This system also effectively eliminated most of the light positives, which were generally more rigid and had a shorter range than protons. In any event, most of the unwanted triggers were found to be due to protons.

Monte Carlo studies of the spectrometer acceptance showed that eliminating the innermost three elements (c,d,e) of G2 reduced the acceptance for π^+ by about 50% over most of the momentum range (see Sec. 4.4.3); however this was more than recovered by the increased percentage of π^+ triggers. Data taken for π^+ at $\theta_{lab} = 60°$ from 246 MeV/nucleon La+La gave the following results for the ratio, R_{trig}, of π^+ triggers to all triggers: with all G2 elements active and the absorber *out*, $R_{trig} = .002(\pm 20\%)$. With G2 a and b only, and the absorber *in*, $R_{trig} = .103(\pm 5\%)$, about a factor of 50 ($\pm 20\%$) improvement. The effectiveness

[†]We originally considered using a plastic Čerenkov counter to identify pions, but the passive system proved to be simpler, as well as easier to construct.

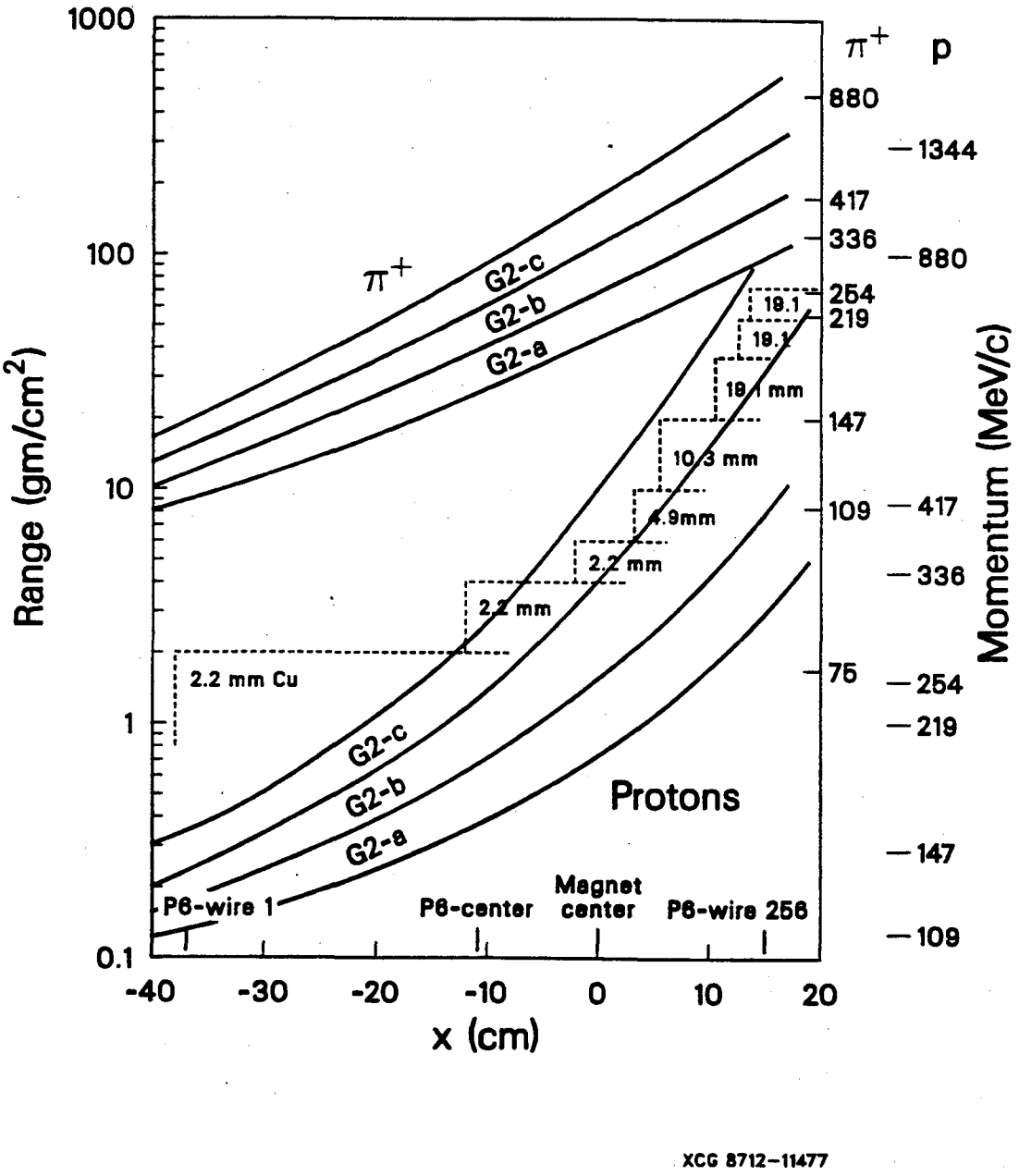

Figure 3.7. Momentum and range in copper for protons and pions accepted in the spectrometer (for B=3.13 kG), as a function of G2 element for the three *outermost* G2 elements (a, b and c). The left ordinate is particle range in gm/cm^2 of copper, the right ordinates are pion and proton momenta. The abscissa is hit position at G3. The absorber thicknesses (in gm/cm^2), including the uniform absorption in the spectrometer before the absorber, are superimposed. (This plot was prepared for this experiment by G. Landaud.)

of this system is illustrated by Fig. 3.8. This can be seen in another way

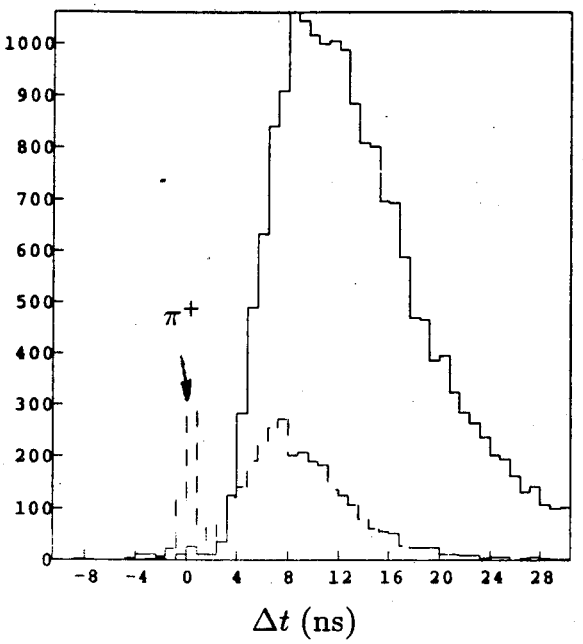

Figure 3.8. Number of π^+ vs. non-pion triggers with (dashed histogram) and without (solid histogram) π^+ trigger enhancement, as implemented by removing G2 c,d,e from the trigger and moving in the copper absorber. In this plot, particles are identified by time-of-flight relative to the expected time-of-flight of a pion with the measured momentum. Thus the pions have $\Delta t \simeq 0\pm \sim 2$ ns. (See Chapter 4.) The data are for 246 MeV/nucleon ^{139}La $+^{139}$La $\rightarrow \pi^+ + X$ at $\theta_{lab} = 60°$. The ratio of events accepted/event triggers was 11701/12630 with trigger enhancement vs. 23729/45456 without. The scale is the same for both histograms.

by looking at the computer live-time, as measured by the percentage of triggers accepted by the computer, for different run conditions. For π^+ at $\theta_{lab} = 60°$ from 246 MeV/nucleon La+La collisions, this was about 50% without the absorber vs. 70% with it. With the absorber in and G2 a and b only, the percentage of triggers accepted increased to 93%. This, despite the fact that the absorber-in runs had almost twice the beam intensity.

The effect of the absorber on pions as a function of pion momentum was determined by taking π^- spectra with and without the absorber. As expected, it was negligible at all but the highest pion momenta (Sec. 4.4.4).

Fig. 3.9 shows the original positions of the absorber plates, relative to the

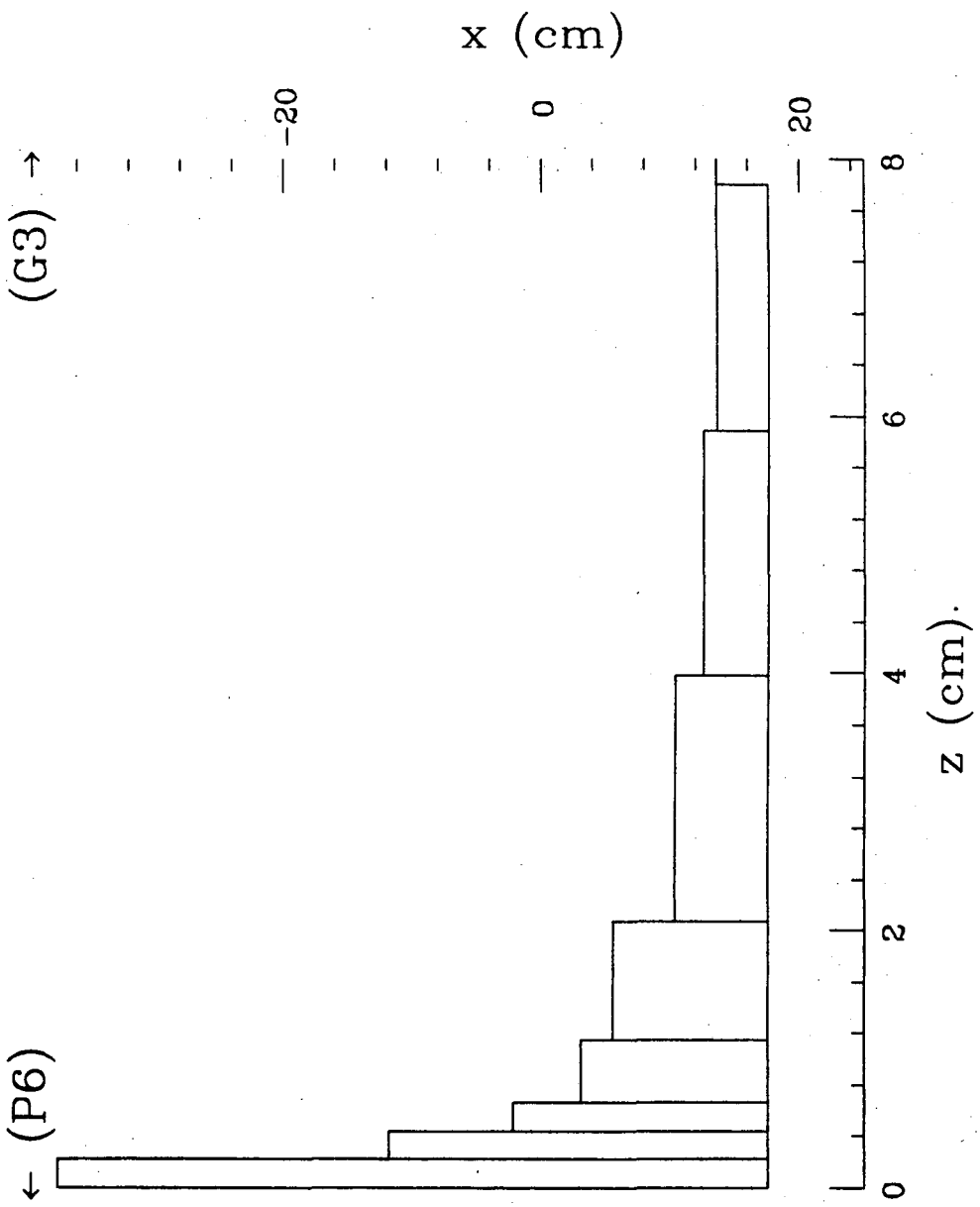

Figure 3.9. Schematic of the absorber, showing positions (in the spectrometer coordinate system) and thicknesses of the copper plates. It is shown as configured at the beginning of the data taking.

magnet, P6 and G3. The performance of this system was studied before the start of data-taking for π^+ , and it was found to be close to the design specifications. After completion of about one third of the pion running, analysis of the ratio of π^+ to non-pion triggers indicated that the performance could be improved by a small adjustment, and the positions of some of the plates were shifted as follows:

#1 (nearest the magnet) (thickness = 19.1 mm) : -2 cm.

#2 (19.1 mm) : -3 cm

#3 (19.1 mm) : -4 cm

#4 (10.3 mm) : -2 cm

Other run conditions

'Fast' trigger vs. 'slow' trigger. In an attempt to further reduce the trigger rate for non-pions, we adjusted the relative timing of the signals from the three scintillators to eliminate the slowest particles. This did eliminate some of the very slow particles, but the primary result was to pile up most of the non-pions at the same apparent time-of-flight (t.o.f.).[†] As this turned out to be well outside the t.o.f. cuts for pions (see Chapter 4), it did not effect the results.

'Straight-throughs'. These were very rigid positive particles which managed to trigger the spectrometer even when it was set to measure negative particles. To reduce this source of background, we inserted lead bricks into the pole gap, on the edge away from the magnet yoke. This reduced the maximum x-value from +17 cm to +10 cm (see Appendix D), but it was determined to have no effect on the acceptance for pions.

[†]This came about as a result of inadvertently using the signal from G3 as both a start and a stop signal, which resulted in an apparent t.o.f. equal to the delay between the G3 signal input to the trigger and the G3 TDC stop signal.

Run Summary

The data were taken over two weekends and several nights during a two week period in March 1985. (Some preliminary test runs had taken place the previous October.) Total beam time was approximately 170 hours. The beam time used to acquire data for the experimental pion cross sections was approximately 67.5 hours. An additional 22 hours was used to take data for protons and light fragments. The remaining time was taken up by beam tuning, detector tests and adjustments, calibration runs (see Chapter 4), target-out and zero-field runs and miscellaneous accelerator downtime. The run times and number of pions taken at each setting are tabulated in Appendix C.

Target-out runs. These were made at each spectrometer setting to determine the background due to beam interactions with material other than the target.

Zero-field runs. Two runs were made with the magnetic field off, in order to determine the precision and accuracy of the spectrometer tracking. (See Chapter 4 for a discussion of how the target-out and zero-field runs were used.)

4. Analysis

This chapter covers the procedures for converting raw data into pion spectra, i.e. cross sections plotted as a function of pion momentum or kinetic energy. The first step was to convert the data stored during the run—ADC[†] and TDC outputs, wire numbers, etc.—to hit patterns on the MWPC's, scintillators and the multiplicity array. This information was then used for track reconstruction, computation of momentum, mass and charge, and particle identification, and finally, computation of the pion cross sections. There were a number of intermediate steps, including calibration of the ADC's and TDC's and correcting for energy loss, absorption and particle decay in the spectrometer. The results also had to be corrected for the efficiencies of the different detectors, and for the spectrometer acceptance.

4.1 Track Reconstruction and Determination of p/Z

Track reconstruction was done using information from the MWPC's. The general reconstruction algorithm was to find hit patterns which met the following criteria:

- in the x-z (bending) plane, straight line trajectories before and after the magnet had to be connectable by a circular arc within the magnet.
- in the y-z plane, a straight line trajectory before the magnet had to be consistent with hits on wire plane P4Y and scintillator G3, after the magnet.
- the hits on the x and y wire planes had to be consistent with hits on the two (45°) angled planes P2U and P4U.

[†]ADC ≡ analog-to-digital converter.

- the x coordinate of the interaction vertex computed based on the reconstructed tracks had to be within ± 3 cm of the target center. This cut was chosen based upon analysis of the data which showed that the reconstructed vertex distribution was consistently gaussian, centered within ± 1 cm of the center of the target and with $\sigma \simeq 1 - 2$ cm. Within this range, there was no correlation between the reconstructed vertex position and quality of the track.

This procedure required hits on at least nine of the twelve wire planes, including P2U, P4U and P4Y, and two out of three from P1X-P3X, P4X-P6X and P1Y-P3Y. The rationale for this was as follows: Despite the fact that the MWPC's were plateaued with minimum ionizing particles, between 30% and 50% of the reconstructed tracks had hits on fewer than twelve planes. This was due to the fact that the chambers were not 100% efficient, and also because it was not always possible to run all the chambers in their plateau regions. (See p. 49.) Particle distributions taken with fewer than twelve wire planes hit were compared to those taken when hits on all planes were required, and were found to be the same in every respect. Based on this, we concluded that the difference between them was due mainly to inefficiencies in the MWPC's. It was therefore decided to reconstruct tracks under the more relaxed criterion of nine wire planes (including certain required ones) hit, on the grounds that it made more sense to include real tracks directly than to eliminate them in the reconstruction and then add them back in when normalizing to the wire chamber efficiencies. The MWPC efficiency calculation is discussed in Sec. 4.4.5, below.

G3 was made up of six horizontal elements, G3-1$\cdots$G3-6, numbered from top to bottom. The criterion for a good hit on G3 was defined to be a hit on the element extrapolated from P1Y-P4Y, or on the neighboring element on the side nearest the predicted y-intercept. For example, if the extrapolated y-intercept

was in the lower half of G3-2, then the reconstruction code demanded a hit in either G3-2 or G3-3.

Fig. 4.1 is a schematic of the elements of the tracking system, taken from the on-line display of a real pion-producing event. In this case there was exactly one hit on each detector, but the reconstruction programs also had to handle the cases where there were multiple hits and/or missed planes. In the case of multiple hits, the average *maximum* number of hits on any wire plane was between 1 and 2 at $\theta_{lab} = 67°$ and about 3 at $\theta_{lab} = 21°$, almost independent of magnet polarity. This is somewhat surprising, since one might expect substantially more hits for positive than for negative polarity, especially at forward angles. One possible explanation is that many of the multiple hits for negative polarity were from very rigid positive particles. In any event, the reconstruction code was designed to handle up to three tracks, and the final particle distributions were found to be independent of the number of tracks per event.

For each reconstructed track, the rigidity, p/Z, was computed from the radius of curvature of the trajectory in the magnetic field. This was obtained from the expression

$$p/Z = \frac{21.1 \cdot B_{eff}}{(\sin\theta_{in} + \sin\theta_{out})} \text{ (MeV/c)} \tag{4.1}$$

where B_{eff}, the effective magnetic field in kG, takes into account the slightly non-uniform character of the magnetic field. When $B = 3.13$ kG at the center of the pole gap, $B_{eff} = 3.24$ kG[57]. Eq. 4.1 is derived from the relation between momentum, charge, radius of curvature and magnetic induction, B, using an effective magnetic field length, l, of 70.4 cm, including the fringe field. (The derivation is given in Appendix E.) The results were also corrected for the fact that most tracks were not confined to the plane normal to the magnetic field. The momentum resolution for pions was 6–8%, which was of the same order as the uncertainty due to multiple Coulomb scattering.

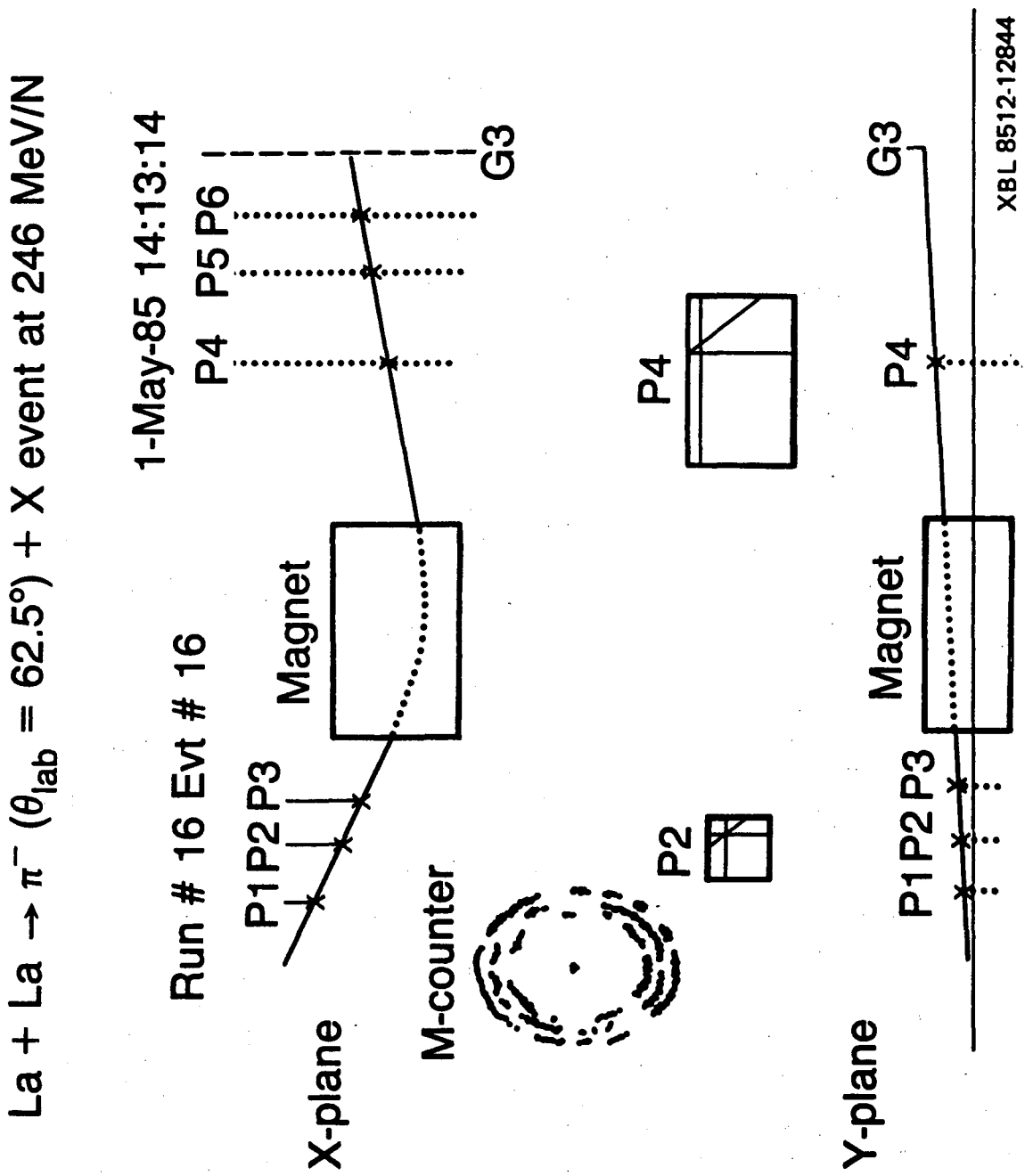

Figure 4.1. Schematic of a pion-producing event, showing hit positions on the detector planes and connecting trajectories in the magnet.

The output of the reconstruction program included the rigidity and a χ^2 for up to three candidate tracks, along with some additional information which was used to calculate reconstruction and wire chamber efficiencies. (See Sec. 4.4.) The χ^2 was computed for the fit to a circular arc in the magnet.[†]

4.2 Particle Identification: Mass and Charge

After calculating the rigidity, the next step was to use time-of-flight and energy loss information to identify the particle which made the track. The t.o.f. from the G3 TDC's was used to calculate the particle's velocity which, combined with its rigidity, gives the mass per unit charge. The energy loss information (from pulse height in the G3 ADC's) was then used to calculate the charge, thus uniquely identifying the particle.

4.2.1 Time-of-flight

TDC calibrations and calculation of the mass. Fig. 4.2 shows scatter-plots of t.o.f. vs. bend angle for positive and negative particles produced in 800 MeV/nucleon Ne+NaF collisions. Since the bend angle is closely related to the rigidity, and the t.o.f. is proportional to the velocity, plotting the raw data in this way effectively separates particles according to their mass per unit charge, and it is clear from the figure that it is possible to identify pions relative to other particles. We wanted a more quantitative measure, however, and this required a knowledge of the TDC offset. This was obtained by selecting particles from the pion band, calculating the expected t.o.f. for a pion with the momentum and flight path calculated by the reconstruction program, and setting the TDC offset so as to give that value. This was done for each of the G3 TDC's. The

[†]The version of the reconstruction code used for highly ionizing particles demands hits in all wire chambers, and computes a combined χ^2 for goodness of fit to straight lines before and after the magnet, and to a circular arc within the field. Since the relaxed criteria used for pions required hits on only two x-planes on each side of the magnet, the straight line χ^2 could bias the total χ^2 to artificially low values and had to be disabled.

process was repeated for a number of runs, and it was determined that a single calibration would work for the entire data set.

Fig. 4.3 shows a mass spectrum produced in this way. The relative positions of the π^+ , proton and d, α peaks show that it was reasonable to assume that the pion band in the scatterplot did, in fact, contain pions.

$\Delta(\equiv$ **t.o.f.(measured)** $-$ **t.o.f.(pion))**. In practice, we chose not to select pions according to mass, for the following reason. Many pions had β close to 1, and for a significant number of these particles the uncertainty in the t.o.f. resulted in an apparent $\beta > 1$, rendering the mass calculation meaningless. These particles were arbitrarily assigned $m = 0$ in Fig. 4.3. What we did instead was to calculate the expected t.o.f. as if the candidate particle were a pion, and subtract that from the actual t.o.f. (including TDC offset).[137] The resulting 'Δt' distribution is a gaussian centered at about zero, with a finite width, due to the uncertainty in the measured t.o.f. . This is equivalent to calculating the mass, but eliminates the problem of '$\beta > 1$' particles. It is effectively the same as transforming the pion bands in Fig. 4.2 into distributions centered about their midlines. Fig. 4.4 is the Δt distribution for the particles in Fig. 4.2a. Note that the non-pions comprise an apparently uncorrelated background, which is actually a superposition of separate peaks for protons of different momenta: the higher the momentum, the greater the value of Δt.[†]

4.2.2 Energy Loss

ADC calibrations and calculation of the charge. The G3 ADC's were calibrated by calculating the energy loss per channel for particles with $m/Z = 1$ (i.e. $Z = 1$). This was done by correlating the average number of ADC channels (after subtraction of the pedestal) corresponding to a given β with the energy

[†]There is also a truly uncorrelated component, as will be discussed below (p. 71).

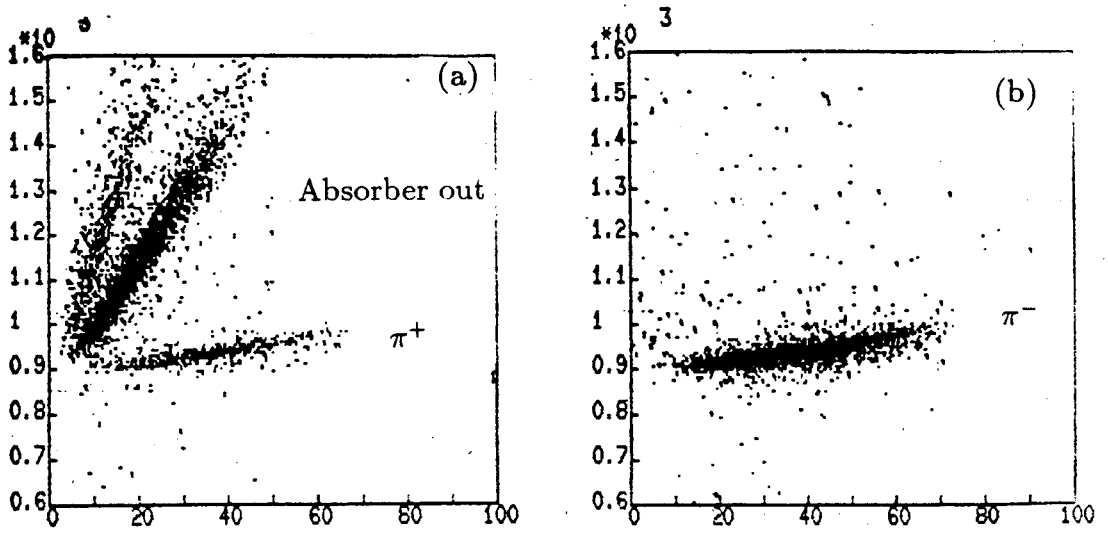

Figure 4.2. Plots of time-of-flight vs. bend angle for (a) positive and (b) negative particles at $\theta_{lab} = 60°$ from 800 MeV/nucleon Ne+NaF collisions. Time of flight is in terms of TDC channels (600-1600). Bend angle is in arbitrary units.

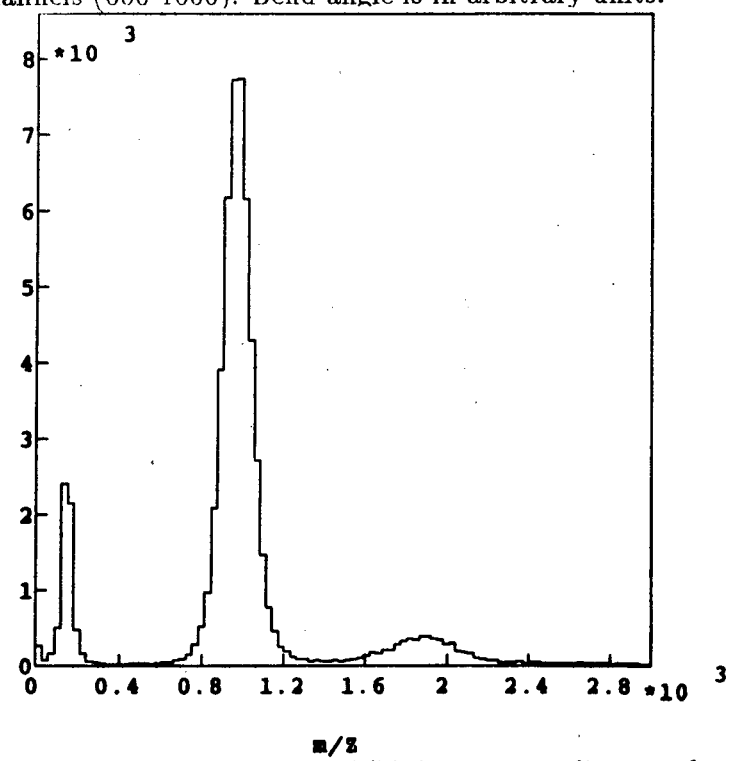

Figure 4.3. Spectrum of masses (in MeV/c^2/Z) corresponding to the scatterplot in Fig. 4.2a.

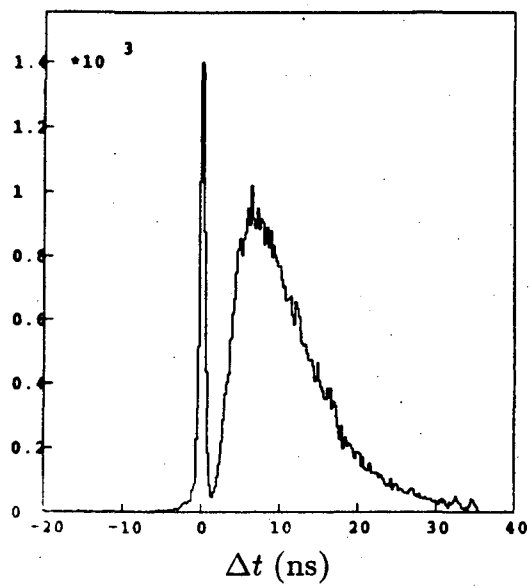

Figure 4.4. Δt distribution corresponding to Fig. 4.2a.

loss in G3 for a $Z = 1$ particle of that velocity.[‡] Each of the six double-ended G3 scintillators was treated separately. Once again, a number of different runs were studied, and it was found that a single calibration was sufficient. With this calibration it was possible to invert the process to obtain the charge of a particle from the number of ADC channels.

The charge calculated in this way had a large uncertainty, since the variation in dE/dx as the particle slowed down was not taken into account. This was a particular problem for highly ionizing particles, which could mimic an incorrectly high charge by depositing more energy than expected for the incident velocity. This, along with Landau fluctuations, tended to broaden the distributions. On the other hand, the average calculated charge for particles with $m/Z = 2$ was about 1 for deuterons, but only 1.6 for α's, many of which apparently stopped in the scintillator, and thus registered an energy loss corresponding to a smaller charge.

[‡]All of our calculations of energy loss due to interactions with atomic electrons were done using the Bethe-Bloch equation.

For identification of pions (and protons), these problems were academic, since their unique values of m/Z made the charge identification redundant. In these cases the charge calculation was done primarily as a consistency check.

4.3 Selecting Pions

At this point in the analysis, each candidate had been assigned values for p/Z, m/Z, Δt, Z and χ^2. The sensitivity of distributions in each of these variables to the others was studied, and it was decided to select pions based almost exclusively on the Δt distribution, for the following reasons. As discussed above, the charge cut was redundant for pions; furthermore, cutting on high Z entailed a risk of eliminating good pions in the Landau tail. Δt and m/Z incorporated the same experimental observables, but the former was better adapted to handling the inherent measurement uncertainties. The χ^2 cut turned out to less restrictive than the Δt cut. The only other cut which was applied on rigidity between 100 and 600 MeV/c/Z. The high-rigidity cut was used to eliminate some fast background particles which contaminated the Δt distributions for π^+ , while the low cut was used to eliminate particles at the edge of the spectrometer acceptance. Studies on the π^- spectra, where the background was much smaller, showed that this cut removed few, if any, pions.

4.4 Corrections to the Raw Pion Distribution

The raw pion yield represented the number of pions observed in the spectrometer. Turning this number into a cross section required corrections for a number of factors relating to the spectrometer geometry and how particles were transported through it. In addition, identification of the pion signal was complicated by the background, which varied from essentially non-existent (246 MeV/nucleon, π^- at $\theta_{lab} = 67°$) to dominant (246 MeV/nucleon, π^+ at $\theta_{lab} = 21°$), as can be

seen in Fig. 4.5.

4.4.1 Background subtraction

Understanding the background

In principle, the Δt cut (or alternatively, the mass cut) should have had sufficient resolution to distinguish pions from protons, but in practice, in the most severe cases, cutting only on Δt would clearly have allowed many non-pions to be included. It was therefore necessary to do a separate background subtraction, and since simply fitting to the tail of the inclusive background and subtracting does not take the momentum dependence into account, the background had to be studied in more detail.[†]

For positive magnet polarity, the Δt distribution consisted of three components:

- a pion peak, which was approximately gaussian, centered at about $\Delta t = 0$.
- a proton background, composed of a superposition of gaussian distributions for different lab momenta, centered about Δt equal to the difference in t.o.f. between pions and protons with a given momentum.
- an incoherent background, not correlated with a particular mass or charge.

Fig. 4.6 illustrates the relative strengths of the π^+, proton and incoherent background signals for positive particles at forward angles as a function of p_{lab}. The domination of the positive signal by non-pions is graphically illustrated by the figure. Note that for p_{lab} = 100-200 MeV/c, the proton peak is off the scale to the right (Δt > 20ns). Note also that the pion peak becomes progressively more prominent with decreasing p_{lab}, as expected. From the figure, it is clear that

[†]We henceforth limit the discussion to protons, which were found to dominate both the coherent and incoherent background at the pion momenta measured in this experiment.

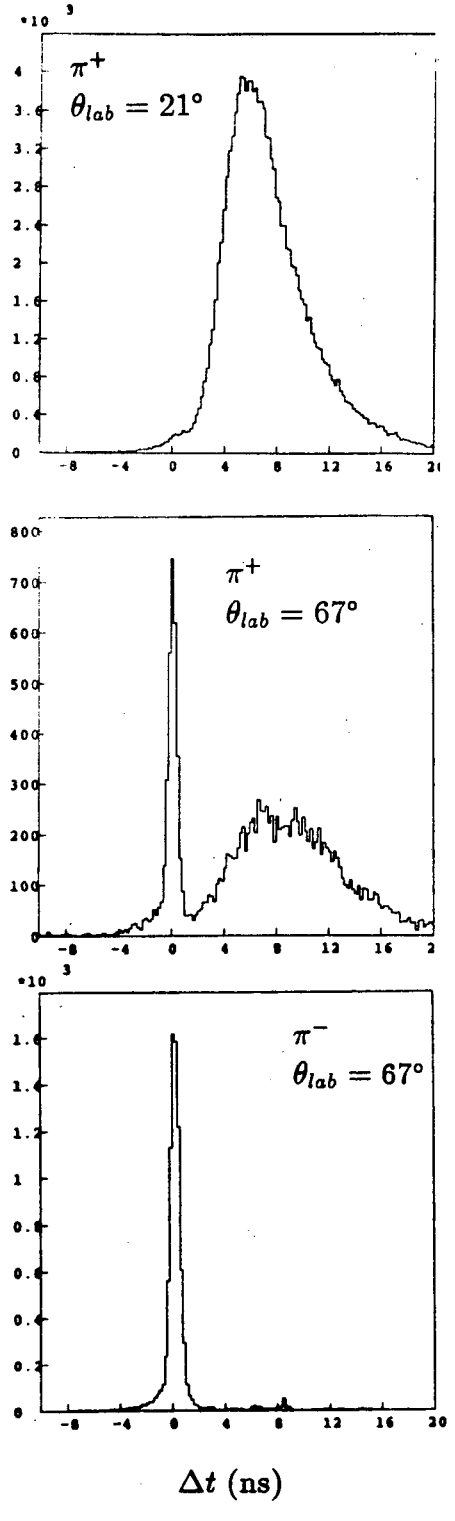

Figure 4.5. Δt distributions from 246 MeV La+La collisions for various settings.

the incoherent signal is the primary source of background over most of the pion momentum range.

The incoherent background was most prominent at forward angles, and was also present—although much weaker—in the negative particle distributions. The systematics of the background suggested that it was random in origin, but the reconstruction algorithm should have eliminated truly random tracks. The explanation seems to be that the background consisted of 'particles' for which the rigidity and t.o.f. information were uncorrelated. This could have happened if the wire chambers were triggered by one particle, while the TDC stop signal came from a different one, correlated only in position, giving an apparently consistent hit position on G3. This combination of events is consistent with the prominence of the background at forward angles and positive polarity—where the general background is greater—and also with the fact that the resolution of the G3 scintillator is much coarser than that of the wire chambers. We checked this scenario by constructing a Δt distribution by randomly matching the p_{lab} from one set of good tracks with the t.o.f. from a different sample. The resulting distribution was consistent with the background observed experimentally.

Understanding the incoherent signal made it possible to devise a background subtraction scheme with the correct momentum dependence. In particular, we know that this part of the background was composed of protons with velocities comparable to those of pions, and that the yield of fast protons falls roughly exponentially with decreasing time-of-flight.

Generating the corrected pion momentum spectrum

The next step was to tabulate the number of pions as a function of momentum, subtracting background counts where necessary. The procedure for this varied according to the severity of the background. Figs. 4.7 and 4.8 summarize the

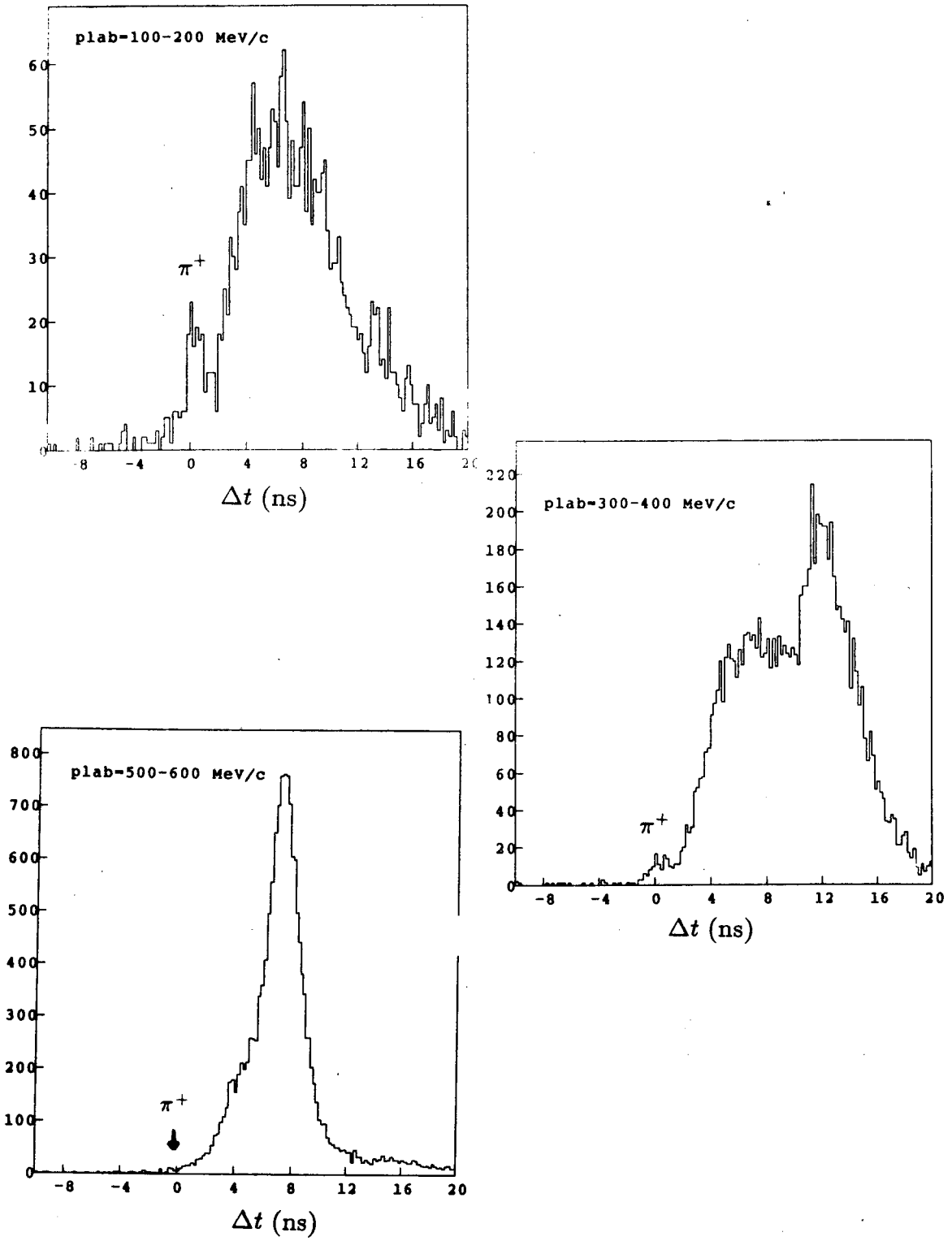

Figure 4.6. Δt distributions for positive particles at $\theta_{lab} = 21°$ from 246 MeV/nucleon La+La collisions, selected on different ranges in p_{lab}.

process for the zero background and high background cases, respectively. In all cases, the Δt distribution around $\Delta t \simeq 0$ was fit by a gaussian distribution. Pions were selected by a cut of width $\pm 2\sigma_{\Delta t}$. Where there was no background, this was the end of the process.

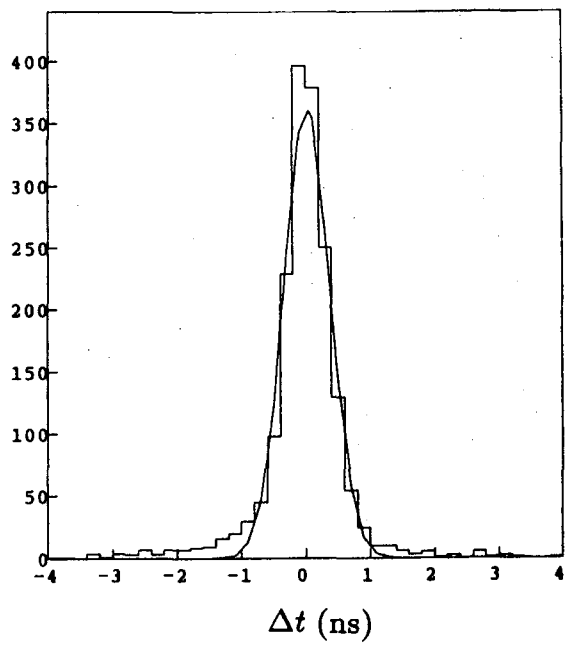

Figure 4.7. Generating a raw pion distribution where no background subtraction is required

Where it was necessary to do a background subtraction, the procedure was as follows:

For *each* bin,

- fit an exponential to the tail of the background which overlaps the pion peak and integrate to get the number of background counts.
- subtract the background from the original value.
- fit the corrected distribution with a gaussian, and apply a new $2\sigma_{\Delta t}$ cut.

The last step was necessary in the cases where the background was large enough to artificially broaden the uncorrected Δt distribution. The process is illustrated in Fig. 4.8a–f.

Some cases required special handling. Where the pion signal was too small to get a reasonable Δt fit, we used a fit to the inclusive distribution; where the overall statistics were too poor to fit the background, the subtraction was done by hand.

4.4.2 Energy Loss and Interactions in the Detector

The emitted particles were subject to interactions in the target, beam pipe and spectrometer. Positive particles could also interact with the absorber, and this case will be treated separately (Sec. 4.4.4). The interactions could be electromagnetic or nuclear, elastic or inelastic. Particles could be removed from the beam by absorption, charge exchange or stopping; their trajectories could be distorted, or they could be scattered out of the spectrometer. Besides the copper absorber, the greatest thicknesses (in gm/cm^2) of material traversed were the La target, the Al beam pipe and the plastic scintillators (mainly carbon). In each case, the amount of material traversed was a function of pion angle.

Rutherford scattering. The probability for single elastic Coulomb scattering through large angles is proportional to Z^2/A; consequently it was greatest for the ^{139}La target, at large lab angles. The probability for a pion to scatter through a large enough angle to be knocked out of the spectrometer was found to be 1% for this case, and was typically much smaller.

Multiple Coulomb scattering. The calculated deflection was less than 1° in all cases.

Nuclear interactions The effects of elastic and inelastic nuclear interactions were estimated from the data of Nakai *et al.*[138] and Ashery *et al.*[139]. The

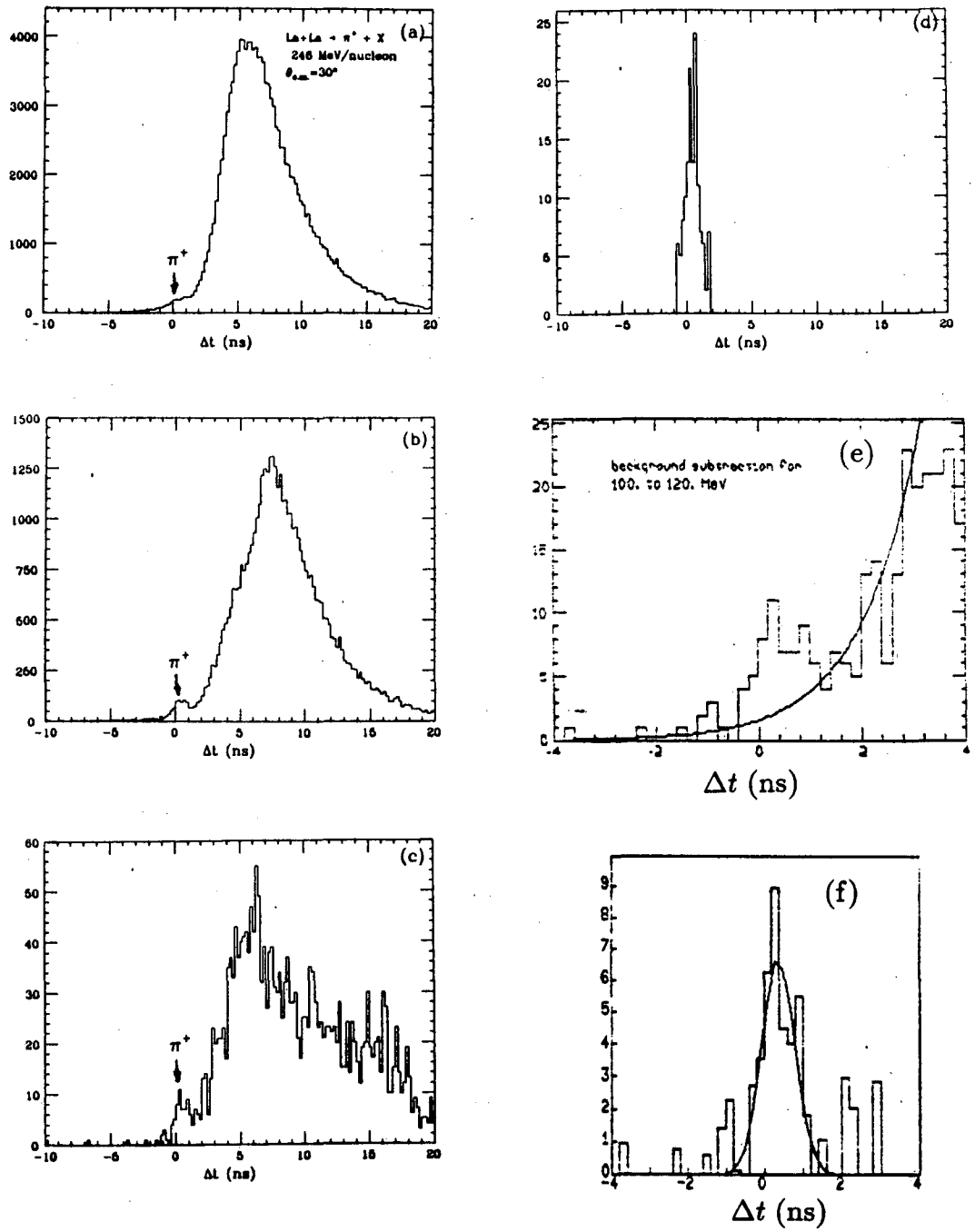

Figure 4.8. Background subtraction for a single bin ($T^{\pi}_{c.m.} = 100 - 120$ MeV) for π^- at $\theta_{c.m.} = 30°$ from 246 MeV/nucleon La+La collisions. (a) Raw Δt distribution. (b) Cut on $p_{lab} > 600$ MeV/c to make the pion peak more clear. (c) Select on $100 < T^{\pi}_{c.m.} < 120$ MeV. (d) Fit a gaussian to the π^- peak and cut on $2\sigma_{\Delta t}$.(e) Fit an exponential to the background near the π^- peak in (c), and integrate under it to get the number of background counts. (f) Subtract the background from (d), and fit a gaussian to the resulting distribution.

cross section for elastic nuclear interactions is highly forward peaked, and therefore does not greatly affect the pion trajectories. For inelastic interactions, we estimated pion losses due to true absorption, charge exchange and inelastic collisions. In the worst case, for 165 MeV π^- in scintillator, the loss was at most 3%.

Inelastic Coulomb Interactions

Since the pion energy is determined by bend angle in the magnet, only those energy losses which occur before the magnet can affect the spectrum. Total energy loss for pions in the target, beam pipe, G1 and G2 scintillators, MWPC's P1-P3 and air before the magnet is never more than 8 MeV, and usually between 3 and 4 MeV. The energy loss for each pion was calculated and each particle's energy was individually corrected. (Pions in the energy range of interest did not stop in the spectrometer.)

4.4.3 Spectrometer Acceptance

The solid angle acceptance of the spectrometer as a function of lab momentum was determined by Monte Carlo methods. The maximum possible phase space accessible to the spectrometer was divided into cells in momentum and angle. For each cell, a large number of particles was generated with simulated momenta and angles uniformly distributed over the cell. The vertex was chosen according to a gaussian distribution centered at the target center. The particles were tracked through the system, and the positions at each detector plane were calculated. In order for a particle to be accepted it had to hit each plane. The solid angle acceptance, $\Delta\Omega$, at a given momentum for each cell was defined to be the product of the solid angle and the ratio of particles accepted to particles thrown. This was summed over all cells to give the spectrometer acceptance. The acceptance

was also corrected for pion decay and (for π^+ running only) for the removal of three of the five elements of G2.

Pion Decay. According to the Monte Carlo simulation, approximately 15% of the pions decay (by the reaction $\pi \rightarrow \mu\nu$) somewhere in the spectrometer, with the higher momentum pions having a somewhat greater likelihood of passing through all the detector planes before decaying. In order to determine if a track made by a pion and daughter muon would be accepted, the acceptance code used the same track reconstruction criteria as were applied to the experimental data. Most of the muons were eliminated at this point. About 5% of the muons were accepted and successfully reconstructed; these comprised about 3% of the total accepted particles. Most of these either came from decays after P6 or were emitted at 0° or 180° in the pion rest frame. Of this number, only those which originated before the magnet presented a problem in the form of incorrectly calculated momentum, since pions which decayed after the magnet were already momentum-analysed. Due to the steep momentum dependence of the pion cross section, the momentum dependence of the muons could still be important, but this turned out not to be the case, for the following reason:

It can be shown from the pion decay kinematics that the 0° and 180° decay muons have lab momenta approximately ±50 MeV/c relative to the parent pion, over the momentum range of interest. The measured pion yield varies by about a factor of 2 to 4 over 50 MeV/c (Fig. 4.9). Folding this together with the small percentage of muons which are accepted, we found that the decay muons did not feed the pion distribution at higher or lower momenta to a significant extent. For the case of lower momentum muons feeding the higher momentum bins, the effect is about 2%, and the high-to-low momentum effect is negligible, due to the steeply–falling cross section.

G2 correction. This consisted simply of recalculating the acceptance with

G2 c, d and e disabled.

Fig. 4.10 summarizes the results of the acceptance calculations. The correction was applied bin-by-bin, and the statistical uncertainties in the acceptance histograms are incorporated in the calculation of the total error in each bin of the cross section. The results are consistent with those of Ref. 57 for essentially for the same spectrometer system.

4.4.4 Absorber

The absorber was designed to range out non-pions via ionization energy loss, and it was expected that a small percentage of slow pions would be stopped, as well (Fig. 3.7, p. 55). The number of pions lost in this way was calculated during the design process. Rutherford scattering in the absorber removes some pions by deflection into the wrong G3 element. This was estimated to be at most a 3% effect, and was corrected for by the reconstruction efficiency which measured the number of otherwise good tracks which failed to hit the correct G3 element (Sec. 4.4.5).

Pions could also be lost through nuclear interactions leading to scattering, charge exchange and absorption, and the magnitude of these effects was calculated from experimental data on pion absorption[138,139], as follows.

Ashery *et al.*[139] determined that pion elastic scattering is very sharply forward peaked, falling by two orders of magnitude between 0° and 30°. Inelastic scatterings are generally through large angles. The inelastic and true absorption cross sections are of comparable magnitude, and together exhaust about 80% of the total cross section. Due to the closeness of the absorber to G3, relatively large scatterings (up to about 40°) were acceptable, and therefore we neglected the effects of elastic scattering. The cross section for charge exchange is about 15–20% that for absorption, and was also neglected.

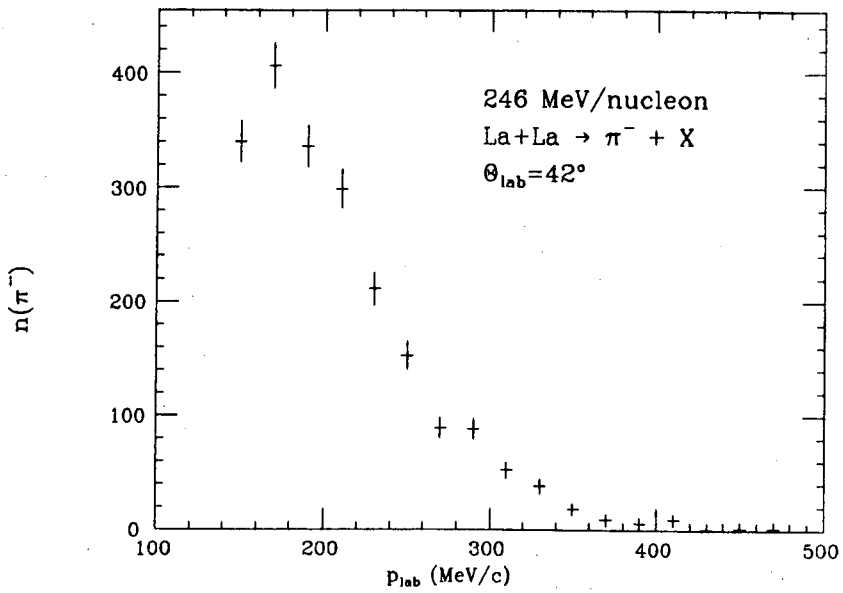

Figure 4.9. A typical pion momentum distribution. Note that the ordinate is linear.

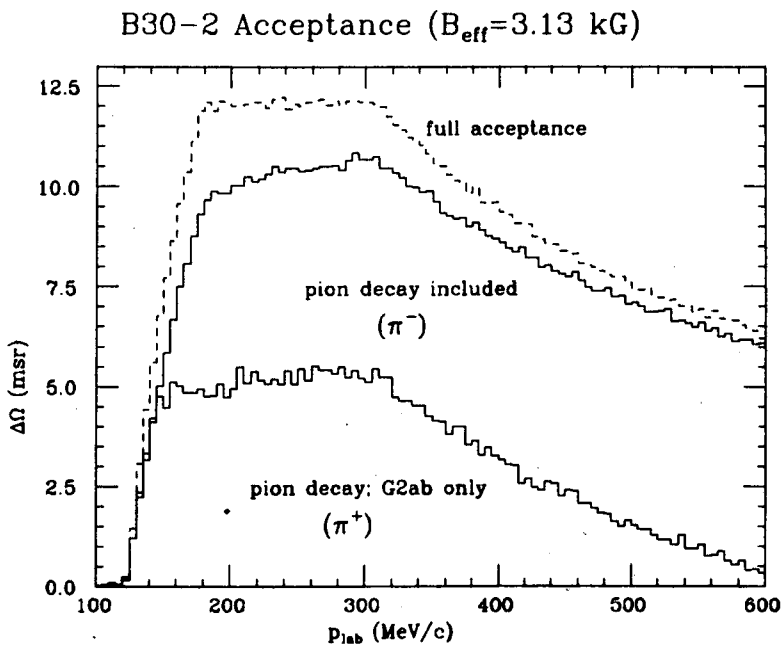

Figure 4.10. B30-2 spectrometer acceptance. In order of decreasing acceptance, the histograms represent 1) the acceptance for the full system, 2) the acceptance with pion decay included (used for π^-) and 3) the acceptance with pion decay and G2c,d,e disabled (used for π^+). Note that this is the acceptance for singly-charged particles at the low magnetic field setting, used for pions. The acceptance is proportional to the magnetic field and inversely proportional to the charge. (See Ref. 57.)

These data were for $\pi^{\pm}$ incident on a range of nuclei from ^{7}Li to ^{209}Bi, but not including Cu. To get the correction factors for the absorber, we combined the information from Ashery *et al.*[139] on angular dependence and relative magnitudes with the true absorption cross sections for charged pions on Cu measured by Nakai *et al.*[138].

The algorithm for computing the correction was:

- *For each momentum bin*, use the acceptance Monte Carlo to determine the relative number of particles traversing a given thickness of absorber.
- Calculate the number of particles stopped due to Coulomb losses.
- Making use of the finding in Ref. 139 that the inelastic and true absorption cross sections are approximately equal, estimate the losses due to nuclear absorption and inelastic scattering, by doubling the true absorption cross sections from Ref. 138.
- Take a weighted average over the width of the absorber to obtain the average fraction of pions lost at this momentum.
- Repeat for the next momentum bin, etc.

The results for π^{+} and π^{-} are shown in Fig. 4.11.

A more direct way of measuring the effect of the absorber was to take π^{-} data with and without the absorber. This is illustrated in Fig. 4.12. The results are consistent with the calculation. Note that the experimental uncertainties in the data are too large to allow us to extract correction factors directly.

Lastly, the shift in position of some of the absorber plates during the data–taking was taken into account by recalculating the absorber correction with the new position information and applying the updated correction factor to data taken after the absorber was moved. (See Fig. 3.9 and the accompanying discussion.)

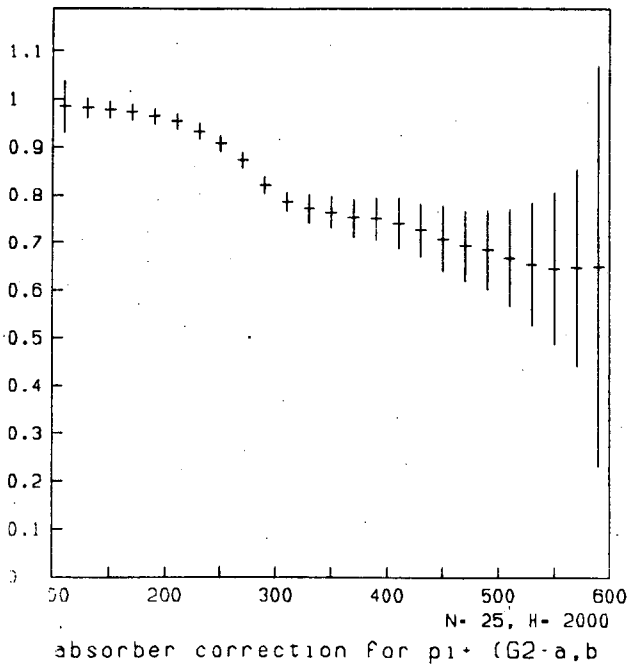

Figure 4.11. Correction factor for pions lost in the copper absorber, plotted as a function of pion laboratory momentum in MeV/c.

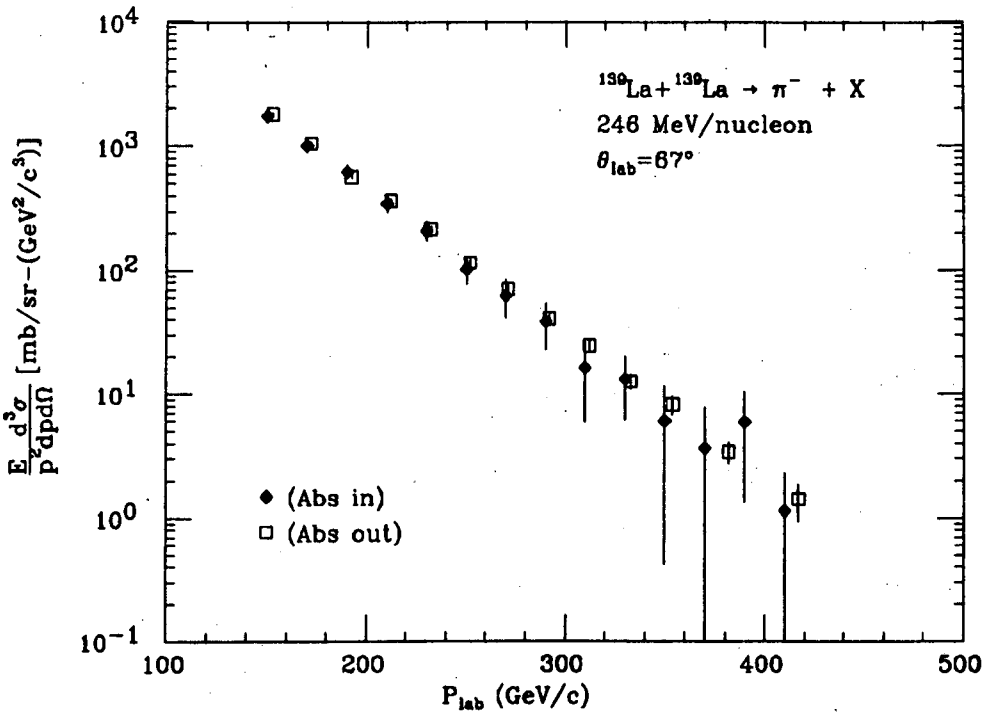

Figure 4.12. Comparison of π^- cross sections with and without the absorber. Data is for 246 MeV/nucleon La+La at $\theta_{lab} = 67°$.

4.4.5 Efficiencies

MWPC efficiency. Although the wire chamber efficiencies were measured directly at the start of data taking, their performance during the run did not always match those figures (p. 49). It was therefore necessary to have a measure of the efficiencies for real data. This was computed by looking at single tracks, i.e. those with no more than one hit on any plane. The efficiency was defined to be:

$$\frac{\text{number of reconstructed single tracks}}{\text{number of single tracks, } \geq 9 \text{ hits}}$$

where a reconstructed track was one which met the criteria regarding wire chamber hits, outlined in Sec. 4.1, above.

This gave a momentum–averaged result for single tracks and was also used for tracks with more than one hit per plane. Studies with experimental data showed that the momentum–averaging and extension of the single track results to multiple hits were reasonable assumptions. The above procedure was not a good measure of any correlated inefficiencies, such as undetected minimum ionizing particles or sagging of the chambers when there was a large number of hits. The former problem was minimized by plateauing the chambers with minimum ionizing particles, while in the latter case, the particle distributions in multiple hit events were consistent with those from single track events.

G3 efficiency. This was defined to be the number of tracks which passed all of the reconstruction criteria (MWPC's and G3) divided by those which passed only the MWPC part.

Both efficiencies tended to fall with decreasing lab angle, and were found to be smaller for positive than for negative pions. They ranged from greater than 90% for π^- at large angles to around 70% for π^+ at forward angles. This indicates a correlation with overall particle multiplicity, as might be expected.

G3-1 failure. During the analysis it was confirmed that G3-1 had failed during the 183 MeV/nucleon La+La running. By studying the results of the runs immediately preceding the failure, it was determined that there was no correlation between momentum or t.o.f. and G3 element, and so we could make a correction by simply multiplying the G3 efficiency by a factor

$$1 - \frac{\text{n(G3-1)}}{\text{total}}$$

where [n(G3-1)/total] is the percentage of good tracks which included a hit on G3-1, as determined from the preceding runs.

Computer live time. This was the percentage of event triggers accepted by the computer. It was correlated mainly with angle, due to the higher trigger rate at forward angles, and ranged from near 100% at $\theta_{lab} = 67°$ to around 60% at $\theta_{lab} = 21°$, independent of pion charge.

4.5 Computing the Pion Cross Sections

The cross section was computed at each momentum according to the formula

$$\frac{d^2\sigma}{dpd\Omega} = \mathrm{N}_\pi \cdot \frac{1}{\Delta\mathrm{p}\Delta\Omega} \cdot \frac{1}{\mathrm{N_{beams}}} \cdot \frac{A_{tgt}}{\mathrm{N}_0\rho l} \cdot \frac{1}{\text{eff.(MWPC)}} \cdot \frac{1}{\text{eff.(G3)}} \cdot \frac{1}{\%\text{live}}$$

where,

N_π is the number of pions obtained in this bin, corrected for background, if any,

Δp is the bin width in p_{lab},

$A_{tgt}/\mathrm{N}_0\rho l$ is the normalization to the target thickness

and

$\mathrm{N_{beams}}$=(#IC counts)·(beam particles/IC count) is the normalization to the beam intensity. The other factors have been discussed above and in Chapter 3. For π^+, the absorber correction was also factored in at this point.

The first pass through the data produced an invariant lab cross section, $(E/p^2)d^2\sigma/dpd\Omega$ with uniform bin width, Δp, = 5 MeV/c. The results of this pass were used to determine the bin width for the final laboratory cross section. The background subtraction was also done, bin by bin, at this point, and the final bin widths reflect the statistics after subtraction. A bin width of 20 MeV/c was found to be reasonable for most of the data. (Smaller bins led to bin-to-bin fluctuations of the same order as the statistical uncertainties, while larger bins tended to wash out structure in the cross sections.) Wider bins were used on the tails of the distributions, with the object of having no fewer than five counts per bin.

For each new bin, we computed a bin-weighted average lab momentum, which was the value used for plotting and tabulating the lab cross sections. The invariant lab cross section was converted to an invariant center of mass cross section vs. pion c.m. kinetic energy by transforming the limits of each bin from p_{lab} to $T_{c.m.}$. This was straightforward, since there is an almost one-to-one correspondence between lab and c.m. angles for the beam energies in this experiment (Fig. 4.13). Finally, the variant c.m. cross section was obtained from the relation $\sigma_{var} = \frac{1}{E}\sigma_{inv}$, where E is the total pion energy in the c.m. .

The range in $\theta_{c.m.}$ was taken to be about $\pm 3°$. This was large enough to cover a reasonable range in pion energy, without washing out any angle dependence. Specifying a range in c.m. angle was equivalent to limiting the range of accepted c.m. energies.

In two cases (both at 246 MeV/nucleon) there are two lab angles covering a given c.m. angle ($\theta_{lab} = 62.5°$ and $67°$ for $\theta_{c.m.} = 90°$ and $\theta_{lab} = 40°$ and $42.5°$ for $\theta_{c.m.} = 60°$). Here, we chose the lab angle which corresponded most closely to the appropriate c.m. angle for a given momentum. The values of the lab cross sections in the overlap region were equal, within uncertainty.

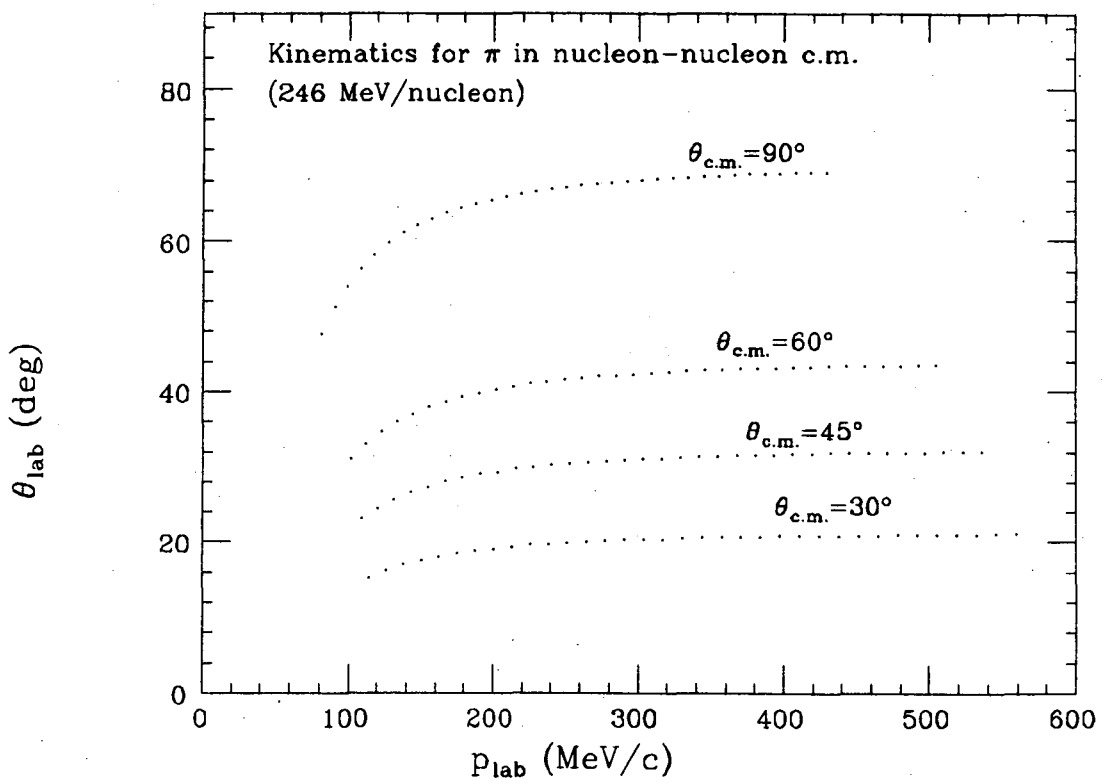

Figure 4.13. Correspondence between lab and c.m. angles for pions from a symmetric system at 246 MeV/nucleon.

Target-Out Runs

At each setting, we took data with the target out, in order to measure the contribution to the pion spectrum from sources other than target interactions. This background was negligible in every case. For example, for the worst case, which was for 246 MeV/nucleon at $\theta_{lab} = 21°$ and positive polarity, 4.4×10^8 La ions produced 415 triggers, of which 23 were successfully reconstructed. Of these, none were pions. The corresponding numbers for a run with the target in were 1.7×10^9 ions, 9.4×10^4 triggers accepted, 3.1×10^4 reconstructed tracks and approximately 30 pions.

4.5.1 Uncertainties

The error bars on the cross sections reflect the uncertainties in the acceptance, the MWPC efficiencies, the background subtraction and the number of counts. The size of the errors varied with the number of pions in the bin, which ranged from a few dozen counts to several thousand (Appendix C).

The other major uncertainty is in the beam intensity. We used the calibration obtained from scintillation counting, which has an uncertainty of about ±10%, but it should be noted that the carbon activation method gave a value which was about 33% higher. (Sec. 3.3.2). In the spirit of Table III. of Ref. 12 Table 4.1 summarizes the experimental uncertainties and corrections.

Type of correction	Size of correction	Uncertainty
(1) Beam intensity*	0	±10%
(2) Computer live time	+20%	±1%
(3) MWPC efficiency	+20%	±5%
(4) G3 efficiency	+20%	±5%
(5) Loss due to Δt cut*	0	-5%
(6) Loss due to pion decay in flight*	+15%	±3%
(7) Scattering in the spectrometer*	0	±1%
(8) Absorption in the spectrometer*	0	-3%
(9) Losses in the absorber	+5%	±5%
(10) Background subtraction	-5%	5%
(11) Target–out background	0	0%
Total systematic uncertainty		$\simeq$ ±10%

Table 4.1. Uncertainties and correction factors for the cross sections measured in this experiment. For those values which vary from run to run, typical values are given. Corrections marked with an asterisk (*) are for systematic uncertainties. All other corrections vary from data point to data point, and are included in the error bars. The total systematic error is in addition to the point to point uncertainties.

4.6 Calibration Against Other Experimental Results

Before analysing the bulk of the data we compared our results at two settings with data from two previous experiments (Figs. 4.14 and 4.15). The consistency of our results with the earlier La+La data,[†] and especially the excellent agreement with both the π^- and π^+ data of Lemaire *et al.*[140], which were obtained using an earlier version of our spectrometer, gave us confidence in the performance of the system and the data analysis procedures.

[†]We attribute the discrepancies between the present results for La+La and those of Krebs *et al.*[13], to differences in the spectrometers and data analysis between the two experiments. In particular, pion decays were not accounted for in the previous experiment.

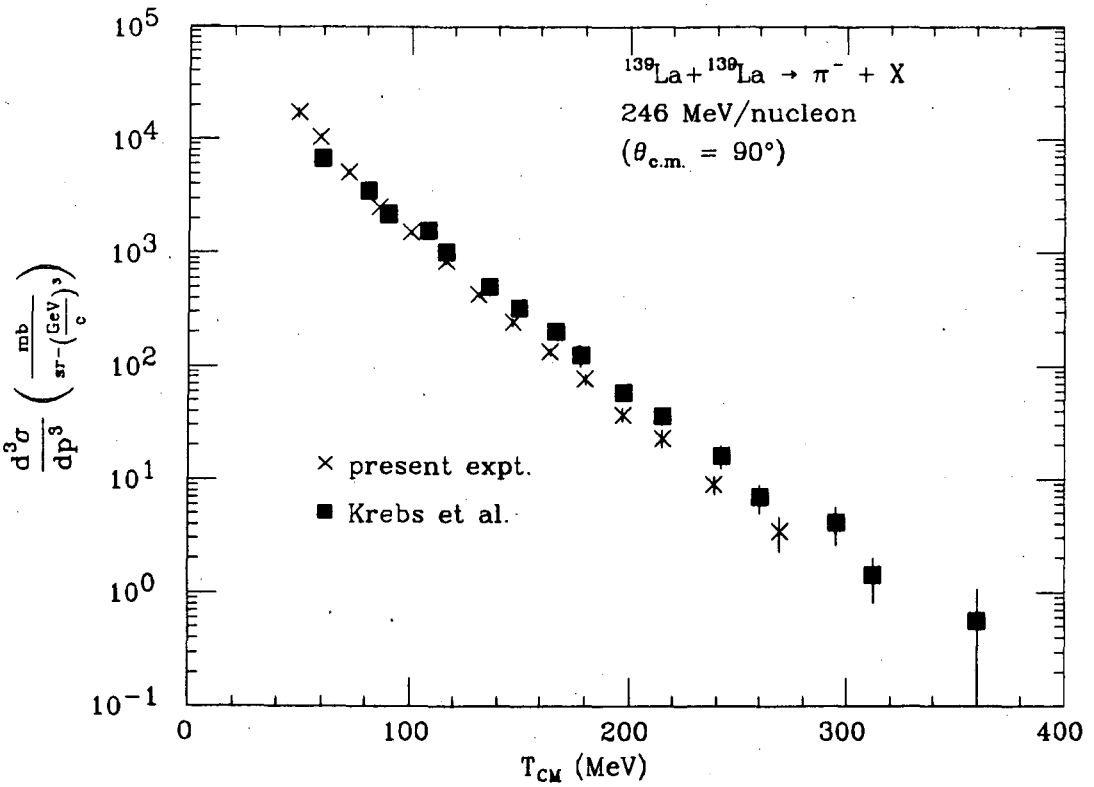

Figure 4.14. Comparison between results of the present experiment and earlier data of Krebs *et al.*(Ref. 13) for 246 MeV/nucleon La + La → π^- + X at $\theta_{c.m.} = 90°$.

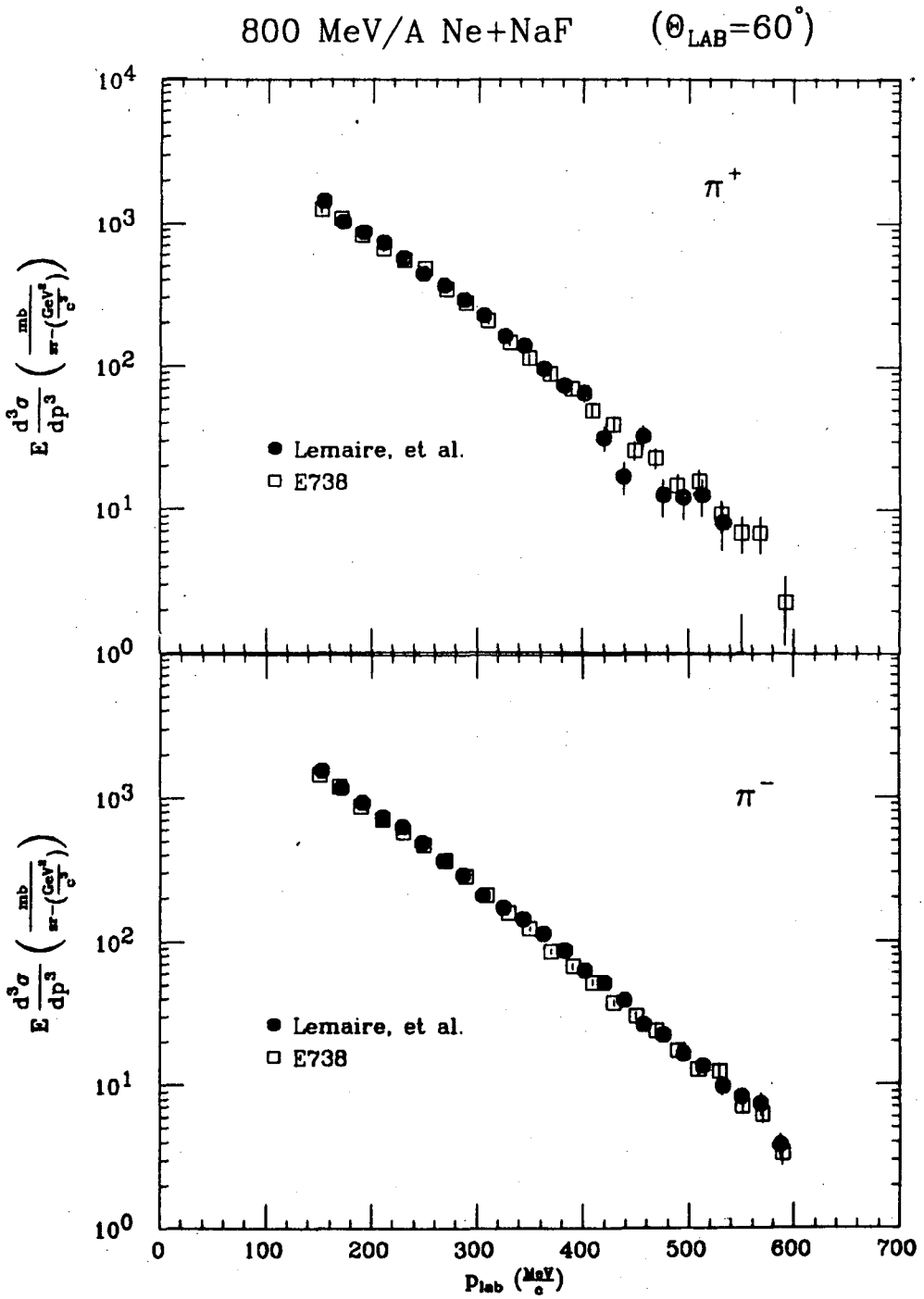

Figure 4.15. Comparison between results of the current experiment and earlier data for 800 MeV/nucleon Ne + NaF $\rightarrow \pi^{\pm} + X$ at $\theta_{lab} = 60°$ (Ref. 140).

5. Results and Discussion[†]

In this chapter we examine in detail the inclusive pion cross sections and associated multiplicity distributions. The phenomenology of the spectra and correlations between experimental observables will be considered in the context of other pion data and theoretical models.

5.1 Pion production cross sections and associated multiplicities

Fig. 5.1 summarizes the data taken for the La+La system, plotted in the center of mass. The error bars represent experimental and statistical uncertainties, but do not include the overall error of about 10%, due to the uncertainty in the beam intensity (Sec. 4.5.1). (The cross sections are tabulated in Appendix A.) These densely populated plots are presented in order to illustrate the scope and general features of the data set. We can generally characterize the data, as follows.

Quality of the data The associated errors and the scatter in the data points give an idea of the quality of the data as a function of beam energy and pion energy, angle and charge. In general, the uncertainty varies directly with pion energy and inversely with beam energy and pion angle, and is larger for π^+ than for π^-. The differences are mainly statistical in origin.

Pion energy dependence The pion cross section in all cases falls off approximately exponentially with pion energy, as observed in other mass systems at beam energies both above and below threshold. (See, for example, Fig. 2.9.)

Angular distribution Within uncertainty, the present results are consistent with isotropic pion emission in the center of mass. However, there are strong

[†]Some of the material presented in this section has been published in Ref. 141.

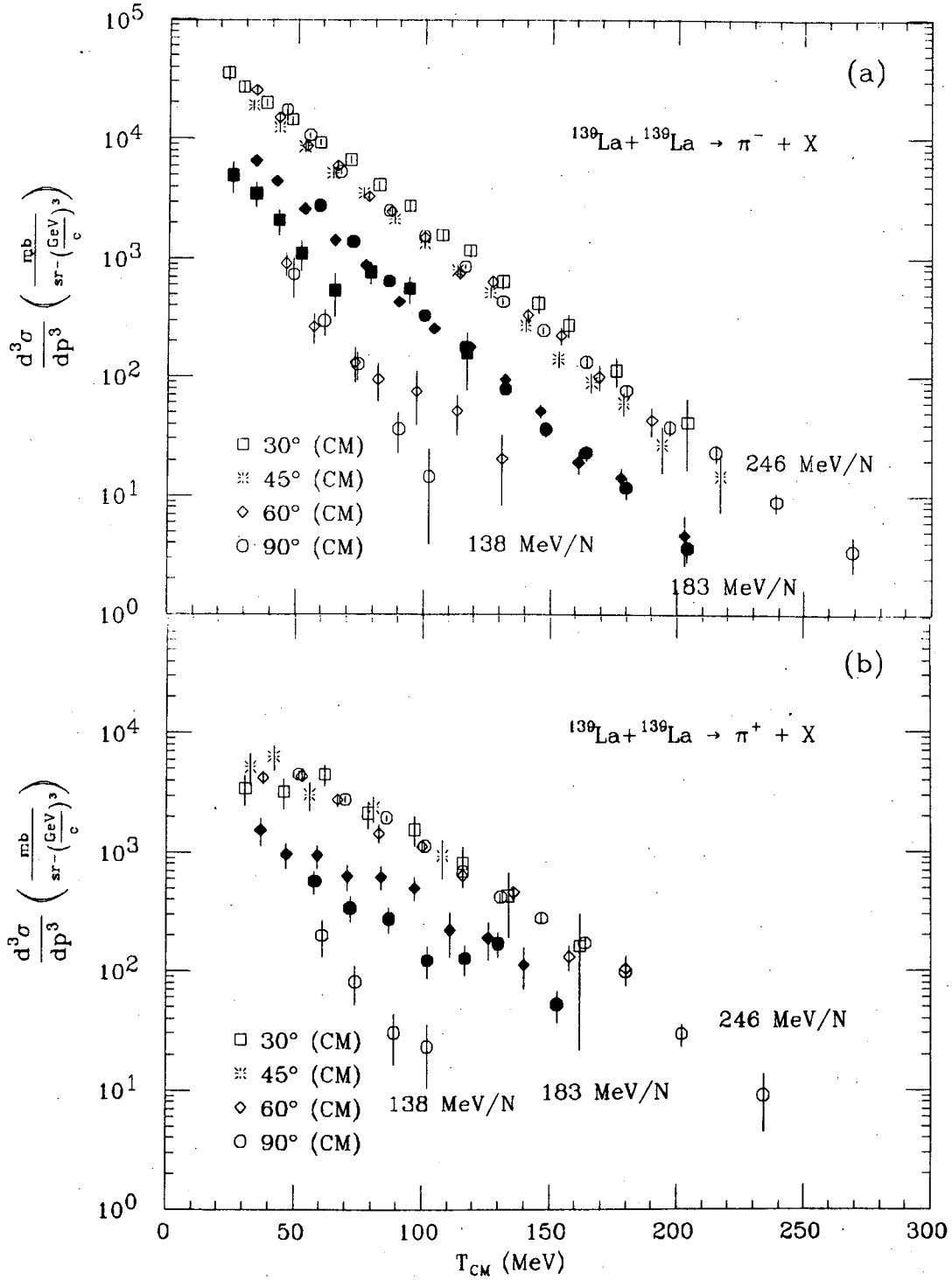

Figure 5.1. Variant cross section $d^3\sigma/dp^3$ as a function of pion kinetic energy in the c.m. for inclusive production of charged pions in La+La collisions at 138, 183 and 246 MeV/nucleon incident beam energy and center of mass angles between 30° and 90°. The data points for 183 MeV/nucleon are solid, the others, open. (a) π^-, (b) π^+.

local variations, especially at the lower beam energies.

Beam energy dependence The inclusive yield decreases monotonically with beam energy, as observed for π^- from the much lighter Ne+NaF system (Fig. 2.9).

There are some significant deviations from these trends, as will be discussed in the following sections.

5.1.1 Dependence on pion energy and angle

Laboratory[†]

Charged subthreshold pions from La+La at T_{beam} = 138–246 MeV/nucleon (Figs. 5.2–5.4) have the same general angular dependence as observed above threshold. (See, e.g., Fig. 2.7). In addition,

- At 246 MeV/nucleon, the π^+ cross sections turn over sharply at low momenta. (This feature will be discussed in detail in Sec. 5.3.)
- At 183 MeV/nucleon, the π^- cross section at 21° shows some unexpected structure in the form of a strong enhancement above 220 MeV/c, accompanied by an apparent depletion below 220 MeV/c. There is also a suggestion of a high-momentum enhancement in the 42° cross section.

Center of Mass

Pion emission between 30° and 90° in the center of mass is almost isotropic, in the sense that the yield at a given pion kinetic energy does not vary much with angle, (Figs. 5.5–5.7), with the following exceptions:

- 246 MeV/nucleon La+La :

[†]The laboratory distributions do not show all the data taken. At the beam energies in this experiment, the kinematics are such that there is almost a 1:1 correspondence between laboratory and c.m. angle. However, in order to pick up the lowest pion momenta at $\theta_{c.m.}$ = 60° and 90°, some data was taken at closely separated lab angles. (θ_{lab} = 40°, 42.5° and 62.5°, 67°, respectively.) The data at θ_{lab} = 40° and 62.5° are omitted here, for clarity; they are tabulated in Appendix A.

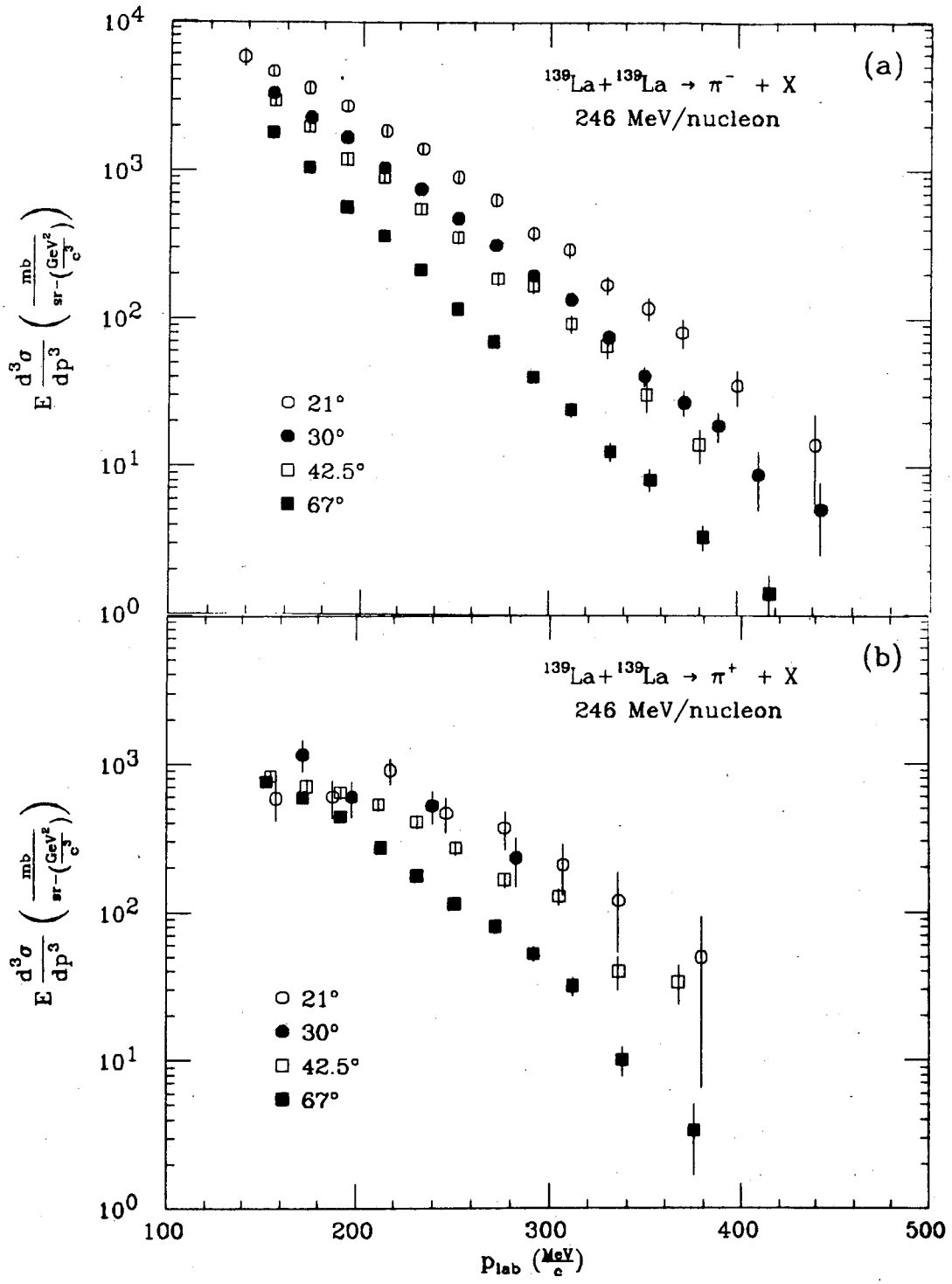

Figure 5.2. Invariant cross section, $Ed^3\sigma/dp^3$, as a function of pion lab momentum for inclusive production of (a) negative and (b) positive pions in La+La collisions at 246 MeV/nucleon incident beam energy and laboratory angles between 21° and 67°. (Note that the abscissa starts at 100 MeV/c.)

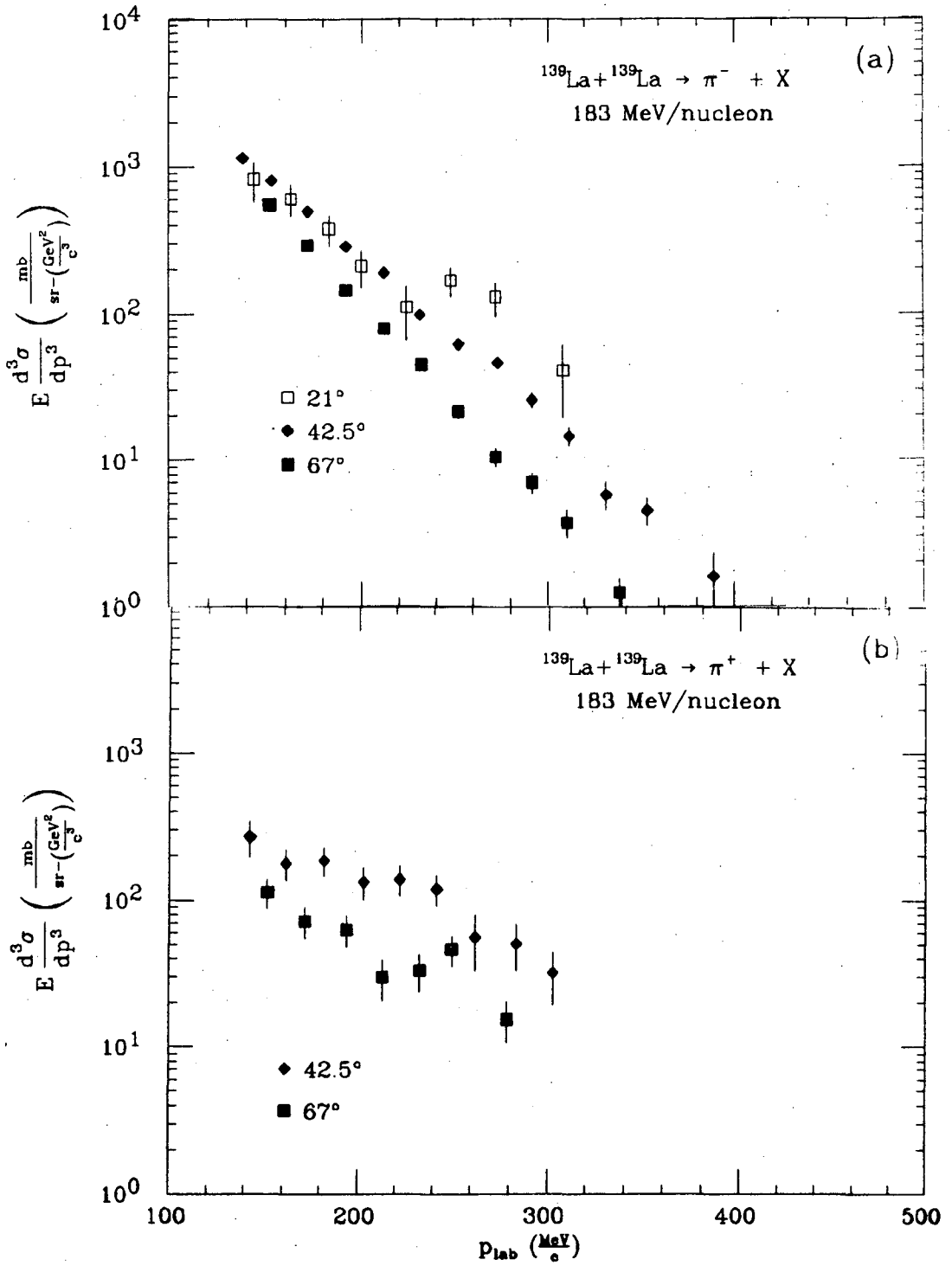

Figure 5.3. Invariant cross section $Ed^3\sigma/dp^3$ as a function of pion lab momentum for inclusive production of (a) negative and (b) positive pions in La+La collisions at 183 MeV/nucleon incident beam energy and laboratory angles between 21° and 67°. (Note that the abscissa starts at 100 MeV/c.)

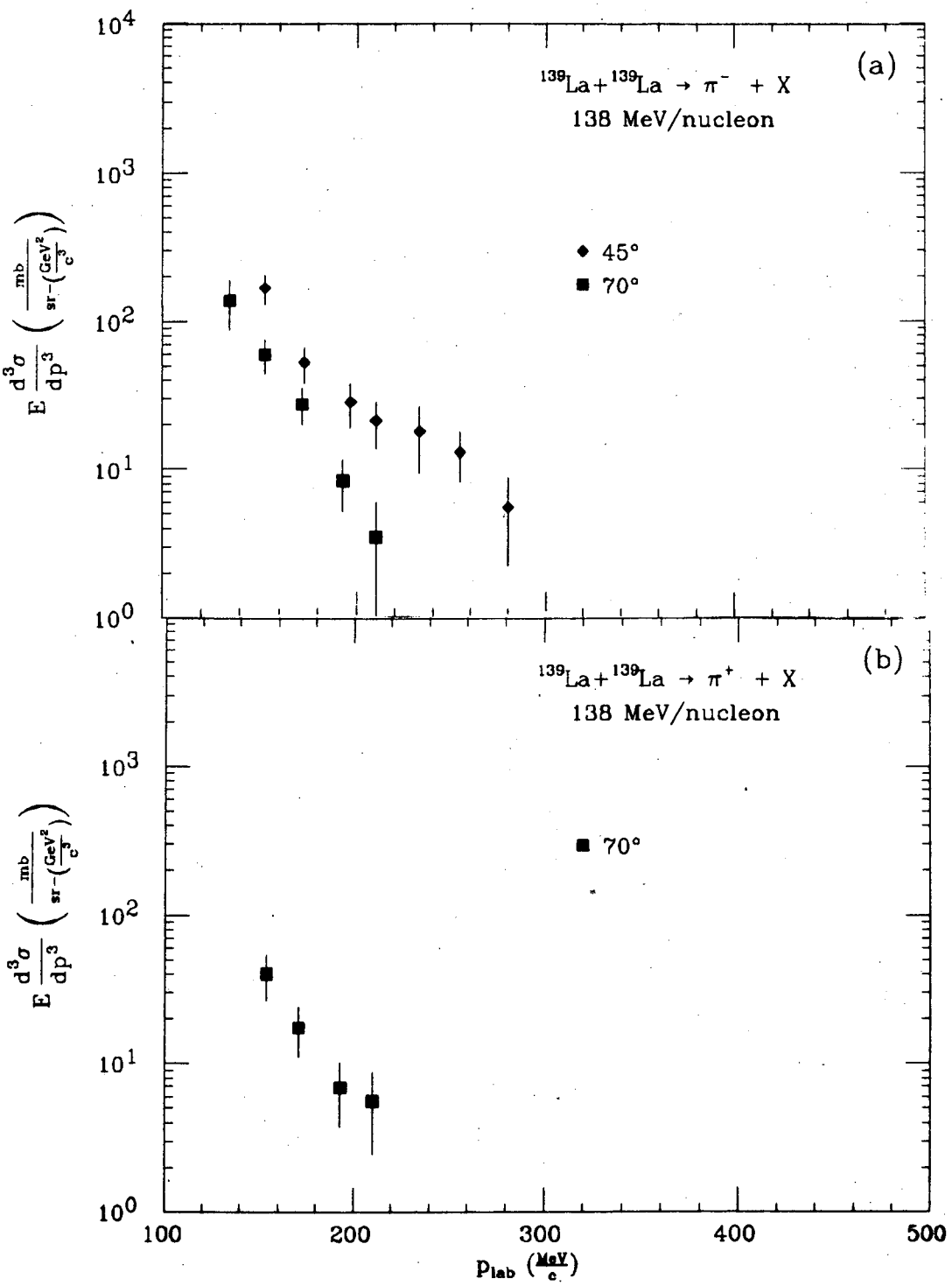

Figure 5.4. Invariant cross section $Ed^3\sigma/dp^3$ as a function of pion lab momentum for inclusive production of (a) negative and (b) positive pions in La+La collisions at 138 MeV/nucleon incident beam energy and laboratory angles of 45° and 70°. (Note that the abscissa starts at 100 MeV/c.)

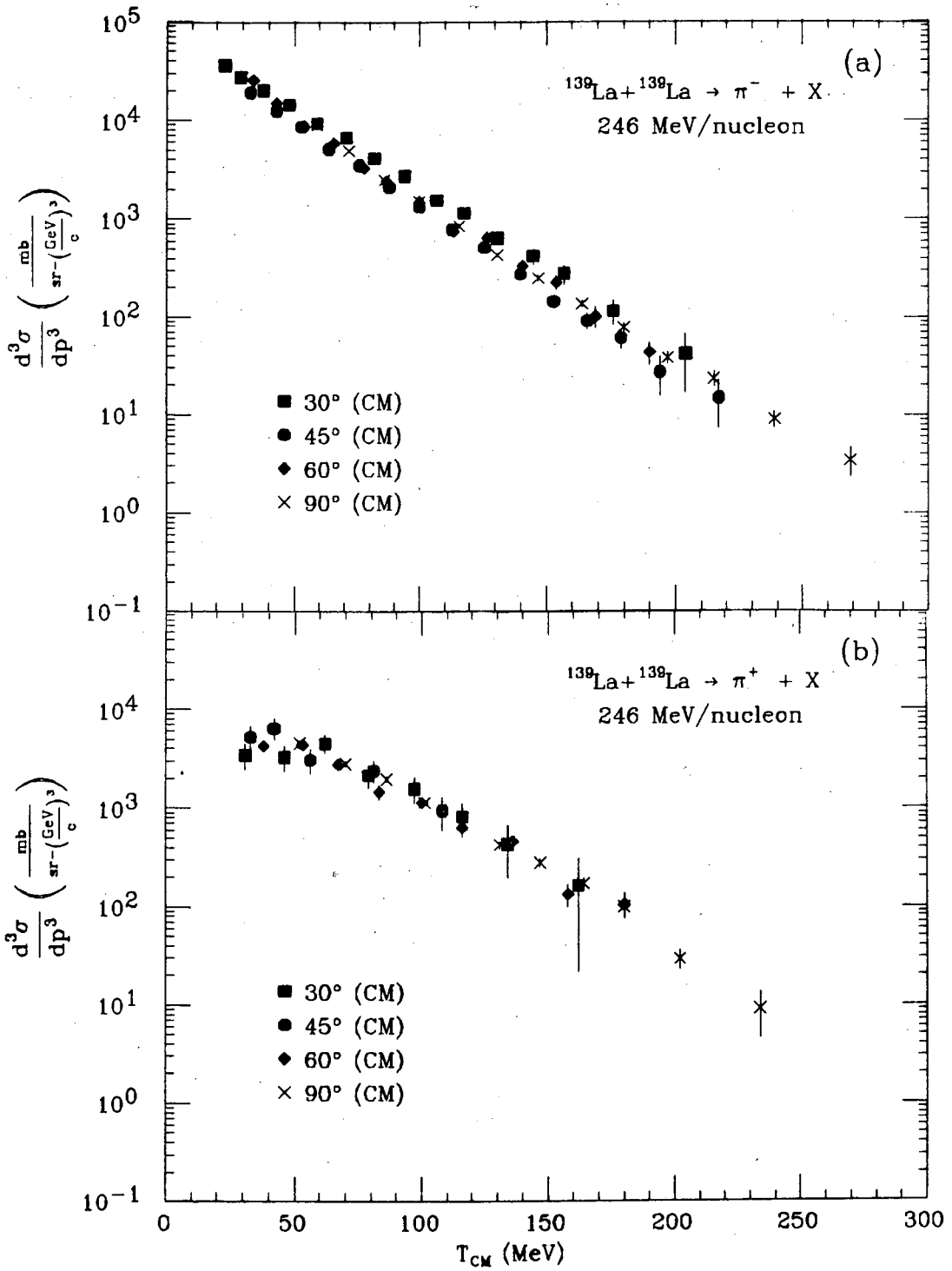

Figure 5.5. Variant cross section $d^3\sigma/dp^3$ as a function of pion center of mass kinetic energy for inclusive production of (a) negative and (b) positive pions in La+La collisions at 246 MeV/nucleon incident beam energy and c.m. angles between 30° and 90°.

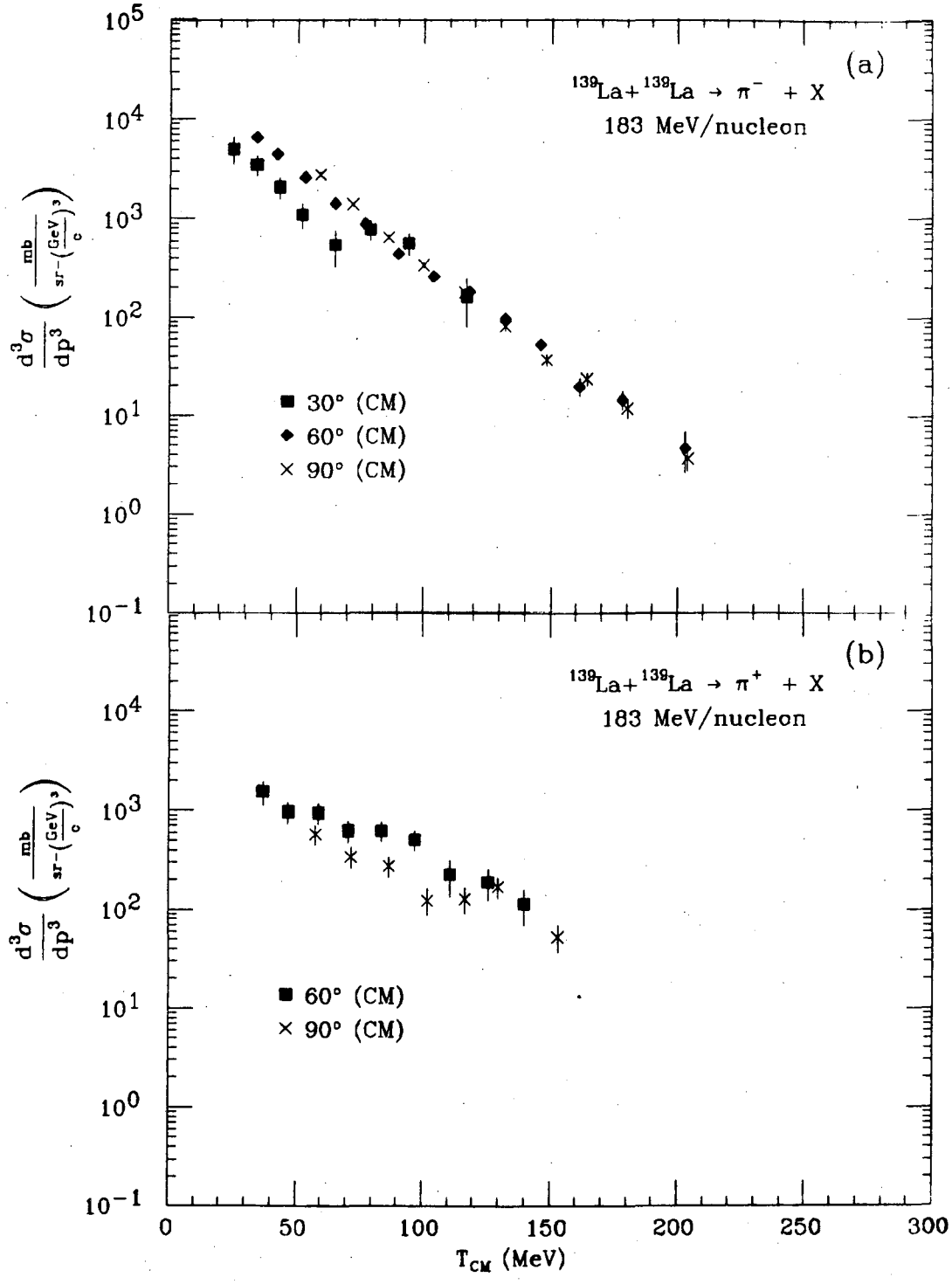

Figure 5.6. Variant cross section $d^3\sigma/dp^3$ as a function of pion center of mass kinetic energy for inclusive production of (a) negative and (b) positive pions in La+La collisions at 183 MeV/nucleon incident beam energy and c.m. angles between 30° and 90°.

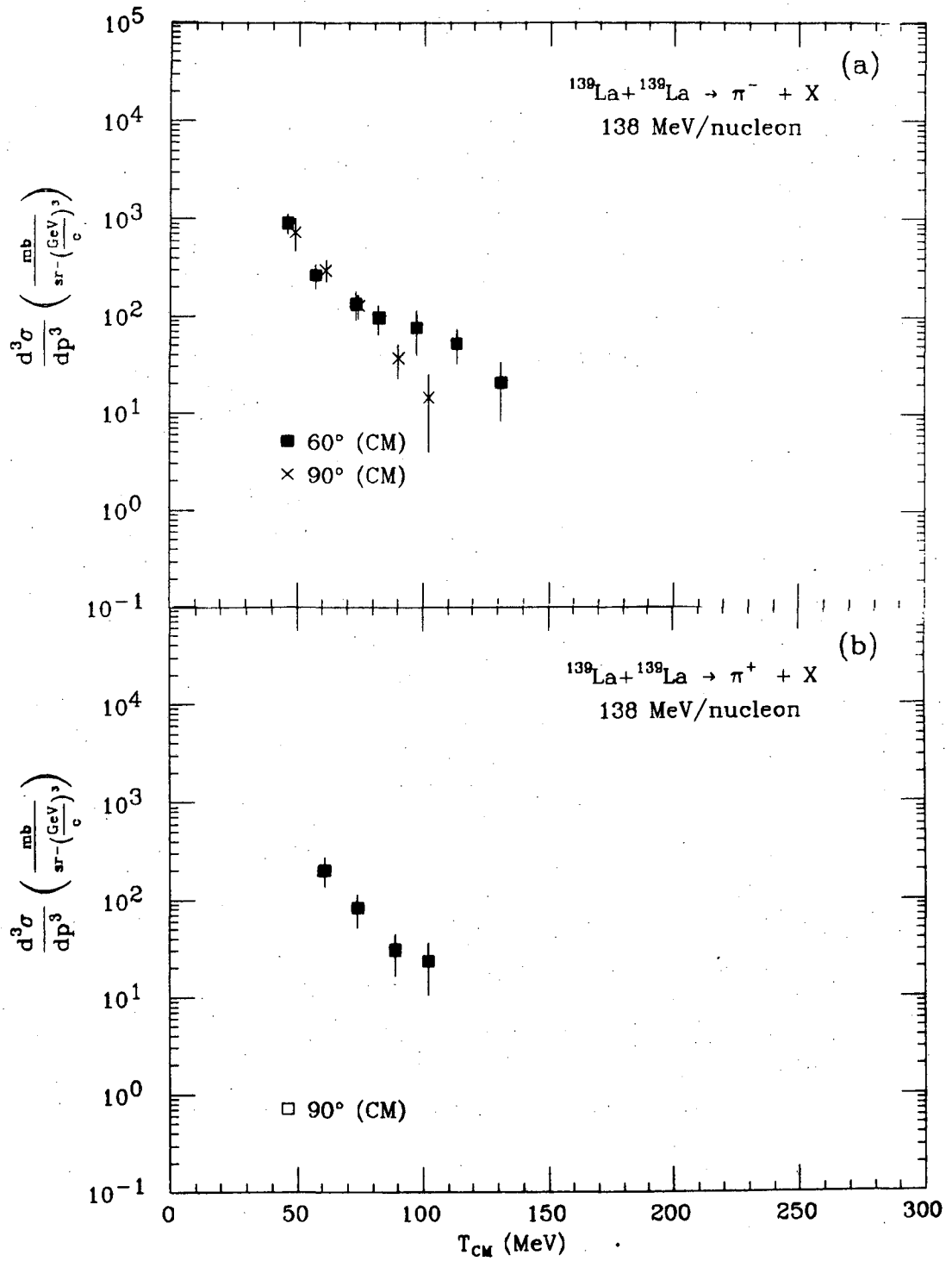

Figure 5.7. Variant cross section $d^3\sigma/dp^3$ as a function of pion center of mass kinetic energy for inclusive production of (a) negative and (b) positive pions in La+La collisions at 138 MeV/nucleon incident beam energy and c.m. angles of 60° and 90°.

- A turnover of the π^+ energy spectrum at low pion energies. (This is also evident in the lab cross section.) The detailed angular dependence of this effect cannot be determined, due to the limited statistics.
- A turn-up in the π^- spectra (i.e. cross sections in excess of those expected from an exponential fit to the data at higher pion energies) below 50 MeV. Fig. 5.8 compares the π^- and π^+ spectra at $\theta_{c.m.} = 60°$ and 90°.
- An increase in the π^- yield at $\theta_{c.m.} = 30°$. For π^+, the uncertainties are too large to show an effect of this magnitude.

• 183 MeV/nucleon La+La:

- The angular distribution for π^- is isotropic above $T^{\pi}_{c.m.} = 80$ MeV. Between 25 and 65 MeV the $\theta_{c.m.} = 30°$ spectrum is strongly depleted. There is evidence for a similar but much smaller effect at $\theta_{c.m.} = 60°$ (as compared to $\theta_{c.m.} = 90°$).
- The π^+ yield at pion energies between 50 and 100 MeV is greater at $\theta_{c.m.} = 60°$ than at $\theta_{c.m.} = 90°$.

• 138 MeV/nucleon La+La:

- The statistics are very limited, but the π^- yield for $T^{\pi}_{c.m.} > 100$ MeV is greater at $\theta_{c.m.} = 60°$ than at $\theta_{c.m.} = 90°$. (Data for π^+ were taken at only one angle.)

The spectra for the reaction ^{20}Ne + NaF $\rightarrow \pi^- + X$ at 244 MeV/nucleon are shown in Figs. 5.9 and 5.10.

The π^- spectra have the same pion energy and angular dependence found for the La+La case, as well as for Ne+NaF at other beam energies[12,57], but here

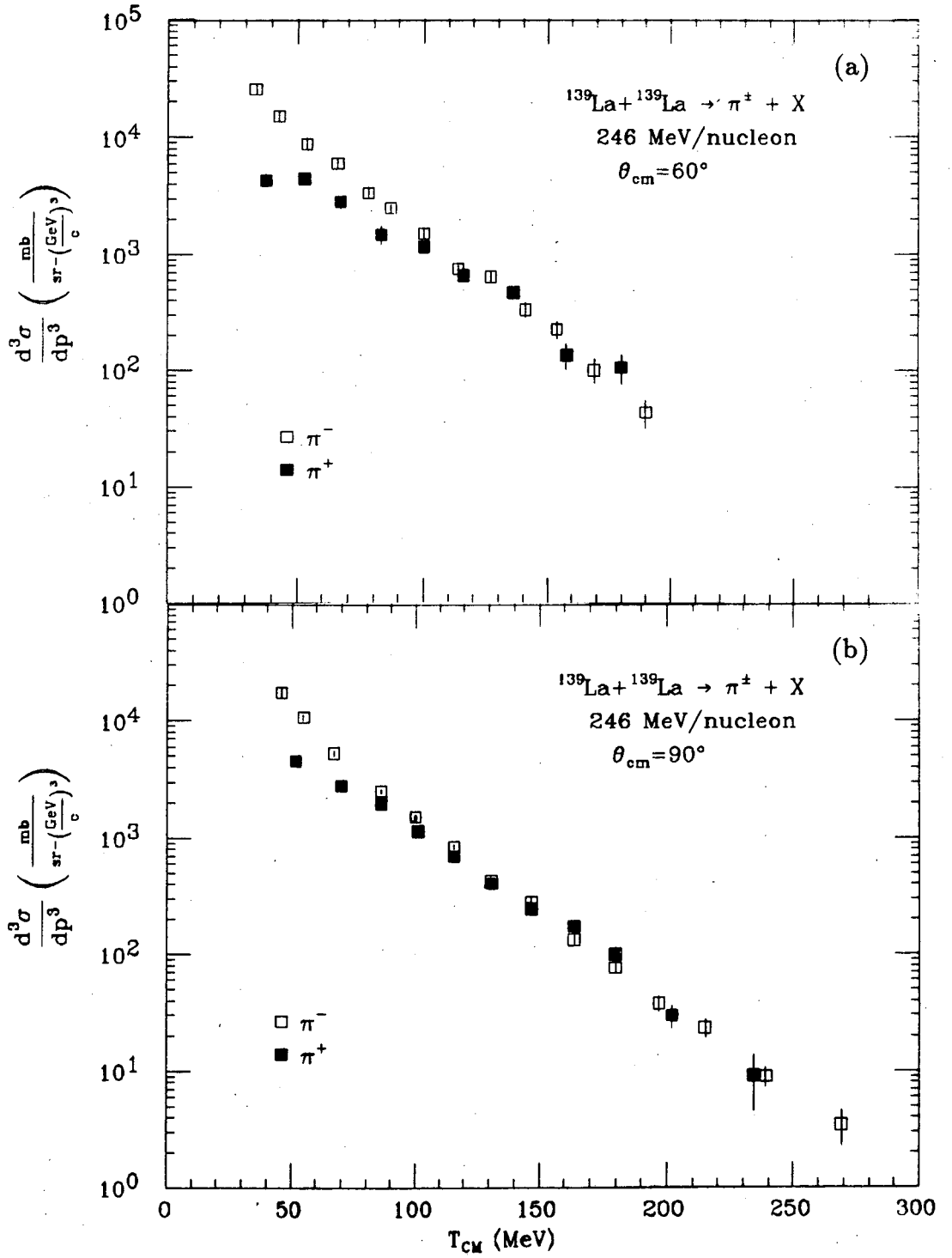

Figure 5.8. Inclusive cross sections $d^3\sigma/dp^3$ for production of π^+ and π^- at (a) $\theta_{c.m.} = 60°$ and (b) $\theta_{c.m.} = 90°$ in La+La collisions at 246 MeV/nucleon.

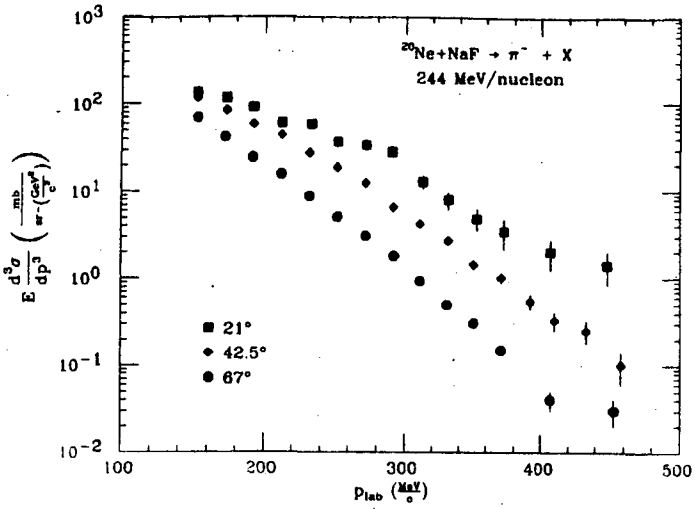

Figure 5.9. Invariant cross section $Ed^3\sigma/dp^3$ as a function of pion lab momentum for inclusive production of negative pions in Ne+NaF collisions at 244 MeV/nucleon incident beam energy and laboratory angles between 21° and 67°. (Note that the abscissa starts at 100 MeV/c.)

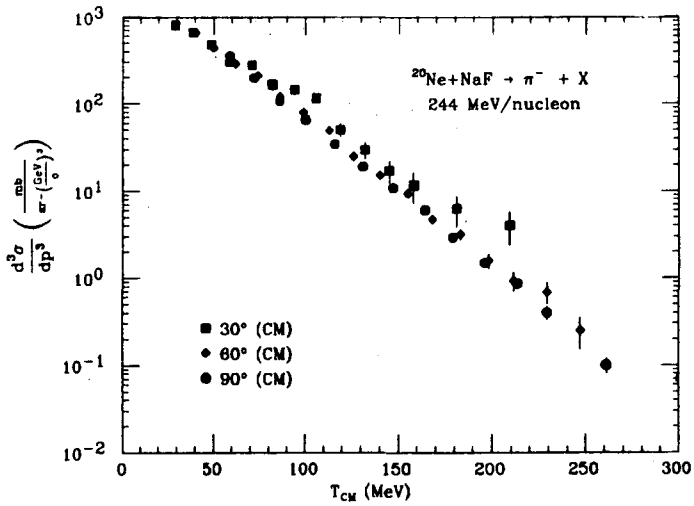

Figure 5.10. Variant cross section $d^3\sigma/dp^3$ as a function of pion center of mass kinetic energy for inclusive production of negative pions in Ne+NaF collisions at 244 MeV/nucleon incident beam energy and c.m. angles between 30° and 90°.

again there is a deviation from the simple pion energy dependence at the smallest angle. The structure in Fig. 5.9 at $\theta_{lab} = 21°$ and p_{lab} around 290 MeV/c is seen in Fig. 5.10 to be a strong deviation from isotropy at $\theta_{c.m.} = 30°$, $T^{\pi}_{c.m.}$=100 MeV. This deviation persists to a lesser extent at higher pion energies. There is also some indication of an enhancement of the $\theta_{c.m.} = 60°$ spectrum at intermediate pion energies.

The contour plots in p_T-rapidity space give a complementary view. (Figs. 5.11 and 5.12.) In each case the contours are close to isotropic, with the exception of the high rapidity, low-p_T region at the lower right of the plot, where the deviation from isotropy shows up variously as a bump, ridge or depression.

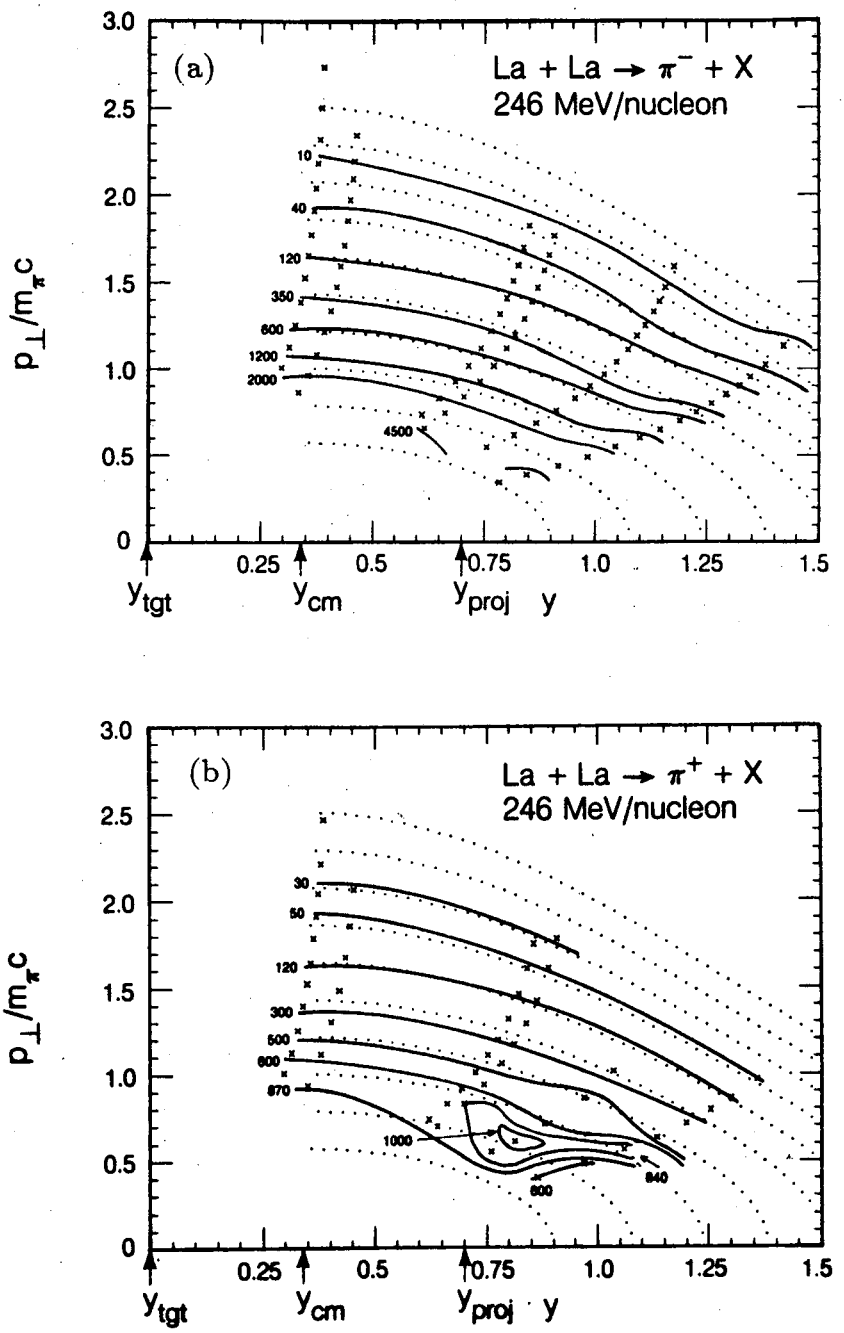

Figure 5.11. Invariant cross section $Ed^3\sigma/dp^3$ for inclusive production of charged pions at $30° \leq \theta_{c.m.} \leq 90°$ plotted in the plane of transverse momentum, p_T, and lab rapidity, y. The solid lines are contours of approximately constant invariant cross section (in $\mathrm{mb/(sr-GeV^2/c^3)}$. The crosses denote the experimental data points . The dotted lines indicate isotropy. The arrows denote the rapidities of the projectile and of the nucleus-nucleus (nucleon-nucleon) center of mass. a) π^-, 246 MeV/nucleon La+La. b) π^+, 246 MeV/nucleon La+La.

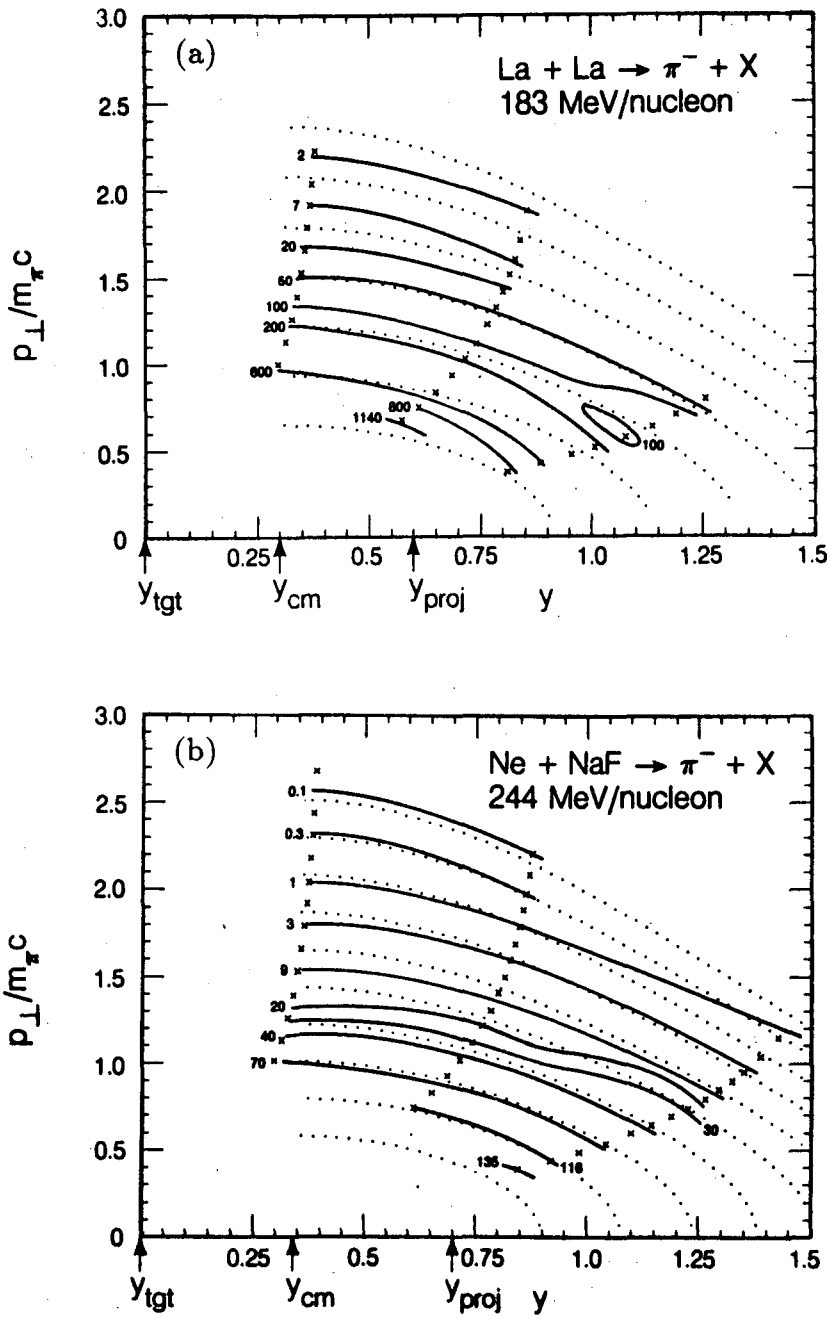

Figure 5.12. Invariant pion cross sections for π^- from (a) 183 MeV/nucleon La+La and (b) 244 MeV/nucleon Ne+NaF, plotted as in the previous figure

There is no apparent p_T dependence, as can also be seen when the inclusive cross section is plotted vs. p_T (Fig. 5.13).

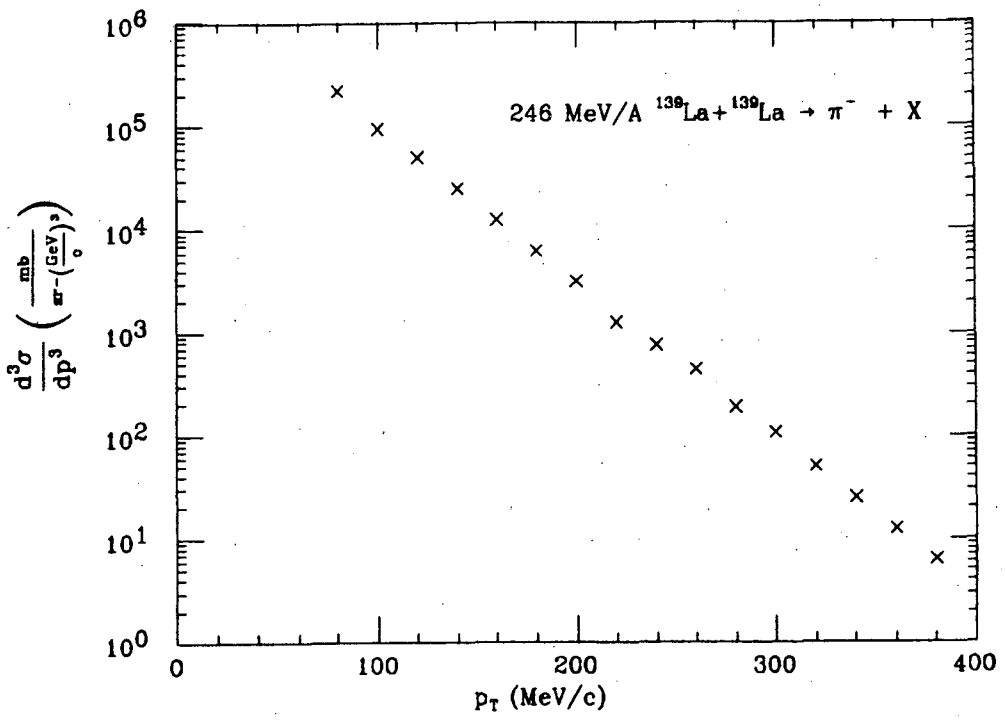

Figure 5.13. Inclusive cross section vs. transverse momentum for 246 MeV/nucleon $^{139}\mathrm{La} + ^{139}\mathrm{La} \rightarrow \pi^- + X$ at $\theta_{c.m.} = 30° - 90°$.

Slope parameters

Assuming that the c.m. cross sections are an exponential function of pion energy, we can extract slope parameters, T_0, from fits to the data. If this function is identified with a Maxwell-Boltzmann distribution, then the slope parameter fit to the variant cross section, $d^3\sigma/dp^3$, corresponds to the temperature of the pion source. Table 5.1 contains values of T_0 from weighted least squares fits to both the variant and invariant cross sections, where the latter are included for easier comparison with other experimental results. The fits for π^- are to all data points. The slopes for π^+ are obtained from fits to the tails of the distributions. Where the statistical uncertainties are too large to give a meaningful result,

T_{beam} (MeV/N)	angle		T_0(var.) (MeV)	T_0(inv.) (MeV)
246	90°	π^-	26(1)	29(2)
La+La		π^+	31(6)	35(8)
	60°	π^-	25(2)	28(2)
		π^+	33(13)	38(17)
	45°	π^-	25(2)	28(2)
		π^+	—	—
	30°	π^-	27(2)	31(3)
		π^+	—	—
183	90°	π^-	21(2)	23(2)
		π^+	—	—
	60°	π^-	23(2)	26(2)
		π^+	—	—
	30°	π^-	31(5)	36(7)
138	90°	π^-	14(5)	15(6)
		π^+	—	—
	60°	π^-	24(9)	26(11)
244	90°	π^-	26(1)	28(1)
Ne+NaF	60°	π^-	27(1)	30(2)
	30°	π^-	33(5)	38(7)

Table 5.1. Slope parameters for exponential fits to variant and invariant cross sections. (Experimental uncertainties are in parentheses.)

values for T_0 are not given. Also, the slope for π^- from 246 MeV/nucleon La+La at $\theta_{c.m.} = 90°$ differs by 1 MeV from the value quoted in Ref. 141, due to the fact that in the earlier work only the 67° lab cross sections were used to obtain the c.m. cross section at 90° .

5.1.2 Dependence on beam energy and system mass

Figs. 5.14 and 5.15 show the π^- spectra at $\theta_{c.m.} = 90°$ for a range of beam energies below and above the pion threshold of 290 MeV/nucleon. The slope and yield fall smoothly as the beam energy is lowered over an order of magnitude, down to more than 100 MeV/nucleon below the free nucleon threshold. We note that the data from the present study for Ne+NaF at 244 MeV/nucleon

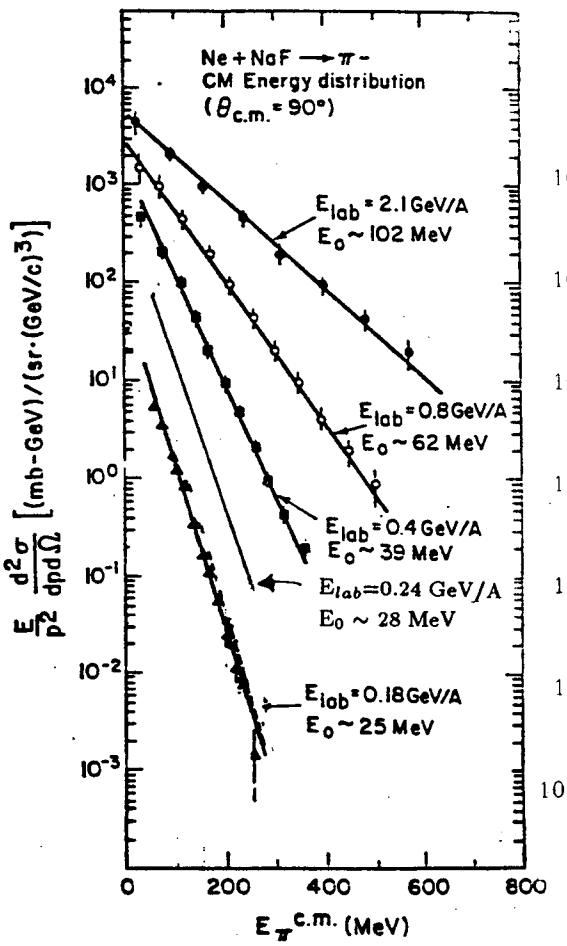

Figure 5.14. Inclusive π^- energy spectra at $\theta_{c.m.} = 90°$ for the reaction Ne + NaF $\rightarrow \pi^- + X$ for T_{beam} = 183–2100 MeV/nucleon. (Data from Refs. 12 (183 MeV/nucleon) and 57 (400–2100 MeV/nucleon), and the present study (244 MeV/nucleon).)

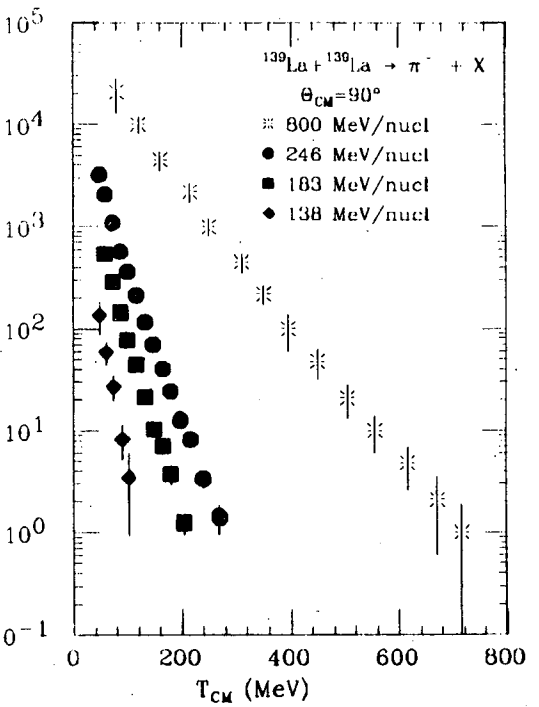

Figure 5.15. Inclusive π^- energy spectra at $\theta_{c.m.} = 90°$ for the reaction La+La $\rightarrow \pi^- + X$ for T_{beam} = 138-800 MeV/nucleon. (Data from Ref. 62 (800 MeV/nucleon) and the present study.)

are consistent in slope and yield with data taken on the same spectrometer at higher[57] and lower[12] beam energies.

Slope Parameter

The exponential dependence of the cross section on pion energy for a wide range of beam energies and target and projectile masses (Figs. 2.4, 2.11 and 5.14 and 5.15) leads naturally to parameterization of the data by the negative inverse slope, T_0. We concentrate here on the data at mid-rapidity, $\theta_{c.m.} = 90°$, which has the advantage of being the least subject to contamination by non–pions, and where the high transverse momentum offers the prospect of interesting physics. There is also a considerable amount of mid-rapidity data to which our results may be compared.

As illustrated by Fig. 5.16,

- The rate of decrease of the slope parameter accelerates as the beam energy is decreased to the pion threshold and below. There is some indication of a leveling off of T_0 below 100 MeV/nucleon. (We note that for π^0 production from ^{12}C, ^{14}N, and ^{16}O projectiles below 100 MeV/nucleon, the slope parameter—calculated in a different way—appears to level off at a beam energy of between 25 and 60 MeV/nucleon[92,102].)

- The slope parameter is not very sensitive to the total system mass, for A_{proj} ($= A_{tgt}$) between 12 and 139, and T_{beam} = 183–800 MeV/nucleon.

- The slopes of the spectra of pions from proton-induced reactions (shown in the inset to Fig. 5.16), are surprisingly close to those from heavy ion collisions; in fact, for $T_{beam} > 400$ MeV, they appear to converge. The sharp deviation at 730 MeV[30] from the trend in T_0 established by the other data is not understood. The fit is to the tail of the π^+ distribution;

when the lower energy pions are included, the slope parameter increases to about 47 MeV (Fig. 2.6). The slopes of the spectra from pA reactions have also been found to be insensitive to target mass and pion charge[30,52,94].

$d\sigma/d\Omega$

The excitation functions of total or partial inclusive cross section vs. beam energy have a similar form for NN (Fig. 2.1), NA (Figs. 2.2, 2.3 and 2.5) and AA (Fig. 2.10) collisions, falling smoothly but sharply with decreasing T_{beam}, near threshold. The same behavior has also been observed below 100 MeV/nucleon[102].

The limited range of this study in pion angle and energy introduces an unknown uncertainty into the calculation of the total inclusive cross section. This is a problem particularly for positive pions, for which the measured behavior of the spectra makes extrapolation to lower pion energies difficult. For this reason, we have chosen to study the mass and beam energy dependence by looking at the differential inclusive cross section, $d\sigma/d\Omega$, in the center of mass.

The value of $d\sigma/d\Omega$ was computed by integrating the double differential cross section:

$$\frac{d^2\sigma}{dpd\Omega} = p^2 \cdot \sigma_{var},$$

with σ_{var} replaced by the fitted function $Ae^{-\frac{T}{T_0}}$:

$$\begin{aligned} d\sigma/d\Omega &= \int_{p_1}^{p_2} \frac{d^2\sigma}{dpd\Omega} dp \\ &= \int_{p_1}^{p_2} p^2 \cdot Ae^{-\frac{T}{T_0}} dp \\ &= \int_{T_1}^{T_2} p(T) \cdot E \cdot Ae^{-\frac{T}{T_0}} dT \ , \end{aligned}$$

where $T \equiv T^{\pi}_{c.m.}$, and we have made use of the relations between relativistic energy and momentum: $pdp = EdE$ and $dE = d(T+m) = dT$. We have again assumed that the pion energy spectra are exponential, and that this dependence can be

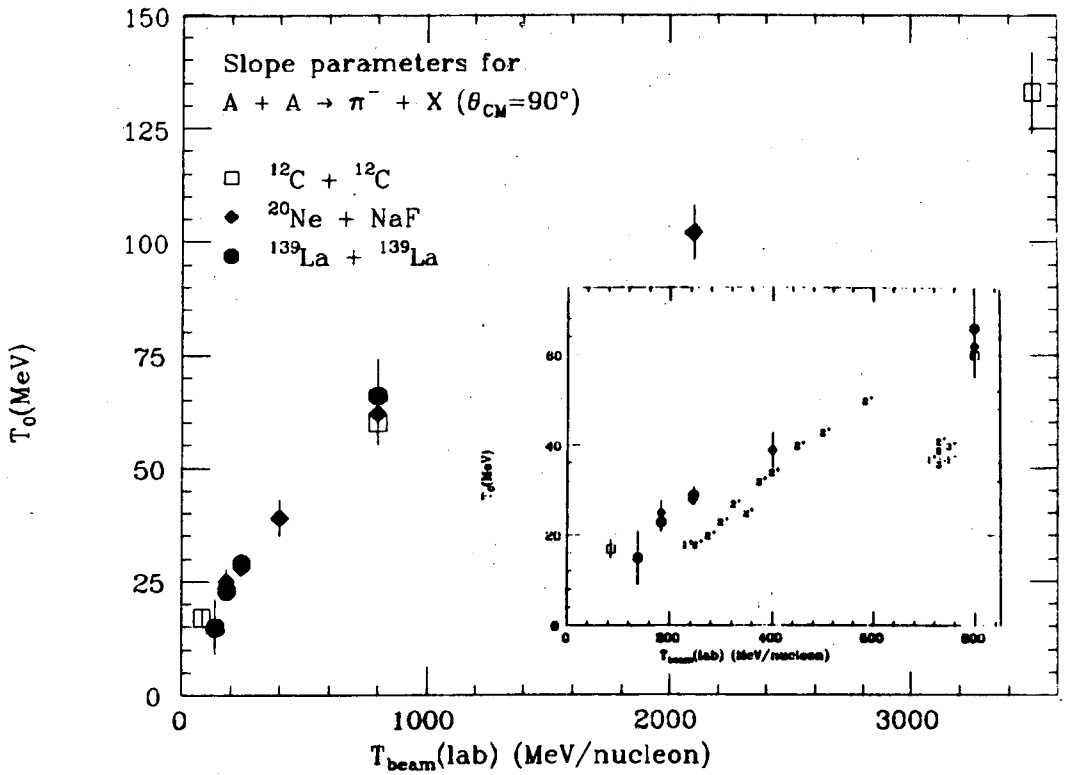

Figure 5.16. Slope parameter, T_0, for π^- spectra at $\theta_{c.m.} = 90°$, plotted as a function of beam energy for a variety of targets and projectiles, at beam energies between 85 and 3500 MeV/nucleon in the laboratory. T_0 is the negative inverse slope extracted from fitting the invariant cross section by a function of the form Ae^{-T/T_0}. The inset shows the slopes for AA collisions at $T_{beam} < 800$ MeV/nucleon, along with the slopes for pA collisions between 200 and 730 MeV. The symbols denote the target, as follows: '1'$\equiv p+^{12}$ C, '2'$\equiv p+^{64}$ Cu, '3'$\equiv p+^{208}$ Pb. The superscripts denote the pion charge. Error bars on the pA points have been deleted for clarity, but errors are in all cases less than 10%. AA data are from Refs. 12,57,62,94,142 and the present study. pA data are from Ref. 52 (240-500 MeV/nucleon), Ref. 32 (585 MeV/nucleon) and Ref. 30 (730 MeV/nucleon). (Note that the pA data were taken at $\theta_{lab} = 90°$, but for the case where the target is much heavier than the projectile, the lab frame and the *nucleus-nucleus* c.m. frame are almost the same.)

used to extrapolate both to higher and lower pion energies. The constants T_0 and A are the negative inverse slope and intercept extracted from a least squares fit of a straight line to the data, plotted as $\ln(\sigma_{var})$ vs. $T^{\pi}_{c.m.}$.[†] The integral was evaluated numerically, with limits of integration $T_1 = 1$ MeV and $T_2 = 300$ MeV, and a step size of 1 MeV.[‡] The results are listed in Table 5.2.

System	T_{beam} (MeV/nucleon)	$d\sigma/d\Omega$ (mb/sr)
La+La	138	3.2(2.0)
	183	10.5(1.5)
	246	29.5(3.0)
Ne+NaF	244	1.3(0.1)

Table 5.2. $d\sigma/d\Omega$ (mb/sr) for π^- at $\theta_{c.m.} = 90°$

In Fig. 5.17 we have plotted a scaled $d\sigma/d\Omega$ at $\theta_{c.m.} = 90°$ for three systems of varying mass, over a range of beam energies above and below threshold. The scaling factor, $A_{tgt}^{\frac{2}{3}} \cdot A_{proj}^{\frac{2}{3}}$, was chosen to conform to the mass dependence observed for subthreshold pion production above 60 MeV/nucleon[92], which corresponds in the AA case to pure surface production[95]. When scaled in this way, the NA and AA data are consistent above 400 MeV/nucleon, with an increasing discrepancy as the beam energy is lowered. The convergence of the scaled cross sections at high energy supports the idea that the pion production mechanism in AA collisions at several hundred MeV/nucleon above threshold is similar to that in NA collisions.

One reason why we might *not* expect such good agreement is that isospin has

[†]The fits in Ref. 57 are to σ_{inv}, which is not strictly correct (see footnote, p. 26), but in this case the exponential dependence holds and the result is the same either way.

[‡]These limits are somewhat arbitrary. The upper limit is chosen according to the limits of the data, but extending it to higher momenta has a negligible effect on the result, since the cross section falls by several orders of magnitude over this energy range. The lower limit was chosen, once again, for comparison with the results of Nagamiya *et al.*[57]; a calculation with this lower limit reproduced the cross sections quoted in Ref. 57 for $T_{beam} = 400$, 800 and 2100 MeV/nucleon Ne+NaF. (Note that for the exponential dependence to hold at all momenta, $d^2\sigma/dpd\Omega = (1/p^2) \cdot \sigma_{var}$ must go to zero at $T^{\pi}_{c.m.} = 0$.)

not been taken into account. For example, another possible scaling is a geometric one[57,95]:

$$\begin{aligned}\sigma(\pi) &\propto A_{tgt}\cdot\sigma_{geom}(proj)+A_{proj}\cdot\sigma_{geom}(tgt)\\ &\propto A_{tgt}\cdot A_{proj}^{\frac{2}{3}}+A_{proj}\cdot A_{tgt}^{\frac{2}{3}}.\end{aligned}$$

This corresponds to scaling by the mean number of participants[95], and is what might be expected from pion production in a first collision model[89]. However, according to the isobar model, over 80% of the positive pions are created in pp collisions. Similarly 80% of the negative pions come from collisions between neutrons. This can be incorporated in the geometric scaling for π^- by replacing $A_{tgt(proj)}$ by the neutron number, $N_{tgt(proj)}$, and by weighting σ_{geom} by the percentage of neutrons in the target, as follows:[†]

$$\begin{aligned}\sigma(\pi^-) &\propto [(N_T)\cdot(\frac{N_P}{A_P})\cdot(A_P^{\frac{2}{3}})+(N_P)\cdot(\frac{N_T}{A_T})\cdot(A_T^{\frac{2}{3}})]\\ &\propto [N_T\cdot N_P\cdot A_P^{-\frac{1}{3}}+N_P\cdot N_T\cdot A_T^{-\frac{1}{3}}]\end{aligned}$$

Similarly, for π^+ :

$$\sigma(\pi^+) \propto [Z_T\cdot Z_P\cdot A_P^{-\frac{1}{3}}+Z_P\cdot Z_T\cdot A_T^{-\frac{1}{3}}]$$

For symmetric systems, these become $N^2\cdot A^{-\frac{1}{3}}$ and $Z^2\cdot A^{-\frac{1}{3}}$, respectively. This weighting overestimates the π^- yield from Ne+NaF relative to La+La which may indicate that pion absorption is significant in the heavier system. A better empirical fit is obtained if only one nucleus is weighted by neutron number, to give $N^2\cdot A^{-\frac{2}{3}}$.

The exact nature of the scaling is not as important here as is its dependence upon the beam energy. The sharp fall off of the p+Cu data below 400 MeV can be interpreted qualitatively in a nucleon-nucleon framework, since in this region

[†] $T\equiv tgt;\ P\equiv proj$

the internal nuclear momentum distributions become important, and the elementary projectile makes no such contribution. The disparity in the nucleus-nucleus results, however, may reflect the action of pion production processes which are different from those above threshold and which are sensitive to the size of the colliding nuclei. This is illustrated by Fig. 5.18, which shows the steep increase in the yield ratio for La+La vs. Ne+NaF collisions as the beam energy is decreased.† The ratio at 800 MeV/nucleon is consistent with a simple surface dependence, with or without weighting by neutron number. At 246 MeV/nucleon, it is somewhat higher, but not conclusively so. At 183 MeV/nucleon, the ratio is three times higher than that expected from a surface dependence, and a factor of two above a neutron number-weighted geometrical scaling. It is also in excess of what the ratio would be for a "volume" (A^2) dependence (48), but is consistent with a volume dependence weighted by neutron number (N^2).

Angular dependence of the mass scaling. In the preceding discussion we have treated the data only at $\theta_{c.m.} = 90°$, which raises the question of whether the mass scaling is somehow associated with high p_T. However, we found the same effect at $\theta_{c.m.} = 60°$ as at $\theta_{c.m.} = 90°$. The situation at $\theta_{c.m.} = 30°$ is not clear, due to the unusual structure in the spectrum from La+La collisions at 183 MeV/nucleon (Fig. 5.6). This is not surprising, since we already know that the inclusive p_T plot (Fig. 5.13) is featureless, and since most of the data at $\theta_{c.m.} = 90°$ are actually at relatively low p_T.

†Although these data are compiled from the results of several experiments, the relative normalization should be close to unity. All the experiments were done on essentially the same spectrometer, calibrated in the same way[143], and the results have been found to be internally consistent. (See, for example, Refs. 12, 57 and 127, and Sec. 4.6.) The major remaining uncertainty is in the beam normalization for different projectile masses and energies, but this is estimated to be 20–30% in each measurement, not enough to account for the observed effect, even in the worst case.

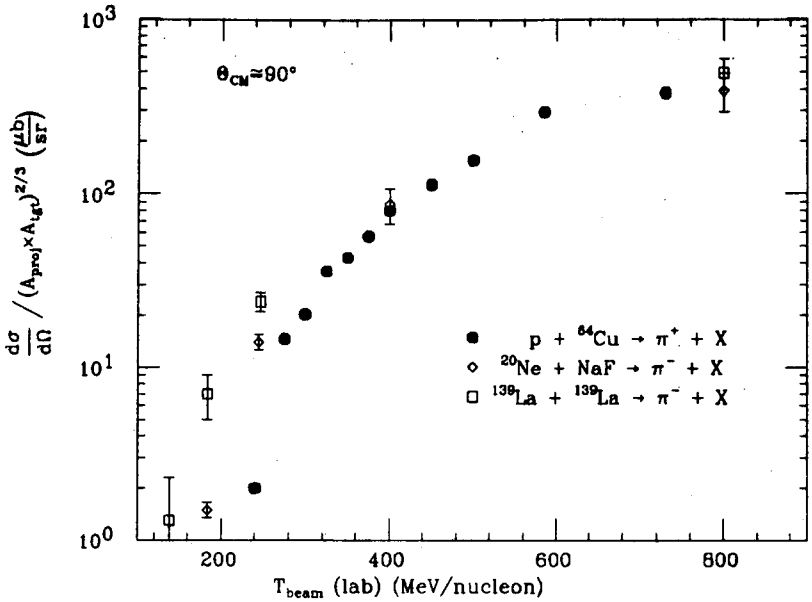

Figure 5.17. Differential cross section, $d\sigma/d\Omega$ (μb/sr) vs. beam energy for $p+{}^{64}\mathrm{Cu} \rightarrow \pi^+ + X$, ${}^{20}\mathrm{Ne}+\mathrm{NaF} \rightarrow \pi^- + X$ and ${}^{139}\mathrm{La}+{}^{139}\mathrm{La} \rightarrow \pi^- + X$ at $\theta_{c.m.} = 90°$. The cross section is scaled by $A_{tgt}^{\frac{2}{3}} \cdot A_{proj}^{\frac{2}{3}}$, and is integrated starting at $T_\pi = 30$ MeV, the minimum value for the proton data. Data is from Refs. 12,30,32,51,57 and 62 and the present work.

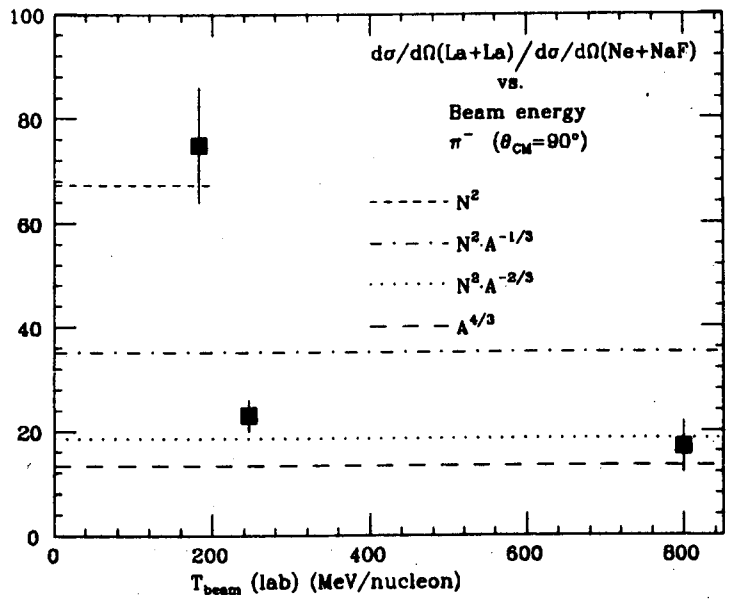

Figure 5.18. Ratio of $d\sigma/d\Omega$ for La+La vs. Ne+NaF as a function of beam energy for π^- at $\theta_{c.m.} = 90°$. The horizontal lines represent the ratios expected from different scalings as a function of target and projectile mass, A, and neutron number, N. Data for Ne+NaF at 183 MeV/nucleon is from Ref. 12. Data for La+La at 800 MeV/nucleon is from Ref. 62. Other data is from the present work. Note that the abscissa is beam energy/nucleon in the center of mass. This is done to give a more reasonable scale, and it also shows the energy available in the center of mass for pion creation.

5.1.3 Correlations with associated multiplicity

The complete multiplicity distributions for charged particles associated with pion production are plotted in Appendix B.[†]

Two significant features in these distributions are the tendency to peak at higher multiplicities and the trend towards a flatter distribution at smaller pion emission angles. This is best seen in the data for π^- at 246 MeV/nucleon (Fig. 5.19).

Fig. 5.20 contrasts associated multiplicities for protons and pions detected at small and large c.m. angles.[‡] At 90°, emission of both particles is dominated by collisions with relatively high associated multiplicities. At more forward angles, the pion distribution is only slightly less strongly peaked, while the proton-associated multiplicity distribution is no longer peaked at all. The multiple hit problem which influences the pion multiplicity distributions applies to protons, also, truncating the distributions at high multiplicities. However, the behavior of the distributions at low and intermediate multiplicities, which is what important here, is not changed significantly.

Earlier work at the Bevalac streamer chamber[§] used a downstream trigger scintillator to correlate the number of participants with charged particle multiplicity. The associated multiplicity distribution for forward angle protons is similar to the distribution produced by the streamer chamber "inelastic" trigger, which accepted all interactions; the pion distribution is close to that produced by the "central" trigger, which accepted only those events with very little charge remaining at the beam velocity. They also resemble the distributions obtained by Hallman *et al.*[67] in a π^0 measurement with a central trigger defined by a

[†]Note that, due to multiple hits in the multiplicity array, these distributions are truncated at high multiplicities. (See Sec. 3.2.2.)

[‡]The proton data was taken at the same time as the pion data which is the subject of this dissertation, and will be published elsewhere.

[§]See, for example, Ref. 144, Figure 14.

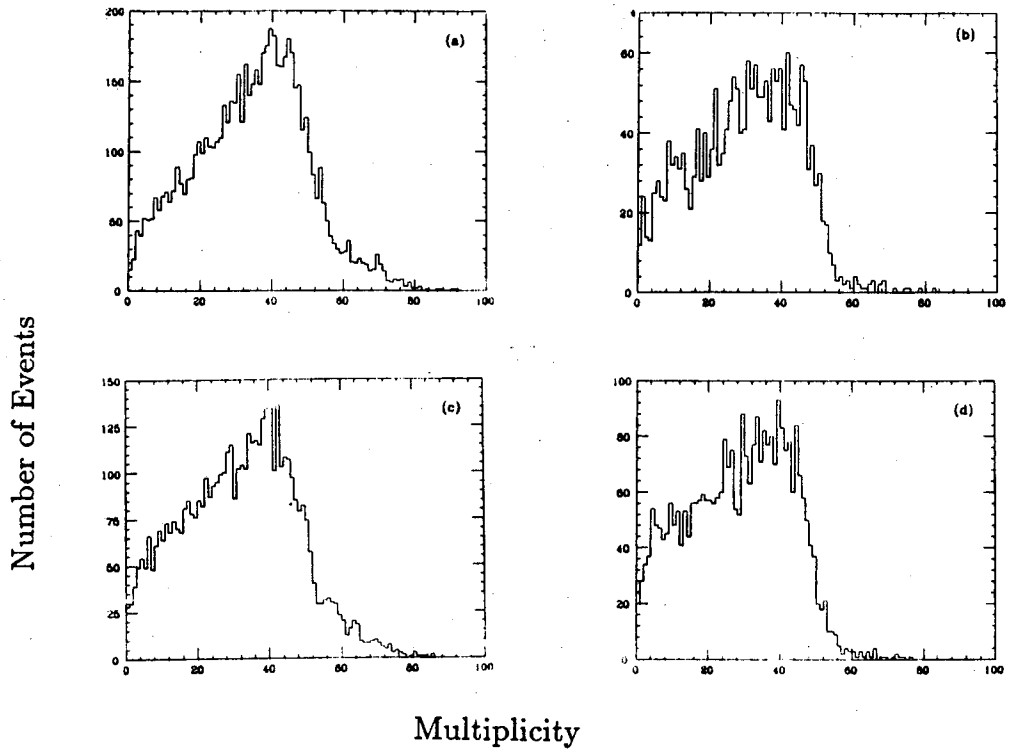

Figure 5.19. Associated multiplicities for charged particles from the reaction 246 MeV/nucleon ^{139}La +^{139} La $\rightarrow \pi^- + X$ at $\theta_{c.m.}$ = a) 30°, b) 45°, c) 60°, d) 90°.

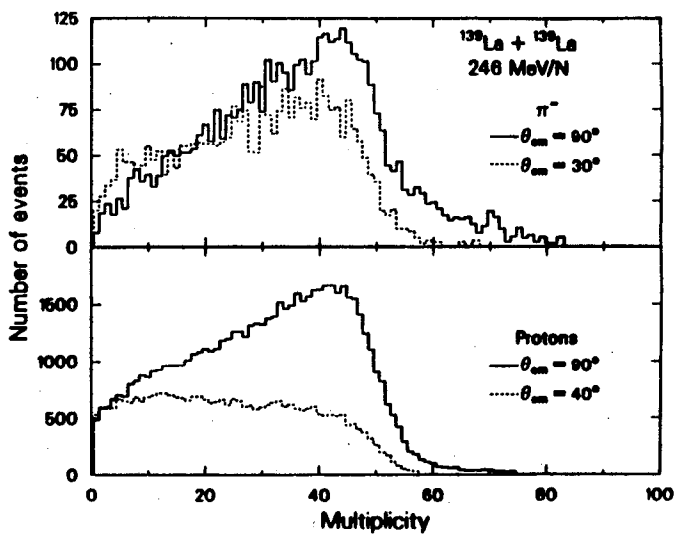

Figure 5.20. Associated multiplicity distributions for protons ($\theta_{c.m.}$=40° and 90°) and π^- ($\theta_{c.m.}$=30° and 90°) from La+La collisions at 246 MeV/nucleon.

minimum associated multiplicity.

The shape of the multiplicity distributions is independent of beam energy, but the position of the peak shifts to the left as the beam energy is decreased. This is reflected in the value of the mean multiplicity, as tabulated in Table 5.3. The distributions are independent of pion charge, with the exception of the mean multiplicities at 246 MeV/nucleon, which tend to be slightly greater for π^+ than for π^- . Note that the multiplicity distributions at lower energies have much lower statistics, but are consistent with the data at 246 MeV/nucleon (Fig. 5.21).

T_{beam} (MeV)	angle		$\langle M \rangle$	$\sigma_{\langle M \rangle}$
246	90°	π^-	34.3(0.2)	15.5(0.1)
La+La		π^+	35.9(0.3)	15.9(0.2)
	60°	π^-	29.8(0.3)	14.3(0.2)
		π^+	34.5(0.3)	14.9(0.2)
	45°	π^-	31.9(0.2)	15.7(0.2)
		π^+	33.5(1.0)	14.4(0.7)
	30°	π^-	28.5(0.3)	14.2(0.2)
		π^+	32.7(0.5)	14.3(0.3)
183	90°	π^-	32.2(0.3)	14.6(0.2)
La+La		π^+	31.6(1.1)	13.7(0.8)
	60°	π^-	29.8(0.2)	13.5(0.2)
		π^+	30.2(0.8)	13.4(0.6)
	30°	π^-	25.4(1.1)	13.2(0.8)
138	90°	π^-	26.9(1.6)	13.9(1.1)
La+La		π^+	28.0(1.4)	11.6(1.0)
	60°	π^-	24.7(1.2)	11.8(0.8)
244	30°	π^-	9.5 (0.2)	7.0 (0.2)
Ne+NaF				

Table 5.3. Means and widths of associated multiplicity distributions for the reaction $^{139}\mathrm{La} + ^{139}\mathrm{La} \rightarrow \pi^{\pm} + X$

compares the multiplicity distributions from La+La and Ne+NaF collisions at $\theta_{c.m.} = 30°$.† The mean multiplicity scales with the nuclear charge, and each

†The $\theta_{c.m.} = 30°$ distribution for Ne + NaF $\rightarrow \pi^-$ + X was not affected by the saturation problems which distorted the other Ne+NaF multiplicity distributions (Sec. 3.2.2).

distribution is peaked at a value of slightly less than one half the total available charge. The difference in shapes is probably due to a smaller incidence of multiple hits for the Ne+NaF system, and for this reason, the associated multiplicity distribution measured for Ne+NaF is probably closer to the actual distribution than is the case for La+La. (Recall the discussion in Sec. 3.2.2.)

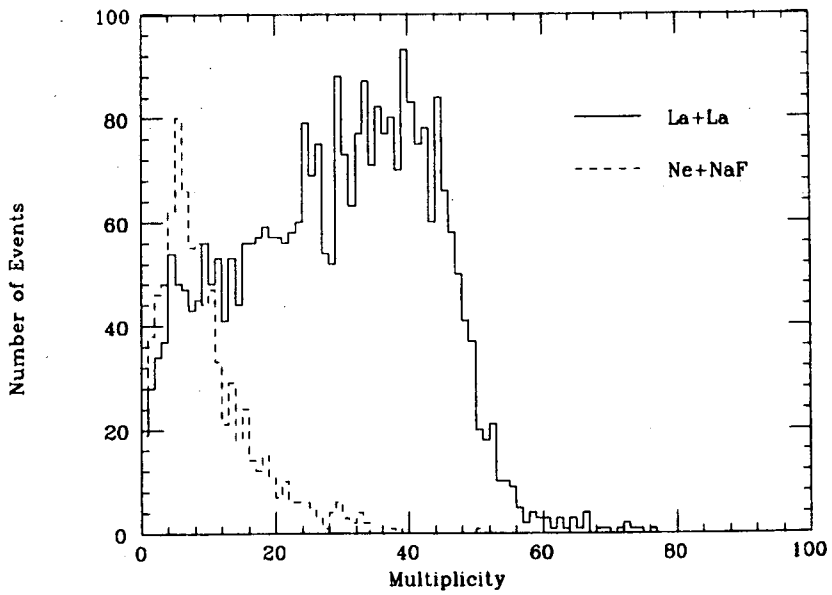

Figure 5.21. Associated multiplicities for charged particles from the reactions 246 MeV/nucleon ^{139}La $+^{139}$ La $\rightarrow \pi^- + X$ and 244 MeV/nucleon Ne + NaF $\rightarrow \pi^- + X$ at $\theta_{c.m.} = 30°$.

Slope parameter vs. multiplicity. Table 5.4 contains the slope parameters extracted from some of the charged pion experimental cross sections after selection on low and high multiplicity. The slope parameters for high and low multiplicity–selected cross sections are in every case equal, within uncertainty. (Not all angles and beam energies had sufficient statistics to permit cutting on multiplicity.)

Multiplicity vs. pion energy. We can also look at the inverse correlation, by cutting the multiplicity distribution on pion energy. The results of some of these correlations are given in Fig. 5.22 and Table 5.5. At $\theta_{c.m.} = 30°$, there

T_{beam} (MeV)	angle	M-cut	T_0(var.) (MeV)
246	90°	< 20	24(2)
		> 40	27(2)
	60°	< 20	26(4)
		> 40	27(4)
	45°	< 20	24(3)
		> 40	26(3)
	30°	< 20	25(3)
		> 40	30(6)
183	90°	< 30	20(2)
		> 30	22(2)
	60°	< 30	22(2)
		> 30	25(2)
	30°	< 30	23(7)
		> 30	25(2)

Table 5.4. Slope parameters for exponential fits to variant cross sections, for π^- from La+La collisions, selected on associated multiplicity. (The experimental uncertainties are in parentheses.)

is a small but definite correlation between higher pion energy and increased multiplicity, with a similar but weaker dependence at $\theta_{c.m.} = 90°$.

Angular distribution vs. multiplicity. In discussing the general characteristics of the pion cross sections we noted that the exponential energy dependence and angular isotropy are not universally the case in these data. For example, for π^- from La+La collisions at 246 MeV/nucleon the isotropy is broken by an enhanced yield at $\theta_{c.m.} = 30°$ (Fig. 5.5). The high statistics for π^- at 246 MeV/nucleon make this a good subject for multiplicity studies.

Fig. 5.23, which shows the π^- spectra after selection on associated multiplicity, M, demonstrates that the increased yield at $\theta_{c.m.} = 30°$ is strongly correlated with M. This increase is evident in the cross section for pions selected on $M < 20$, whereas for $M > 40$ the cross section is essentially isotropic. This result indicates that the bulk of the yield (at least for $\theta_{c.m.} = 30° - 90°$) is isotropic, with an additional component, associated with low multiplicity, probably peripheral

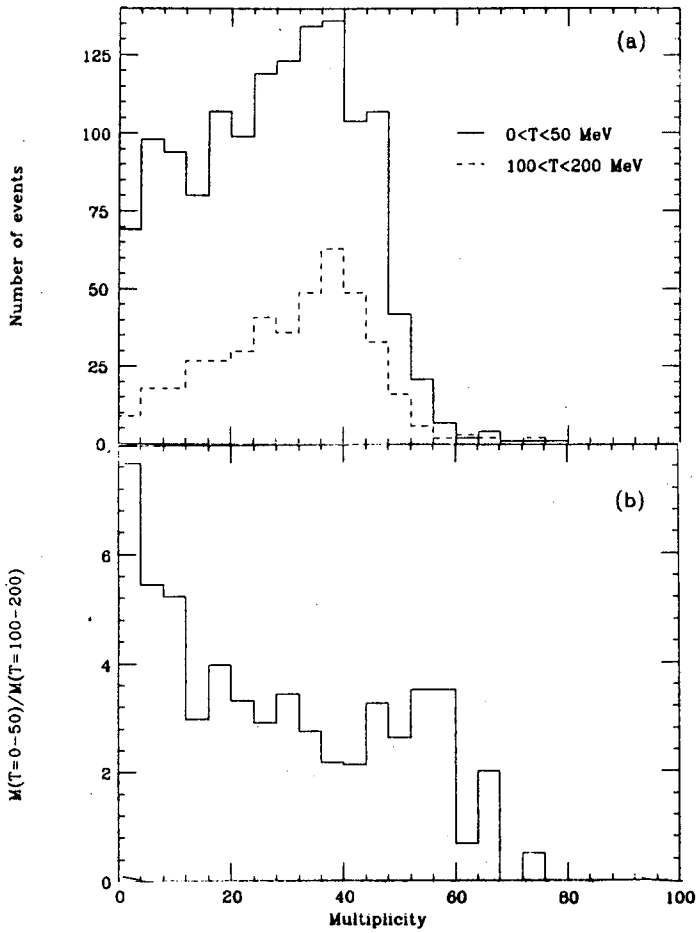

Figure 5.22. a) Associated multiplicity for 246 MeV/nucleonLa + La $\rightarrow \pi^- + X$ at $\theta_{c.m.} = 30°$, cut on pion kinetic energy. b) The ratio of the two distributions in (a).

angle	$T^{\pi}_{c.m.}$ – cut (MeV)	⟨M⟩	$\sigma_{(M)}$
30°	≤ 50	27.4(0.4)	14.5(0.3)
	$100 - 200$	30.9(0.7)	13.5(0.5)
90°	≤ 80	33.6(0.3)	15.8(0.2)
	$100 - 200$	35.2(0.4)	14.9(0.3)

Table 5.5. Means and widths of associated multiplicity distributions for 246 MeV/nucleon ^{139}La +^{139} La $\rightarrow \pi^- + X$, cut on pion kinetic energy.

collisions. We also note that the two sets of cross sections in Fig. 5.23b seem

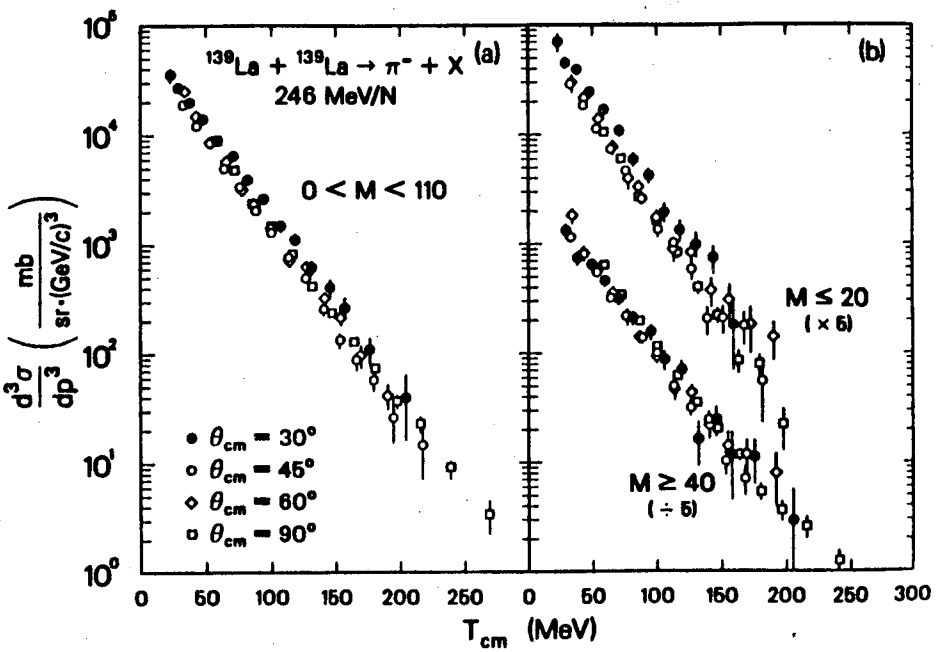

Figure 5.23. (a) Inclusive cross sections for negative pions produced at $30° \leq \theta_{c.m.} \leq 90°$ in 246 MeV/nucleon La+La collisions. (b) The same cross sections, selected on multiplicities $M \leq 20$ and $M \geq 40$. For clarity, the cross sections for $M \leq 20$ have been multiplied by 5 before plotting, and those for $M \geq 40$ have been divided by 5.

manifestly different in slope, although the spectra at each angle are not, within uncertainty (Table 5.4).

One of the more distinctive features in the pion cross sections is the break in the spectrum of negative pions from 183 MeV/nucleon La+La collisions at $\theta_{c.m.} = 30°$, which may be interpreted as a deviation from isotropy at low pion energy (p. 99). A simple test for multiplicity dependence was performed by cutting the raw pion spectrum (number of pions vs. T^{π}_{CM}) on multiplicity. Fig. 5.24 compares the multiplicity–cut raw pion distributions with the inclusive distribution. The break in the cross section is seen here as a dip in the number of counts between 60 and 75 MeV, which does not appear to be correlated with associated multiplicity.

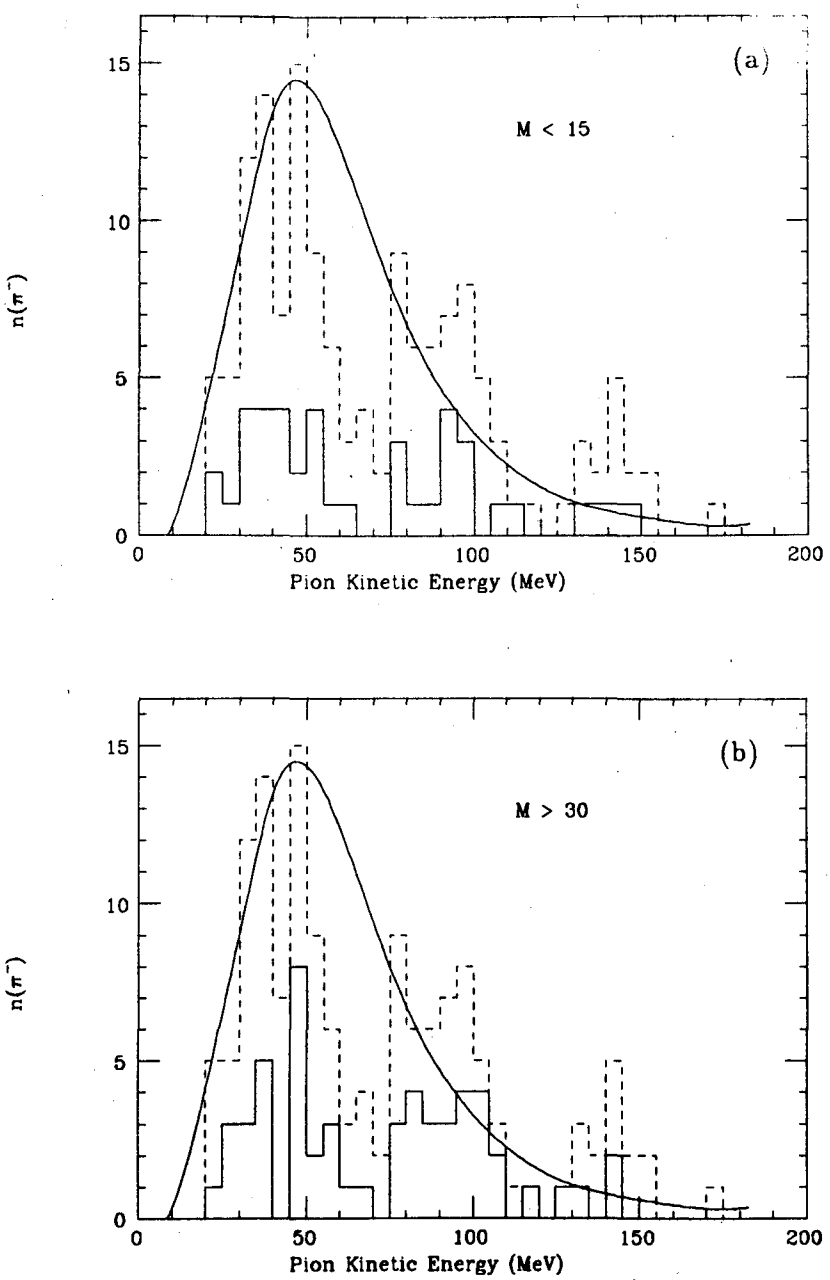

Figure 5.24. Number of π^- at $\theta_{c.m.} = 30°$ vs. kinetic energy for the reaction $^{139}\mathrm{La} + ^{139}\mathrm{La} \rightarrow \pi^- + X$ at 183 MeV/nucleon, selected on associated multiplicities (a) less than 15 and (b) greater than 30. The dashed histogram in each case is the distribution before the multiplicity cut. The solid curve is a fit to the distribution for the same system at $\theta_{c.m.} = 90°$, normalized to the 30° data.

5.2 Model comparisons

5.2.1 Thermal

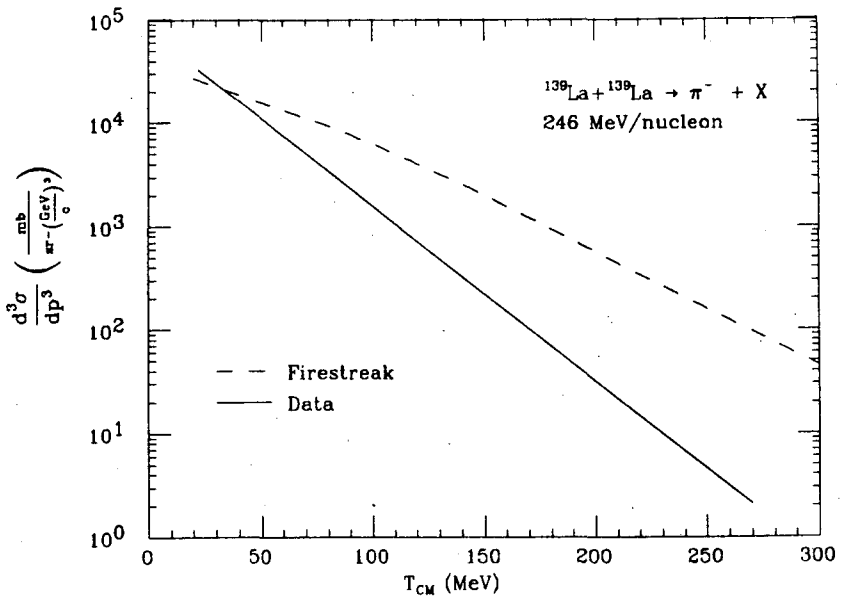

Figure 5.25. Comparison between experimental data for the reaction 246 MeV/nucleon ^{139}La+^{139}La $\rightarrow \pi^- + X$ and a calculation based upon the nuclear firestreak model. The curves are fits to spectra at c.m. angles of 30, 60 and 90 degrees. The slope parameter for the data is 26(1) MeV. The slope parameter for the model, extracted from a fit to the tail of the cross section, is 55 MeV.

Firestreak model. Fig. 5.25 compares a fit to the data for π^- to a firestreak model calculation[145]. The firestreak model[77,78] is an extension of the fireball thermal model (p. 26). The calculation has the same exponential energy dependence and isotropic angular dependence observed experimentally—the model has these properties by definition—but differs strongly from the data in both slope and yield.

In addition, a close look at the (dashed) firestreak curve reveals a shoulder at about 150 MeV. This feature appears when (delta) resonance production is included in the model calculation, and is independent of whether the width of the resonance is zero[76] or finite[78,145]. It is not observed in the inclusive data, nor

is it seen in the results of cascade calculations, which produce pions only through the delta. It is probably due to the absence of rescattering in the thermal model.†

If this is the case, then the effect of the delta might become evident when the experimental cross section is cut on low associated multiplicity, since pions produced in peripheral collisions may be less likely to rescatter.‡ Viewed in this way, the last few points of the $\theta_{c.m.} = 30°$ π^- cross section cut on low associated multiplicity (Fig. 5.23b) may be evidence for a resonance shoulder.

Blast wave. We conclude this section with a comparison between the data and the blast wave model of Siemens and Rasmussen[79]. In this model, the explosive expansion of the fireball pumps excitation energy into translational degrees of freedom, resulting in particle spectra which are cooler than purely thermal distributions and which are peaked at particle momenta corresponding to the expansion velocity.

Thermal motion is converted into a coherent blast wave through frequent multiple collisions; consequently, the authors suggest that the effect would most likely be observed in central collisions in a heavy system. To minimize background due to other effects, they further propose looking specifically at the $\theta_{c.m.} = 90°$ spectra. Our data fulfill these criteria, and we note that the slope parameter for pions is considerably less than what is predicted by the firestreak model. There is also a peak at low pion energy in the π^+ spectrum, but as there is no evidence of a corresponding peak in the π^- spectrum, as predicted by the model, the π^+ peak is probably due to Coulomb effects, as suggested also in Ref. 79. It is also pos-

†In Ref. 146, a peak in the cascade cross section at low energy is attributed mainly to the assignment of a fixed mass to the delta (Figure 3 in Ref. 146). When the resonance is given a finite width, the cascade cross section falls monotonically. However, when this cross section is divided according to the density of the nuclear matter with which the outgoing pions interact, the cross section for pions which interact with relatively dilute matter (the "non-direct" pions) exhibits a shoulder similar to the one in the firestreak result, while the cross section for "direct" pions, which interact first with compressed nuclear matter (and which therefore are likely to undergo more rescattering) does not.

‡A similar analysis could be made of the cascade results, as discussed in the section on the INC, below.

sible that Coulomb distortion of the pion spectra might partially mask the blast wave peak. This will be discussed in more detail in Sec. 5.3.

5.2.2 Statistical

Fig. 5.26 compares some of the results of the present experiment at 246 MeV/nucleon to the prediction of an early version[81] of the phase space model developed by Bohrmann, Shyam and Knoll. The excellent agreement supports the view that subthreshold pion production may be treated as a cooperative process.[†] (The specific nature of the process is not a feature of the model.) It may also be evidence for the importance of the major distinction between this statistical model and the firestreak model: their different assumptions regarding particle number.

The phase space model[81] treats equilibrated but *finite* systems, whereas the firestreak model implicitly assumes infinite particle number.[‡] But the probability for pion production is proportional to the available phase space, which increases with particle number. Thus the implicit, unphysical assumption about the number of interacting particles can lead to an overestimate of the probability for production of pions of a given energy. This is particularly true near the phase space limit, i.e. for high energy pions. In this connection, we note that the discrepancy between the predictions of the phase space and firestreak models (and between the firestreak model and the data) increases with pion energy, as would be expected if finite particle number effects are important.

It is interesting to note that for Ne+NaF collisions at 183 MeV/nucleon[12], similarly good agreement was obtained only after the model was extended[112] to allow the formation of light nuclear fragments in the final state, with the cluster

[†]The model does not reproduce the proton spectrum, as pointed out in Ref. 13.

[‡]As noted in Ref. 81, in statistical mechanical terms, the phase space model treats the interacting tubes of nucleons as microcanonical ensembles, whereas the firestreak treats them as grand canonical ensembles.

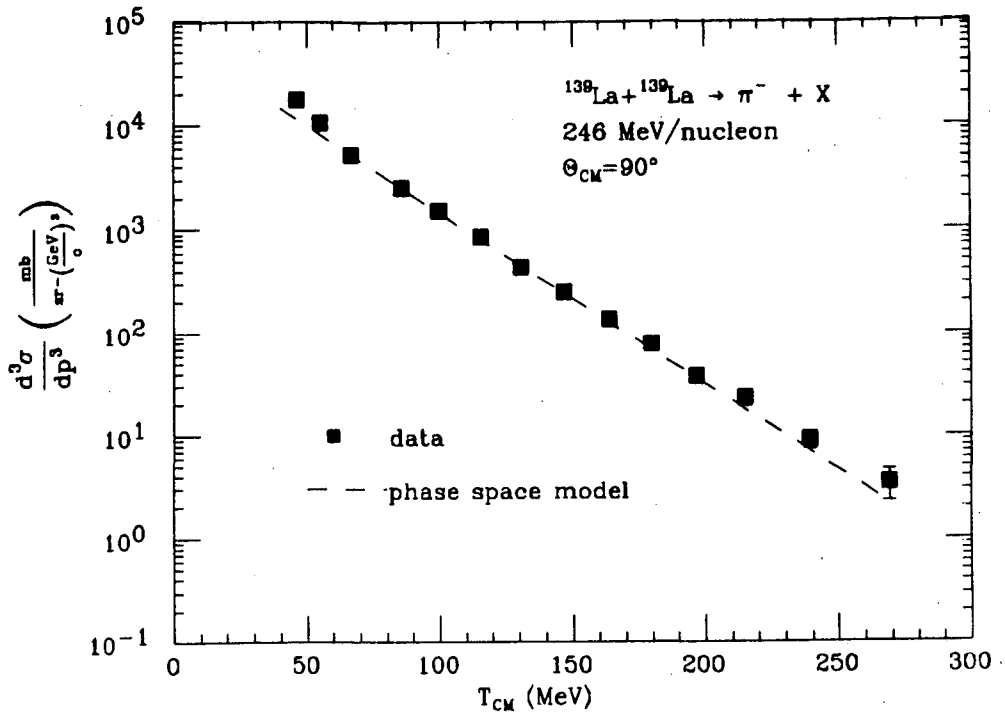

Figure 5.26. Comparison between the present experiment and the result of a statistical model. The data is for the reaction ^{139}La $+^{139}$La $\rightarrow \pi^- + X$ at 246 MeV/nucleon. The dashed line is the result of a calculation based on the phase space model of Bohrmann and Knoll[81].

formation cross sections taken from a cascade calculation rather than a simple rows-on-rows model. This may indicate a change in the nature of pion producing reactions as the beam energy is lowered from 246 to 183 MeV/nucleon, with the higher energy subthreshold collisions retaining the character of collisions above threshold, where the collision geometry is relatively simple and cluster formation is limited, especially in small impact parameter collisions. Unfortunately, the only phase space calculations available for the La+La system are at 246 MeV/nucleon.

5.2.3 Intranuclear cascade

In this section we compare the experimental data to results obtained from an intranuclear cascade (INC) developed by J. Cugnon and collaborators. This

cascade is described in detail in Refs. 113 and 146–149.† In Appendix F we discuss some of the features which are relevant to the present work. The INC simulates[148] a nucleus-nucleus interaction as a series of classical, on-shell, binary nucleon-nucleon collisions, with physics input limited to the internal nuclear momentum distribution and the experimental NN and πN cross sections. By providing a mechanism for extrapolating the elementary cross sections into the nucleus-nucleus regime, it provides an extended baseline against which to compare the nucleus-nucleus data in the search for collective effects.

As discussed in Ref. 148, an elementary condition for applicability of the cascade is that the incident nucleons be able to resolve the target nucleons. This requires that the de Broglie wavelength, λ, be small compared to the typical internucleon distance of about 2 fm. In this experiment, λ ranges from 0.27 fm (246 MeV/nucleon) to 0.37 fm (138 MeV/nucleon). This makes the classical collision approximation reasonable, at least for the first collision; however, the slowing down of nucleons in successive collisions, and the possibility of locally high densities within the interaction region, may make it much less reasonable. Thus the simple cascade may be appropriate for simulating only the early part of the collision, before quantum effects become significant; in order for an INC to be applied to later stages of the interaction, these effects would have to be incorporated, as they are in the phase space model, for example (p. 36).

Another consideration regarding subthreshold pion production in the cascade is that it can occur only with the aid of Fermi momentum, and is thus sensitive to the nature of the input momentum distribution. Consequently, the comparison between cascade results and data might also be taken as a test of the cascade assumptions regarding that distribution.

Cross sections from the cascade. The results of the cascade simulations

†Our results were obtained with a slightly modified version of the cascade provided by J.W. Harris[150].

are summarized in Table 5.6. The cross sections were calculated by normalizing

System	T_{beam} (MeV/nucl)	events	pions	π/event
La+La	138	56627	7365	0.13
	183	51591	20044	0.39
	246	57300	57595	1.01
	800	2648	31914	12.1
Ne+NaF	183	640144	18896	0.03
	244	117400	10796	0.09
	800	11000	18755	1.71

Table 5.6. Statistics for cascade simulations

the number of pions produced per event to the geometric cross section, as follows:

$$\sigma_\pi = \sigma_{geom} \cdot \left(\frac{n(\pi)}{n(events)} \right)$$

where σ_π is the total pion cross section and

$$\sigma_{geom} = \pi(1.12)^2(A_1^{\frac{1}{3}} + A_2^{\frac{1}{3}})^2$$

The differential cross section is obtained by normalizing to the angular and momentum acceptance of the spectrometer.

Table 5.7 compares slope parameters and differential cross sections for cascade results and experimental data at $\theta_{c.m.} = 90°$. The cascade reproduces the slope parameters, within uncertainty, while overestimating the yield by a factor which increases with beam energy, but does not depend strongly on system mass. Similar results are obtained at the smaller angles. The distribution of cascade pions is almost isotropic, but the yield increases slightly with decreasing c.m. angle (see Fig. 5.27), as opposed to the sharper enhancement at $\theta_{c.m.} = 30°$ which is observed in the data. This smooth increase could reflect the forward-backward peaking characteristic of isobar production through the delta resonance, somewhat smoothed out by multiple scattering.

System	T_{beam} (MeV/nucl)	T_0 (MeV)		$d\sigma/d\Omega$ (mb/sr)	
		cascade	expt.	cascade	expt.
La+La	138	20(1)	14(5)	17(3)	3.2(2.0)
	183	24(1)	21(2)	41(7)	10.5(1.5)
	246	26(1)	25(1)	80(10)	29.5(3.0)
	800	52(2)	56(–)	838(150)	368(73)
Ne+NaF	183	23(1)	24(–)	1.1(0.2)	0.1(–)
	244	25(1)	26(1)	3.4(0.7)	1.3(0.1)
	800	51(2)	54(–)	36(8)	24(6)

Table 5.7. Comparison between experimental data for negative pions and the results of a cascade calculation of $d\sigma/d\Omega$ and T_0 at $\theta_{c.m.} = 90°$. Experimental results are from the present study and from Refs. 12 (183 MeV/nucleon Ne+NaF), 57 (800 MeV/nucleon Ne+NaF) and 127 (800 MeV/nucleon La+La). The cascade yield has been divided by three to obtain the estimated π^- yield. (See Appendix F.)

We considered the possibility that the structure in some of the pion cross sections near $T^{\pi}_{c.m.} = 100MeV$ (Figs. 5.6, 5.7 and 5.10) is related to $\Delta(1232)$ decay, since the emitted pions would have a peak energy of about 128 MeV in the rest frame of the Δ. One would expect to see similar effects in the cross sections from the cascade, but there is no sign of them. (Compare Fig. 5.28 to Fig. 5.6.)

Mass dependence. The mass dependence of the pion yield from the cascade is illustrated in Fig. 5.29. There is a small increase in the ratio of yields at 183 MeV/nucleon, where a similar but much stronger effect is observed in the data (Fig. 5.18).

Associated multiplicities. Fig. 5.30 shows the associated multiplicity distributions for the cascade calculation and for the data at both small and large angles, where the cascade results were filtered through the acceptance of the multiplicity array. (Compare to Fig. 5.19.)

The shapes of the distributions are in excellent agreement, although the cascade distributions are peaked at higher associated multiplicities, probably due to

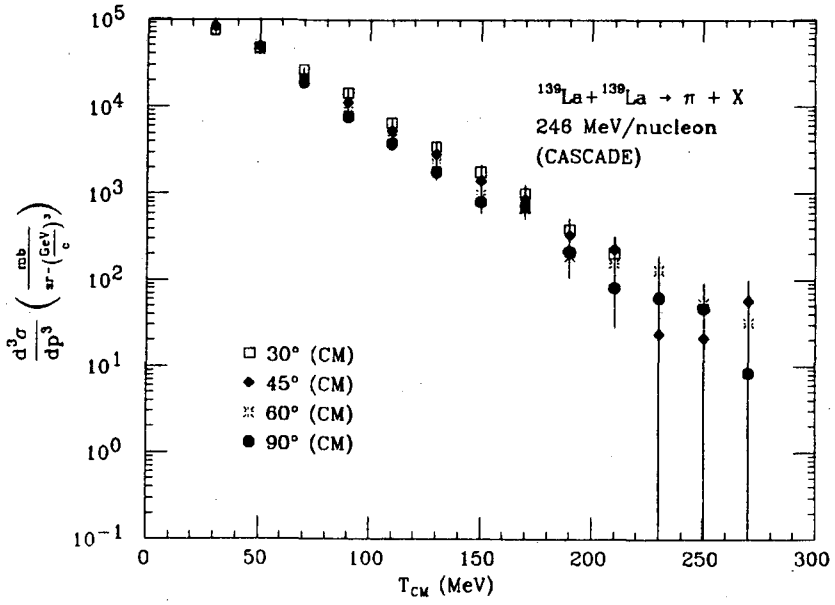

Figure 5.27. Pion cross sections from the Cugnon cascade, for the reaction 246 MeV/nucleon La + La → $\pi + X$

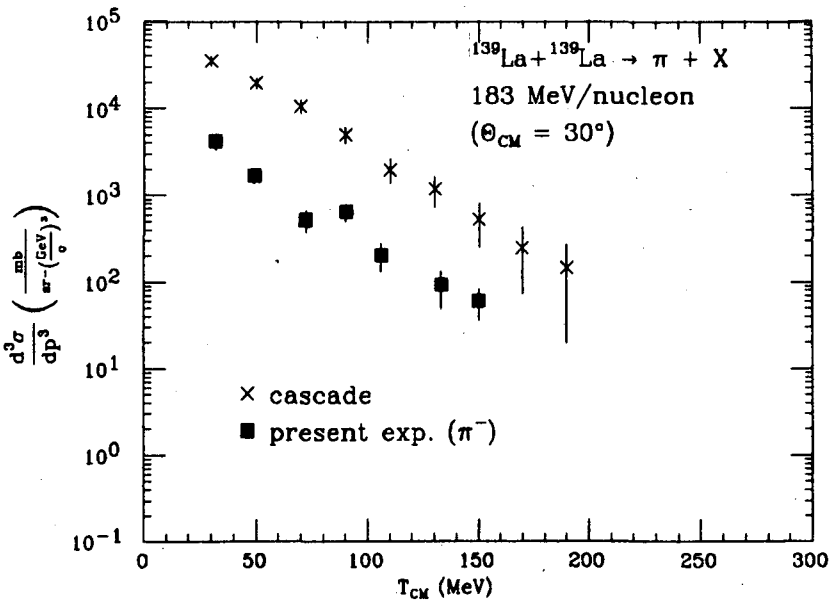

Figure 5.28. Comparison between the Cugnon cascade and the present experiment, for the reaction 183 MeV/nucleon La + La → $\pi + X$ at $\theta_{c.m.} = 30°$. Note that the data are for π^- , and also that the cascade yield has not been corrected for isospin.

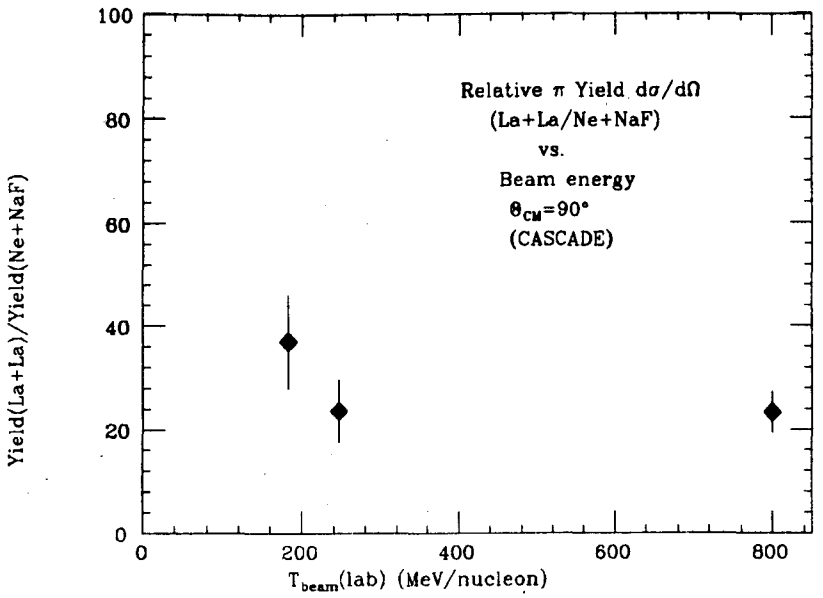

Figure 5.29. Ratio of pion yields, $d\sigma/d\Omega$ for cascade pions from La+La and Ne+NaF collisions.

the absence of clusters in the INC.† The cascade analysis code takes into account the number of nuclear charges by randomly assigning a charge to Z nucleons.

The shape of the multiplicity distributions associated with cascade pions is almost independent of the pion emission angle, although at very small angles, the cascade distributions have a slightly more peripheral shape (Fig. 5.31).

Slope parameter vs. multiplicity. The multiplicity cuts applied to the data (Table 5.4) were applied to the cascade with similar results: the slope parameters of the high multiplicity-cut spectra are 1-2 MeV higher than for the inclusive case, the low multiplicity-cut spectra are lower by the same amount.

Angular dependence vs. multiplicity. As previously noted, the cascade angular distribution is slightly forward peaked. In order to see if this effect is related to the increase in yield at $\theta_{c.m.} = 30°$ observed in the data, we took

†Recall that multiple hits are handled in such a way as to simulate the actual experimental conditions, i.e. the maximum number of hits per element allowed in the cascade is 1. (See the discussion in Sec. 3.2.2.)

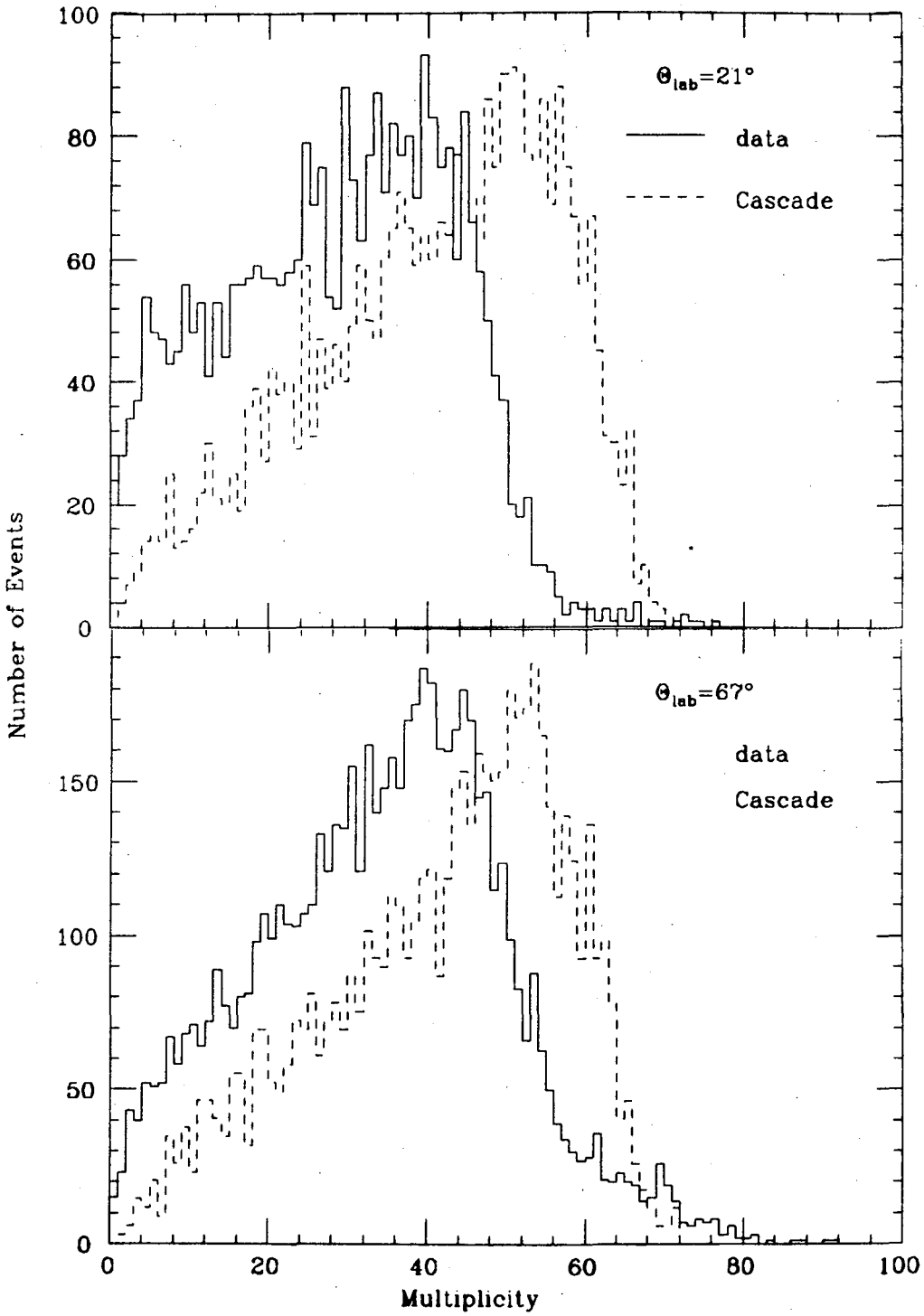

Figure 5.30. Comparison of associated multiplicity distributions between Cugnon cascade and experiment, for pion-producing La+La collisions at 246 MeV/nucleon. The distributions are normalized to have the same peak value.

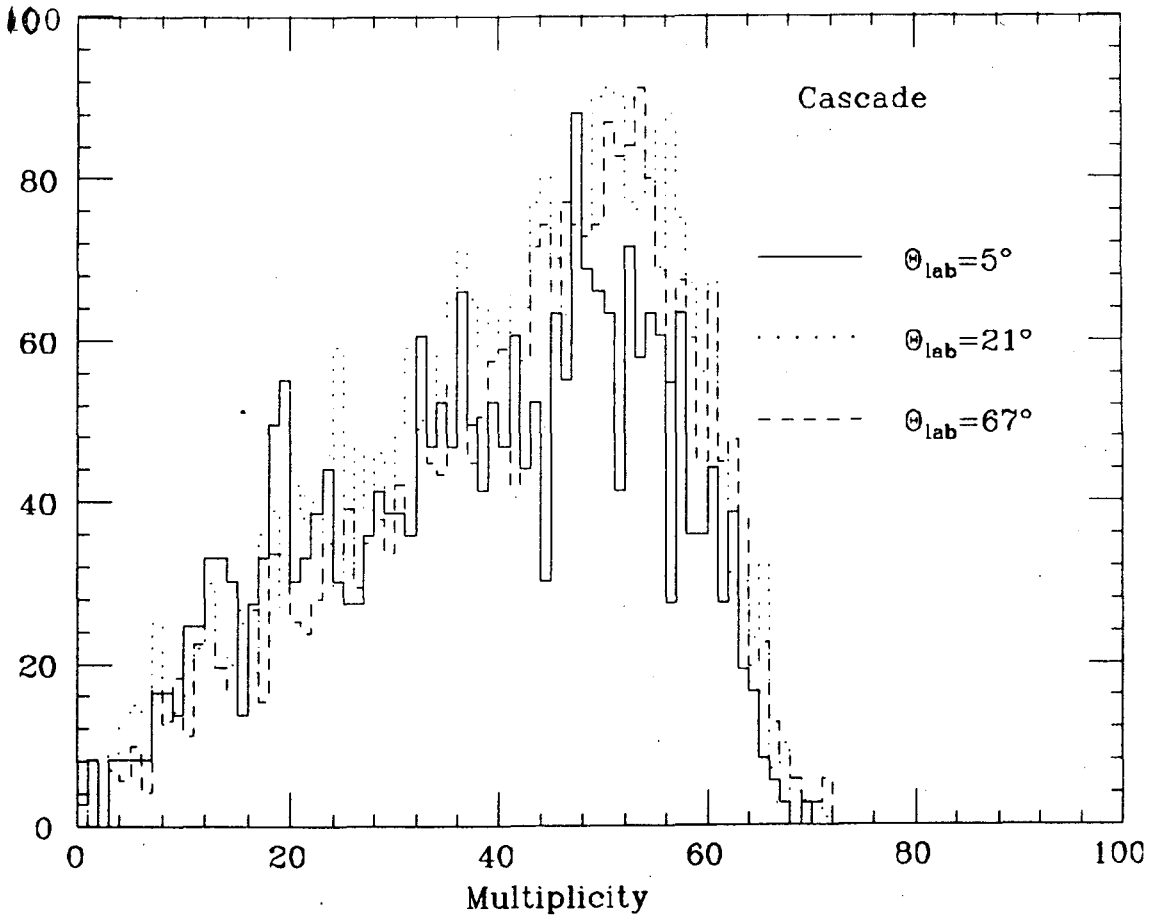

Figure 5.31. Associated multiplicity distributions from the Cugnon cascade for pions at θ_{lab} = 67°, 21° and 5°, from 246 MeV/nucleon La+La collisions. The distributions have been normalized to have the same peak value.

multiplicity cuts on $M < 20$ and $M > 40$. When the experimental data is cut in a similar way (p. 118), the yield at high multiplicity is seen to be isotropic. In the cascade, the yield for $M > 40$, is closer to isotropy than for for $M < 20$, but the cross section at $\theta_{c.m.} = 30°$ is still somewhat greater than that at larger angles. Also, for the low multiplicity cut, there is a suggestion of a shoulder at pion kinetic energy between 100-150 MeV, similar to the results of the thermal model (p. 123). These distributions are consistent with delta resonance production partially washed out by the effects of rescattering.

The influence of rescattering on the cascade results can be studied by considering the correlation between the number of participants and the number of collisions *per participant* for collisions where at least one pion is produced. This correlation is shown in Fig. 5.32. For pion production, the average number of

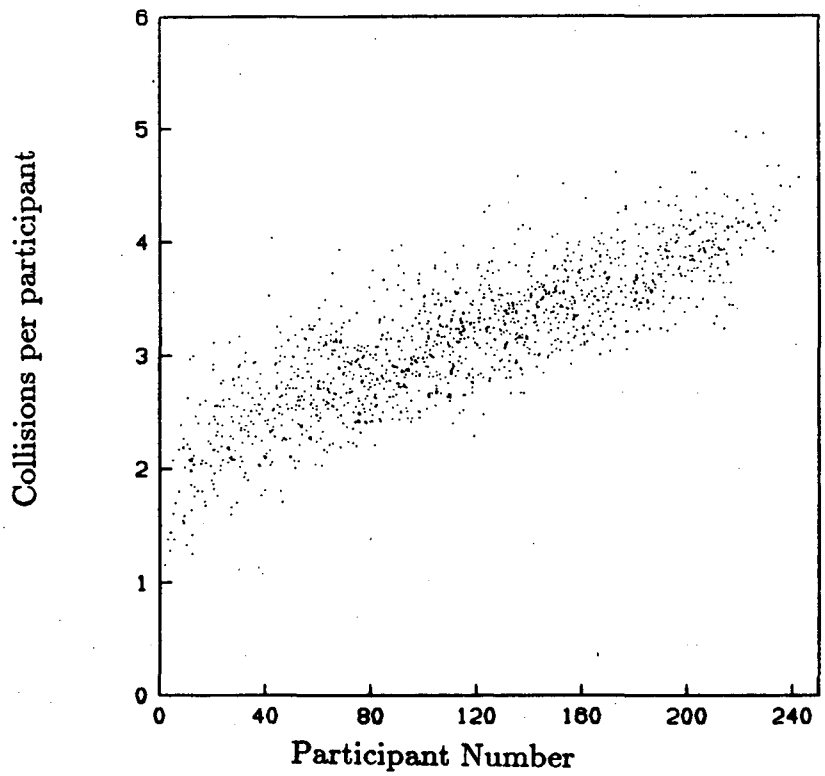

Figure 5.32. Scatterplot of number of collisions per participant nucleon vs. number of participants, for cascade events which produce pions from 246 MeV/nucleon La+La collisions.

collisions per participant, $n_{cp}(\pi)$, is 3.2. For collisions with fewer than 45 participants $n_{cp}(\pi) = 2.3$; for more than 110 participants†, $n_{cp}(\pi) = 3.6$. This tends to confirm the intuitive idea that—at least in a classical collision model—a small impact parameter nucleus–nucleus collision will involve more *nucleon–nucleon* collisions than a large impact parameter collision.

Estimation of impact parameters. By studying the correlation between associated multiplicity and impact parameter in the cascade simulation we can make some rough, model-dependent inferences about typical impact parameters for collisions in which subthreshold pions are created.† Except at the highest multiplicities, data and cascade associated multiplicity distributions are approximately congruent when the cascade distributions are shifted to lower values by $M \simeq 10$. From Table 5.3 we see that for pion production in La+La collisions the typical mean associated multiplicity in the data is about 30 ± 5, which corresponds to a cascade value of approximately 40 ± 5. Fig. 5.33 relates associated multiplicity to impact parameter in the cascade. Projecting a range in multiplicity of 40 ± 5 onto the abscissa yields a gaussian distribution with mean 4.9 fm and $\sigma = 0.9$ fm, which is consistent with the value of 4.6(0.2) fm obtained by our group in a previous study[13] of the reaction 246 MeV/nucleon $^{139}\mathrm{La}+^{139}\mathrm{La} \rightarrow \pi^- + X$ at $\theta_{c.m.} = 90°$. Assuming a clean-cut collision geometry, this corresponds to participation by about half the target and projectile nucleons.

Summary. In no respect do the results of the cascade simulation differ dramatically from the experimental results. Significantly, the slope parameters

†There are more participants than there are hits recorded in the multiplicity array, since the majority of the participants are neutrons. The measured multiplicity is also limited by multiple hits in the array.

†Here again the problem of multiple hits in the multiplicity array should be kept in mind. However, particularly for purposes of estimating the impact parameter in this way, the most straightforward way to handle the situation is to take cascade distributions under experimental conditions, i.e. with multiple hits not recorded. The fact that the impact parameter is being extracted based on apparent, rather than actual multiplicities should not then affect the result.

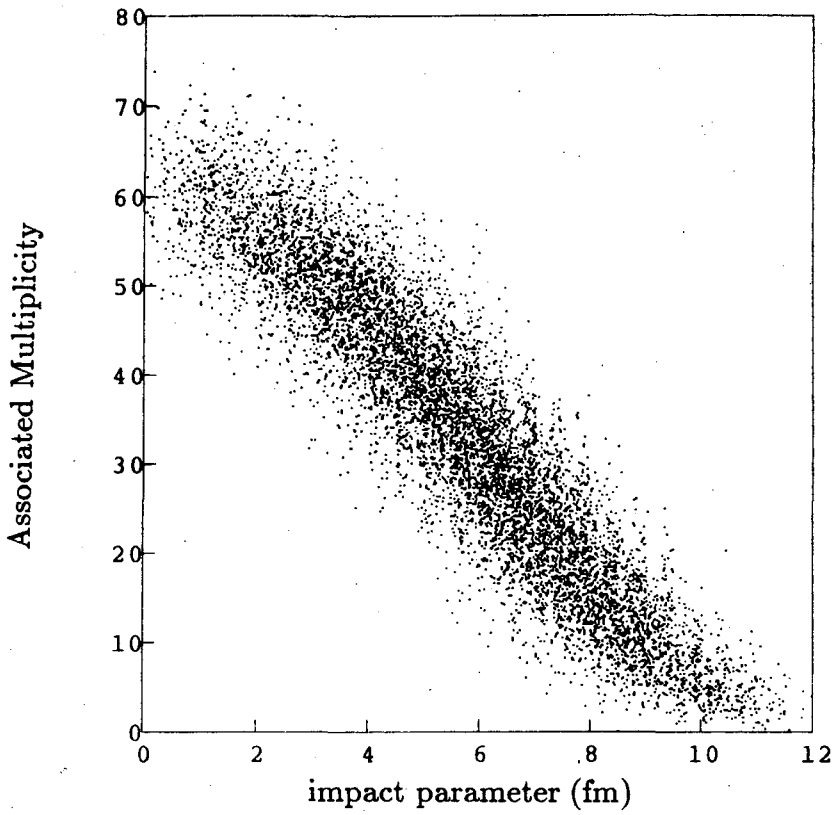

Figure 5.33. Associated multiplicity vs. impact parameter (fm) for cascade pion events with $A_{tgt} = A_{proj} = 139$ at $T_{beam} = 246$ MeV/nucleon. Multiplicity is for charged particles, i.e. protons. (For La+La, 114 of the interacting nucleons are assigned to be protons.) The acceptance of the multiplicity array is folded into the cascade analysis program.

extracted from the cascade are in excellent agreement with the data at beam energies down to at least 183 MeV/nucleon, demonstrating that a simulation based solely on nucleon-nucleon interactions can reproduce the energy dependence of the pion yield even at pion kinetic energies several times greater than the beam energy in the center of mass.

It has been suggested[5] that the difference between the pion yield found experimentally and that predicted by the cascade may be explained in terms of compression of the nuclear matter; however the constraints on applicability of the cascade to subthreshold pion production make it difficult to extend this interpretation to our energy range. We simply note that the discrepancy in yield between cascade and data increases with decreasing beam energy, below the pion

threshold.

It is also difficult to interpret the difference between the data and the cascade prediction of the mass dependence of the yield below threshold. The fact that the yield ratio for cascade pions exhibits a small increase at 183 MeV/nucleon suggests that the similar but much stronger effect observed in the data may be at least partially due to non-collective effects. One explanation is that the larger size of the La+La system increases the probability of multiple collisions, making it more likely that several nucleons can pool their energy (via successive binary interactions) to produce a pion.† Such a scenario takes on increasing importance as the beam energy is lowered, and fewer nucleons have sufficient energy—even with Fermi motion—to produce a pion in a first collision. In support of this hypothesis, we note that for cascade events at a beam energy of 183 MeV/nucleon where at least one pion is produced, the mean number of collisions per participant nucleon is 2.2 for Ne+NaF and 2.9 for La+La. For all events with at least two participants, the corresponding numbers are 1.1 and 2.0, respectively. For 246 MeV/nucleon (244 MeV/nucleon for Ne), the figures are about 10% higher.

Other cascade codes. Kitazoe and collaborators[7-9,152] have recently developed a cascade code which reproduces the pion yield from collisions of light systems ($A_{tgt} \simeq A_{proj} \leq 40$) for $T_{beam} \geq 800$ MeV/nucleon. They plan to apply the code to heavy systems and subthreshold collisions[153].

Lastly, we note that the Cugnon code has very recently been modified to include isospin[154]. However, the large amount of computer time required to generate cascade results has made it impractical to include calculations with the new code in this dissertation.

†This idea has also recently been discussed by Schürmann[151], in the context of subthreshold kaon production.

5.3 Charge dependence

The observation of the charge dependence of the pion spectra from La+La collisions is an unexpected and striking feature of the experimental results.[†] Fig. 5.34 illustrates the effect. The cross section for π^- at $30° \leq \theta_{c.m.} \leq 90°$ has been fit by a single exponential, and is shown as the solid line in the figure. The small uncertainty is indicative of the quality of the fit. The π^+ cross sections are plotted individually. The inset is a plot of the ratio, $R_{-/+}$, of the π^- and π^+ cross sections.

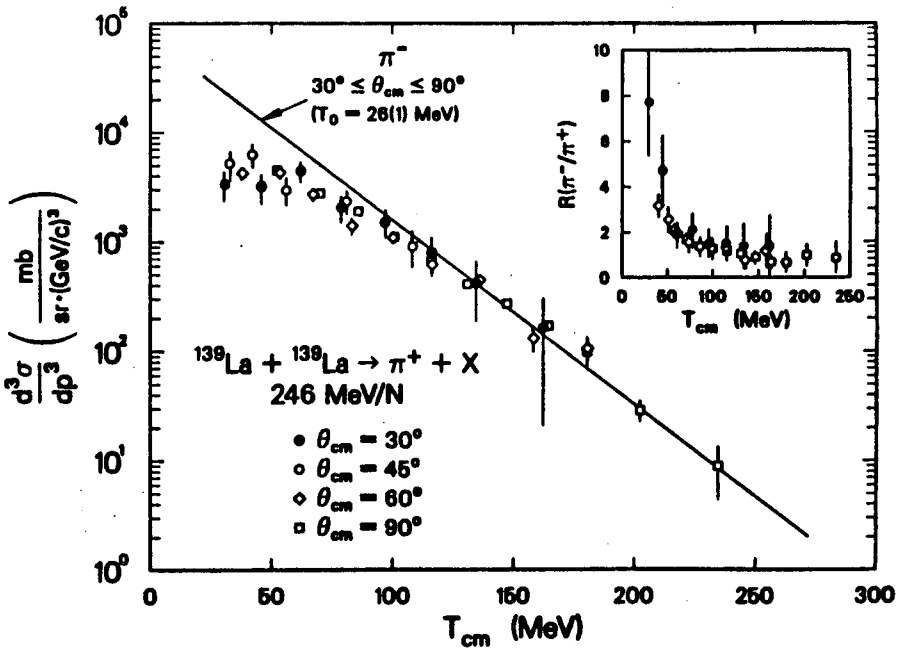

Figure 5.34. Comparison of inclusive π^+ and π^- cross sections for 246 MeV/nucleon La+La collisions at $30° \leq \theta_{c.m.} \leq 90°$. The solid line is a fit to all the π^- cross sections. The data points are for π^+ , with each angle plotted individually. The inset shows the ratio of the π^- to π^+ cross sections at $\theta_{c.m.} = 30°, 60°$ and $90°$, vs. pion kinetic energy in the c.m..

If charged pions were produced according to the isospin of the interacting

[†]The discussion in this section is limited to 246 MeV/nucleon, where the effect is most clear. There is some evidence for charge dependence at 183 MeV/nucleon, as well. At 138 MeV/nucleon, the data is too limited for this sort of analysis.

nuclei, the neutron excess of the La+La system ($N/Z = 82/57$) would lead to a value for $R_{-/+}$ of between 1 and 2, independent of pion energy. This would be the case for pure resonance production, for example (Appendix F, p. 195).† In the figure, one can see two distinct (and possibly related) features: the turnover in the π^+ spectra at low pion energy, and the tendency of $R_{-/+}$ towards unity at high energy.‡ Neither feature is sensitive to cuts on multiplicity. In the following discussion we will examine the charge dependence of the pion spectra in the context of previous experimental and theoretical results.

Experimental evidence for charge dependent effects

Charge-dependent effects in pion spectra have previously been observed in nucleon-nucleus (Refs. 30,32) and in nucleus-nucleus collisions above (Refs. 54, 55,57,58,59,61,72) and below (Refs. 59,72,93,94) the pion threshold. The nucleon-nucleus (p. 15) and above-threshold nucleus-nucleus (p. 25) cases were summarized earlier. We note that there is no evidence in our data for either charge for the "mid-rapidity bump(s)" reported in Refs. 54, 55 and 61. We now take up the subthreshold results in more detail.

The majority of the data below threshold is for light projectiles ($A \leq 20$) at forward angles ($\theta_{lab} \leq 30°$). Benenson *et al.*[72] and Sullivan *et al.*[59] have measured $R_{-/+}$ at $\theta = 0°$ for ^{20}Ne incident on a variety of targets ($12 \leq A_{tgt} \leq 238$) at beam energies between 80 and 280 MeV/nucleon. They found $R_{-/+}$ to be strongly peaked (up to a maximum value of about 10) at $\theta = 0°$ for pion velocities near the beam velocity, and $R \simeq 1$ elsewhere (Fig. 5.35). For beam energies below 200 MeV/nucleon, the asymptotic value of $R_{-/+}$ is between 0.5 and 1. Also, for

†In this instance, the value of the constant depends upon which isobars are accessible, and thus the ratio is a function of beam energy. This could also lead to a slight pion energy dependence for beam energies near the next lowest-lying resonance, the $N(1440)$.

‡Note that the asymptotic value of $R_{-/+}$ at $\theta_{c.m.} = 30°$ is somewhat higher than that at the other angles. This is due to the enhancement in the π^- spectrum at that angle. When $R_{-/+}$ is calculated using the multiplicity-selected 30° data (p.118), the result is consistent with that at the other angles.

80 MeV/nucleon there are no data points in the region of the peak. The peaking falls off rapidly with pion angle, becoming negligible above $\theta_{lab} = 12°$. Similar results were obtained above threshold, up to 480 MeV/nucleon ^{20}Ne and also for 535 MeV/nucleon ^{40}Ar $+^{12}$C, KCl.

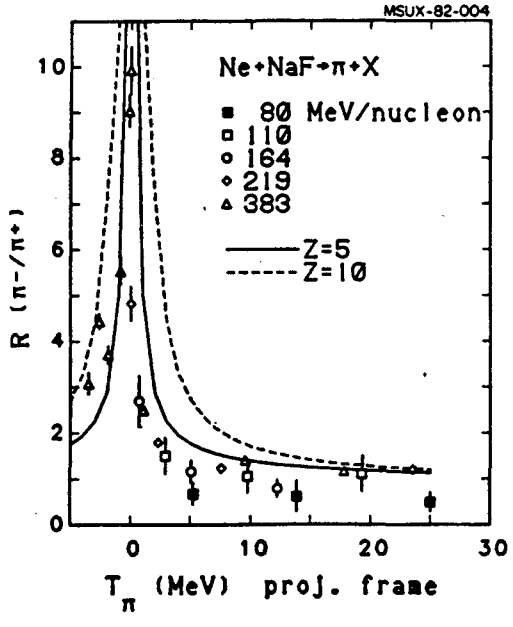

Figure 5.35. Ratio of π^- to π^+ cross sections in Ne+NaF at 0°, as a function of pion kinetic energy in the projectile frame. The curves are the results of a model calculation, which will be discussed below. (From Ref. 155. This is a corrected version of Figure 1 of Ref. 72.)

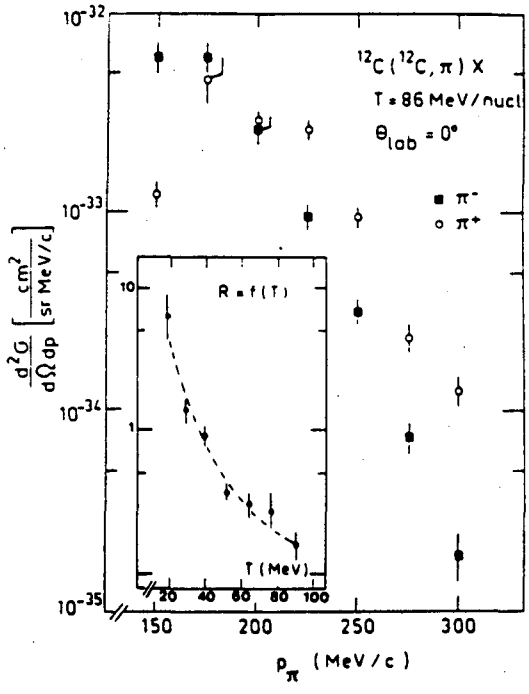

Figure 5.36. Double differential cross sections for the reaction 86 MeV/nucleon ^{12}C $+^{12}$C $\rightarrow \pi^{\pm} + X$ at 0°. The inset shows the ratio of π^- to π^+ cross sections as a function of pion kinetic energy in the projectile frame. (From Ref. 93.)

Chiavassa *et al.*[93] measured $R_{-/+}$ at 0° for the reaction ^{12}C $+^{12}$C $\rightarrow \pi^{\pm} + X$ at 86 MeV/nucleon (Fig. 5.36). The value of $R_{-/+}$ was found to fall smoothly as a function of pion kinetic energy in the *projectile* frame, from almost 10 at $T^{\pi}_{proj} = 20$ MeV to about 0.2 at $T^{\pi}_{proj} = 90$ MeV. The authors note a significant difference between these data and the 0° data of Benenson *et al.*: the large value

of $R_{-/+}$ at pion energies where $R \simeq 1$ in Ref. 72.

$R_{-/+}$ at larger angles was studied by Bernard *et al.*[94], who measured the reactions $^{12}C + ^{7}Li, ^{12}C, ^{208}Pb \rightarrow \pi^{\pm} + X$ at $20° \leq \theta_{lab} \leq 150°$ for beam energies of 60, 75 and 85 MeV/nucleon. Fig. 5.37 shows the data for 85 MeV/nucleon at $\theta_{lab} = 90°$. $R_{-/+}$ is approximately constant in each case, with values of approximately 2, 0.5 and 1 for the Li, C and Pb targets, respectively.

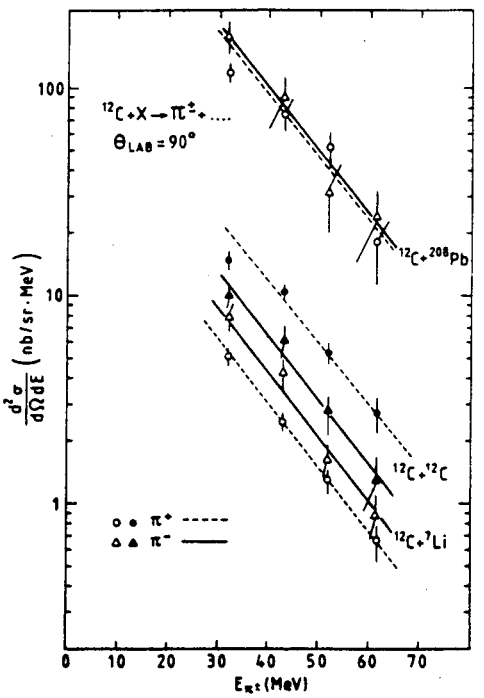

Figure 5.37. $d^2\sigma/dEd\Omega$ for π^+ and π^- produced at $\theta_{lab} = 90°$ by 85 MeV/nucleon ^{12}C incident on ^{7}Li, ^{12}C and ^{208}Pb targets. (From Ref. 94.)

The variation in $R_{-/+}$ at low pion energy for several target- projectile combinations is summarized in Fig. 5.38. Bearing in mind that this plot compares data at different c.m. angles, there are several things to note about it. First, in each case $R_{-/+}$ increases with decreasing pion energy below 80 MeV. At higher energies $R_{-/+}$ approaches a constant value. In the p+Cu case, that value is about 0.2, which is what would be predicted for pion production through the Δ isobar.[†]

[†]In the p+Cu data the π^+ and π^- spectra both turn over at $T_\pi < 90$ MeV. In Ref. 30 the difference in the number of π^+ and π^- at low energies is attributed to charge exchange scattering. However, the Monte Carlo calculation which includes charge exchange does not reproduce the data below 100 MeV. (Ref. 30, Figures 16 and 17.)

For the C+C case, there is no data above $T^{\pi}_{c.m.} = 62$ MeV, but $R_{-/+}$ is clearly less than 1, which is the value expected based on isospin considerations.[‡] For the La+La data taken in the present experiment, the asymptotic value of $R_{-/+}$ is about 1, which is a little more than half the value expected from isospin.

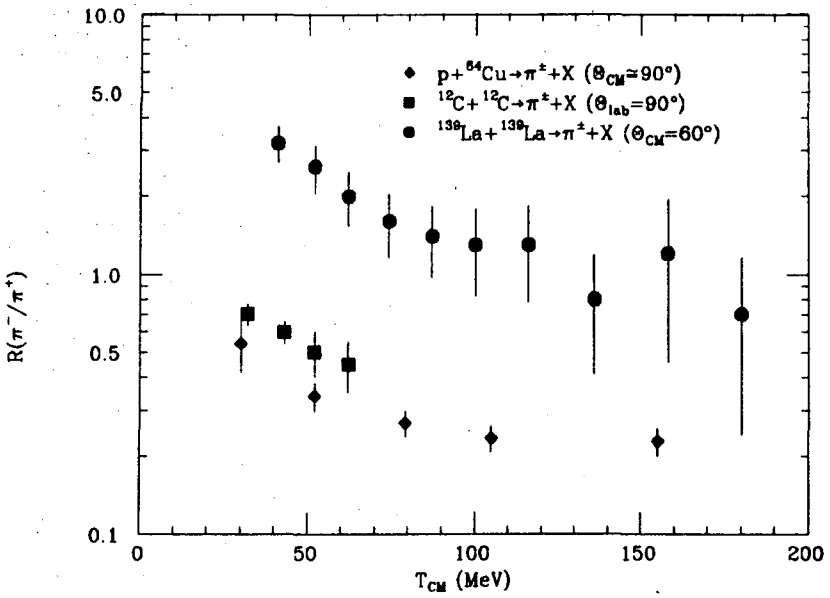

Figure 5.38. Comparison of π^-/π^+ ratios for 730 MeV p+^{64}Cu at $\theta_{c.m.} \simeq 90°$ (Ref. 30), 85 MeV/nucleon ^{12}C +^{12}C at $\theta_{lab} = 90°$ ($\theta_{c.m.} \simeq 110°$) (Ref. 94) and 246 MeV/nucleon ^{139}La +^{139}La at $\theta_{c.m.} = 60°$. (Notes: The p+Cu data was taken at 90° in the lab, but for this highly asymmetric system the lab and c.m. frames are almost the same. The similar results of Ref. 32 have been omitted for clarity. For La+La, $R_{-/+}$ at $\theta_{c.m.} = 60°$ is comparable to $R_{-/+}$ at $\theta_{c.m.} = 90°$, but the data at 60° extend to lower pion energy.)

Interpretation of the charged pion results

The structure in the charged pion spectra may arise during the pion production process. It may also be due to interactions between the outgoing pions and their environment, or it may be a combination of the two.

[‡] $R_{-/+}$ in this case is also consistent with the data[93], for 85 MeV/nucleon C+C at $\theta = 0°$, which continues to fall at higher pion energies, reaching a value of about 0.2 at $T_\pi = 135$ MeV.

In the first case, studying charged pion production can give us insights into how particle production in nuclear matter differs from production in more elementary interactions. In the second case, the charged pion spectra can act as a probe to map the space-time evolution of a heavy ion interaction. In neither case is the physics necessarily limited to subthreshold energies; however, it may be true that the nature of pion-producing interactions —for example, the number of participants at rest in the c.m.— at these energies makes charge-dependent effects more likely.

Coulomb distortion

It is reasonable to expect that charged pions emitted from an interaction volume containing a large number of charged nucleons might be affected by the Coulomb field of those charges, and Coulomb distortion of charged pion spectra has been investigated theoretically by several authors[156-161]. For example, Libbrecht and Koonin[156] attribute the mid-rapidity bump observed by Wolf and others to "focusing" of charged pions by a nuclear charge distribution dispersed along the beam direction. In the same vein, the peaking in $R_{-/+}$ for beam-rapidity pions at forward angles observed by Benenson *et al.* and Sullivan *et al.* has been explained as being due to Coulomb interactions between the pions and the projectile fragments, and calculations[158,159] based on this idea are in good agreement with the data[59].

As pointed out in Ref. 72, it might be expected that many of the pions with velocities close to that of the projectile are created in peripheral collisions. (For example, by excitation and subsequent decay of a projectile nucleon.) The relatively small charge of the Ne+NaF system ($Z_{tgt} + Z_{proj} = 20$) argues in favor of this: a small impact parameter collision involving this system would probably leave little charge at the beam velocity. Benenson *et al.* concluded that Coulomb

effects associated with the target remnants and with the charge left at rest in the center of mass should also be detectable, although out of the range of their experiment.

The data presented in Refs. 59 and 72 is concentrated on the area in p_T–y space at low p_T and $y \simeq y_{proj}$. The charged pion results of the present study, along with those of Refs. 30, 32, 93 and 94, fill in other parts of the p_T–y plot, including regions where the charge of the projectile remnants can have little effect on the outgoing pions.

Some of the features in the contour plots of the 246 MeV/nucleon La+La data (Fig. 5.11), become more clear when looked at together with the particle spectra (e.g. Fig. 5.34).† For example, in the region near $p_T \simeq m_\pi c$ and y slightly greater than y_{proj}, a peak in the π^+ plot has a counterpart in the form of a valley in the π^- plot. In the π^+ spectra there is a tendency at all angles for the spectra to flatten out and in some cases to turn downward as the pion energy decreases. On close examination, it can be seen that the $\theta_{c.m.} = 30°$ and 45° spectra are distinctly peaked. This corresponds to the peaking in the π^+ contour plot. For π^- , the increased yield at $\theta_{c.m.} = 30°$ is seen as a ridge in the π^- contour plot. On the other hand, the flattening in the π^+ spectra at $\theta_{c.m.} = 60°$ and 90° is not obvious in the contour plot, nor is the decrease in $R_{-/+}$ with increasing pion energy.

The contour plots do allow us to locate these features relative to the target and projectile rest frames, and from this it is clear that at least some of the structure at forward angles and low energy may be associated with the projectile spectators, while the effects at mid-rapidity or high energy very likely are not.

The multiplicity–cut spectra provide additional evidence: we know that the

†There are some difficulties in viewing the data in this way. The low density of data points makes it hard to localise features, and changes in slope don't show up well, especially if they are isotropic. Also, there is no clear way to indicate the uncertainty in the data, which may be large, especially for π^+ .

increased π^- yield at $\theta_{c.m.} = 30°$ is not present when there is high associated multiplicity. In this case there has probably been a central collision, with relatively little charge remaining at the beam rapidity and therefore little or no focusing, even at forward angles. Unfortunately the statistics for π^+ do not permit a similar cut; however if the above hypothesis is correct, then, with sufficient statistics, the π^+ spectra selected on high multiplicity would still exhibit the low energy turnover, but the peak at forward angles would disappear, and the turnover would be isotropic, since the source charge would be at rest in the center of mass.

How can we reconcile these results with those of Ref. 59, where no anomaly in $R_{-/+}$ is observed beyond $\theta_{lab} = 20°$? The La+La system has almost six times the nuclear charge of Ne+NaF; proportionally greater charge near the beam rapidity might be expected to extend the effects of projectile focusing out to larger angles. If the La+La measurements were carried out at 0°, one presumably would observe very strong projectile focusing for $T_\pi \simeq T_{proj}$, correlated with low associated multiplicity.

We cannot reconcile the 0° data of Ref. 72 for 80 MeV/nucleon Ne+NaF with that of Ref. 93 for 86 MeV/nucleon C+C. For pion kinetic energy between 5 and 25 MeV in the projectile frame, $R_{-/+}$ for Ne+NaF was found to be approximately constant at about 0.5, while for C+C, $R_{-/+}$ decreases smoothly from about 7 at 18 MeV to 0.2 at 90 MeV. Any relative normalization between the two experiments should be cancelled by taking the ratio of π^- to π^+ , and would in any case not account for the very different shapes of the respective π^- /π^+ ratios.

Focusing by the projectile fragment aside, we would like to understand the remaining charge-dependent effects, the low energy depletion and high energy enhancement in the π^+ spectra. The depletion seems to be isotropic, excepting projectile focusing. It also begins at about the same pion energy and it is

approximately independent of system mass and beam energy for the three systems studied (Fig. 5.38).† The enhancement is also isotropic and is observed for $^{12}C + ^{12}C$ and for $^{139}La + ^{139}La$, but not for $p + ^{64}Cu$.

Distortion by the Coulomb field of a compound nucleus. In order to explain the observed excess in π^+ production at $\theta_{lab} = 90°$ in 85 MeV/nucleon C+C collisions (Fig. 5.37), Bernard *et al.*[94] introduced a simple energy shift in the pion spectra by an amount equal to the Coulomb potential energy of an uncompressed compound nucleus. For pions emitted from a hypothetical ^{24}Mg nucleus,

$$\begin{aligned} \Delta E &= \frac{Ze^2}{r} \\ &= \frac{Z\alpha(\hbar c)}{r} \\ &\simeq \frac{(12)(\frac{1}{137})(197)}{1.12(24)^{\frac{1}{3}}} \quad (\frac{\text{MeV-fm}}{\text{fm}}) \\ &\simeq 5.3 \text{ MeV} \end{aligned}$$

Assuming that π^- and π^+ are produced in equal numbers from the isospin– symmetric C+C system, then shifting the π^+ spectrum to higher energy by ΔE and shifting the π^- spectrum to lower energy by a like amount reproduces the experimental result. The agreement is somewhat less good for $^{12}C + ^{7}Li$, and is poor for $^{12}C + ^{208}Pb$, unless one assumes π^- production much greater than that expected based on isospin.

For the La+La system, the difference between the observed $R_{-/+} \simeq 1$ at high pion energies and the approximate $82/57 \simeq 1.4$ predicted from the neutron/proton ratio requires an energy shift of about the same magnitude as observed in the C+C reaction. From cascade and associated multiplicity studies (p. 134) we know that a typical pion-producing interaction involves, on the average, about half the target and projectile nucleons, almost independent of pion

†There is also an apparent depletion at about the same pion energy in the π^+ spectra for 240 MeV $p + ^{64}Cu$ (Fig. 2.4). There are no comparable data for π^- , however.

angle and energy. Assuming a pion source consisting of 82 neutrons and 57 protons leads to a predicted energy shift, $\Delta E \simeq 14$ MeV, which is much too large. In addition, this picture cannot explain the energy dependence of $R_{-/+}$ at low pion energies.

Coulomb effects on the density of nucleon final states. Bertsch[162] proposed that the nuclear charge affects the pion spectra in two ways: through distortion of the pion wave functions and by modification of the density of nucleon final states. The density of states, ρ_f^N, was found to depend upon the nucleon chemical potentials, μ_p and μ_n:

$$\rho_f^N(\pi^\pm) \propto e^{-(T_{\pi^\pm} \mp (\mu_p - \mu_n))/kT},$$

where kT is the nucleon temperature. (This treatment assumes an equilibrated system.) For a given pion kinetic energy, $T_{\pi^\pm}$, the density of states contributes a term,

$$e^{-2(\mu_p - \mu_n)/kT},$$

to $R_{-/+}$, where the difference in chemical potential,

$$\mu_p - \mu_n = \frac{Ze^2}{r},$$

arises in the Coulomb potential of the pion source. In this respect contact is made with the ideas of Ref. 94.

The Coulomb distortion of the pion wave functions depends upon pion energy relative to the nuclear fragments, and therefore it most strongly affects pions with rapidity close to that of a strong charge, e.g. the beam remnant. The dependence of the density of states on the nucleon temperature means that it will contribute more strongly to the shapes of the pion spectra at low beam energies. However, the absence of any pion energy dependence in the density of states contribution to $R_{-/+}$ means that the Coulomb distortion must also be important, at least at low pion energies, where $R_{-/+}$ depends on T_π.

At high pion energy (i.e. $y_\pi \gg y_{beam}$), where $R_{-/+}$ is constant, we may assume that the pion wave functions experience little or no Coulomb distortion, and therefore that the density of states dominates. Then we can use $R_{-/+}$ to estimate the size and charge of the pion source, as follows. Substituting the Coulomb potential for the chemical potential, as above:

$$R_{-/+}\ (Coul.) = e^{-2\frac{Ze^2}{rkT}}, \tag{5.1}$$

where kT is the nucleon temperature and r is the radius of the charge source. Following Bertsch, we assume that the pions come from a thermalized nucleon gas, and from Boltzmann statistics, $kT = \frac{2}{3}(60) = 40$ MeV, where 60 MeV is the beam energy per nucleon in the center of mass. This is consistent with the experimental temperature of 42 MeV extracted from our proton spectra for central collisions at $\theta_{c.m.} = 90°$. Assuming, once again based upon comparison of experimental associated multiplicities to the cascade, that about half the nucleons participate, then the Coulomb potential energy, calculated as above, is about 14 MeV and

$$R_{-/+}\ (Coul.) \simeq e^{-2\left(\frac{14}{40}\right)} = 0.5$$

In a simple delta resonance model, the neutron excess of the La+La system leads to a predicted charged pion production ratio (Appendix F, p. 197),

$$R_{-/+}\ (prod.) \simeq 1.8$$

Assuming that all *pn* collisions can produce pions—effectively, including the $N(1440)$ resonance—reduces the ratio to 1.7. (See Appendix F.) Folding together the contributions from delta resonance production and density of states gives $R_{-/+} = (0.5)(1.8) = 0.9$, consistent with the observed value of about 1 at high pion energies. However, as was the case with the compound nucleus hypothesis of Ref. 94, the structure at low energies cannot be treated in this way.

Coulomb impulse and phase space distortion. Gyulassy and Kauffmann[158] have treated Coulomb final state interactions analytically. They first make a simple classical derivation, followed by a formal development using first-order relativistic perturbation theory, with a limited extension into the non-perturbative regime. Details and examples of their calculations may be found in Refs. 59 and 158. Here, we will outline their classical treatment, in order to make clear the nature of the Coulomb effects, and how they qualitatively explain the observed energy-dependent structure of the charged pion spectra.

The single particle inclusive cross section $\sigma(\mathbf{k})$ for charged particles may be related to the cross section $\sigma_0(\mathbf{k})$ for neutrals by:

$$\sigma(\mathbf{k}) = \sigma_0(\mathbf{k}_0(\mathbf{k}))\left|\frac{\partial^3 k_0}{\partial^3 k}\right|, \tag{5.2}$$

where $\mathbf{k}_0$ and $\mathbf{k}$ are the initial and final particle momenta, respectively.

The total Coulomb effect may be considered in two parts:

1. a **Coulomb impulse**, or momentum shift[†] $\pm\delta\mathbf{p}(\mathbf{k}) \equiv \mathbf{k} - \mathbf{k}_0(\mathbf{k})$, which shifts the positive particle spectra to higher energies, and the negative spectra to lower energies, and

2. a **Coulomb phase space distortion**, which affects the density of states in momentum space and is embodied in the jacobian, $|\partial^3 k_0/\partial^3 k|$. It tends to enhance the negative and deplete the positive spectra.[‡]

Now consider the special case of a static, spherically symmetric positive charge distribution, with Coulomb potential energy $Z\alpha/R$. ($\alpha = e^2/\hbar c$, $\hbar = c = 1$) Energy conservation is applied to get $\mathbf{k}_0(\mathbf{k})$:

$$\frac{k^2}{2m} = \frac{k_0^2}{2m} \pm \frac{Z\alpha}{R},$$

[†]The upper sign in all cases refers to positive spectra

[‡]Although the terminology might imply otherwise, the Coulomb impulse term corresponds to the contribution from the "density of states" in Ref. 162.

from which

$$\mathbf{k}_0(\mathbf{k}) = \mathbf{k}\left(1 \mp \frac{2mZ\alpha}{k^2R}\right)^{1/2}$$

Then

$$\begin{aligned}\left|\partial^3 k_0/\partial^3 k\right| &= \frac{k_0(k)}{k} \\ &= \left(1 \mp \frac{2mZ\alpha}{k^2R}\right)^{1/2}\end{aligned}$$

For the neutral particle cross section, we assume a simple exponential:

$$\begin{aligned}\sigma_0(\mathbf{k}_0) &\propto e^{-\frac{k_0^2}{2mT_0}} \\ &\propto e^{-\frac{1}{2mT_0}\left[k^2 \mp \frac{2mZ\alpha}{R}\right]}\end{aligned}$$

This leads to the expression for the final state charged particle cross sections:

$$\sigma_\pm(\mathbf{k}) = \sigma_0(\mathbf{k}) e^{\pm\frac{Z\alpha}{RT}}\left(1 \mp \frac{2mZ\alpha}{k^2R}\right)^{1/2\ddagger} \tag{5.3}$$

In eq.(5.3), the exponential is closely related to the momentum shift, while the term in parentheses corresponds to the phase space distortion. The momentum shift is independent of particle energy, and tends to enhance the yield of positive particles and depress that for negatives. The phase space distortion has the opposite effect and also introduces an energy (momentum) dependence. Both effects are angle-independent, as expected with a symmetric source charge.

Note that at low temperature or high particle momentum, eq.(5.3) almost reduces to eq.(5.1), with the difference that the temperature, T in eq.(5.1) is the temperature of the nucleons, whereas T in eq.(5.3), which enters through the assumption of a thermal spectrum for the neutral particles, is for the emitted

‡At this point our approach diverges from that of Ref. 158. They expand eq.(5.3) in $Z\alpha$, anticipating the perturbative approach they will take later on. We will not do so, since for subthreshold pion production from the La+La system the experimental evidence, in the form of the associated multiplicity distributions and the angular isotropy of the pion spectra, makes it reasonable to expect to see Coulomb effects dominated by a single charge distribution, at rest in the center of mass. Consequently $Z\alpha$ may be of order unity and the perturbative expansion will not work, nor is it required for this special case. (See also Ref. 163.)

particle. The two temperatures are not necessarily the same. (See, for example, Ref. 57.)

We can include the effect of an expanding charge distribution in a simple way, in analogy to eqs.(2.11) and (2.12) of Ref. 158. Let $k^2 \rightarrow k^2 + k_T^2$, where k_T is the thermal average momentum:

$$k_T^2 = 3mT_p(m/m_p),$$

with T_p the temperature of the charge source, and m and m_p the particle and proton masses, respectively. Then,

$$\sigma_\pm(\mathbf{k}) = \sigma_0(\mathbf{k}) \left(e^{\pm \frac{Z\alpha}{RT}}\right) \left(1 \mp \frac{2mZ\alpha}{(k^2+k_T^2)R}\right)^{1/2} \left(e^{-\frac{k_T^2}{2mT}}\right), \tag{5.4}$$

and

$$\begin{aligned} R_{-/+} &= \frac{\sigma_{\pi^-}}{\sigma_{\pi^+}} \\ &= e^{-\frac{2Z\alpha}{RT}} \left[\frac{(k^2+k_T^2)R + 2mZ\alpha}{(k^2+k_T^2)R - 2mZ\alpha}\right]^{1/2}. \end{aligned} \tag{5.5}$$

From eqs.(5.2)–(5.5) we can see qualitatively how the competing effects of particle momentum and temperature give the detected spectra their form. At high temperature and/or low momentum, $R_{-/+}$ tends to increase with decreasing momentum. At low temperature and/or high momentum, $R_{-/+}$ decreases asymptotically with increasing momentum. The absence of any angle dependence in eq.(5.5) is consistent with the data for La+La. Angle dependence may be introduced by an asymmetric charge source, by multiple charge sources or when the particle source and charge source are separated in space. (The latter is probably the strongest influence on the data of Refs. 59 and 72.) It can also come in through an angle dependence of the neutral particle cross section, σ_0. The small anisotropy in $R_{-/+}$ at low momenta at forward angles may be due to the influence of beam fragments from peripheral collisions, but the spectra cut on low multiplicity (p. 143) do not provide conclusive evidence of this.

Fig. 5.39 shows $R_{-/+}$, calculated using eq.(5.5), for p+Cu, C+C and La+La interactions at the same beam energies as above, but with isotropy assumed. For La+La and C+C, approximately half the interacting nucleons are assumed to be involved, with the non-interacting proton charges assumed to have relatively little effect on the spectra. As expected, eq.(5.5) qualitatively reproduces the main features of the data. Quantitatively, the calculated low energy increase in $R_{-/+}$ occurs at lower pion energy than observed experimentally, while the predicted asymptotic value of $R_{-/+}$ is consistent with experiment for C+C, but is too small for La+La and p+Cu. For C+C at 0° (not shown) $R_{-/+}$ is more than two times too large.

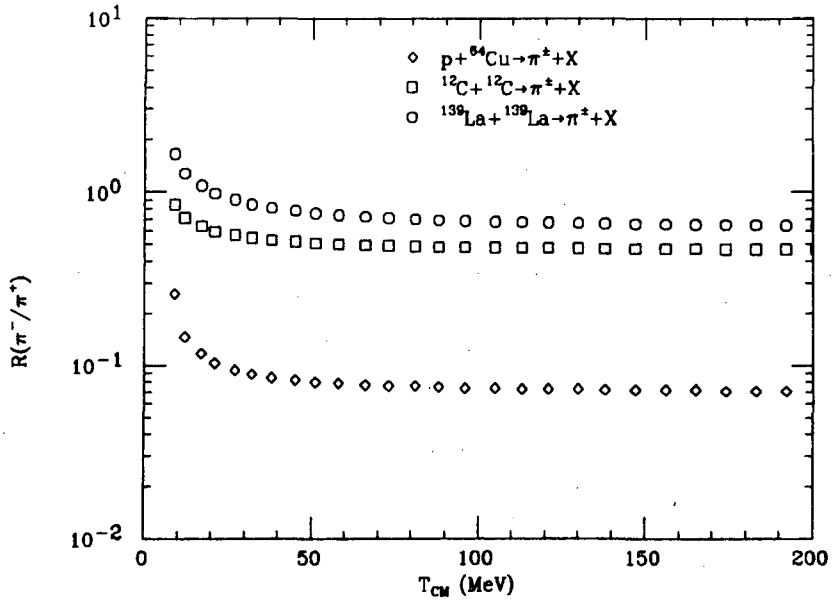

Figure 5.39. $R_{-/+}$ calculated according to the development of Gyulassy and Kauffmann (Ref.158) for an expanding spherical charge, coincident with the pion source. Parameters are, for p+Cu, C+C and La+La, respectively: source size $R = 4.5, 2.6$ and 5.8 fm, charge $Z = 29, 6$ and 57, pion temperature $T = 40, 17$ and 26 MeV. (Temperatures are from charged pion cross sections. For C+C, $T = 17$ MeV is consistent with slope parameters from angle integrated data for neutral pions[92].)

For La+La, the experimental value of $R_{-/+}$ at high pion energy is reproduced

if we use a pion temperature of 40 MeV. This is not surprising, since it makes the calculation equivalent to that of Bertsch, discussed above. However, this higher temperature for neutral pions is inconsistent with the data for charged pions; when substituted into eq.(5.4), it leads to incorrect predictions for the temperature. By contrast, using $T = 26$ MeV gives too low a value for $R_{-/+}$. We will not pursue this further, but it is clear that a full treatment of Coulomb effects on the charged pion spectra must confront the fact that different temperatures are observed for proton and pion spectra from the same interaction.

Finally, the energy at which $R_{-/+}$ starts to increase is rather insensitive to changes in any of the parameters. If the assumption of a dominant central charge source is correct, then the discrepancy between the calculation and the data would have to come from the low energy structure of the neutral pion spectrum. In particular, there may be a low energy depletion in the production of pions. For π^+ the peak would be Coulomb-shifted to higher pion energies, for π^- the shift is in the opposite direction, and in our case would have to be big enough to shift the peak to an energy below the minimum accepted by the spectrometer. For example, in this way a peak due to a blast wave (p. 27) might be obscured by Coulomb effects.

We examined this possibility as follows. Starting with eq.(5.2), we substituted for the jacobian as before, but rather than assuming an exponential σ_0, we substituted the measured π^+ spectrum for $\sigma_+(\mathbf{k})$ on the left side of the equation, and inverted to obtain $\sigma_0(\mathbf{k})$. The new σ_0 was then used to compute σ_-. Using this method it was found that a peak in the neutral spectrum could, in principle, be shifted in such a way as to give a π^- spectrum which is exponential over the entire spectrometer acceptance. However, this was accomplished only by assuming the participation of all the available charge (i.e. a Coulomb shift due to a compound nucleus with $Z = 114$ and $A = 278$) and this gives an asymptotic

value of $R_{\pm}$ which is much too low.

Pion evaporation from a compound nucleus. In a recent publication[118], Bonasera and Bertsch have adapted the statistical theory of Weisskopf[115] to the problem of charged pion production. In this model, which essentially combines the approaches of Refs. 114 and 162, the pion production cross section is determined by the probability of thermal evaporation of a pion from a compound nucleus. This probability is proportional to the level density of the evaporation residue and to the inverse cross section for pion absorption on a nucleus, both of which depend on the pion charge, and to some other terms which are charge-independent. Thus, the ratio of cross sections for charged pion production depends only on the level density and on the absorption cross section. The level density is related to the difference in proton and neutron chemical potentials and thence to the Coulomb energy of the nucleus, as in Ref. 162, resulting in the expression for the ratio:

$$R_{-/+} = \frac{\sigma_{abs}(\pi^-)}{\sigma_{abs}(\pi^+)} \cdot e^{-2(\mu_p - \mu_n)/T},$$

where T is determined from the experimental pion spectra, and the absorption cross sections are obtained from a parameterization of the existing data for pion absorption on nuclei (Refs. 138, 139 and 164).

Bonasera and Bertsch found reasonable agreement with our data for La+La at both 138 and 246 MeV/nucleon (Fig. 5.40), as well as with other pion data. It is easy to see empirically why this is so. At $T_\pi > 150$ MeV, the absorption cross section is approximately independent of charge, and the ratio depends most strongly on the level density term, which we know accounts for the ratio for high energy pions (p. 147).† At lower pion energies, the π^+ absorption cross section falls off rapidly[138], and this produces the increase in $R_{-/+}$ at low energy. Note

†It is interesting to note that in Ref. 118 the temperature used is that for the pions, rather than for the protons as in Ref. 162. In fact, Ref. 118 somewhat underpredicts the ratio for 246 MeV/nucleon, and the discrepancy is reduced by using the higher temperature.

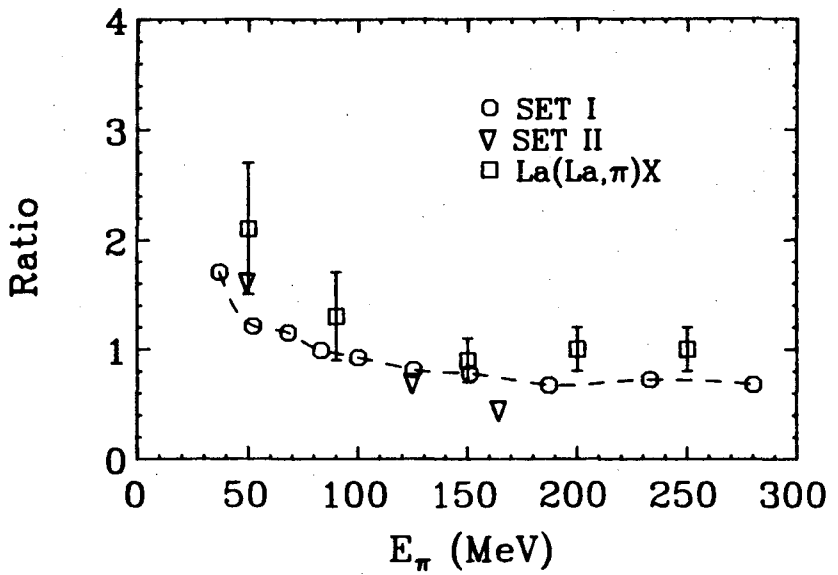

Figure 5.40. Comparison between a statistical compound nucleus model and the data for $R_{-/+}$. The boxes are data points for our data for 246 MeV/nucleon La+La. The circles and triangles are for two different sets of pion absorption data. (From Ref. 118.)

also that the inverse cross section in this model corresponds to the phase space distortion term in the Gyulassy–Kauffmann formulation. Qualitatively, the two approaches can be connected by considering the phase space term to reflect the effect of the Coulomb field on the pion production amplitude, as discussed in Sec. 3 of Ref. 158.

n/p Ratios and Clustering. The influence of Coulomb final-state interactions on protons emitted from heavy ion collisions has been extensively investigated (Refs.6,10,158,161,165 and 166), particularly in regard to the low energy n/p ratios at forward angles. The work of Madey *et al.*[10] and of Barghouty and Fai[161] has demonstrated the importance of considering composite fragment formation as well as Coulomb effects. Barghouty and Fai also report good agreement with the experimental π^-/π^+ ratios of Refs. 57 and 72, although a model without fragment formation[158] does equally well.

The possible relevance of fragment (or cluster) formation to the π^-/π^+ ratio

has been pointed out by Stock[167]. He notes that, to first order, clusters remove equal numbers of neutrons and protons from the system. Thus, if the primordial system is neutron-rich, then in the final state the free nucleons will be even more dominated by neutrons. Furthermore, π^+ and π^0 are "unstable in 'neutron matter' ", by way of the charge exchange reactions

$$\pi^+ n \rightarrow \pi^0 p$$

and

$$\pi^0 n \rightarrow \pi^- p$$

with the daughter protons being absorbed into additional clusters. The strength of the effect at low beam energy is due to the low entropy per baryon in the initial state, resulting in more clusters; the strength at low *nucleon* energy comes from the fact that the cross section for formation of a cluster of mass A is proportional to the A^{th} power of the nucleon cross section[14], and the nucleon cross section decreases roughly exponentially with energy. This may at least partially account for the observed n/p ratios[14].†

The exact pion energy dependence of clustering effects is not clear from the above discussion; however, taken together with the quantitative inadequacy of Coulomb distortion calculations, it argues for a calculation of pion production for all three charge states which incorporates all of the effects discussed above: Coulomb distortion, fragment formation and pion absorption.

†An interesting implication of this argument is that it should affect the neutral as well as the charged pion cross sections; thus a comparison of the experimental charged and neutral pion cross sections should test the relative importance of clustering and Coulomb effects.

6. Summary and Conclusions

Summary of results and model comparisons

We have measured inclusive cross sections for pion production in the reactions ^{139}La $+^{139}$ La $\rightarrow$ $\pi^{\pm} + X$ at 138, 183 and 246 MeV/nucleon and ^{20}Ne + NaF $\rightarrow \pi^{-} + X$ at 244 MeV/nucleon for $30° \leq \theta_{c.m.} \leq 90°$. Associated multiplicities for charged particles were recorded with a 110–element scintillator multiplicity array.

Pion energy and angular dependence. To a first approximation, the exponential dependence of the pion cross sections on pion energy was found to hold for charged pions from La+La collisions at 246, 183 and 138 MeV/nucleon, and for π^{-} from Ne+NaF collisions at 244 MeV/nucleon. At 246 (La+La) and 244 (Ne+NaF) MeV/nucleon, pions are emitted almost isotropically in the center of mass, for c.m. angles between 30 and 90 degrees. There are local deviations from both isotropy and the exponential energy dependence, especially at the lower beam energies, in the form of bumps and discontinuities in the energy spectra.

Beam energy and system mass dependence. In previous experiments the slope parameter, T_0, and yield of the pion cross sections have been found to fall smoothly with beam energy, above and below threshold. (T_0 is defined to be the negative inverse slope, when the cross section is parameterized by a Maxwell-Boltzmann distribution.) Our data follow these trends, and the La+La and Ne+NaF data are consistent with the trends identified in the earlier experiments. The slope parameter was found to be rather insensitive to target and projectile mass, even for proton projectiles.

The scaling behavior of the inclusive yield, $d\sigma/d\Omega$, of π^{-} from La+La and

Ne+NaF collisions changes from approximately $A_{tgt}^{\frac{2}{3}} \cdot A_{proj}^{\frac{2}{3}}$ above threshold to close to $N_{tgt}^2 \cdot N_{proj}^2$ at 183 MeV/nucleon, beam energy. The N^2–scaling could be interpreted as a volume dependence, weighted by neutron number.

Associated multiplicities. The distributions are peaked at relatively high multiplicities (25–35 for La+La) for all angles, with the position of the peak shifting to lower multiplicities with decreasing beam energy. The distributions resemble those taken in the streamer chamber with the central(i.e. small spectator charge) trigger. We interpret this to mean that subthreshold pion production typically takes place in small impact parameter collisions. There are slightly more low-multiplicity π^--producing events at the most forward angle measured ($\theta_{c.m.} = 30°$). The slope parameter is found to depend only weakly on multiplicity.

An increase in the 246 MeV/nucleon π^- yield at $\theta_{c.m.} = 30°$ is identified with low multiplicity events; when cut on multiplicity greater than 40, the cross section is isotropic. A sharp break in the 183 MeV/nucleon π^- cross section at $\theta_{c.m.} = 30°$ is not correlated with multiplicity, however.

Charge dependence. The ratio of π^- and π^+ yields was found to vary strongly as a function of pion energy. This dependence takes the form of a peak in the π^-/π^+ ratio at low pion energy, with a gradual fall off towards an asymptotic value of unity at high energy. It is found at all angles, and persists at pion rapidities well–removed from those of the target and projectile. It is generally independent of associated multiplicity. Qualitatively similar effects have been observed in collisions of light nuclei below threshold and in p-nucleus collisions above threshold.

Model comparisons. We have compared the data with several different types of models. The firestreak thermal model predicts isotropy and exponential energy dependence, but considerably overestimates the slope and yield of the

cross section. There is also no evidence in the data of delta resonance decay, which appears as a shoulder in the model calculation.

The blast wave thermal model predicts a low energy peak in the pion spectra. We have tested the assumption that the observed peak in the π^+ spectra might be a Coulomb–shifted blast wave peak, but the required shift is inconsistent with other aspects of the data.

A statistical model in which pion production is proportional to the available phase space is in excellent agreement with the data for π^- from La+La collisions at 246 MeV/nucleon. A similar calculation for 183 MeV/nucleon Ne+NaF was made to agree only when cluster formation was included. This may be evidence of a difference in the pion production mechanism, but additional calculations are needed. The success of the statistical model vs. the firestreak model also points up the importance of taking the finite particle number into account.

We have made extensive calculations with an intranuclear cascade code, in order to compare as many of the experimental observables as possible with a purely binary, nucleon–nucleon model. The cascade code reproduces the slope parameters, but underestimates the yield. This is also the case at higher beam energies. The angular distribution of cascade pions is slightly forward–peaked, in contrast to the data, which show a clear enhancement only at $\theta_{c.m.} = 30°$.

The scaling of cascade yields with the system mass deviates from a simple $A^{\frac{2}{3}}$ at low beam energy, but not to the extent seen in the data. Associated multiplicity distributions in the cascade are quite similar in shape to those obtained experimentally, although shifted towards higher multiplicity, most likely due to the absence of clusters in the cascade simulation.

The anisotropy in the angular dependence of pions from the cascade is weakened, but not removed, by a high multiplicity cut. For low associated multiplicity, there appears to be a resonance shoulder at the expected pion energy. We

attribute the results of the cascade simulation to rescattering effects, which we found to be more likely at higher multiplicity. The results support the idea that the cascade angular distribution reflects the delta kinematics. In attempting to extend these arguments to the experimental data, we find that there is a similarity: the correlation between angular distribution and multiplicity, and several differences: the forward peaking is much sharper in the data, it is completely removed by a high multiplicity cut and there is no evidence in the data of a resonance shoulder for pions with low associated multiplicity.

Using the cascade results to relate associated multiplicity and impact parameter, we estimate the average impact parameter for pion–producing La+La collisions at 246 MeV/nucleon to be 4.9(0.9) fm.

Interpretation of the results

Our data on angular distributions and multiplicities strongly suggest that subthreshold pions (at c.m. angles between 30° and 90°) are emitted primarily from a single source, at rest in the center of mass and involving, on the average, at least half the target and projectile nucleons. However, some of the data at $\theta_{c.m.} = 30°$, especially when considered in the context of 0° pion results, indicates that peripheral interactions may play a significant role at more forward angles.

Two aspects of our results argue in favor of pion production in binary nucleon–nucleon collisions. The first is phenomenological: the inclusive cross sections we have measured follow the trends in slope and yield established in measurements above threshold. Secondly, the intranuclear cascade, which is essentially a Monte Carlo simulation folding together the effects of many nucleon–nucleon collisions, describes many of the features of the data. In particular, it is able to reproduce the high energy tails of the pion spectra. Moreover, where the cascade fails to reproduce the data, it fails in a manner similar to its characteristic behavior at

higher energies.

There is also evidence which suggests that mechanisms other than binary production are involved. For example, a statistical model which implicitly assumes that clusters of nucleons cooperate in pion production has had the most success at reproducing the π^- data. Perhaps most importantly, the change in the mass scaling of the pion yield as the beam energy is lowered is not readily interpreted in a nucleon–nucleon framework. However at this time there are too few data points to make any conclusive statements about this effect. Additional measurements of the mass dependence are needed.

Some other features of the data do not directly relate to collective effects, but are interesting in their own right. Charge–dependent structure in the pion spectra echo similar effects in widely disparate interactions above and below threshold. The mid–rapidity peak observed at higher beam energies has not been seen below threshold, but has not been universally observed above threshold, either. Several possible interpretations involving electromagnetic interactions between emitted pions and the charged nucleons are at least qualitatively consistent with our results, as are other, perhaps complementary scenarios involving fragment formation and charge exchange.

The increased yield in the 246 MeV/nucleon La+La π^- cross section at $\theta_{c.m.} = 30°$ is correlated with low associated multiplicity. It is not clear whether this effect is associated with pion creation or merely with pion emission. During pion emission, the enhancement could arise due to Coulomb interactions between the outgoing pion and a high-Z projectile fragment, which would more likely be present in a peripheral (hence low multiplicity) collision. This picture is consistent with the observed angular distribution, as one would expect the effect to be strongest near the beam direction. It is also consistent with the forward angle data of Ref. 72 for Ne+NaF. Thus there should be an even stronger effect at

more forward angles, which were outside the range of our spectrometer. Still another possibility is that of decreased pion absorption associated with a peripheral interaction.

Alternatively, low associated multiplicity does not necessarily mean large impact parameter. If the enhancement does arise during pion creation, one could envision a scenario where a central collision takes place, but with energy channeled into pion creation rather than into dissassembling the target and boosting the target fragments. This does not explain the anisotropy of the effect, however.

There are some other intriguing deviations from purely exponential and isotropic spectra. The most striking of these is probably the discontinuity in the spectrum of π^- from 183 MeV/nucleon La+La collisions, in which isotropy at high energies is coupled with a drastic depletion of low energy pions at $\theta_{c.m.} = 30°$. Unlike the case for the 30° π^- spectrum at 246 MeV/nucleon, this effect is not sensitive to cuts on associated multiplicity. We should also note that the possibility of instrumentation effects cannot be ruled out, although there is no evidence for this in either the raw data or in the records of the data taking.

Suggestions for further experiments

A number of measurements and calculations might be done to amplify and extend the investigations reported in this dissertation. For example,

- A systematic mass and beam energy dependence, taken under consistent experimental conditions to minimize uncertainty due to relative normalization. Ideally, this would be done for all three pion charge states, at beam energies from a few tens of MeV/nucleon to near threshold, over the widest possible range of system masses.

- Improved statistics for π^- production at the lower beam energies, and for π^+ production at all beam energies. This would help nail down possible

deviations from exponential energy dependence and angular isotropy, and would make possible more precise cuts on associated multiplicity.

- A complete angular distribution, especially including forward angles. This would help to resolve the spectral irregularities, in particular those attributed to Coulomb effects. For example, some or all of the deviations from isotropy may involve pions pushed into or removed from a region in phase space which was out of the angular range of our spectrometer.

- Extension of the measurements to the lowest accessible pion energies, for the same reason.

- Measuring π^0 production, for general purposes of comparison with the charged pion spectra, and to establish the relative influence of Coulomb effects and cluster formation on the final–state pion spectra.

- Experimenting with different Fermi distributions within the Cugnon cascade code, in order to study the sensitivity of nucleon–nucleon pion production to assumptions about the internal nucleon momenta.

- Running the latest version of the cascade code, which takes isospin into account, in order to determine how much of the charge–dependent structure might be accounted for in a binary collision model.

Two related experiments, each of which is a full scale study in itself, are:

- Extend the studies of fully coherent pion production (p. 34) by light ions to the much heavier ^{139}La $+^{139}$La system.

- Measure the production of high energy gamma rays from the La+La system. Lately, there has been considerable interest in such measurements (Refs. 168 and 169, and references therein), and a recent Bevalac experiment measured gamma ray production from La+La collisions up to 138

MeV/nucleon beam energy[170]. Gamma rays may probe some of the same processes as do pions[†], while undergoing fewer final state interactions to distort the cross sections. They may also provide complementary information: for example, the multipolarity of the gamma rays (as manifested in their angular distribution) can be used to rule out some modes of interaction[168].

Conclusions

We have taken a considerable amount of data on charged pion production below the free nucleon threshold, at projectile masses and energies where little or no data has previously been recorded. The use of a multiplicity array has made it possible to characterize pion–producing events according to impact parameter, and we have found that, at least for c.m. angles between 30° and 90°, subthreshold pions are produced predominantly in small impact parameter collisions.

The overall picture which has emerged from this study is that, by measuring subthreshold pions produced at moderate to large c.m. angles we are in effect triggering on central collisions, with a large number of participants, which is further enhanced by use of a relatively heavy target and projectile. The large number of interacting nucleons makes it reasonable to think that subthreshold pion production in heavy systems will be promising venue in which to search for collective effects. In studying our results for the La+La system, both by themselves and in comparison them with the results of previous experiments, we have not found conclusive evidence of such effects. However, some aspects of the results do not have a clear interpretation in terms of simple binary (nucleon–nucleon) production, and may be signals that collective effects are beginning to assert themselves above the nucleon–nucleon background. The mass dependence

[†]Stevenson *et al.*[168] have noted that if the gamma ray spectra are extrapolated to the energy equivalent of the pion mass, then gamma and pion spectra are similar

of the pion yield, in particular, falls in this category.

Finally, the discovery of charge–dependent structure in the pion cross sections is interesting in its own right. The combination of a heavy system and small impact parameter may not only make possible collective effects in pion production, but seems also to affect the emitted pion spectra. This may be due to the intense Coulomb field from the large number of charges present, or to effects relating to the large neutron excess in the system, or to a combination of the two. In any case, the final–state interactions which influence the charged pion spectra, if they can be fully understood, may reveal much about the space–time structure of nucleus–nucleus interactions.

Appendix A. Pion Inclusive Cross-Sections (Tables)

These tables contain invariant cross sections for laboratory angles, and variant cross sections for center of mass angles. The variant and invariant cross sections in a given reference frame are related by the expression

$$\sigma_{inv} = E \cdot \sigma_{var}$$

where

$$\begin{aligned} E &= (p_\pi^2 + m_\pi^2)^{\frac{1}{2}} \\ &= T_\pi + m_\pi \end{aligned}$$

The cross sections for $\theta_{c.m.} = 30°$ and $45°$ correspond to $\theta_{lab} = 21°$ and $30°$, respectively. For $\theta_{c.m.} = 60°$ and $90°$, most of the data points are from $\theta_{lab} = 42.5°$ and $67°$, but the first few low momentum (or energy) points are from $\theta_{lab} = 40°$ and $62.5°$, respectively. (See Sec. 4.5.)

Laboratory Cross Sections

$^{139}La + ^{139}La \rightarrow \pi^- + X$

246 MeV/nucleon

$\theta_{lab} = 21°$

p_{lab} (MeV/c)	$\frac{E}{p^2}\frac{d^2\sigma}{dpd\Omega}$ $\left(\frac{mb}{sr-\frac{GeV^2}{c^3}}\right)$
138	5800 ± 800
153	4600 ± 400
172	3600 ± 200
192	2700 ± 200
213	1800 ± 100
233	1400 ± 100
252	910 ± 80
272	640 ± 60
292	380 ± 40
311	300 ± 30
331	170 ± 30
353	120 ± 20
371	80 ± 20
400	40 ± 10
441	14 ± 9

$\theta_{lab} = 30°$

p_{lab} (MeV/c)	$\frac{E}{p^2}\frac{d^2\sigma}{dpd\Omega}$ $\left(\frac{mb}{sr-\frac{GeV^2}{c^3}}\right)$
153	3300 ± 200
173	2300 ± 100
192	1660 ± 80
212	1050 ± 50
232	760 ± 40
252	480 ± 30
272	320 ± 20
292	200 ± 20
312	130 ± 10
332	75 ± 9
351	41 ± 6
372	27 ± 5
390	19 ± 4
411	9 ± 4
444	5 ± 3

$\theta_{lab} = 40°$

p_{lab} (MeV/c)	$\frac{E}{p^2}\frac{d^2\sigma}{dpd\Omega}$ $\left(\frac{mb}{sr-\frac{GeV^2}{c^3}}\right)$
144	4400 ± 400
163	2800 ± 200
183	1700 ± 100
202	1200 ± 100
222	720 ± 70
243	470 ± 50
261	310 ± 40
282	150 ± 30
302	120 ± 20
320	50 ± 10
342	50 ± 10
362	23 ± 9
385	20 ± 10

$\theta_{lab} = 42.5°$

p_{lab} (MeV/c)	$\frac{E}{p^2}\frac{d^2\sigma}{dpd\Omega}$ $\left(\frac{mb}{sr-\frac{GeV^2}{c^3}}\right)$
154	2900 ± 200
172	2000 ± 100
192	1190 ± 80
212	900 ± 60
232	550 ± 40
252	360 ± 30
273	190 ± 20
292	170 ± 20
312	90 ± 10
331	70 ± 11
352	31 ± 7
380	14 ± 4

$\theta_{lab} = 62.5°$

p_{lab} (MeV/c)	$\frac{E}{p^2}\frac{d^2\sigma}{dpd\Omega}$ $\left(\frac{mb}{sr-\frac{GeV^2}{c^3}}\right)$
137	3200 ± 300
153	2100 ± 100
172	1090 ± 60
192	630 ± 40
212	370 ± 30
233	210 ± 20
253	130 ± 10
272	80 ± 9
293	52 ± 7
312	30 ± 5
332	15 ± 4
348	7 ± 3
371	4 ± 2

$\theta_{lab} = 67°$

p_{lab} (MeV/c)	$\frac{E}{p^2}\frac{d^2\sigma}{dpd\Omega}$ $\left(\frac{mb}{sr-\frac{GeV^2}{c^3}}\right)$
153	1790 ± 70
172	1050 ± 40
192	570 ± 20
212	360 ± 10
232	220 ± 10
252	116 ± 7
271	70 ± 5
292	41 ± 3
312	25 ± 3
333	13 ± 2
354	8 ± 1
382	3.3 ± 0.6
417	1.4 ± 0.4

$^{139}La + ^{139}La \rightarrow \pi^+ + X$

246 MeV/nucleon

$\theta_{lab} = 21°$

p_{lab} (MeV/c)	$\frac{E}{p^2}\frac{d^2\sigma}{dpd\Omega}$ $\left(\frac{mb}{sr-\frac{GeV^2}{c^3}}\right)$
158	600 ± 200
188	600 ± 200
218	900 ± 200
247	500 ± 100
277	400 ± 100
307	210 ± 80
336	120 ± 70
379	50 ± 40

$\theta_{lab} = 30°$

p_{lab} (MeV/c)	$\frac{E}{p^2}\frac{d^2\sigma}{dpd\Omega}$ $\left(\frac{mb}{sr-\frac{GeV^2}{c^3}}\right)$
154	900 ± 300
172	1200 ± 300
198	600 ± 200
240	500 ± 100
283	230 ± 80

$\theta_{lab} = 40°$

p_{lab} (MeV/c)	$\frac{E}{p^2}\frac{d^2\sigma}{dpd\Omega}$ $\left(\frac{mb}{sr-\frac{GeV^2}{c^3}}\right)$
153	800 ± 100
180	840 ± 90
204	570 ± 70
230	320 ± 60
254	300 ± 50
280	160 ± 30
309	120 ± 20
351	50 ± 20
388	20 ± 20

$\theta_{lab} = 42.5°$

p_{lab} (MeV/c)	$\frac{E}{p^2}\frac{d^2\sigma}{dpd\Omega}$ $\left(\frac{mb}{sr-\frac{GeV^2}{c^3}}\right)$
155	830 ± 70
174	710 ± 80
192	640 ± 60
212	530 ± 50
232	410 ± 40
252	270 ± 30
277	170 ± 20
305	130 ± 20
336	40 ± 10
367	30 ± 10

$\theta_{lab} = 62.5°$

p_{lab} (MeV/c)	$\frac{E}{p^2}\frac{d^2\sigma}{dpd\Omega}$ $\left(\frac{mb}{sr-\frac{GeV^2}{c^3}}\right)$
148	860 ± 60
177	590 ± 40
206	340 ± 20
235	200 ± 20
265	130 ± 10
294	52 ± 8
327	18 ± 4

$\theta_{lab} = 67°$

p_{lab} (MeV/c)	$\frac{E}{p^2}\frac{d^2\sigma}{dpd\Omega}$ $\left(\frac{mb}{sr-\frac{GeV^2}{c^3}}\right)$
153	760 ± 40
172	590 ± 30
192	440 ± 30
213	270 ± 20
232	180 ± 10
251	110 ± 10
272	80 ± 8
292	52 ± 6
312	32 ± 5
338	10 ± 2
375	3 ± 2

$^{139}La + ^{139}La \rightarrow \pi^- + X$

183 MeV/nucleon

$\theta_{lab} = 21°$		$\theta_{lab} = 42.5°$		$\theta_{lab} = 67°$	
p_{lab}	$\frac{E}{p^2}\frac{d^2\sigma}{dpd\Omega}$	p_{lab}	$\frac{E}{p^2}\frac{d^2\sigma}{dpd\Omega}$	p_{lab}	$\frac{E}{p^2}\frac{d^2\sigma}{dpd\Omega}$
(MeV/c)	$\left(\frac{mb}{sr-\frac{GeV^2}{c^3}}\right)$	(MeV/c)	$\left(\frac{mb}{sr-\frac{GeV^2}{c^3}}\right)$	(MeV/c)	$\left(\frac{mb}{sr-\frac{GeV^2}{c^3}}\right)$
144	800 ± 200	138	1140 ± 100	152	550 ± 30
163	600 ± 100	153	800 ± 40	172	290 ± 20
183	380 ± 90	172	500 ± 20	192	144 ± 8
200	200 ± 60	192	290 ± 10	212	78 ± 5
224	110 ± 40	212	190 ± 10	232	45 ± 4
248	170 ± 40	231	98 ± 7	252	21 ± 2
272	130 ± 30	252	61 ± 5	272	10 ± 1
309	40 ± 20	273	46 ± 4	292	7 ± 1
		292	26 ± 3	311	3.7 ± 0.7
		312	15 ± 2	339	1.2 ± 0.3
		332	6 ± 1		
		354	4.5 ± 0.9		
		389	1.6 ± 0.7		

$^{139}La + ^{139}La \rightarrow \pi^+ + X$

183 MeV/nucleon

$\theta_{lab} = 42.5°$		$\theta_{lab} = 67°$	
p_{lab}	$\frac{E}{p^2}\frac{d^2\sigma}{dpd\Omega}$	p_{lab}	$\frac{E}{p^2}\frac{d^2\sigma}{dpd\Omega}$
(MeV/c)	$\left(\frac{mb}{sr-\frac{GeV^2}{c^3}}\right)$	(MeV/c)	$\left(\frac{mb}{sr-\frac{GeV^2}{c^3}}\right)$
143	270 ± 70	152	110 ± 30
162	180 ± 40	172	70 ± 20
182	190 ± 40	194	60 ± 20
203	130 ± 30	213	30 ± 9
222	140 ± 30	233	33 ± 9
242	120 ± 30	250	46 ± 10
262	60 ± 20	279	15 ± 4
284	50 ± 20		
303	30 ± 10		

$^{139}La + ^{139}La \rightarrow \pi^- + X$

138 MeV/nucleon

$\theta_{lab} = 45°$			$\theta_{lab} = 70°$		
p_{lab}	$\frac{E}{p^2}\frac{d^2\sigma}{dpd\Omega}$		p_{lab}	$\frac{E}{p^2}\frac{d^2\sigma}{dpd\Omega}$	
(MeV/c)	$\left(\frac{mb}{sr-\frac{GeV^2}{c^3}}\right)$		(MeV/c)	$\left(\frac{mb}{sr-\frac{GeV^2}{c^3}}\right)$	
153	170 ±	40	135	140 ±	50
173	50 ±	10	153	60 ±	15
197	28 ±	9	172	27 ±	7
210	21 ±	7	193	8 ±	3
233	18 ±	9	210	3 ±	3
254	13 ±	5			
280	5 ±	3			

$^{139}La + ^{139}La \rightarrow \pi^+ + X$

138 MeV/nucleon

$\theta_{lab} = 70°$

p_{lab}	$\frac{E}{p^2}\frac{d^2\sigma}{dpd\Omega}$	
(MeV/c)	$\left(\frac{mb}{sr-\frac{GeV^2}{c^3}}\right)$	
154	40 ±	10
171	18 ±	6
193	7 ±	3
210	6 ±	3

$^{20}Ne + NaF \rightarrow \pi^- + X$

244 MeV/nucleon

$\theta_{lab} = 21°$		$\theta_{lab} = 42.5°$		$\theta_{lab} = 67°$	
p_{lab}	$\frac{E}{p^2}\frac{d^2\sigma}{dpd\Omega}$	p_{lab}	$\frac{E}{p^2}\frac{d^2\sigma}{dpd\Omega}$	p_{lab}	$\frac{E}{p^2}\frac{d^2\sigma}{dpd\Omega}$
(MeV/c)	$\left(\frac{mb}{sr-\frac{GeV^2}{c^3}}\right)$	(MeV/c)	$\left(\frac{mb}{sr-\frac{GeV^2}{c^3}}\right)$	(MeV/c)	$\left(\frac{mb}{sr-\frac{GeV^2}{c^3}}\right)$
153	140 ± 20	153	118 ± 4	153	70 ± 2
173	120 ± 10	173	84 ± 2	172	41.9 ± 0.8
192	90 ± 9	192	58 ± 2	192	24.5 ± 0.5
212	60 ± 7	212	45 ± 1	212	15.6 ± 0.4
233	58 ± 6	232	27.6 ± 0.9	232	8.8 ± 0.3
252	37 ± 5	252	18.8 ± 0.7	252	5.1 ± 0.2
272	34 ± 4	272	12.4 ± 0.5	272	3.1 ± 0.1
291	28 ± 4	292	6.6 ± 0.3	292	1.83 ± 0.09
313	13 ± 2	311	4.2 ± 0.3	311	0.94 ± 0.06
332	8 ± 2	332	2.8 ± 0.2	331	0.50 ± 0.05
353	5 ± 1	351	1.5 ± 0.1	351	0.31 ± 0.04
373	3 ± 1	371	1.0 ± 0.1	371	0.15 ± 0.02
407	2.0 ± 0.7	392	0.50 ± 0.1	407	0.04 ± 0.01
448	1.4 ± 0.5	410	0.33 ± 0.08	453	0.03 ± 0.01
		433	0.25 ± 0.07		
		458	0.10 ± 0.04		

$^{20}Ne + NaF \rightarrow \pi^{\pm} + X$
800 MeV/nucleon
$\theta_{lab} = 60°$

π^-		π^+	
p_{lab} (MeV/c)	$\frac{E}{p^2}\frac{d^2\sigma}{dpd\Omega}$ $\left(\frac{mb}{sr-\frac{GeV^2}{c^3}}\right)$	p_{lab} (MeV/c)	$\frac{E}{p^2}\frac{d^2\sigma}{dpd\Omega}$ $\left(\frac{mb}{sr-\frac{GeV^2}{c^3}}\right)$
151	1470 ± 30	151	1250 ± 70
170	1200 ± 20	170	1070 ± 50
190	880 ± 20	190	810 ± 30
210	720 ± 10	210	660 ± 30
230	590 ± 10	230	550 ± 20
250	480 ± 10	250	480 ± 20
270	371 ± 8	270	340 ± 20
290	291 ± 7	289	270 ± 10
310	213 ± 5	310	210 ± 10
330	160 ± 5	330	150 ± 10
350	124 ± 4	349	111 ± 9
370	86 ± 3	369	86 ± 7
390	67 ± 3	389	69 ± 7
409	52 ± 3	409	49 ± 5
429	37 ± 2	429	39 ± 5
450	30 ± 2	449	26 ± 4
469	24 ± 2	469	23 ± 4
490	18 ± 1	489	15 ± 3
509	13 ± 1	510	16 ± 3
529	12 ± 1	531	9 ± 2
551	7.1 ± 0.9	550	7 ± 2
570	6.2 ± 0.8	568	7 ± 2
589	3.4 ± 0.6	592	2 ± 1

Center of Mass Cross Sections

$^{139}La + ^{139}La \rightarrow \pi^- + X$

246 MeV/nucleon

$\theta_{c.m.} = 30°$

$T_{c.m.}$ (MeV)	$\frac{1}{p^2}\frac{d^2\sigma}{dpd\Omega}$ $\left(\frac{mb}{sr-\left(\frac{GeV}{c}\right)^3}\right)$
23	36000 ± 5000
29	27000 ± 2000
38	20000 ± 1000
48	14000 ± 1000
59	9300 ± 700
71	6700 ± 500
82	4100 ± 400
94	2700 ± 300
107	1500 ± 200
118	1100 ± 100
131	630 ± 90
145	410 ± 70
157	270 ± 60
176	100 ± 30
204	40 ± 20

$\theta_{c.m.} = 45°$

$T_{c.m.}$ (MeV)	$\frac{1}{p^2}\frac{d^2\sigma}{dpd\Omega}$ $\left(\frac{mb}{sr-\left(\frac{GeV}{c}\right)^3}\right)$
33	19000 ± 1000
43	12400 ± 600
53	8600 ± 400
64	5100 ± 300
76	3500 ± 200
88	2100 ± 100
100	1320 ± 90
113	780 ± 60
126	510 ± 50
140	270 ± 30
153	140 ± 20
166	90 ± 20
179	60 ± 10
194	30 ± 10
217	15 ± 8

$\theta_{c.m.} = 60°$

$T_{c.m.}$ (MeV)	$\frac{1}{p^2}\frac{d^2\sigma}{dpd\Omega}$ $\left(\frac{mb}{sr-\left(\frac{GeV}{c}\right)^3}\right)$
34	26000 ± 3000
43	15000 ± 1000
54	8700 ± 700
66	5900 ± 500
78	3300 ± 300
87	2500 ± 200
100	1500 ± 100
114	740 ± 80
127	630 ± 70
141	330 ± 50
154	220 ± 40
169	100 ± 20
190	40 ± 10

$\theta_{c.m.} = 90°$

$T_{c.m.}$ (MeV)	$\frac{1}{p^2}\frac{d^2\sigma}{dpd\Omega}$ $\left(\frac{mb}{sr-\left(\frac{GeV}{c}\right)^3}\right)$
46	18000 ± 2000
55	10700 ± 600
67	5300 ± 300
86	2510 ± 90
100	1510 ± 60
116	850 ± 40
131	430 ± 20
147	250 ± 20
164	130 ± 10
180	77 ± 8
197	38 ± 5
215	23 ± 4.
239	9 ± 2
269	3 ± 1

$^{139}La + ^{139}La \rightarrow \pi^+ + X$

246 MeV/nucleon

$\theta_{c.m.} = 30°$

$T_{c.m.}$ (MeV)	$\frac{1}{p^2}\frac{d^2\sigma}{dpd\Omega}$ $\left(\frac{mb}{sr-\left(\frac{GeV}{c}\right)^3}\right)$
31	3000 ± 1000
46	3000 ± 1000
62	4500 ± 900
79	2100 ± 600
97	1600 ± 400
116	800 ± 300
134	400 ± 240
162	200 ± 100

$\theta_{c.m.} = 45°$

$T_{c.m.}$ (MeV)	$\frac{1}{p^2}\frac{d^2\sigma}{dpd\Omega}$ $\left(\frac{mb}{sr-\left(\frac{GeV}{c}\right)^3}\right)$
33	5000 ± 2000
42	6000 ± 2000
56	3100 ± 800
81	2400 ± 600
108	900 ± 300

$\theta_{c.m.} = 60°$

$T_{c.m.}$ (MeV)	$\frac{1}{p^2}\frac{d^2\sigma}{dpd\Omega}$ $\left(\frac{mb}{sr-\left(\frac{GeV}{c}\right)^3}\right)$
38	4300 ± 600
53	4400 ± 500
67	2800 ± 400
83	1500 ± 300
100	1140 ± 130
116	650 ± 70
136	460 ± 60
158	130 ± 30
180	100 ± 30

$\theta_{c.m.} = 90°$

$T_{c.m.}$ (MeV)	$\frac{1}{p^2}\frac{d^2\sigma}{dpd\Omega}$ $\left(\frac{mb}{sr-\left(\frac{GeV}{c}\right)^3}\right)$
52	4500 ± 300
70	2800 ± 200
86	2000 ± 100
101	1140 ± 80
116	690 ± 50
131	420 ± 40
147	280 ± 30
164	170 ± 20
180	100 ± 10
202	29 ± 7
234	9 ± 5

$^{139}La + ^{139}La \rightarrow \pi^- + X$

183 MeV/nucleon

$\theta_{c.m.} = 30°$

$T_{c.m.}$ (MeV)	$\frac{1}{p^2}\frac{d^2\sigma}{dpd\Omega}$ $\left(\frac{mb}{sr-\left(\frac{GeV}{c}\right)^3}\right)$	
29	5000 ±	1000
38	3400 ±	800
48	2000 ±	500
58	1100 ±	300
72	500 ±	200
86	700 ±	200
101	500 ±	100
126	150 ±	80

$\theta_{c.m.} = 60°$

$T_{c.m.}$ (MeV)	$\frac{1}{p^2}\frac{d^2\sigma}{dpd\Omega}$ $\left(\frac{mb}{sr-\left(\frac{GeV}{c}\right)^3}\right)$	
34	6600 ±	600
42	4400 ±	200
53	2600 ±	100
65	1410 ±	70
77	880 ±	50
90	430 ±	30
104	250 ±	20
118	180 ±	20
132	90 ±	10
146	51 ±	7
161	19 ±	4
178	14 ±	3
203	5 ±	2

$\theta_{c.m.} = 90°$

$T_{c.m.}$ (MeV)	$\frac{1}{p^2}\frac{d^2\sigma}{dpd\Omega}$ $\left(\frac{mb}{sr-\left(\frac{GeV}{c}\right)^3}\right)$	
59	2770 ±	140
72	1380 ±	70
86	640 ±	40
100	330 ±	20
116	170 ±	10
132	78 ±	8
148	36 ±	5
164	23 ±	4
180	12 ±	2
204	3.6 ±	0.9

$^{139}La + ^{139}La \rightarrow \pi^+ + X$

183 MeV/nucleon

$\theta_{c.m.} = 60°$

$T_{c.m.}$ (MeV)	$\frac{1}{p^2}\frac{d^2\sigma}{dpd\Omega}$ $\left(\frac{mb}{sr-\left(\frac{GeV}{c}\right)^3}\right)$	
37	1500 ±	400
47	1000 ±	200
59	900 ±	200
71	600 ±	200
84	600 ±	100
97	500 ±	100
111	230 ±	90
126	190 ±	70
140	110 ±	40

$\theta_{c.m.} = 90°$

$T_{c.m.}$ (MeV)	$\frac{1}{p^2}\frac{d^2\sigma}{dpd\Omega}$ $\left(\frac{mb}{sr-\left(\frac{GeV}{c}\right)^3}\right)$	
58	600 ±	100
72	340 ±	80
87	270 ±	70
102	120 ±	40
117	130 ±	40
130	170 ±	40
153	50 ±	20

$^{139}La + ^{139}La \rightarrow \pi^- + X$

138 MeV/nucleon

$\theta_{c.m.} = 60°$			$\theta_{c.m.} = 90°$		
$T_{c.m.}$	$\frac{1}{p^2}\frac{d^2\sigma}{dpd\Omega}$		$T_{c.m.}$	$\frac{1}{p^2}\frac{d^2\sigma}{dpd\Omega}$	
(MeV)	$\left(\frac{mb}{sr-\left(\frac{GeV}{c}\right)^3}\right)$		(MeV)	$\left(\frac{mb}{sr-\left(\frac{GeV}{c}\right)^3}\right)$	
46	900 ±	200	49	700 ±	300
57	260 ±	70	61	300 ±	80
73	130 ±	40	74	130 ±	40
82	100 ±	30	90	40 ±	10
97	70 ±	40	102	10 ±	10
113	50 ±	20			
131	20 ±	10			

$^{139}La + ^{139}La \rightarrow \pi^+ + X$

138 MeV/nucleon

$\theta_{c.m.} = 90°$

$T_{c.m.}$	$\frac{1}{p^2}\frac{d^2\sigma}{dpd\Omega}$	
(MeV)	$\left(\frac{mb}{sr-\left(\frac{GeV}{c}\right)^3}\right)$	
61	200 ±	70
74	80 ±	30
89	30 ±	10
102	20 ±	10

$^{20}Ne + NaF \rightarrow \pi^- + X$

244 MeV/nucleon

$\theta_{c.m.} = 30°$			$\theta_{c.m.} = 60°$			$\theta_{c.m.} = 90°$		
$T_{c.m.}$	$\frac{1}{p^2}\frac{d^2\sigma}{dpd\Omega}$		$T_{c.m.}$	$\frac{1}{p^2}\frac{d^2\sigma}{dpd\Omega}$		$T_{c.m.}$	$\frac{1}{p^2}\frac{d^2\sigma}{dpd\Omega}$	
(MeV)	$\left(\frac{mb}{sr-\left(\frac{GeV}{c}\right)^3}\right)$		(MeV)	$\left(\frac{mb}{sr-\left(\frac{GeV}{c}\right)^3}\right)$		(MeV)	$\left(\frac{mb}{sr-\left(\frac{GeV}{c}\right)^3}\right)$	
29	800 ±	100	40	660 ±	20	59	353 ±	8
39	650 ±	70	50	440 ±	10	72	198 ±	4
49	480 ±	50	62	289 ±	8	86	109 ±	2
59	300 ±	30	74	209 ±	6	100	65 ±	2
71	280 ±	30	86	123 ±	4	116	34.9 ±	0.9
82	170 ±	20	99	79 ±	3	131	19.0 ±	0.6
94	140 ±	20	113	49 ±	2	147	10.8 ±	0.4
106	120 ±	10	126	25 ±	1	164	6.0 ±	0.3
119	50 ±	9	140	15 ±	1	179	2.9 ±	0.2
132	30 ±	7	155	9.4 ±	0.8	196	1.5 ±	0.1
145	17 ±	5	168	4.7 ±	0.5	213	0.9 ±	0.1
158	12 ±	4	183	3.2 ±	0.4	229	0.40 ±	0.07
181	6 ±	2	198	1.6 ±	0.3	261	0.10 ±	0.02
209	4 ±	2	211	0.9 ±	0.2	301	0.07 ±	0.02
			229	0.7 ±	0.2			
			247	0.3 ±	0.1			

Appendix B. Associated Multiplicity Distributions

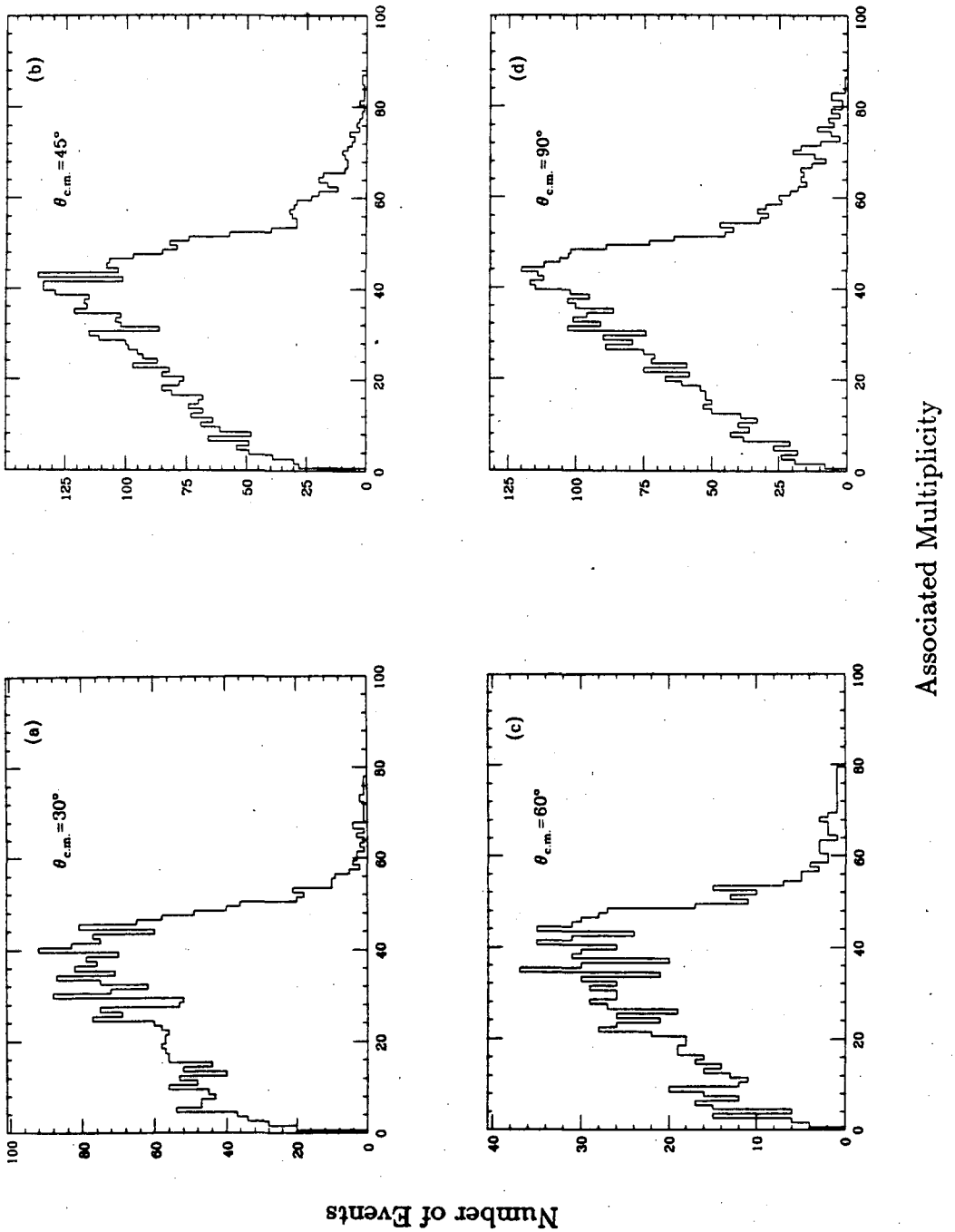

Figure B.1. Associated multiplicities for charged particles from the reaction 246 MeV/nucleon ^{139}La $+^{139}$La $\rightarrow \pi^- + X$ at $\theta_{c.m.}$ = a) 30°, b) 45°, c) 60°, d) 90°.

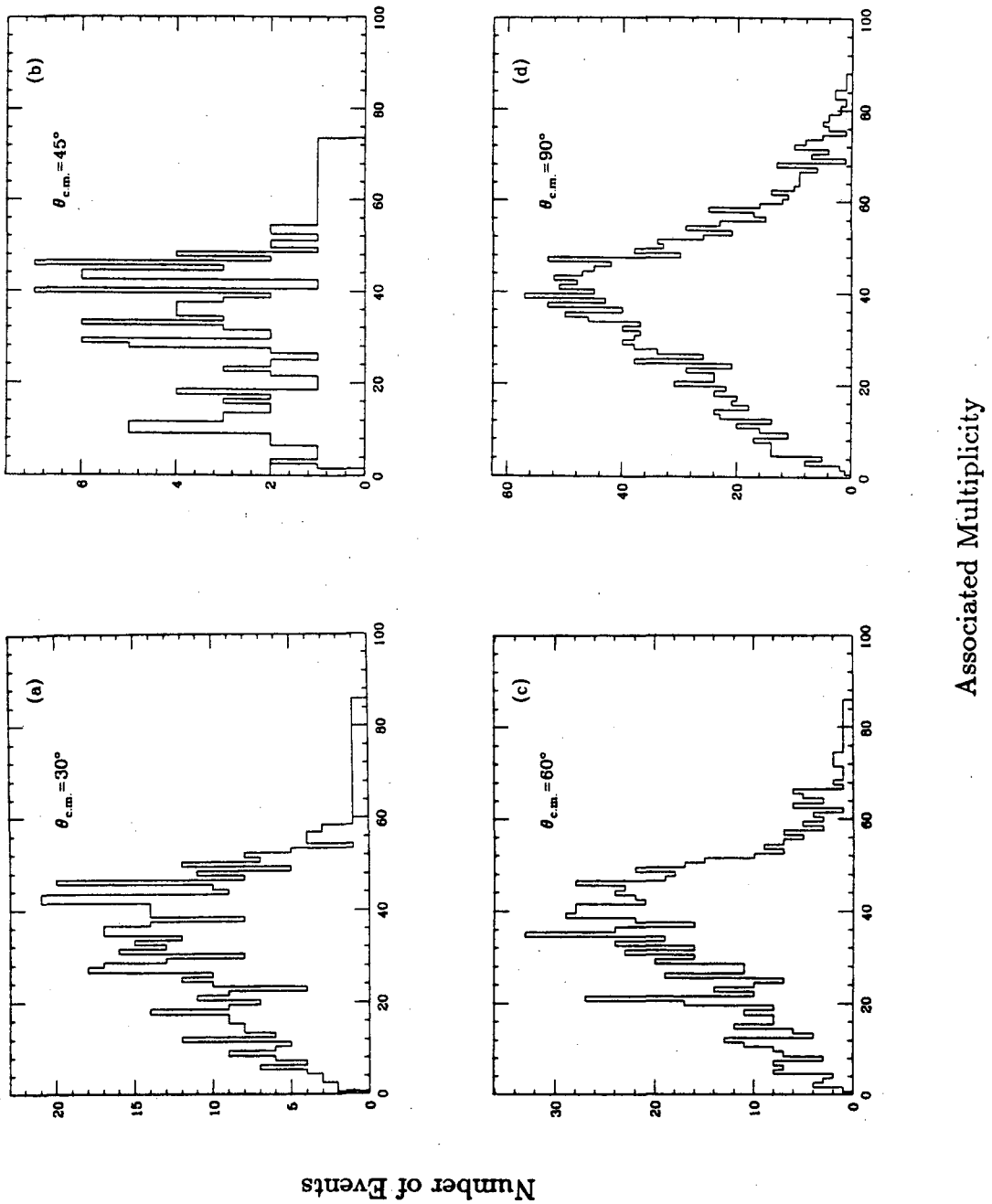

Figure B.2. Associated multiplicities for charged particles from the reaction 246 MeV/nucleon ^{139}La $+^{139}$La $\rightarrow \pi^+ + X$ at $\theta_{c.m.}$ = a) 30°, b) 45°, c) 60°, d) 90°.

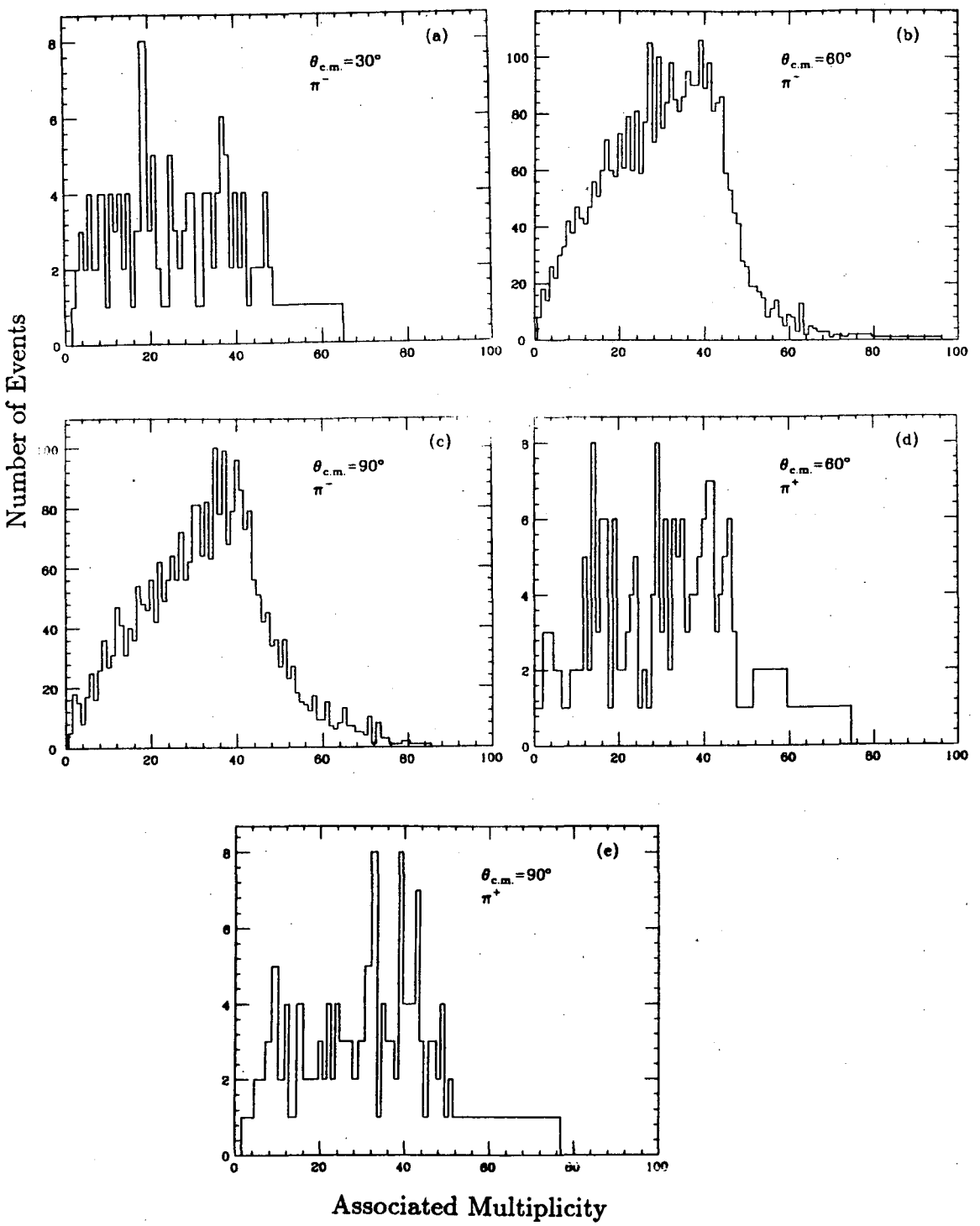

Figure B.3. Associated multiplicities for charged particles from the reaction 183 MeV/nucleon ^{139}La + ^{139}La $\rightarrow \pi^{\pm} + X$ at $\theta_{c.m.}$ = a) 30°, π^- b) 60°, π^- c) 90°, π^- d) 60°, π^+ e) 90°, π^+ .

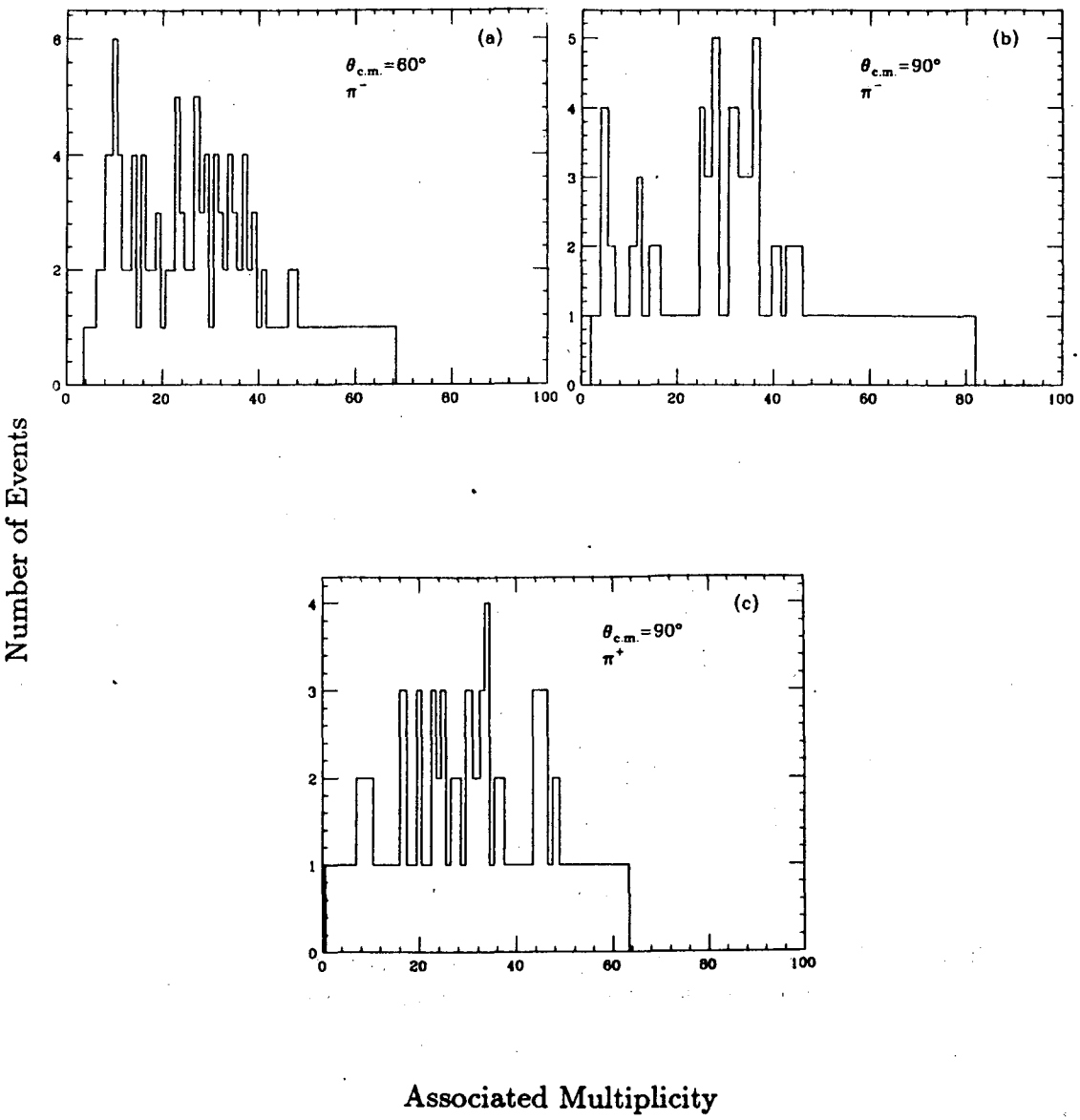

Figure B.4. Associated multiplicities for charged particles from the reaction 138 MeV/nucleon ^{139}La +^{139}La $\rightarrow \pi^{\pm} + X$ at $\theta_{c.m.}$ = a) 60°, π^- b) 90°, π^- c) 90°, π^+ .

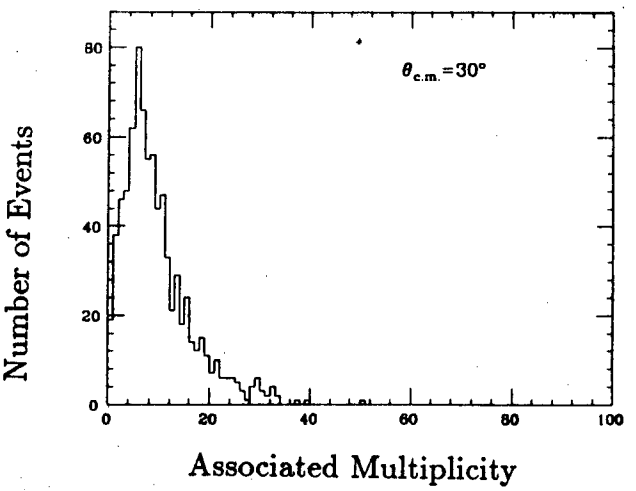

Figure B.5. Associated multiplicity for charged particles from the reaction 244 MeV/nucleon $^{20}\mathrm{Ne} + \mathrm{NaF} \rightarrow \pi^- + X$ at $\theta_{c.m.} = 30°$.

Appendix C. Raw Pion Data

This table summarizes the pion data taking. The number of pions per beam ion, when normalized by the computer live time, beam intensity, target thickness and spectrometer acceptance can be used to estimate the raw pion data rates for a comparable experiment. The rates are of course also sensitive to the target and projectile mass, with a scaling factor of at least $A_{tgt}^{\frac{2}{3}} \cdot A_{proj}^{\frac{2}{3}}$, as discussed in Chapter 5.

T_{beam} (MeV/N)	θ_{lab}		Run times (hrs:min)	Number of ions ($\times 10^{10}$)	Computer live time	Number of pions
La+La	21°	π^-	4:32	.67	.73	3115
246		π^+	3:59	.77	.56	911
	30°	π^-	2:02	2.2	.69	4903
		π^+	0:18	.42	.35	214
	40°	π^-	1:15	.30	.93	1106
		π^+	0:47	.97	.72	662
	42°	π^-	5:00	.62	.99	2060
		π^+	4:09	3.0	.80	1848
	62°	π^-	1:02	1.2	.97	2158
		π^+	3:47	3.0	.94	1355
	67°	π^-	4:28	4.4	.99	6442
		π^+	5:42	6.4	.97	2553
183	21°	π^-	2:09	.23	.94	146
	42°	π^-	5:16	5.5	.87	3289
		π^+	1:38	9.9	.95	252
	67°	π^-	6:01	6.6	.99	2851
		π^+	1:37	2.0	.99	154
138	45°	π^-	2:15	1.1	.98	105
	70°	π^-	3:57	2.2	.99	74
		π^+	2:34	2.3	.94	65
Ne+NaF	21°	π^-	0:32	0.7	.60	806
244	42°	π^-	1:11	12.	.75	9243
	67°	π^-	1:23	52.	.69	17474
800	60°	π^-	0:21	2.6	.48	29550
		π^+	0:15	.74	.31	5377

Appendix D. Detector Specifications

D.1 Spectrometer Coordinate System

The spectrometer coordinate system was as follows:

The origin is at the center of the magnet pole gap. The z-axis is along the long axis of the magnet, with positive z defined to be in the direction looking from the target towards the spectrometer. Positive x is to the right, as one looks from the target towards the magnet. Positive y is down. (i.e. a right handed coordinate system.) All detector planes are parallel to the pole gap. (Normal to the z-axis.) The line from the target to the magnet center makes an angle of 13.134 degrees with the negative z-axis. A particle coming in along this line is defined to have zero entrance angle.

D.2 Counter Locations

Fig. D.1 shows the layout of the counters. The locations are given in Table D.1. All counters were centered at y=0.

D.3 Scintillation Counters

The scintillation counters were constructed from "Pilot B" plastic and had the following dimensions:

Counter No.	No. of Elements	Dimensions (each element) (cm) width	height	thickness
G1	1	5.08	3.81	0.64 (1/4″)
G2	5	2.54	7.62	0.32 (1/8″)
G3	6	55.6	8.89	1.27 (1/2″)

G2 was segmented vertically, G3 horizontally. Each element was optically connected to a single photomultiplier tube, except for G3, which had pmt's on each end.

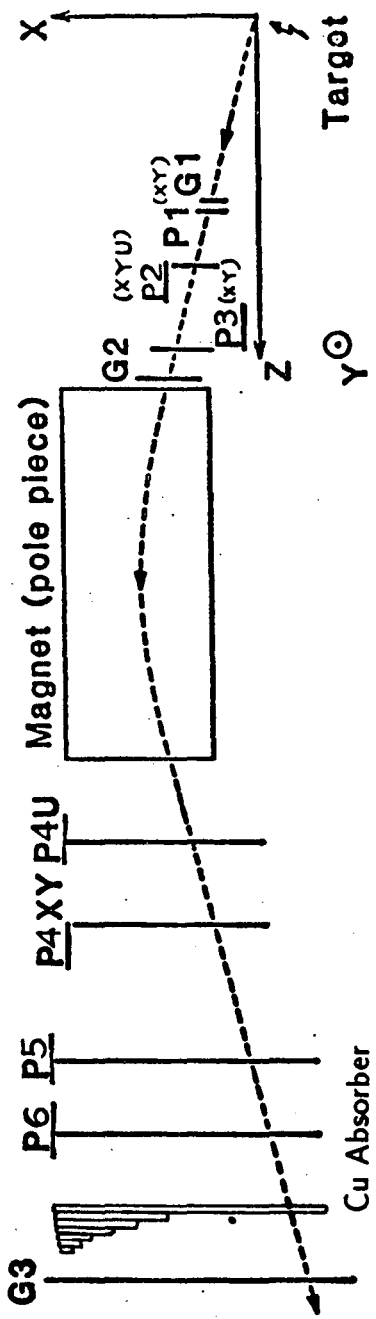

Figure D.1. Layout of the spectrometer magnet and detectors

Counter No.	Location (counter center) (cm) z	x
Target	-114.3	40.
G1	-76.	-17.6
P1X	-74.2	-17.6
P1Y	-73.	-17.6
P2U	-60.5	-15.3
P2Y	-59.5	-15.3
P2X	-58.5	-15.3
P3X	-46.2	-11.4
P3Y	-44.1	-11.4
G2	-42.0	-11.
Mag. Ent.	-35.2	0.
Mag. Exit	35.2	0.
P4U	66.5	-10.9
P4Y	72.1	-10.9
P4X	73.4	-10.9
P5X	99.8	-10.7
P6X	116.6	-10.6
G3	134.6	-11.4

Table D.1. Counter locations

D.4 Wire Chambers

There were six wire chambers, P1–P6, with a total of twelve wire planes, oriented as follows:

MWPC	Number of Wires	Wire Spacing (mm)
P1X	64	1
P1Y	64	1
P2U	128	1.5
P2Y	64	2
P2X	64	2
P3X	64	2
P3Y	64	2
P4U	136	3
P4Y	112	2
P4X	256	2
P5X	256	2
P6X	256	2

The "X" planes had vertical wires, and therefore measured horizontal position. The "U" planes were tilted at 45° with respect to X and Y. The chambers were filled with "magic" gas (4.0% methylal, 23.52% isobutane, either 0.2% or 0.48% (P4U only) Freon and the balance Argon).

D.5 Multiplicity Array

Fig. D.2 gives the specifications of the three sizes of array elements (one for each ring).

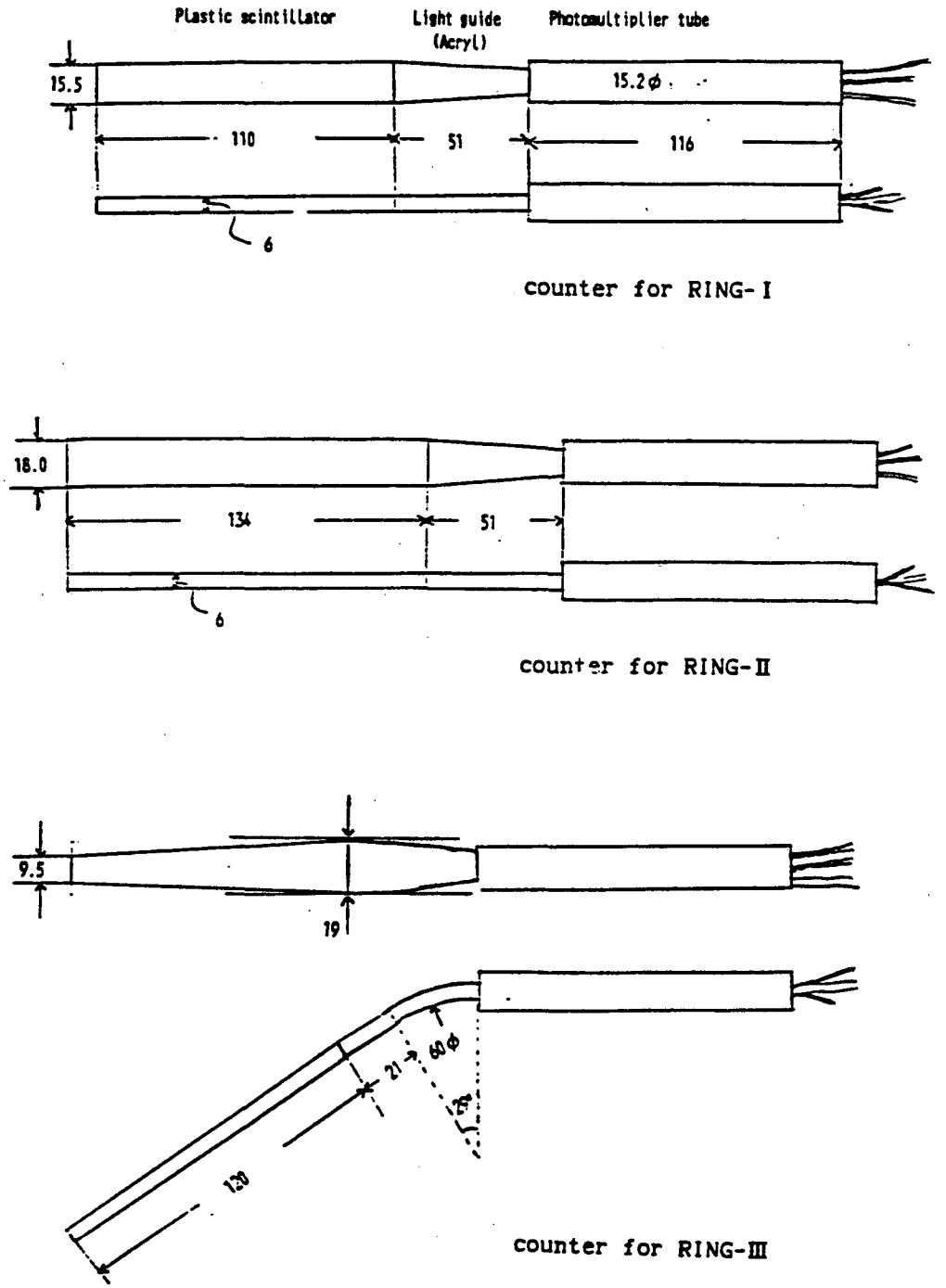

Figure D.2. Multiplicity array element specifications. Dimensions are in cm. (From Ref. 128.)

Appendix E. Definitions and Kinematics

Rapidity

For a particle with total energy, E, and longitudinal momentum, $p_{\parallel}$, the rapidity, y, is defined as

$$y = \frac{1}{2}\ln\left(\frac{E + p_{\parallel}}{E - p_{\parallel}}\right)$$

The rapidity has the advantage that under a Lorentz boost to a frame with velocity β with respect to the lab, it undergoes a simple linear transformation:

$$y' = y + \Delta$$

where $\Delta = \tanh^{-1}\beta$. Consequently, distributions taken with respect to rapidity do not change shape under a Lorentz transformation; they simply undergo a translation along the y-axis. Rapidity is sometimes thought of as a relativistic velocity variable.

Cross Sections

The *variant* cross section is

$$\frac{d^3\sigma}{dp^3} = \frac{1}{p^2}\frac{d^2\sigma}{dpd\Omega}$$

The ***invariant*** cross section is

$$E\frac{d^3\sigma}{dp^3} = \frac{E}{p^2}\frac{d^2\sigma}{dpd\Omega}$$

The invariant cross section is invariant under a Lorentz transformation.

The Lorentz transform of the variant cross section is

$$\frac{d^3\sigma'}{dp'^3} = \frac{E}{E'}\frac{d^3\sigma}{dp^3}$$

Calculation of rigidity, p/Z, from bend angle

Start with the simple expression for the centripetal force acting on a charged particle in a magnetic field:

$$\frac{mv^2}{\rho}\hat{\rho} = q\mathbf{v} \times \mathbf{B}$$

where m, q and v are the particle mass, charge and velocity, ρ is the radius of curvature and $\mathbf{B}$ is the magnetic induction. Then, for motion normal to the field lines,

$$\frac{p}{q} = \rho B$$

where $\rho = l/(\sin\theta_{in} + \sin\theta_{out})$, with $l \equiv$ the length of the magnetic field traversed by the particle (Fig. E.1). Applying the appropriate conversion factors to get p/Z (in MeV/c per unit charge)† from B (kG), l (cm) and q (coul) gives

$$\frac{p}{Z} = \frac{0.3 \cdot l \cdot B}{(\sin\theta_{in} + \sin\theta_{out})}$$

(See Fig. E.1.)

† $Z = q/e$ is the particle charge in units of e, the charge of the electron.

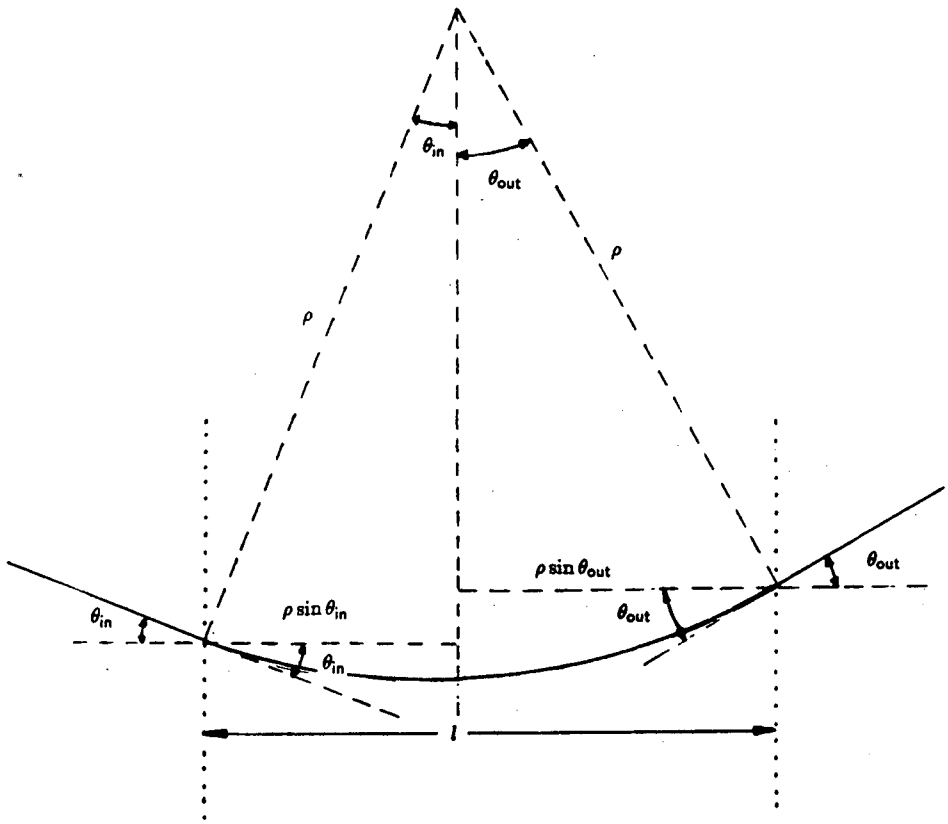

Figure E.1. The solid line represents the particle trajectory, where the particle is moving from left to right. The dotted lines delimit the magnetic field. (The field lines are normal to the page.)

Appendix F. The Cugnon Cascade

Here, we outline some of the important features of the "Cugnon" cascade. (The cascade calculation is discussed in detail in Refs. 147-149.)

- a nuclear radius of $1.12A^{\frac{1}{3}}$.

- nucleon initial positions $\mathbf{r}_{12}$ and momenta $\mathbf{p}$ assigned randomly according to a Fermi gas law with $p_f = 270$ MeV/c.

- complete isospin degeneracy

- scattering occurs when

$$\mathbf{r}_{12} < \left(\frac{\sigma_{tot}(\sqrt{s})}{\pi}\right)^{\frac{1}{2}},$$

  where $\sigma_{tot}(\sqrt{s}) \equiv$ total NN cross section at $T_{c.m.} = \sqrt{s}$. Whether the interaction is elastic or inelastic is determined randomly according to the experimental values of σ_{el} and σ_{inel} at $\sqrt{s}$.

- inelastic NN scattering is assumed to proceed through the $\Delta(1232)$ and to be dominated by pion production. The allowed reactions are:

(a) $N + N \rightarrow N + N$	(elastic)	expt'l. pp_{el}
(b) $N + N \rightarrow N + \Delta$	(inelastic)	expt'l. pp_{inel}
(c) $N + \Delta \rightarrow N + \Delta$	(elastic)	(same as (a))
(d) $N + \Delta \rightarrow N + N$	(inelastic)	(same as (b))
(e) $\Delta + \Delta \rightarrow \Delta + \Delta$	(elastic)	(same as (a))

The following features are of particular relevance to pion production:

- the Δ production is taken to be isotropic.

- the Δ mass is chosen according to a lorentzian distribution centered at 1232 MeV and with a width, Γ, of 112 MeV, truncated at the pion threshold.

- the Δ lifetime is determined by the decay law $e^{-\Gamma\tau}$, where τ is the proper time of the resonance.

- the decay to a nucleon and a pion is isotropic in the Δ rest frame.

- the pion is allowed to propagate freely in the nuclear medium. Pion absorption by a nucleon (with resulting Δ production) occurs when the distance between the pion and a nucleon becomes less than a distance $d = \sqrt{\sigma/\pi}$, where σ is obtained from a fit to the experimental formation cross section for the Δ resonance.

Corrections for isospin

Two of the principal assumptions of the INC are (i) that of complete isospin degeneracy of nucleons and (ii) that inelastic nucleon-nucleon scattering proceeds through the $\Delta(1232)$ resonance, which is also the mechanism for pion production in this model.

Assumption (i) makes the cascade inappropriate for estimating relative yields within a family of particles; assumptions (i) and (ii) will affect the total yield, as well. Consequently it is useful to study how the pion yield as predicted by the cascade is modified by the inclusion of isospin.

Pion production in the cascade proceeds via the "generic" two-stage process:

$$\mathrm{N} + \mathrm{N} \rightarrow \mathrm{N} + \Delta$$
$$\Delta \rightarrow \pi + \mathrm{N}$$

With the inclusion of isospin, the nucleon(N), delta and pion become the multiplets (p,n), $(\Delta^{++}, \Delta^{+}, \Delta^{0}, \Delta^{-})$ and $(\pi^{+}, \pi^{0}, \pi^{-})$, respectively. Each initial nucleon-nucleon state can form either of two possible delta charge states. The Δ^{+} and Δ^{0} each have two possible decay modes. Finally, the isospins in the *pn* initial state can sum with equal probability to total isospin 1 or 0; however only

the I=1 state can form a delta. Combining Clebsch-Gordan coefficients for the possible combinations of states gives the relative probabilities for finding each type of pion in the final state. (See Table F.1.) Note that the total probability

$$
\begin{aligned}
pp \rightarrow \pi^+ pn &: \tfrac{5}{6} \\
pp \rightarrow \pi^0 pp &: \tfrac{1}{6} \\
pn \rightarrow \pi^+ nn &: \tfrac{1}{12} \\
pn \rightarrow \pi^0 pn &: \tfrac{1}{3} \\
pn \rightarrow \pi^- pp &: \tfrac{1}{12} \\
nn \rightarrow \pi^0 nn &: \tfrac{1}{6} \\
nn \rightarrow \pi^- pn &: \tfrac{5}{6}
\end{aligned}
$$

Table F.1. Probabilities for various initial states to produce a final state pion

for a pn initial state to produce a pion is one half that of a pp or nn initial state. The overestimate in the number of pn initial states which can produce a delta will lead to an overestimate of up to 33% in the total pion yield. (This is an upper limit; due to delta and pion reabsorption, not every delta will yield a final-state pion.)

To obtain the relative probability that a given type of pion will be found in the final state, the probabilities in Table F.1 are weighted by the probability for each NN initial state to be formed in the nucleus-nucleus collision. These are, for a target projectile combination $A_1(Z_1, N_1) + A_2(Z_2, N_2)$:

$$pp : (\tfrac{Z_1}{A_1})(\tfrac{Z_2}{A_2})$$

$$nn : (\tfrac{N_1}{A_1})(\tfrac{N_2}{A_2})$$

$$pn : (\tfrac{Z_1}{A_1})(\tfrac{N_2}{A_2}) + (\tfrac{Z_2}{A_2})(\tfrac{N_1}{A_1})$$

For a symmetric system with $N = Z$, each type of pion will be equally represented, although correcting the overestimate in the probability of the reaction

$pn \rightarrow \Delta NN$ will reduce the total yield to 75% of the cascade prediction. For $N > Z$, however, there will be an enhancement in yields of π^- and π^0 over that of π^+. In the case of ^{139}La $+^{139}$La (82 neutrons and 57 protons), the isospin-corrected pion yields (expressed as percentages of the total pion yield predicted by the cascade) are 18% π^+, 25% π^0, 33% π^-. Note that the total yield in this case is 76% of the cascade result.(The correction to the total yield varies weakly with neutron excess.) The isospin-corrected ratio $\frac{\pi^+}{\pi^-} = \frac{.18}{.33} = 55\%$.

References

[1] Emilio Segre. *Nuclei and Particles.* Benjamin/Cummings, 1980. pp. 236-240.

[2] H.A. Gustafsson, et al. *Phys. Rev. Lett.* **52**, 1590 (1984).

[3] R.E. Renfordt, et al. *Phys. Rev. Lett.* **53**, 763 (1984).

[4] R. Stock, et al. *Phys. Rev. Lett.* **49**, 1236 (1982).

[5] J.W. Harris, et al. *Phys. Rev. Lett.* **58**, 463 (1987).

[6] O. Scholten, H. Kruse and W.A. Friedman. *Phys. Rev.* **C26**, 1339 (1982).

[7] Y. Kitazoe, et al. *Phys. Rev.* **C29**, 828 (1984).

[8] Y. Kitazoe, et al. *Phys. Rev. Lett.* **53**, 2000 (1984).

[9] Y. Kitazoe, et al. *Phys. Rev. Lett.* **58**, 1508 (1987).

[10] R. Madey, et al. *Phys. Rev.* **C34**, 1342 (1986).

[11] M. Gyulassy. *Nucl. Phys.* **A354**, 395c (1981).

[12] S. Nagamiya et al. *Phys. Rev. Lett.* **48**, 1780 (1982).

[13] G.F. Krebs et al. *Phys. Lett.* **B171**, 37 (1986).

[14] S. Nagamiya and M. Gyulassy. *Adv. Nucl. Phys.* **13**, 201 (1984).

[15] Review of Particle Properties. *Phys. Lett.* **170B**, 1 (1986).

[16] H. Yukawa. *Proc. Phys. Math. Soc. of Japan* **17**, 48 (1935).

[17] C.M.G. Lattes, G.P.S. Occhialini and C.F. Powell. *Nature* **160**, 453 (1947).

[18] Eugene Gardner and C.M.G. Lattes. *Science* **107**, 270 (1948).

[19] John Burfening, Eugene Gardner and C.M.G. Lattes. *Phys. Rev.* **75**, 382 (1949).

[20] W.G. McMillan and E. Teller. *Phys. Rev.* **72**, 1 (1947).

[21] Kenneth M. Watson and Keith A. Brueckner. *Phys. Rev.* **83**, 1 (1951).

[22] M. Gell-Mann and K.M. Watson. *Ann. Rev. Nucl. Sci.* **4**, 219 (1954).

[23] A.H. Rosenfeld. *Phys. Rev.* **96**, 139 (1954).

[24] L.C.L. Yuan and S.J. Lindenbaum. *Phys. Rev.* **103**, 404 (1956).

[25] S.J. Lindenbaum and R.M. Sternheimer. *Phys. Rev.* **105**, 1874 (1957).

[26] S. Mandelstam. *Proc. Roy. Soc. (London)* **244**, 491 (1958).

[27] Yu.D. Prokoshkin and A.A. Tyapkin. *J. Exptl. Theoret. Phys. (U.S.S.R.)* **32**, 750 (1957) (Soviet Physics JETP **5**, 618 (1957)).

[28] A.F. Dunaitsev and Yu.D. Prokoshkin. *J. Exptl. Theoret. Phys. (U.S.S.R.)* **36**, 1656 (1959) (Soviet Physics JETP **9**, 1179 (1959)).

[29] A.F. Dunaitsev and Yu.D. Prokoshkin. *J. Exptl. Theoret. Phys. (U.S.S.R.)* **38**, 747 (1960) (Soviet Physics JETP **11**, 540 (1960)).

[30] D.R.F. Cochran et al. *Phys. Rev.* **D6**, 3085 (1972).

[31] J. Hudomalj-Gabitzsch et al. *Phys. Rev.* **C18**, 2666 (1978).

[32] J.F. Crawford et al. *Phys. Rev.* **C22**, 1184 (1980).

[33] M.E. Schillaci and R.R. Silbar. *Phys. Rev.* **D2**, 1220 (1970).

[34] S. Passman, M.M. Block and W.W. Havens, Jr. *Phys. Rev.* **88**, 1247 (1952).

[35] E. Fermi. *Prog. Theor. Phys.* **5**, 570 (1950).

[36] C. Guet and M. Prakash. *Nucl. Phys.* **A428**, 119 (1984).

[37] D.C. Peaslee. *Phys. Rev.* **103**, 404 and **95**, 1580 (1954).

[38] Yu.D. Prokoshkin. *J. Exptl. Theoret. Phys. (U.S.S.R.)* **38**, 455 (1960) (Soviet Physics JETP **11**, 334 (1960)).

[39] Yu.D. Prokoshkin and A.A. Tyapkin. *J. Exptl. Theoret. Phys. (U.S.S.R.)* **33**, 313 (1957) (Soviet Physics JETP **6**, 245 (1958)).

[40] A.F. Dunaitsev and Yu.D. Prokoshkin. *Nucl. Phys.* **56**, 300 (1964).

[41] N.J. DiGiacomo et al. *Phys. Rev.* **C31**, 292 (1985).

[42] L. Bimbot et al. *Nucl. Phys.* **A440**, 636 (1985).

[43] M.M. Sternheim and R.R. Silbar. *Phys. Rev.* **D6**, 3117 (1972).

[44] D.A. Sparrow, M.M. Sternheim and R.R. Silbar. *Phys. Rev.* **C10**, 2215 (1974).

[45] H.W. Fearing. *Prog. Part. Nucl. Phys.* **7**, 113 (1981).

[46] R.E. Marrs, R.E. Pollock and W.W. Jacobs. *Phys. Rev.* **C20**, 2308 (1979).

[47] R.E. Marrs and R.E. Pollock. *Phys. Rev.* **C20**, 2446 (1979).

[48] J.L. Clark et al. *Phys. Rev.* **C26**, 2073 (1982).

[49] D.G. Long, M.M. Sternheim and R.R. Silbar. *Phys. Rev.* **C26**, 586 (1982).

[50] F.F. Guber et al. *Pis'ma Zh. Exsp. Teor. Fiz.* **31**, 696 (1980) (JETP Lett. **31**, 656 (1980)).

[51] Yu.K. Akimov et al. *Yad. Fiz.* **33**, 33 (1981) (Sov. J. Nucl. Phys. **33**, 17 (1981)).

[52] V.A. Krasnov et al. *Phys. Lett.* **108B**, 11 (1982).

[53] S. Nagamiya et al. *J. Phys. Soc. Jpn. Suppl.* **44**, 378 (1978).

[54] K.L. Wolf et al. *Phys. Rev. Lett.* **42**, 1448 (1979).

[55] J. Chiba et al. *Phys. Rev.* **C20**, 1332 (1979).

[56] K. Nakai et al. *Phys. Rev.* **C20**, 2210 (1979).

[57] S. Nagamiya et al. *Phys. Rev.* **C24**, 971 (1981).

[58] K.A. Frankel et al. *Phys. Rev.* **C25**, 1102 (1982).

[59] J.P. Sullivan et al. *Phys. Rev.* **C25**, 1499 (1982).

[60] J.W. Harris et al. *Nuclear Science Division, Annual Report 1983-1984.* Technical Report LBL-18635, Lawrence Berkeley Laboratory, May 1985. p.108.

[61] K.A. Frankel et al. *Phys. Rev.* **C32**, 975 (1985).

[62] S. Hayashi, private communication.

[63] S.Y. Fung et al. *Phys. Rev. Lett.* **40**, 292 (1978).

[64] R. Brockmann et al. *Phys. Rev. Lett.* **53**, 2012 (1984).

[65] J.W. Harris et al. *Phys. Lett.* **153B**, 377 (1985).

[66] W. DeJarnette et al. *Phys. Lett.* **94B**, 327 (1980).

[67] T. Hallman et al. *Nucl. Phys.* **A440**, 697 (1985).

[68] J. Papp et al. *Phys. Rev. Lett.* **34**, 601 (1975).

[69] James Papp. *Single Particle Inclusive Spectra Resulting from the Collision of Relativistic Protons, Deuterons, Alpha Particles and Carbon Ions with Nuclei.* PhD thesis, University of California, Berkeley, May 1975. LBL-3633.

[70] L.S. Schroeder et al. *Phys. Rev. Lett.* **43**, 1787 (1979).

[71] S.A. Chessin. *Pion Production at* 180° *in Nucleus-Nucleus Collisions.* PhD thesis, University of California, Berkeley, May 1983. LBL-14262.

[72] W. Benenson et al. *Phys. Rev. Lett.* **43**, 683 (1979) and **44**, 54 (1980).

[73] J. Hüfner and J. Knoll. *Nucl. Phys.* **A290**, 460 (1977).

[74] G.F. Chapline, M.H. Johnson, E. Teller and M.S. Weiss. *Phys. Rev.* **D8**, 4302 (1973).

[75] G.D. Westfall et al. *Phys. Rev. Lett.* **37**, 1202 (1976).

[76] J.I. Kapusta. *Phys. Rev.* **C16**, 1493 (1977).

[77] W.D. Myers. *Nucl. Phys.* **A296**, 177 (1978).

[78] J. Gosset, J.I. Kapusta and G.D. Westfall. *Phys. Rev.* **C18**, 844 (1978).

[79] Philip J. Siemens and John O. Rasmussen. *Phys. Rev. Lett.* **42**, 880 (1979).

[80] Jörn Knoll. *Phys. Rev.* **C20**, 773 (1979).

[81] Steffen Bohrmann and Jörn Knoll. *Nucl. Phys.* **A356**, 498 (1981).

[82] A.A. Amsden, F.H. Harlow and J.R. Nix. *Phys. Rev.* **C15**, 2059 (1977).

[83] J.I. Kapusta and D. Strottman. *Phys. Rev.* **C23**, 1282 (1981).

[84] R.B. Clare, D. Strottman and J. Kapusta. *Phys. Rev.* **C33**, 1288 (1986).

[85] G.F. Bertsch, H. Kruse and S. Das Gupta. *Phys. Rev.* **C29**, 673 (1984).

[86] H. Kruse, B.V. Jacak and H. Stöcker. *Phys. Rev. Lett.* **54**, 289 (1985).

[87] F. Reif. *Fundamentals of Statistical and Thermal Physics.* McGraw-Hill, 1965. pp. 494ff.

[88] E.A. Uehling and G.E. Uhlenbeck. *Phys. Rev.* **43**, 552 (1933).

[89] G.F. Bertsch. *Phys. Rev. C* **15**, 713 (1977).

[90] T. Johansson et al. *Phys. Rev. Lett.* **48**, 732 (1982).

[91] B. Jakobsson. *Phys. Scr.* **T5**, 207 (1983).

[92] H. Noll et al. *Phys. Rev. Lett.* **52**, 1284 (1984).

[93] E. Chiavassa et. al. *Nucl. Phys.* **A422**, 621 (1984).

[94] V. Bernard et. al. *Nucl. Phys.* **A423**, 511 (1984).

[95] Ch. Michel. Subthreshold neutral pion production in heavy ion collisions. In *XXI Meeting on Nuclear Physics, Bormio*, January 1983.

[96] P.J. McNulty et al. *Phys. Rev. Lett.* **38**, 1519 (1977).

[97] P.J. Lindstrom et al. *Phys. Rev. Lett.* **40**, 93 (1978).

[98] R. Kullberg, A. Oskarsson and I. Otterlund. *Phys. Rev. Lett.* **40**, 289 (1978).

[99] H. Heckwolf et al. *Z. Phys.* **A315**, 243 (1984).

[100] P. Braun-Munzinger et. al. *Phys. Rev. Lett.* **52**, 255 (1984).

[101] G.R. Young et al. *Phys. Rev.* **C33**, 742 (1986).

[102] J. Stachel et al. *Phys. Rev.* **C33**, 1420 (1986).

[103] E. Aslanides et al. *Phys. Rev. Lett.* **43**, 1466 (1979), **45**, 1738 (1980).

[104] Y. LeBornec et al. *Phys. Rev. Lett.* **47**, 1870 (1981).

[105] L. Bimbot et al. *Phys. Lett.* **114B**, 311 (1982).

[106] Y. LeBornec et al. *Phys. Lett.* **133B**, 149 (1983).

[107] N. Willis et al. *Phys. Lett.* **136B**, 334 (1984).

[108] T. Bressani et al. *Phys. Rev.* **C30**, 1745 (1984).

[109] B. Jakobsson, J.P. Bondorf and G. Fái. *Phys. Lett.* **82B**, 35 (1979).

[110] V. Bellini, M. Di Toro and A. Bonasera. Technical Report P. 85.18, GANIL, 1985.

[111] R. Shyam and J. Knoll. *Phys. Lett.* **136B**, 221 (1984).

[112] R. Shyam and J. Knoll. *Nucl. Phys.* **A426**, 606 (1984).

[113] J. Cugnon, J. Knoll and J. Randrup. *Nucl. Phys.* **A360**, 444 (1981).

[114] J. Aichelin and G. Bertsch. *Phys. Lett.* **138B**, 350 (1984).

[115] V. Weisskopf. *Phys. Rev.* **52**, 295 (1937).

[116] J. Aichelin. *Phys. Rev. Lett.* **52**, 2340 (1984).

[117] M. Prakash, P. Braun-Munzinger and J. Stachel. *Phys. Rev.* **C33**, 937 (1986).

[118] A. Bonasera and G.F. Bertsch. Technical Report MSUCL-600, Michigan State University Cyclotron Laboratory, April 1987.

[119] D. Vasak, B. Müller and W. Greiner. *Phys. Scr.* **22**, 25 (1980).

[120] D. Vasak, H. Stöcker, B. Müller and W. Greiner. *Phys. Lett.* **93B**, 243 (1980).

[121] D. Vasak, et al. *Nucl. Phys.* **A428**, 291 (1984).

[122] Brigitte Hiller and Hans J. Pirner. *Phys. Lett.* **109B**, 338 (1982).

[123] K. Klingenbeck, M. Dillig and M.G. Huber. *Phys. Rev. Lett.* **47**, 1654 (1981).

[124] J.W. Norbury, F.A. Cucinotta, P.A. Deutchman and L.W. Townsend. *Phys. Rev. Lett.* **55**, 681 (1985).

[125] P.A. Deutchman, J.W. Norbury and L.W. Townsend. *Nucl. Phys.* **A454**, 733 (1986) (and references therein).

[126] *Bevatron/Bevalac Users's Handbook: Nuclear Science.* Available from the Accelerator Research Coordination (ARC) Office, Lawrence Berkeley Laboratory Building 51, Room 208.

[127] T. Nagae et al. In preparation for publication.

[128] S. Hayashi. *Production of Pions and Light Fragments in 0.8 GeV/A La+La Collisions.* Master's thesis, University of Tokyo, 1986.

[129] F. Sauli. *Principles of Operation of Multiwire Proportional and Drift Chambers.* Technical Report 77-09, CERN, 1977.

[130] C. Tull, private communication.

[131] T. Kobayashi and T. Nagae, private communication.

[132] B. Gabioud et al. *DISPLAY.* Technical Report Group A Physics Programming Note P-269, Lawrence Berkeley Laboratory, July 1980. Revised May 1987.

[133] A.R. Smith et al. *Phys. Rev.* **C28**, 1614 (1983).

[134] I. Tanihata, private communication.

[135] G.F. Krebs, private communication.

[136] H.J. Crawford. *Single Electron Attachment and Stripping Cross Sections for Relativistic Heavy Ions.* PhD thesis, University of California, Berkeley, June 1979. LBL-8807.

[137] This approach was suggested by A.R. Baden.

[138] K. Nakai et al. *Phys. Rev. Lett.* **44**, 1446 (1980).

[139] D. Ashery et al. *Phys. Rev.* **C23**, 2173 (1981).

[140] M.-C. Lemaire et al. Technical Report LBL-8463, Lawrence Berkeley Laboratory, November 1978.

[141] J. Miller et al. *Phys. Rev. Lett.* **58**, 2408 (1987) and **59**, 519 (1987).

[142] L.A. Didenko et al. Technical Report EI-84-354, JINR, 1984.

[143] I. Tanihata, private communication.

[144] Karl Van Bibber and Andres Sandoval. Streamer chambers for heavy ions. In D.A. Bromley, editor, *Treatise On Heavy Ion Science*, page 333ff., Plenum, 1985.

[145] G. Westfall, private communication.

[146] J. Cugnon, D. Kinet and J. Vandermeulen. *Nucl. Phys.* **A379**, 553 (1982).

[147] J. Cugnon, T. Mizutani and J. Vandermeulen. *Nucl. Phys.* **A352**, 505 (1981).

[148] J. Cugnon. *Nucl. Phys.* **A387**, 191 (1982).

[149] M. Cahay, J. Cugnon and J.Vandermeulen. *Nucl. Phys.* **A411**, 524 (1983).

[150] J.W. Harris, private communication.

[151] B. Schürmann. Invited talk, 8th High Energy Heavy Ion Study, Lawrence Berkeley Laboratory, Nov. 16-20, 1987.

[152] Y. Kitazoe, et al. *Phys. Lett.* **166B**, 35 (1986).

[153] Y. Kitazoe, private communication.

[154] J. Cugnon, private communication.

[155] W. Benenson. What do angular distributions of subthreshold pions tell us about heavy ion reactions? In R.D. Bent, editor, *Proceedings of the Workshop on Pion Production and Absorption in Nuclei—AIP Conference Proceedings No. 79*, pages 381–388, IUCF, 1981.

[156] K.G. Libbrecht and S.E. Koonin. *Phys. Rev. Lett.* **43**, 1581 (1979).

[157] J. Cugnon and S.E. Koonin. *Nucl. Phys.* **A355**, 477 (1981).

[158] M. Gyulassy and S.K. Kauffmann. *Nucl. Phys.* **A362**, 403 (1981).

[159] H.M.A. Radi et al. *Phys. Rev.* **C25**, 1518 (1982).

[160] H.M.A. Radi et al. *Phys. Rev.* **C27**, 606 (1983).

[161] A.F. Barghouty and G. Fai. *Phys. Rev.* **C35**, 950 (1987).

[162] G. Bertsch. *Nature* **283**, 280 (1980).

[163] M. Bawin and J. Cugnon. *Phys. Rev.* **C25**, 387 (1982). The authors have obtained an exact, non-perturbative expression for the Coulomb phase

space distortion introduced by Gyulassy and Kauffmann, and have calculated the ratio of the perturbative and exact solutions. For large charges, the difference at low pion energy is significant.

[164] I. Navon et al. *Phys. Rev.* **C28**, 2548 (1983).

[165] W. Schimmerling, et al. *Phys. Rev. Lett.* **43**, 1985 (1979).

[166] R.A. Cecil, et al. *Phys. Rev.* **C24**, 2013 (1981).

[167] R. Stock, private communication.

[168] J. Stevenson et al. *Phys. Rev. Lett.* **57**, 555 (1986).

[169] B.A. Remington, M. Blann and G.F. Bertsch. *Phys. Rev. Lett.* **57**, 2909 (1986).

[170] W. Benenson, private communication.

LAWRENCE BERKELEY LABORATORY
TECHNICAL INFORMATION DEPARTMENT
UNIVERSITY OF CALIFORNIA
BERKELEY, CALIFORNIA 94720